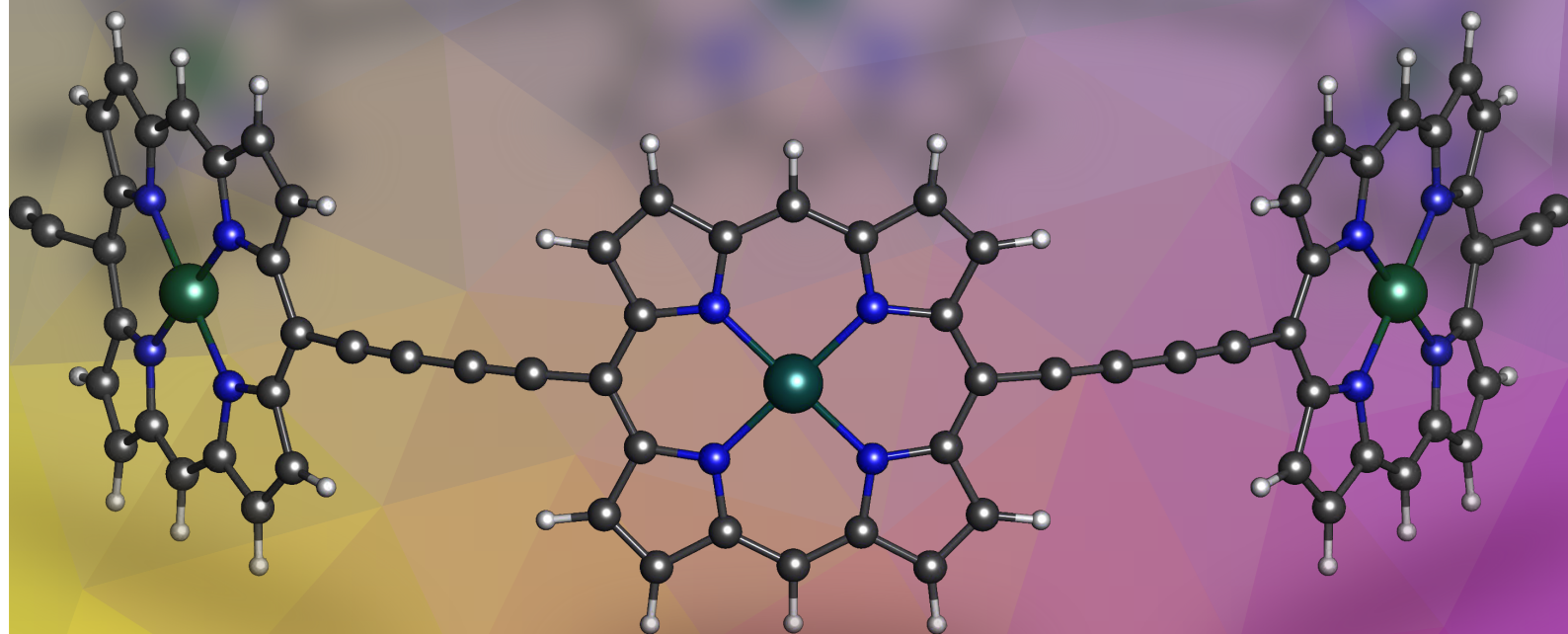


Computational study of Aromaticity in Porphyrinoid Systems and Photosensitizers from Chemical Bonding Descriptors

 **Irene Casademont Reig** 

2021



Computational study of Aromaticity in Porphyrinoid Systems and Photosensitizers from Chemical Bonding Descriptors

A dissertation submitted to
Universidad del País Vasco/Euskal Herriko Unibertsitatea
(UPV/EHU)
presented by
Irene Casademont Reig

2021, Donostia

Doctoral Program in Theoretical Chemistry and Computational Modeling
Supervised by Dr. Eduard Matito Gras
Cosupervised by Dr. Eloy Ramos Cordoba
Tutorized by Dr. Jesus M. Ugalde Uribe-Etxebarria



Dedication

I want to start this thesis by explaining what I have been studying since I left high school. Maybe it is not the usual way to start, but I have always wanted to think for a while about how I can explain it easily. A way that all my relatives can understand it, especially my grandmother. For this reason, I am going to shift to my mother language.

Sempre ha estat difícil contestar les preguntes del tipus: 'què estudies?' 'Química, ah sí!, Física i Química...' 'Però no has acabat ja d'estudiar, encara no has acabat la carrera?' 'Ah! el doctorat..., i què és aixó?' 'Estudies?' 'Vas a classe?' 'Cobres?'

El dia a dia està ple de química i processos químics que podem definir sense utilitzar la paraula explícita 'química', des de que et lleves i prepares una torrada per esmorzar fins que vas a dormir després de fer la digestió. La química és la ciència que estudia les propietats, la composició, l'estructura i la transformació de la matèria. Com en moltes altres àrees de coneixement, la química es divideix en diferents branques, de les quals podem destacar la orgànica, inorgànica, analítica i teòrica. Sí!, jo em vaig decidir per la química teòrica i més aviat la computacional. Per tant, el meu dia a dia no és en un laboratori sinó en un despatx, i no el dedico a fer experiments sinó càlculs amb l'ordinador. Dit d'una forma molt senzilla, els químics teòrics podem arribar a simular el que un químic experimental pot fer en el laboratori.

Aquesta tesi està centrada bàsicament en el concepte químic de l'Aromaticitat. Sempre penso: 'Químicament, aquest concepte no té una definició clara perquè no correspon a cap propietat observable d'una molècula. Per tant, si científicament és difícil explicar aquesta propietat imagineu-vos explicar-la en llenguatge coloquial!' Però ho provaré fent el seu anàleg cotidià i dient que una molècula aromàtica és equivalent a una ciutat amb diferents cotxes distribuïts per tots els carrers i sense que hi hagin retencions en cap punt concret, on la molècula seria la ciutat i els cotxes serien els electrons (un tipus de partícula amb càrrega negativa que trobem en les molècules). Els cotxes poden circular per diferents carrers de la ciutat igual que els electrons es poden moure entre els àtoms de la molècula per diferents enllaços. Una ciutat pot tenir més o menys cotxes igual que una molècula pot tenir més o menys electrons. I així podria anar fent analogies per poder explicar el que he fet durant aquests anys..."

Per en Teti i en Toni!

Acknowledgements

Tot va començar un estiu molt incert, no tenia cap viatge programat, cap feina, ... i almenys dos mesos per endavant. Quan un matí vaig rebre un correu d'un professor de la uni del que no havia sentit mai el seu nom. Qui ho havia de dir que aquell correu decidiria els meus propers anys!

M'agradaria agrair a tota la gent que m'ha acompanyat en aquest camí! L'últim any ha sigut com d'una pel·lícula de ciència ficció degut a la pandèmia de la COVID-19 (tampoc podia deixar d'esmentar-la, molt sovint és l'únic tema de conversa) i m'ha fet valorar moltíssim els anys anteriors! Moltes gràcies!/Mila esker!/Muchas gracias!/Thank you!

Especialment, m'agradaria agrair enormement als meus dos directors de tesi l'Edu i l'Eloy. Des del primer moment van confiar en mi i en donar-me una oportunitat per treballar amb ells tot i no saber absolutament res de Química computacional (i és ben veritat! Aixó ho sé segur, no ho dubto=)). Gràcies per tot el que he après al vostre costat i per les oportunitats que m'heu donat, que no són poques! I a en Miquel, el nostre principal col·laborador en quasi tots els projectes de la meva tesi, sempre disposat a ajudar-me en tot el que calgués i dedicar el temps necessari a explicar-me allò que no entenien, quasi el meu tercer supervisor.

Kimika teoriko talde guztiari eskerrak eman nahi dizkiot. Zuek gabe, urte guzti hauek ez ziren gauza bera izango! Tengo que reconocer que cuando llegué, con lo tímida que soy y viendo que había pocos estudiantes pensé uy! Dónde te has metido!...Pero en seguida me sentí como en casa, empezando con Jesus, hablando en Catalán, quedé enormemente sorprendida ('I el forn?') Mila esker Jesus, nire euskara urte hauetan hobetu izana espero dut. Zer diozu? Desde el primer día que conocí a Mario Piris supe que la timidez se quedaria atrás ('Qué Eloy, la llevarás a bailar esta noche?', 'uy Irene no sabía que estabas aquí, no te había escuchado' y 'recuerda, te lo dice uno desde la atalaya de la edad...'), las visitas a mi despacho que terminaban con una bonita representación del grupo en la pizarra o incluso vídeos explicando los proyectos de una=)). Rafa, siempre estaba cuando necesitaba algo. Espero verte pronto! Elisa (y su kariño y los martes locos!), Elena (mi traductora de referencia), Claire (y la tortilla!), Vero (i els cafès després de dinar, sobretot en època de pandèmia quan érem quatre gats al DIPC, bé set comptant

els gatets mai millor dit!), Txema (y las prácticas compartidas), Xabi (y sus KT-TO news), Eli, Txoni (y su ayuda con la burocracia), DavidC, Joni, Abel, DavidS.

Los pocos estudiantes que estaban en el grupo cuando llegué: Mau (ratainmunda con cariño=), 'Siempre pensé que tú no venías a Donostia engañada por el tiempo!') Juranga (sin tus bromas en el despacho no hubiera sido lo mismo y esas noches en la parte Vieja!") Ion (el primero en hacerme un hueco en su piso sin problema) y Olatz (C π C team).

Las Montserrats! Gracias por todos estos años en el DIPC pero sobretodo fuera, todas las saliditas hechas y las pendientes! Mireia, sempre sabia que el teu 'Hola' quan entraves al despatx de bon matí era Català i no Castellà=)) Maru, como buena mexicanocatalana que eres no hace falta traducir esto: Recuerdo el primer día que ens vam conèixer, que cap de les dues recordava fins que en Rafa ens va fer memòria i el primer cafè a Gros un dissabte recent acabada d'arribar de nou a Donostia. Al resto de miembros de Quantum Chemistry Development Group (alias Matito's Group o La Comarca): Xiang, Carmelo ('Si no haces no te vas a graduar!'), Sebastian, Aaron, Silvia E ('Vinga, ara que no vigila el socorrista, aprofitem per tirar-nos!'), Rubén, Luis, Markel y Xuban. Un gusto compartir con vosotros todas las discusiones científicas, Literature Meetings, Congresos, Coffe Time during confinement, pero sobretodo las cenas en la sociedad que ya se echan de menos!

Los primeros estudiantes de doctorado que llegaron en septiembre: Jorge y Cris (siempre se puede contar con vosotros incluso si hay que partir unas piernas a alguien...hahahaha), Sofía, María (y el intento de torrijas), y al resto 'DIPC+arrimados', Mikel1 (Olano) Milkel2 (Arruabarrena), Alejandro y nuevas incorporaciones (en su momento) Pepitooo (Pep@Pig), Txantxot (o Dr. Txantxot? y la primera 'fiesta' después del confinamiento), Telleria ('HF house'), MaríaZ e Irene2 (Ruiz). También a mis compis de Euskera!



I want to thank the opportunity to be in Trygve Helgaker's group in the Hylleraas Centre for Quantum Molecular Sciences and all the members. I really enjoyed my Ph.D. stay in Oslo. Moltes gràcies David Balcells per la teva supervisió durant l'estada i també a l'Ainara. Muchas gracias también a Abril, Lluís, Juan ('holisssss, qué toca hoy para comer? verduritaaaa'), Stephanie de México y Katica, sin vosotros no hubiera sido lo mismo, 'Mexico 2021????'

No oblidarme dels companys de uni i profes, en especial a l'Eila, en Christian, l'Edu, la Mayo i sobretot a la Marga (he après moltíssim de tu!). També volia agrair a en Sergio, la Carla, l'Arnau i en Julio Lloret per ajudar-me en el seu moment i per proporcionar-nos les dades experimentals.

Los biólogos pivones David i MarinaC, Carla (la distància hi ha sigut però per casualitats de la vida vam acabar estudiant el mateix!) i la MarinaZ (la super aventurera!)

Per últim però no per això menys important, tot el contrari, m'agradaria agrair a tota la meva família, però especialment a la meva mare per tot el seu suport durant tot aquest temps i podria dir que tota la vida i, en Raúl por su soporte infinito, su paciencia conmigo sobretodo durante estos últimos meses y sus enormes ganas de ayudarme siempre con todo lo que necesite!

Asko maite zaituztet! Besarkada handi bat! Us estimo!

Full list of publications

This thesis is presented as a compendium of publications:

- I. Casademont-Reig, T. Woller, J. Contreras-García, M. Alonso, M. Torrent-Sucarrat and E. Matito. **New electron delocalization tools to describe the aromaticity in porphyrinoids**, *Phys. Chem. Chem. Phys.* **2018**, *20*, pp. 2787-2796.
- I. Casademont-Reig, E. Ramos-Cordoba, M. Torrent-Sucarrat and E. Matito. **How do the Hückel and Baird Rules Fade away in Annulenes?**, *Molecules*, **2020**, *25*, pp. 711.
- I. Casademont-Reig, E. Ramos-Cordoba, M. Torrent-Sucarrat and E. Matito. **Aromaticity descriptors based on electron delocalization** in *Aromaticity. Modern computational methods and applications*, Elsevier, **2021**, pp.235-258.
- I. Casademont-Reig, R. Guerrero-Avilés, E. Ramos-Cordoba, M. Torrent-Sucarrat and E. Matito. **How aromatic are molecular nanorings? The case of a six-porphyrin nanoring**, *submitted to Angew. Chem. Int. Ed.*
- I. Casademont-Reig, A. Call, C. Casadevall, S. Fernández, J. Lloret-Fillol, E. Ramos-Cordoba and E. Matito. **Computational modeling of UV-Vis spectra and redox potentials**, *In preparation*.

Publications not included in this thesis:

- A. H. Dardir, I. Casademont-Reig, D. Balcells and N. Hazari. **Synthesis of Triarylmethanes via Palladium-Catalyzed Suzuki-Miyaura Reactions of Diarylmethyl Esters**, *accepted in Organometallics*, **2021**.
- T. Woller, I. Casademont-Reig, V. García, J. Contreras-García, W. Tiznado, M. Torrent-Sucarrat, E. Matito and M. Alonso. **Is the annulene model still valid for (de)protonated expanded porphyrins?**, *In preparation*.
- I. Casademont-Reig, E. Matito and M. Torrent-Sucarrat. **Does Baird's rule apply to Expanded Porphyrins?**, *In preparation*.

List of abbreviations

Abbreviation	Description
1-RDM	First-order reduced density matrix
2-RDM	Second-order reduced density matrix
ACID	Anisotropy of the induced current density
ACP	Attractor critical point
AIM	Atom in a molecule
AOM	Atomic overlap matrix
ASE	Aromatic stabilization energy
BLA	Bond length alternation
BO	Bond order
BOA	Bond order alternation
BCP	Bond critical point
CASSCF	Complete active space self-consistent field
CBO	Coulson bond order
CC	Coupled cluster
CCP	Cage critical point
CCSD	Coupled cluster including only single and double excitations
CCSD(T)	Coupled cluster including only single, double, and an estimation of triple excitations
CI	Configuration interaction
CIS	Configuration interaction with single excitations
CISD	Configuration interaction with single and double excitations
CP	Critical point
CT	Charge transfer
DFA	Density functional approximation
DFT	Density functional theory
DE	Delocalization error
DI	Delocalization index
DLPNO	Domain localized pair natural orbital (method)
DSSC	Dye-sensitized solar cell

Abbreviation	Description
eff-AO	Effective atomic orbital
EOS	Effective oxidation potential
ESI	Electron-sharing index
E_{XC}	Exchange correlation energy
FCI	Full-configuration interaction
FLU	Aromatic fluctuation index
GGA	Generalized gradient approximation
GTO	Gaussian-type orbital
HF	Hartree-Fock
HOMA	Harmonic oscillator model of aromaticity
HOMO	Highest occupied molecular orbital
HMO	Hückel molecular orbital
KS	Kohn-Sham
KS-DFT	Kohn-Sham density functional theory
LDA	Local density approximation
LED	Light-emitting diode
LI	Localization index
LPNO	Localized pair natural orbital (method)
LR	Long range
LSDA	Local spin-density approximation
LUMO	Lowest unoccupied molecular orbital
MCI	Multicenter index
MO	Molecular orbital
MP	Møller-plesset perturbation theory
MP2	Second-order Møller-plesset perturbation theory
NICS	Nuclear independent chemical shifts
OLED	Organic light-emitting diode
OS	Oxidation state
PAO	Projected atomic orbitals
PDI	Para-delocalization index
PES	Potential energy surface
PNO	Pair natural orbitals
PS	Photosensitizer
QTAIM	Quantum theory of atoms in molecules
RCP	Ring critical point
RDM	Reduced density matrix
RSF	Range-separated functionals

Abbreviation	Description
SD	Single determinant
SIE	Self-interaction error
SR	Short range
STO	Slater-type orbital
TFVC	Topological fuzzy Voronoi cells
WS	Water splitting
XC	Exchange correlation
XCD	Exchange-correlation density

List of Figures

1.1	Scheme of Turing test, an aromatic version.	3
1.2	Michael Faraday (1791-1867) ³¹	7
1.3	Most relevant advances in the field of aromaticity from 1825 to 1931. Figure adapted from Ref. 34 and modified by Prof. Miquel Solà and the present author.	9
1.4	Most relevant advances in the field of aromaticity from 1938 to 1983. Figure adapted from Ref. 34 and modified by Prof. Miquel Solà and the present author.	10
1.5	Most relevant advances in the field of aromaticity from 1985 to 2015. Figure adapted from Ref. 34 and modified by Prof. Miquel Solà and the present author.	11
1.6	Porphin structure with labeled relevant positions. In purple, its annulene path.	15
1.7	Schematic representation of three expanded porphyrin topologies. . . .	16
2.1	Representation of Jacob's Ladder.	31
2.2	Schematic plot of exact exchange percentage included in B3LYP (HF[%]=19), M06-2X (HF[%]=54), CAM-B3LYP (HF[%]=19-65) functionals and LC general scheme (HF[%]=0-100).	33
3.1	QTAIM analysis of benzene. In grey the relief map of electron density (ρ) is plotted. The carbon atoms in grey, hydrogen atoms in white, BCP in green, RCP in red, bond path in black lines and ring path in yellow dashed lines are represented.	44
3.2	Schematic representation of bonds used in AV1245 index.	57
3.3	1245-index distribution profile of porphin and isophlorin along the most aromatic path. This path corresponds to the annulene one for porphin and to the outer one for isophlorin. Horizontal solid line corresponds to the AV1245 value and dashed line to the AV_{min} value (see Table 3.1). . .	59
3.4	ACID isosurface plots (isocontour value 0.06) for (left) porphin and (right) isophlorin.	62

10.1	Values of the I_{ring}^{HMO} normalized index for the annulenes series against the number of carbon atoms (N) for different singlets and triplets. . . .	160
10.2	Porphyrin pathways. To label each path, the top left 5-MR is taken and follow the clockwise direction. The green and the orange circuits highlight the annulene and the anti-annulene paths, respectively. . . .	163
10.3	AV1245 colored representations for the inner pathway of 18H (left) and 32E (right). The numerical values correspond to the DIs.	165
10.4	Values of $\overline{I}_{ring}^{-1/N}$ for the singlet and triplet lowest-lying states of the studied annulenes obtained with HF, M06-2X, CAM-B3LYP, and B3LYP.	167
10.5	Schematic representation of the potential energy surface of c-P6 ⁶⁺ species described by different computational methods. Circles represent the porphyrins of the structure.	169
10.6	Scheme of the global aromatic character of the nanoring species according to the optimized geometries obtained with different DFAs. Full, half-full and empty circles represent aromatic, weakly aromatic and nonaromatic porphyrins, respectively. The electron delocalization in the linkers increases from single solid lines (no delocalization), to solid-dashed lines and double lines.	170
10.7	NICS(0) _{iso} grid plots for the c-P6 ⁶⁺ species. The <i>l.h.s.</i> plot corresponds to CAM-B3LYP optimized geometry and the <i>r.h.s.</i> to B3LYP one. . . .	171
10.8	Nanoring structure and the studied model without the bridging butadiyne linkers. Small red dots indicate the position of ortho protons of the aryl substituent and the α and β protons of the template, respectively.	172
10.9	Relationship of AV_{min} among nine porphyrinoid systems calculated with M06-2x and B3LYP against CAM-B3LYP values for all the annulene pathways.	173
10.10	Comparison of the 1245-index distributions including the individual MCI(1,2,4,5) values along the most aromatic path of c-P6 · T6 ⁶⁺ species calculated at different levels of theory. Horizontal solid line corresponds to the AV1245 value (1.48) and dashed horizontal line to the AV_{min} value (0.64), both from CAM-B3LYP calculation.	174
10.11	Simulated UV-Vis absorption spectrum with LC- ω PBE-opt, LC- ω PBE and B3LYP functionals, and the experimental spectrum of a copper photosensitizer (PS ₈). The spectra are plotted using a standard deviation of 0.4eV. For LC- ω PBE-opt functional, we have also plotted the orange vertical lines corresponding to the different vertical excitations.	176

List of Tables

3.1	Aromaticity descriptors values of porphin, isophlorin, benzene, cyclohexane, and cyclohexatriene ($a/b=0.8$) at CAM-B3LYP/6-311G(d,p) level of theory.	50
10.1	Aromaticity indices for different systems calculated at the CAM-B3LYP/6-311G(d,p) level of theory.	161
10.2	Aromaticity indices for different pathways in 18H, calculated at the CAM-B3LYP/6-311G(d,p) level of theory. The number in parentheses indicates the equivalent pathways.	164
10.3	Selected $^1\text{H-NMR}$ chemical shifts differences of the different nanoring species (in ppm). Root-mean-square deviations (RMSD) are based on the experimental differences. ^{1,58}	172
10.4	Redox potentials (E_{red}^o , in V) calculated using B3LYP, LC- ω PBE-opt, and CAM-B3LYP. The experimental available data is also included. Maximum error (MAX), root mean square error (RMSE), and mean absolute error (MAE) of each method are also given.	177

Abstract

Theoretical and computational chemistry has gained a crucial role among the disciplines that study chemical phenomena because it provides low-cost accurate results avoiding risky laboratory tasks and contamination. Nowadays, the method of choice to simulate medium to large molecules is density functional theory. It provides an excellent balance between accuracy and computational cost. In principle, DFT is an exact theory but, as the exact energy functional is unknown, in practice, we employ density functional approximations. These approximations have improved over the years, however, they still suffer from large errors. One of the most important errors is the delocalization error. It is responsible for many failures in different chemical properties, such as the underestimation of band gaps, the incorrect description of nonlinear optical properties, the over/underestimation of aromatic character, and the incorrect description of charge-transfer excitations.

The first part of this thesis focuses on studying one of the properties affected by the delocalization error, the aromatic character of (large) conjugated systems. *Aromaticity* is an ill-defined chemical property that does not correspond to any physical observable. However, we can measure the aromatic character of molecules by studying several manifestations of aromaticity: energy stabilization, bond-length equalization, exalted magnetic properties, and electron conjugation and delocalization. These properties have been used to define several aromaticity indices that can be classified as energetic, geometric, magnetic, and electronic. Some of them are used in the present dissertation to study the aromatic character of large systems as well as to test the recently developed electronic indices, AV1245 and AV_{min} . Firstly, simple expanded porphyrins and an annulene series are studied to test the new aromatic descriptors, and compare their behavior against the well-established ones. Interestingly, we find that only the AV_{min} index is capable of recognizing the annulene pathway as the most aromatic one in neutral porphyrinoids.

The study of simple porphyrinoids is used to establish a protocol to study larger and more complicated systems like a six-porphyrin nanoring. The larger the system, the less aromatic character is expected to be due to out-of-plane distortions and the exhibition of a poor overlap between p orbitals. For this reason, it is difficult to find large aromatic macrocycles. Accordingly, geometrical constraints are imposed in some large macrocyclic structures with the hope to preserve conjugation, aromaticity, and quantum coherence. One of the most relevant large macrocycles lately synthesized is a six-porphyrin nanoring which is aromatic in its +6-oxidation state according to the authors.¹ We study this and other oxidation states of the nanoring and conclude that some of those molecules suffer from large delocalization errors. As a consequence, the +6-oxidation state is found to be nonaromatic.

In all aforementioned works, we paid special attention to the computational method used to perform the aromaticity analysis. We find that density functional approximations with a low percentage of exact exchange at large interelectronic distances are prone to present large delocalization errors, leading to an overdelocalization of electrons. Hence, the geometry of these compounds is affected, giving a spurious enhancement of the aromaticity.

In the last part of this thesis, different families of photosensitizers and catalysts involved in different photocatalytic processes are examined. The aim of this work is to design a rigorous protocol to unravel the electronic structure of this family of complexes, simulate their UV-Vis spectra, and compute their redox potentials. *Photosensitizers* are light-harvesting molecules that present charge-transfer excitations. These excitations are also affected by deficiencies of the density functional approximations like the delocalization error, and are usually treated with range-separated functionals. We also study them using an optimally-tuned range-separation functional and compare the UV-Vis absorption spectrum and redox potential with the available experimental data. We find that an optimally-tuned range-separation functional highly improves the UV-Vis absorption spectra of systems that present charge-transfer excitations and, in general, it also slightly improves the reduction potentials.

We expect that this thesis will provide a solid computational framework to study the aromaticity of large conjugated circuits such as extended porphyrins and macrocycles, as well as the analysis of UV-Vis absorption spectra and redox potentials of molecules involved in photocatalytic processes.

Resumen

La Química teórica y computacional ha adquirido un papel crucial entre las disciplinas que estudian los fenómenos químicos, porque permite obtener resultados precisos a un coste bajo, evitando los posibles riesgos asociados con los experimentos y la contaminación ambiental. Hoy en día, los métodos que se usan para el estudio de medianas y grandes moléculas están basados en la teoría del funcional de la densidad. Estos métodos proporcionan el mejor balance entre precisión y coste computacional. En principio, la teoría del funcional de la densidad es exacta, pero como se desconoce el funcional exacto de la energía, en la práctica tenemos que usar aproximaciones al funcional de la densidad. Aunque estas aproximaciones se han mejorado durante los últimos años, aún presentan diferentes errores. Uno de los errores más importantes es el error de deslocalización. Este error es responsable de muchos fallos en diferentes propiedades químicas, como por ejemplo la subestimación de la diferencia entre niveles energéticos, la descripción incorrecta de las propiedades ópticas no lineales, la sobre o infravaloración del carácter aromático y la descripción incorrecta de las excitaciones de transferencia de carga.

La primera parte de esta tesis se centra en una de las propiedades afectadas por el error de deslocalización, el carácter aromático de sistemas (grandes) conjugados. La aromaticidad es una propiedad química que carece de definición dentro de la mecánica cuántica, porque no se corresponde con ningún observable físico. Sin embargo, podemos medir el carácter aromático de las moléculas mediante el estudio de varias manifestaciones de la aromaticidad: estabilización de la energía, eualización de la longitud de los enlaces, propiedades magnéticas realzadas y conjugación y deslocalización de los electrones. Estas propiedades se han utilizado para definir distintos índices de aromaticidad que pueden clasificarse como energéticos, geométricos, magnéticos y electrónicos. Algunos de estos índices se utilizan en la presente tesis para estudiar el carácter aromático de grandes sistemas, y también para probar los índices electrónicos desarrollados recientemente, AV_{1245} y AV_{min} . En primer lugar, se estudia una familia de porfirinas expandidas simples y una serie de anulenos para probar los nuevos descriptores aromáticos y así, comparar su comportamiento con los índices más conocidos. Curiosamente, encontramos que sólo el índice AV_{min} es capaz de reconocer el circuito anulenico como el más aromático en porfirinas neutras.

El estudio de sistemas porfirínicos simples se utiliza con el fin de establecer un protocolo para estudiar sistemas más grandes y más complejos, por ejemplo un nanoanillo de seis porfirinas. Cuanto más grande es el sistema, se espera que el carácter aromático sea menor debido a las distorsiones fuera del plano y al escaso solapamiento entre los orbitales p . Por esta razón, es difícil encontrar macrociclos aromáticos de gran tamaño. En consecuencia, se imponen restricciones geométricas en algunas estructuras macrocíclicas para tratar de mantener la conjugación, la aromaticidad y la coherencia cuántica. Uno de los macrociclos grandes más relevante sintetizado últimamente es un nanoanillo de seis porfirinas que según los autores¹ es aromático en su estado de oxidación +6. Estudiamos este y otros estados de oxidación del nanoanillo concluyendo que algunos de estos sistemas sufren grandes errores de deslocalización. Como consecuencia, se encuentra que el estado de oxidación +6 no es aromático.

En todos los trabajos mencionados, prestamos especial atención al método computacional utilizado para el análisis de aromaticidad. Encontramos que las aproximaciones al funcional de la densidad con un pequeño porcentaje de intercambio exacto para distancias interelectrónicas largas, son propensas a presentar grandes errores de deslocalización, dando lugar a una sobre deslocalización de los electrones. Por lo tanto, la geometría de estos compuestos se ve afectada, dando un aumento espurio de la aromaticidad.

En la última parte de la tesis se han examinado diferentes familias de fotosensibilizadores y catalizadores implicados en diferentes procesos fotocatalíticos. El objetivo de este trabajo es diseñar un protocolo riguroso para el estudio de la estructura electrónica, la simulación de espectros UV-Vis y para el cálculo de potenciales redox. Los fotosensibilizadores son moléculas captadoras de luz que presentan excitaciones de transferencia de carga. Estas excitaciones, cuya simulación está afectada también por las deficiencias de las aproximaciones al funcional de la densidad, suelen tratarse con funcionales de separación de rango. También estudiamos estos fotosensibilizadores utilizando un funcional de separación de rango optimizando el parámetro de atenuación, y compararemos los resultados con los datos experimentales disponibles. Utilizando este último funcional, encontramos que hay una mejora significativa en los espectros de absorción UV-Vis de los sistemas que presentan excitaciones de transferencia de carga, y en general, también mejoran ligeramente los potenciales de reducción.

Esperamos que esta tesis proporcione un marco computacional sólido para estudiar la aromaticidad de sistemas grandes conjugados como porfirinas extendidas y macrociclos, así como el análisis de los espectros de absorción UV-Vis y los potenciales redox de moléculas implicadas en procesos fotocatalíticos.

Contents

List of abbreviations	ix
List of Figures	xiii
List of Tables	xv
Abstract	xvii
Resumen	xix
1 Introduction	3
1.1 Theoretical background	4
1.1.1 Limitations of current DFAs	5
1.2 Aromaticity and its rules	7
1.2.1 A pinch of history	7
1.2.2 The aromaticity definition	12
1.2.3 The most highlighted aromaticity rules and models	13
1.3 Porphyrinoid systems	14
1.4 Photosensitizers	18
2 Quantum chemistry methods	21
2.1 Hartree-Fock and a brief overview of post-HF methods	22
2.1.1 Coupled-cluster (CC) methods	25
2.1.2 Domain localized pair natural orbitals (DLPNOs)	26
2.2 Density Functional Theory (DFT)	28
2.2.1 Delocalization error (DE)	32
2.3 Range-separated functionals (RSF)	33
2.3.1 Tuning of the attenuating parameter	34
2.4 Time dependent density functional theory (TDDFT)	36
3 Aromaticity	39

3.1	Density and high-order density matrices	40
3.2	An atom in a molecule (AIM)	41
3.2.1	Effective oxidation states (EOS)	41
3.2.2	The quantum theory of atoms in molecules (QTAIM)	42
3.2.3	Population Analysis	44
3.2.4	Electron-sharing indices (ESI)	45
3.2.5	Multicenter indices	48
3.3	Aromaticity Descriptors	49
3.3.1	Energetic indices	51
3.3.2	Geometric indices	51
3.3.3	Electronic indices	53
3.3.4	Magnetic indices	59
4	Objectives	63
5	New electron delocalization tools to describe the aromaticity in porphyrinoids	65
6	How do the Hückel and Baird Rules Fade away in Annulenes?	77
7	Aromaticity descriptors based on electron delocalization	97
8	How aromatic are molecular nanorings? The case of a six-porphyrin nanoring	123
9	Computational modeling of UV-Vis spectra and redox potentials	137
10	Results and discussion	159
10.1	Aromaticity from the HMO method	160
10.2	Aromaticity from DFAs	161
10.2.1	Examples of presumably aromatic molecules	161
10.2.2	The most aromatic path in porphyrinoid systems	162
10.2.3	AV1245 colored representations	165
10.3	Delocalization error in DFAs	166
10.3.1	Geometry evaluation	166
10.3.2	Aromaticity indices	173
10.3.3	UV-Vis absorption spectra	175
10.3.4	Redox potentials	177
11	Conclusions	179

Bibliography	183
Appendices	205
A Supporting Information Chapter 5	207
B Supporting Information Chapter 6	221
C Supporting Information Chapter 8	227
D Supporting Information Chapter 9	247

Notation

Unless otherwise stated, throughout the current doctoral thesis the same notation has been used as detailed below.

Notation	Description
$r \equiv \vec{r}$	Coordinates of an electron in the Cartesian space indicated by a three-dimensional vector
$\mathbf{1} \equiv (r_1, \sigma_1)$	Cartesian coordinates of an electron including the spin polarization
$d_1 \equiv dr_1 d\sigma_1$	Electron position derivatives
N	Total number of electrons in the system
ψ	Electronic wavefunction
ϕ_μ	Atomic orbital
ϕ_i	Molecular orbital
i and j	Occupied orbitals
a and b	Virtual orbitals
ρ	Electron density
ρ_2	Pair density
\mathcal{A}	String $\mathcal{A} = \{A_1, A_1, \dots, A_n\}$ of a molecule with n atoms

Chapter 1

Introduction

*"Behave so the aroma of your actions may enhance
the general sweetness of the atmosphere."*

Henry David Thoreau

As chemists, we are interested in understanding chemical reactions, the thermodynamics of a system, the properties of a molecule, how a transition state looks like, and how a molecule behaves if we apply a magnetic field, among a significant number of phenomena. Some scientists would design an experiment while others would perform a simulation to investigate any of these properties or phenomena. Some time ago, when there were not as many computer resources as today, the first question that someone might have asked was: *'Could we come up with the same results using a computer and the necessary algorithms instead of going to the laboratory and design the proper experiment?'*

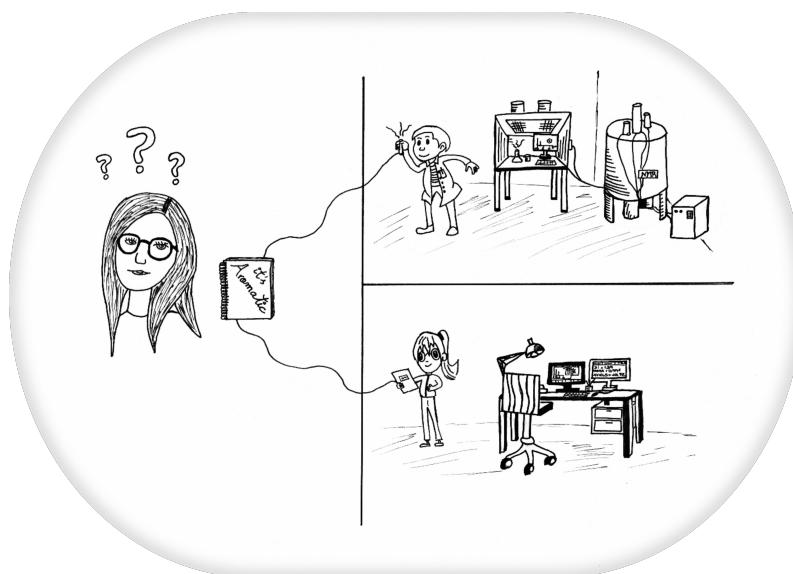


Figure 1.1: Scheme of Turing test, an aromatic version.

Going beyond the previous question, we could ask ourselves: '*Could we replace laboratory tasks with a computer?*', '*Could ultimately computers take over and do research?*'. For this to happen, machines should be able to think. For this reason, it is pertinent to try to connect this group of questions with the Turing test.²

Turing proposed a test based on the question '*Can machines think?*', in which he tried to test a machine's ability. The test consists in sitting a person in a room alone in contact with something that could be either a computer or a human. Then, asking intelligent questions, the person needs to figure out whether it is a computer or a human.³

Continuing with the exposed situation, we could imagine an ideal scenario where an applied experimental technique gives precisely the same conclusion as computational calculations. The only difference is that one conclusion comes from experimental measurements, while the other comes from a computation. Concretely, we could imagine the following situation: We have a ¹H-RMN spectrum indicating that some molecule is aromatic but, we do not know if it is an experimental spectrum or a simulated one, '*Are we collaborating with an experimental or a computational chemist?*' (Figure 1.1).

Machines can be so well designed that, in the Turing test, one can come to think that one is talking to a human rather than a machine. In the same manner and generally speaking, computational chemistry simulations can be as accurate as experiments.

The present thesis is a computational investigation that mainly focuses on studying the chemical property of aromaticity in large conjugated systems using different indices, testing the newly developed ones, and comparing them with the well-established descriptors. Furthermore, a deep analysis of how the delocalization error present in some density functionals approximations affects the aromatic characterization of large systems and the description of photosensitizers with charge-transfer excitations is done. The obtained results have been compared with the existing rules or theories, experimental results, or calculations obtained at a higher computational level.

1.1 Theoretical background

Theoretical chemistry is the branch of chemistry that treats molecules with the aid of classical and quantum physics. Although classical mechanics is used to accurately reproduce the behavior of macroscopic objects such as cars or people's movements, it is sometimes advantageous to approximate molecular properties by applying the laws of classical physics using molecular mechanics.⁴ The parameters in molecular mechanics methods are obtained by fitting to known experimental data or higher-level methods; in other words, they are empirical models. Quantum mechanics, by contrast, is the theory applied to the study of microscopic objects (for instance, electrons with a mass of 9.109×10^{-31} kg).⁵ For this reason, quantum mechanics plays a crucial role in theoreti-

cal chemistry to study electrons in atoms and molecules. The application of quantum mechanics to theoretical chemistry is also known as quantum chemistry. Moreover, the application of quantum chemistry together with molecular mechanics, minimization, simulations, conformational analysis, and other computer-based methods to study molecular systems is termed *computational chemistry*.⁶

With computational chemistry, we can study, in principle, any atom, molecule or group of molecules. The size of the system, the computational cost of the methods and the computational resources available will limit the scope of our study. Quantum chemistry is dedicated to develop new approximations to solve the Schrödinger equation, improve the applicability of existing approaches, build methods to analyze the results, and apply the methods to study a specific chemistry problem. In many cases, one can assist or complement the experimental studies providing direct evidence of the reaction mechanism, performing simulations of complicated or dangerous experimental procedures, or screening large families of molecules, often by reducing the associated economic costs.

One of the main goals of quantum chemistry is understanding the electronic structure of molecules by solving the Schrödinger equation usually employing the Born-Oppenheimer approximation.⁷ Ground-state properties of molecular systems are obtained by solving the time-independent Schrödinger equation. Since this equation cannot be solved exactly (beyond the hydrogen atom and hydrogenoid atoms), many approximate methods have been proposed. These methods are characterized by their computational cost and accuracy.

Almost all quantum chemistry methods can be broadly classified either as wavefunction-based methods (Hartree-Fock (HF) and post-HF methods exposed in more detail in Section 2.1), density functional based methods (density functional theory (DFT) and density functionals approximations (DFAs)) or *semi-empirical* methods.^{8,9} The latter, will not be covered in this thesis.

The vast majority of the calculations for the different studies presented in this thesis are performed within the DFT framework (see section 2.2). In the next subsection, we will see the main limitations of the density functionals approximations used in DFT. To assess the accuracy of the DFT methods, HF and some post-HF methods have been used (see Section 2.1 and Section 10).

1.1.1 Limitations of current DFAs

Density Functional Theory was introduced by Hohenberg and Kohn in 1964 and states that any ground state property of a system can be calculated from the electron density. In other words, it exists a universal density functional for any property. However, the expression of the energy as a functional of the electron density is not entirely known, and several approximations must be carried out. As a result, we have several DFAs. We

will further discuss DFT theory in the following chapter (Section 2.2).

Despite the enormous popularity of DFAs and their high success, they still suffer from large errors, which can be analyzed considering the exact conditions violated by the approximate density functionals.¹⁰ These errors may result in qualitative and quantitative failures in the description of targeted properties and they occur even in elementary molecules (e.g., H_2^+ or H_2 molecule). Current DFA errors can be mostly classified into three types: (i) lack of nondynamic correlation, (ii) the lack of description of long-range dispersion interactions (such as van der Waals), and (iii) the self-interaction error (SIE) or the delocalization error (DE). In this thesis, we will not be concerned with the lack of nondynamic correlation.

In the present dissertation, the accurate description of long-range dispersion interactions, such as π -stacking interactions, is addressed using the empirical approach by Stefan Grimme.^{11,12} Grimme's dispersion correction is an on-top energy correction.¹³ It changes the electronic energy and, as a consequence, the potential energy surface. Subsequently, the optimized geometry of the system will also be different because the dispersion correction contributes to the forces between the atoms, but it does not explicitly modify the electron density. This treatment is adequate for the compounds studied in this thesis, some of which are affected by dispersion but only on the geometrical arrangements of the molecule.

Within the present thesis, the DFA limitation that plays a crucial role in the calculations performed is the SIE. The SIE is the spurious interaction of an electron with itself. This term is often used for one-electron systems. For a many-electron system, it is termed many-electron self-interaction error¹⁴ or, in general, it is also known as the delocalization error.

The exact energy varies piecewise-linearly with the number of electrons. To reduce the repulsion energy caused by the DFAs giving SIE, the iterative process of self-consistent field carried out to minimize the energy tends to separate the electrons, causing an extra delocalization of the electron, and consequently an underestimation of the electronic energy. The violation of piecewise-linearity gives rise to the so-called delocalization error.^{15,16} On the other hand, using HF we will overlocalize the electrons giving a positive curve in the variation of the energy with the number of electrons.

The delocalization error is responsible for many failures in the description of several chemical properties such as the over/underestimation of aromaticity character,¹⁷⁻¹⁹ the underestimation of reaction barriers, the band gaps of materials, the energies of dissociating molecular ions, or the incorrect description of charge-transfer (CT) excitations,²⁰⁻²³ nonlinear optical properties^{24,25} or Rydberg states.²⁶ This type of error will be present, being more or less critical, in all the properties described with DFAs that need an accurate energy description at large interelectronic distances, and it will increase with

the system size.

In the following chapters, we will see this error reflected in describing the aromatic character of different porphyrinoid systems, and the computed UV-Vis absorption spectra and redox potentials of several photosensitizers using some particular DFAs.

1.2 Aromaticity and its rules

1.2.1 A pinch of history

The term aromaticity comes from the Ancient Greek term *aroma*, ἄρωμα, which means "seasoning/a spice or sweet herb/agreeable odor", and is of unknown origin.^{27,28} Originally, aromaticity was used only to describe classical organic molecules such as benzene, the most paradigmatic aromatic molecule. Nowadays, this concept has extended well beyond the realm of organic chemistry, giving rise to a great variety of new aromatic molecules as well as different rules and descriptors.²⁹ In the following lines some of the most relevant advances in the aromaticity field, gathered in Figures 1.3-1.5, will be highlighted.

Benzene, initially named *bicarburet of hydrogen*, was synthesized for the first time in 1825 by Michael Faraday and formulated as C_6H_6 .³⁰ In 1865, Kékulé proposed the structure of benzene as a hexagon containing at each vertex a carbon and a hydrogen atom.³² Later on, it was himself who arrived at the actual structure corresponding to a mixture of cyclohexatrienes in equilibrium. At that time, benzene was classified as an aromatic molecule, probably for its pleasant smell. After the discovery of benzene, a large number of aromatic molecules were discovered and studied:^{33,34} going from simple benzene-based systems (polycyclic rings),^{35,36} and small rings containing heteroatoms to transition states,³⁷⁻³⁹ excited states,^{19,40-43} porphyrins,⁴⁴⁻⁴⁷ radical species,⁴⁸ all-metal clusters,⁴⁹⁻⁵³ fullerenes^{54,55} or nanorings,^{1,56-58} among others.



Figure 1.2: Michael Faraday (1791-1867)³¹

In 1884, the first proposal of the porphyrin structure was given by Nencki.⁵⁹ However, it was not until 1926 when Fisher confirmed this structure with the synthesis of etio-porphyrin.⁶⁰ Already in the 20th century, Hückel proposed a rule to distinguish aromatic from nonaromatic molecules (see Section 1.2.3).

The topological method to treat pericyclic reactions by applying the principle of

aromaticity of transition states was an essential finding due to Evans and Warhurst in 1938.⁶¹ In pericyclic reactions, a cyclic delocalized system is formed through a transition state which can be either aromatic or antiaromatic. Based on this statement, Evans and Warhurst explained that ethylene does not react with itself to produce cyclobutane but reacts with butadiene resulting in cyclohexene. The transition state formed is aromatic and more stable.

The study of all these new species led to the emergence of different variants of aromaticity up to the point that in 2017, Jörg Grunenberg collected up to 45 different aromaticity types.⁶² Two examples are the multifold aromaticity or bicycloaromaticity.^{63–65} The former involves π , σ -, δ - (implying d orbitals) and even ϕ - (implying f orbitals) electron delocalization. Bicycloaromaticity refers to molecules that present two (or more) potentially aromatic circuits within the same non-planar molecular framework and share the same π electrons.

Among all the synthesis of large aromatic molecules, in 2001, Boldyrev *et al.* characterized the first all-metal aromatic cluster, Al_4^{2-} .⁴⁹ Another relevant discovery was in 2007 when Anderson *et al.* synthesized a six-porphyrin nanoring. This porphyrin nanoring was the first of a series of similar large macrocyclic structures exhibiting (anti)aromaticity.^{1,56–58,66} Finally, a recent finding in the field of aromaticity, reported by Li *et al.* in 2015, is a multicenter-bonded $[Zn^1]_8$ cluster with cubic aromaticity.⁶⁷ They state that their findings extend the aromaticity concept to cubic metallic systems and enhance Zn-Zn bonding chemistry.

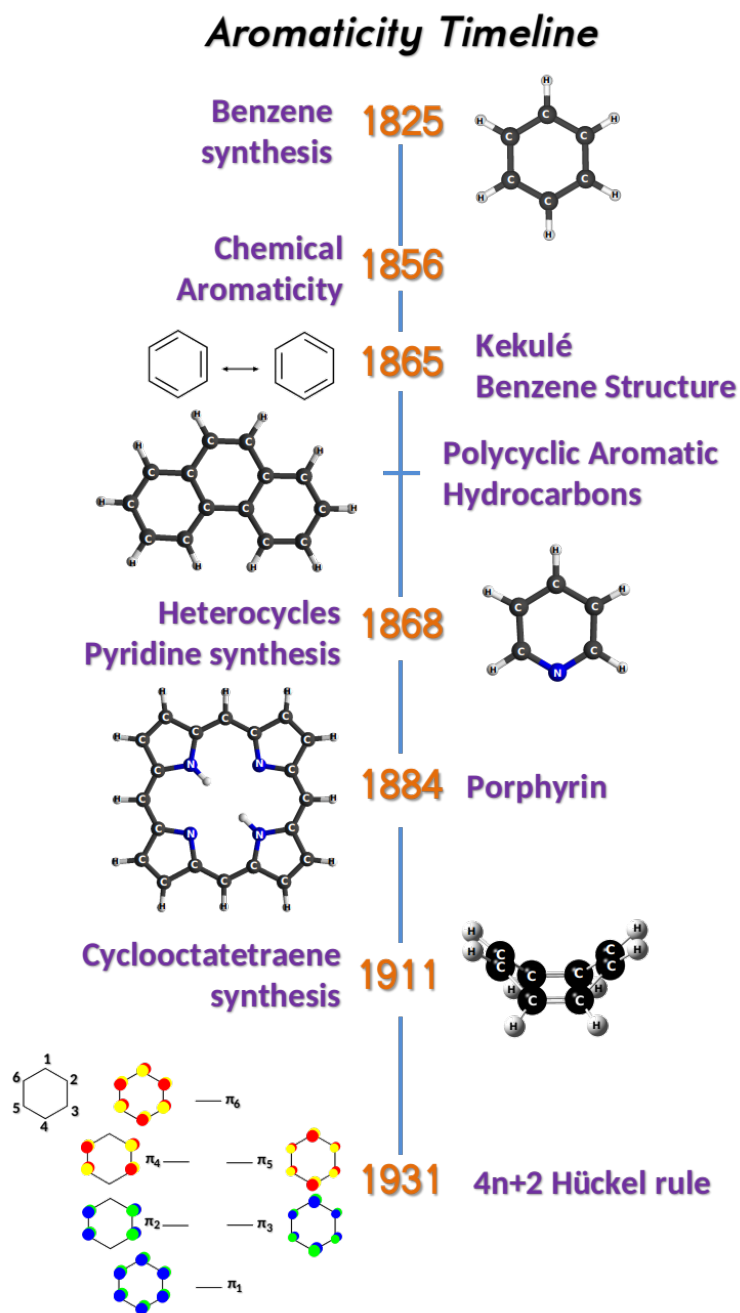


Figure 1.3: Most relevant advances in the field of aromaticity from 1825 to 1931. Figure adapted from Ref. 34 and modified by Prof. Miquel Solà and the present author.

Aromaticity Timeline

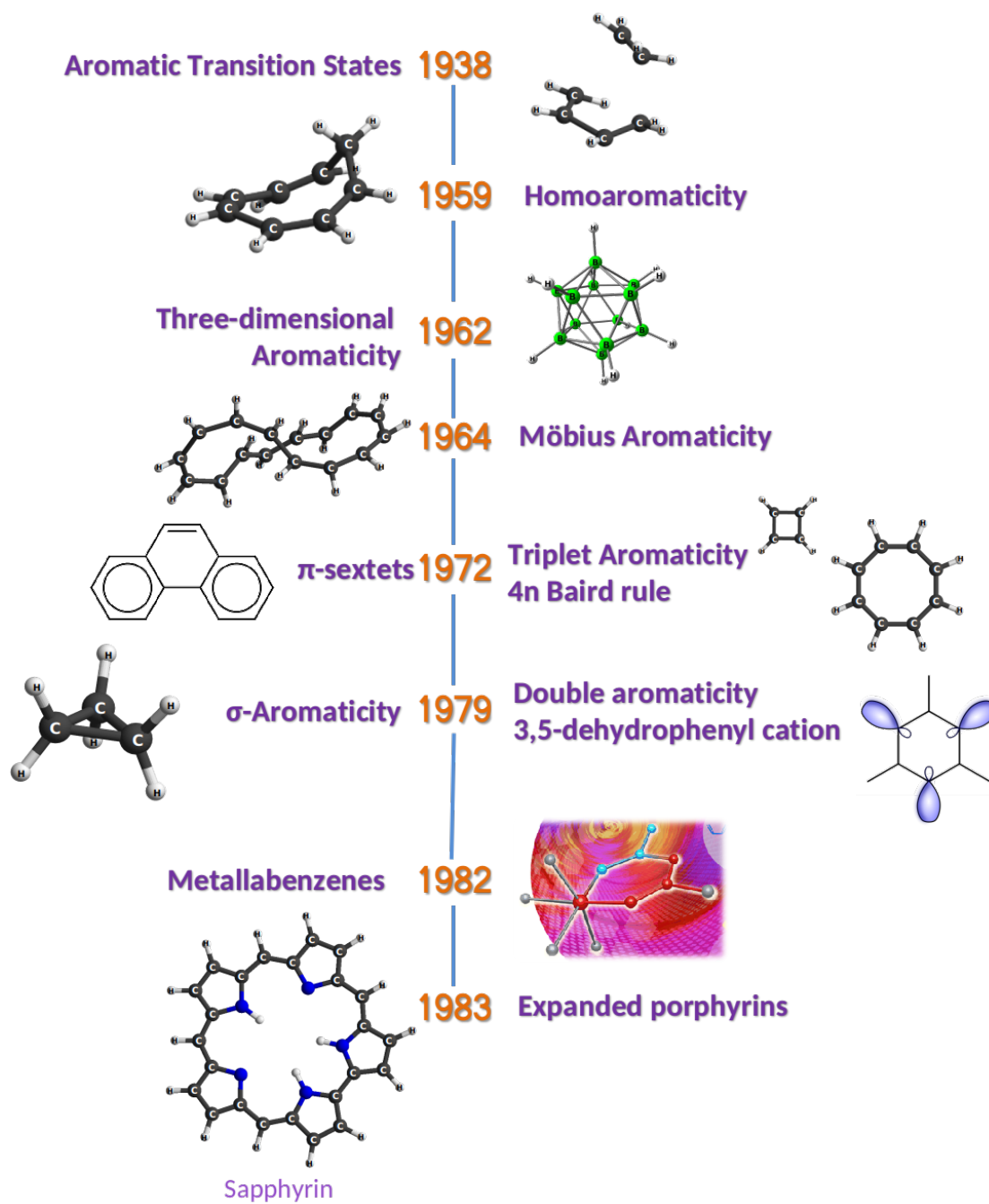


Figure 1.4: Most relevant advances in the field of aromaticity from 1938 to 1983. Figure adapted from Ref. 34 and modified by Prof. Miquel Solà and the present author.

Aromaticity Timeline

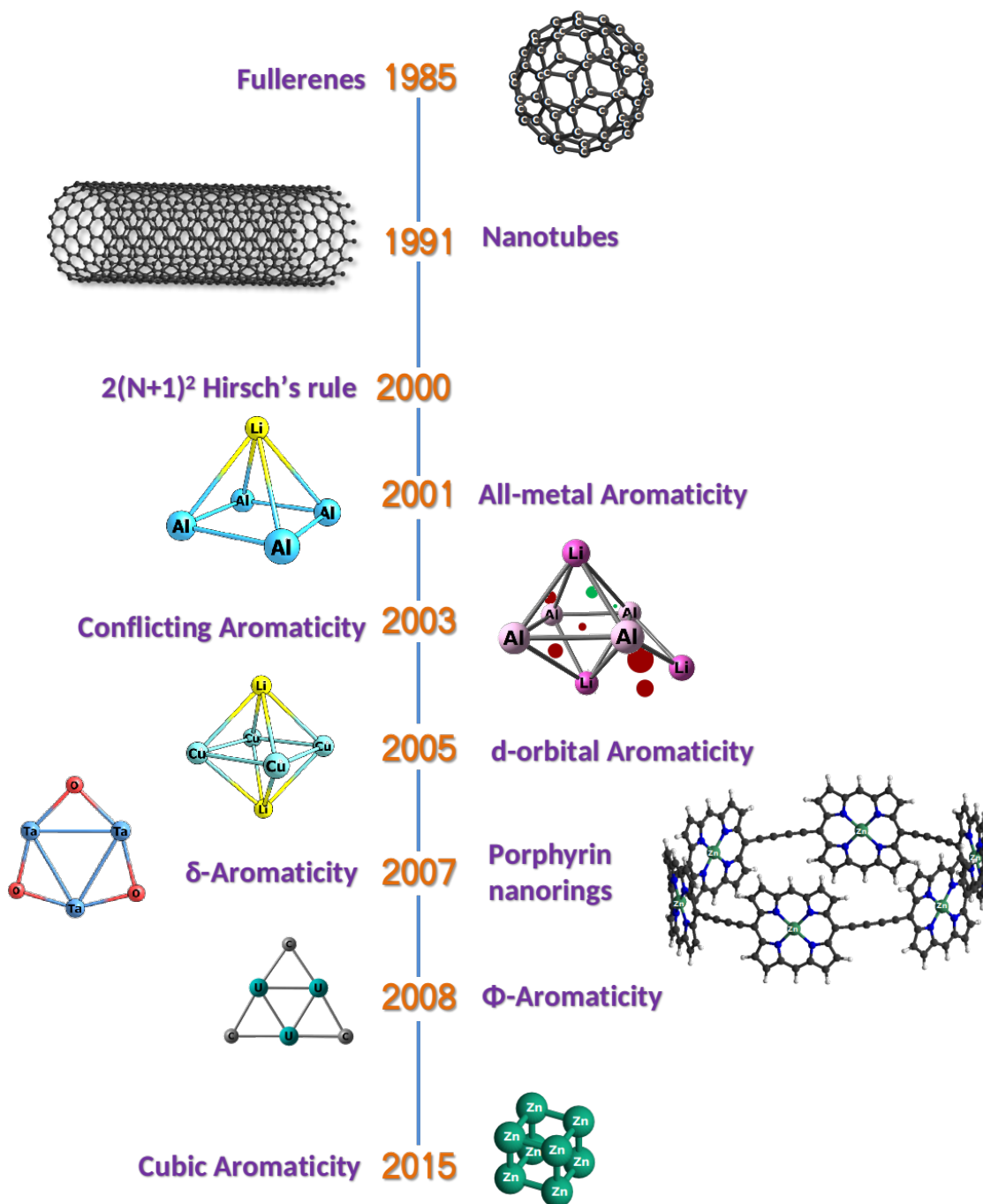


Figure 1.5: Most relevant advances in the field of aromaticity from 1985 to 2015. Figure adapted from Ref. 34 and modified by Prof. Miquel Solà and the present author.

1.2.2 The aromaticity definition

The concept of aromaticity lacks a solid root in quantum chemistry.^{62,68} As other useful chemical concepts to describe the electronic structure of the molecules (chemical bonding, bond order, ionicity, oxidation states, or electron population), it does not correspond to any physical observable.⁶⁹ For this reason, this ill-defined property has been under debate for many years, and several definitions have come to light. Specifically, we prefer to define aromaticity in terms of the electronic structure. Accordingly, a good starting definition would be the one given by F. Sondheimer (1963): "*A compound is considered to be aromatic if there is a measurable degree of delocalization of a π -electron system in the ground state of the molecule.*"⁷⁰

Aromaticity is a multifold property,⁷¹⁻⁷⁵ meaning that it refers to several properties that are not necessarily mutually related. This multifold character is the main reason for being one of the most controversial and sophisticated concepts in the literature.⁷⁶ Aromaticity is associated with cyclic electron delocalization in a closed circuit, producing bond length equalization, large magnetic anisotropies, abnormal chemical shifts, etc. All these properties have been used in theoretical chemistry to define a great variety of aromaticity descriptors to analyze different systems, not only organic molecules.^{49,50,77,78} On the other hand, one could also use experimental techniques, such as nuclear magnetic resonance (NMR) spectroscopy⁷⁹ or UV-Vis spectra⁸⁰ to measure some of the manifestations of aromaticity.

Aromaticity indices can be divided according to its different manifestations as energetic,⁸¹ magnetic,^{33,82} geometric,⁸³ and electronic.^{84,85} The most used and relevant indices will be further discussed in Section 3.3, paying particular attention to the electronic aromaticity indices, such as AV_{1245} ⁸⁶ and AV_{min} ,^{18,87} which have been tested on large π -conjugated systems for the first time in this thesis.

The first thing to consider in an aromaticity study is which manifestation we want to examine, and then chose the adequate theoretical descriptor or experimental technique to use. Then, it is important to take into account the advantages and limitations of the descriptor or technique used.^{88,89} Moreover, in computational chemistry, it is essential to be aware that depending on which index is used, one could examine expressions of aromaticity associated with the entire molecule (*global aromaticity*) or only a particular region of the molecule (*local aromaticity*). An example of aromatic indices that evaluate *global aromaticity* is the HOMO-LUMO gap, which is an energetic descriptor, expected to be large in aromatic molecules. The indices that determine the local aromaticity only take into consideration an annular structure or a pathway within the molecule (e.g., MCI or HOMA).⁹⁰ Sometimes, it is difficult to make such differentiation in the classification of an aromaticity index, like the Anisotropy of the induced current density (ACID) index.

For all these reasons, it is highly recommendable to use not only one index but a set of them to study the aromaticity of a system. It has been demonstrated that no aromaticity index is infallible.^{91,92} For example, it has been proved that the NICS descriptor overestimates the aromatic character of all-metal and semimetal clusters.⁹¹

1.2.3 The most highlighted aromaticity rules and models

Efforts to understand the fundamental principles of aromaticity and its conceptual counterpart, antiaromaticity,⁹³ gave rise to some of the most important advances in chemistry. Several models have been designed to characterize aromaticity^{78,94–97} and from these models, different aromaticity rules have been obtained.^{98,99}

The first and the most widely known rule was proposed by Hückel in 1931,^{100,101} which states that a planar (or with an even number of half twists) singlet system with $4n + 2$ π electrons (where n is an integer number) is aromatic. In the 1960s, Breslow introduced the term antiaromaticity to defined the destabilized planar systems containing $4n$ π electron in contrast to the stability of aromatic compounds. Afterward, this statement was included as part of what we have nowadays known as Hückel's rule.¹⁰² In terms of electron (de)localization, one could also understand antiaromaticity as the localization of π electrons in specific fragments of the system. In the beginning, this rule was only applied to monocyclic conjugated hydrocarbons,¹⁰³ but then it was extended to all sorts of molecules, including non-organic molecules.^{50,52} As the Hückel rule does not consider out-of-plane distortions, we have investigated in the present thesis how valid it is in a simple annulene series (see Chapter 6).

Later, in 1964, Heilbronner¹⁰⁴ anticipated that for planar π -conjugated systems with an odd number of half twists Hückel's rule is reversed, *i.e.*, a singlet Möbius system with $4n(+2)$ π electrons is (anti)aromatic.¹⁰⁵ Approximately eight years later, Baird affirmed that the aromatic character of the singlet ground state is reversed for the lowest triplet state.^{106,107} Baird's rule was considered the photochemistry analog of Hückel's rule¹⁰⁸ as it has been employed to modify molecules with enhanced photochemical activity.⁴⁰ Some authors propose to extend Baird's rule also to the first singlet excited state.^{109,110}

In addition to the already explained rules, there exist many other ones such as Clar's aromatic π -sextet rule,^{111,112} which specifies that the most relevant Kekulé resonance structure for characterizing the properties of polycyclic aromatic hydrocarbons (PAHs) is the one that presents the largest number of unconnected aromatic π -sextets (benzene-like moieties); or Hirsch's rule, which allows to predict the aromatic character of fullerenes and nanotubes.¹¹³ The last highlighted rule corresponds to the $2N^2 + 2N + 1$ (with $S = N + \frac{1}{2}$) rule, which is an extension of the Hirsch rule for spherical aromatic species of open-shell spherical compounds.⁹⁷ In 2019, this latter rule was extended to atomic clusters.¹¹⁴ Hückel's, Heilbronner's (or Möbius) or Baird's rules are the ones that will

be further discussed in the present thesis as they are the most important for large π -conjugated systems and porphyrins.

Although it is not widely used today, Hückel molecular orbital (HMO) method^{100,101,115,116} needs to be mentioned as it is the basis of Hückel's rule. It is a simple method that determines the electronic energy of π molecular orbitals as a linear combination of atomic orbitals. HMO method was later extended to conjugated molecules including heteroatoms. It does not take into account the geometry of the molecules, and consequently, it only works correctly for planar systems. Within the HMO method it is easy to calculate the atomic overlap matrices (AOMs), bond orders, and several aromaticity indices.^{19,117}

1.3 Porphyrinoid systems

Porphyrins are a well-known group of heteromacrocyclic organic compounds with crucial roles in biological processes. Two prominent examples are chlorophylls, key molecules in the photosynthesis process; and hemoglobin, the iron-containing metalloprotein responsible for the oxygen transport throughout almost all vertebrates' bodies.^{118,119} Porphyrins can coordinate metal ions inside their ring structure through the nitrogen atoms giving them applications such as a catalyst, electron-transport, functional dyes or sensors, stable organic radicals, or in supramolecular chemistry.

Porphin is the simplest aromatic tetraphyrin and is almost only of theoretical interest. Nonetheless, it is the parent macrocycle structure of several substituted derivatives of biochemical importance.¹²⁰ Its antiaromatic counterpart is isophlorin (same structure as porphin but with all the nitrogen atoms protonated).¹²¹ Isophlorin is the simplest example of air-stable antiaromatic porphyrinoids.¹²² The structure of porphin consists of four pyrrole subunits connected through their α -carbon by a methine carbon bridge (see Figure 1.6). The extensive exploration of porphyrins' structural and functional properties gives rise to a plethora of new compounds that present great applications in several fields such as biomedicine or material science.¹²³ We can define these new compounds as porphyrinoid systems because they are based on the porphyrin structure. Moreover, we call expanded porphyrins the "*macrocycles that contain pyrrole, furan, thiophene, or other heterocyclic subunits linked together either directly or through one or more spacer atoms in such a manner that the internal ring pathway contains a minimum of 17 atoms*" as Seesler and Seidel proposed.^{124,125}

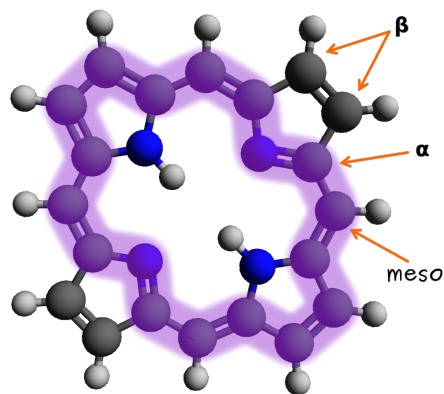


Figure 1.6: Porphin structure with labeled relevant positions. In purple, its annulene path.

Some authors prefer to distinguish between '*contracted*' and '*expanded*' porphyrinoids.¹²⁰ The size of the smallest macrocyclic circuit of the porphyrinoid is the one used to classify them. If the size of this circuit is smaller than 16 atoms, the molecule is designated as '*contracted*' porphyrinoid, and if it is bigger than 16 atoms, it will belong to the group of '*expanded*' porphyrinoids. A macrocyclic circuit size equal to 16 atoms corresponds to the porphin one and other tetrapyrins. It is also usual to talk about giant porphyrinoids if the structure contains more than eight cyclic subunits.

The chemistry of expanded porphyrins started after the discovery of sapphyrin (see Figure 1.6) by Woodward *et al.* in 1966, but it was not until 1983 when the first report was published.¹²⁶ After the synthesis of sapphyrin, countless expanded porphyrins were developed and caught the attention of chemists due to their fascinating applications as near-infrared dyes,¹²⁷ anion sensors,¹²⁸ nonlinear optical materials,¹²⁹ photosensitizers,¹³⁰ and photodynamic therapy.¹³¹ In the last few years, the ability of expanded porphyrins to stabilize radicals by spin-delocalization has also been exploited.¹²³ Also, despite their difficult synthesis, expanded porphyrins oligomers have attracted a lot of attention as they may be promising materials for applications in photonics or as near-infrared dyes, for example.

The systematic nomenclature proposed by Frank and Nonn¹³² is used for naming expanded porphyrins. In this nomenclature, the name of an expanded porphyrin consists of three parts: the prefix is a square-bracketed number indicating the number of π electrons in the effective macrocyclic conjugation path; secondly, the core name, displaying the number of pyrrole subunits of the expanded porphyrin; and thirdly, in a round-bracketed suffix, the number of bridging carbon atoms between the pyrrole cycles starting on the largest unit. One example would be [22]pentaphyrin(1.1.1.1.0), an expanded porphyrin with 22 π electrons and five pyrrole subunits linked among them by methine carbon groups, except the last one that the pyrroles are directly connected. This molecule corresponds to sapphyrin, which as other expanded porphyrins, was named after the

observation of their color (see Figure 1.4 for the structure of this expanded porphyrin).

The huge interest in expanded porphyrins is due to one of their most significant features, their conformational flexible π -conjugated structure, which furnishes them with a wide range of applications. Their conformational flexibility enables them to adopt more than one (non-)planar topology: Hückel, Möbius, and figure-eight conformers (Figure 1.7). Seemingly, it was in 1993 when the first inspection of an unusual conformation (Möbius conformation) in a porphyrin analog was done in the palladium(II) complex of a [26]hexaphyrin(1.1.1.1.1.1).¹³³ The latter porphyrin analog presented two pyrrole rings inverted, *i.e.*, the nitrogen atoms were in the periphery of the macrocycle. The figure-eight conformation started to attract interest after the first report of a decaphyrin by Sessler *et al.* in 1994.¹³⁴ These conformations present structural strains and effective intra-molecular hydrogen bonding interactions, which could stabilize large expanded porphyrins. These flexible conformations can be switched and easily controlled via various methods: regulating the temperature, protonating and deprotonating the system with acids and bases, playing with the polarity and viscosity of the solvent, among others.^{118,135} The control of the molecular topology is relevant to understand the molecular structure-property relationships.

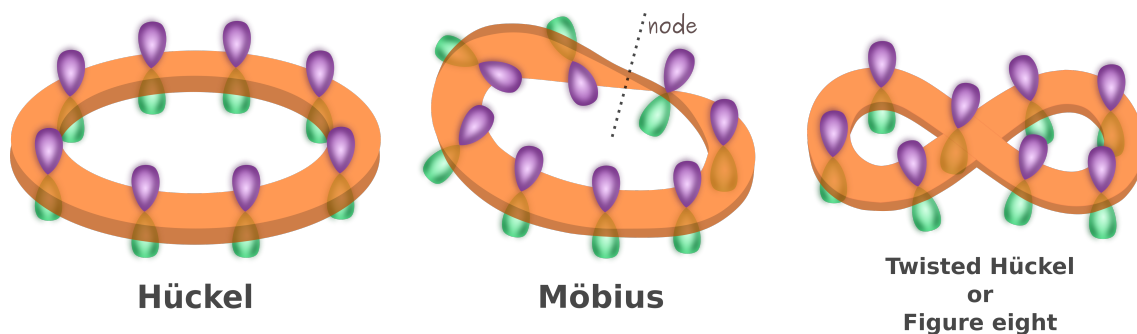


Figure 1.7: Schematic representation of three expanded porphyrin topologies.

Heilbronner assumed that a molecule could present Möbius aromatic stabilization if the molecular structure was twisted, ensuring that the p orbitals forming the π -system would contain an odd number of nodes. In a Hückel topology, the π -plane has two sides, above and below the ring plane. Therefore, there is a continuous overlap of p orbitals above and below the ring plane. Möbius topology, by contrast, presents only one side in the π system due to the presence of at least one node (which involves the presence of an inversion of orbital phase).¹³⁶ Consequently, the overlap of adjacent p orbitals is reduced. Forst-Musulini introduced a mnemonic device to memorize π orbital energies for Hückel systems. Likewise, Zimmerman proposed the corresponding method for Möbius systems.^{137,138} It has been demonstrated that neglecting the reduced overlap of the twisted adjacent p orbitals, the annulenes with $4n + 2$ π electrons prefer

a Hückel topology, and the ones that have $4n$ π electrons are more stable with a Möbius structure.¹³⁶ Lastly, a figure-of-eight topology contains an even number of twists and the p -orbital overlap is once again continuous. The figure-of-eight conformers follow the same rules as Hückel conformers.

Expanded porphyrins' topology is closely linked to their aromatic character. It is possible to control the aromaticity by an external trigger such as, lowering the temperature, protonating and deprotonating the system, changing the chemical environment, or changing the electronic state by photoexcitation.¹³⁵ Besides, the modification of the aromatic character also affects the molecular properties of the molecules, e.g., chemical reactivities, spectroscopic, magnetic, or photophysical properties.

Synthesizing an antiaromatic annulene was a tedious task due to its instability, but synthesizing an antiaromatic expanded porphyrin is easier thanks to its conformational flexibility.¹³⁵ For this reason, expanded porphyrins have been recognized as one of the most stringent test beds to study both Hückel and Möbius aromaticity.⁸⁰

Initially, the Hückel rule was derived for monocyclic systems with identical atoms. The extended version of this rule also allows the treatment of systems that contain heteroatoms. However, the main pitfall of the Hückel rule is that it cannot be applied for non-planar molecules, like porphyrinoid system, because assumed optimal overlap between p orbitals no longer exists. To solve this problem, several descriptors have been suggested¹³⁹ among which the annulene model stands out.^{140,141} This model treats the porphyrin analogs as bridged heteroannulenes. Thereby, in aromaticity studies, it is assumed that porphyrins have the same properties as all-carbon annulenes.¹²⁰ Within this model, the most aromatic circuit follows the annulene-like conjugation pathway and determines the macrocyclic aromaticity of the porphyrin. The annulene-like pathway follows the internal circuit except when it passes through a protonated nitrogen (see Figure 1.6 as an example). The bridged annulene model no longer holds if metals are coordinated to a porphyrinoid π system.¹⁴² Contrarily, several authors¹⁴³⁻¹⁴⁶ affirm that all the π electrons of the system are necessary to describe the aromaticity in porphyrinoid systems correctly. From this inconsistency, we can determine that it is crucial to find a new aromaticity index that can accurately choose the most aromatic path from a π -electron macrocyclic structure. Moreover, knowledge of the most aromatic path could be important in magnetic applications, for example.

Like other π -conjugated systems, we could use several criteria to evaluate the aromaticity of expanded porphyrins.^{118,135} Two of the most studied features of expanded porphyrins are photophysical and magnetic properties. On one hand, expanded porphyrins show a significantly red-shifted absorption spectrum. The larger the expanded porphyrin, the larger the bathochromic shift (to larger wavelength) in the absorption spectrum. As the absorption spectrum of these large macrocycles presents specific bands depending

on the aromatic character, it is often used to determine their aromatic character. Another property related to the degree of aromaticity would be the two-photon absorption cross-section value or the excited-state lifetimes.⁸⁰ Using photophysical properties, it is possible to distinguish between aromatic, antiaromatic, or nonaromatic systems but they can not be quantitatively characterize as being more or less aromatic, for example. On the other hand, magnetic properties, such as ¹H-NMR chemical shifts, are one of the most commonly used experimental techniques. The chemical shift of the peripheral pyrrolic β protons is a diagnostic of expanded porphyrins aromaticity because inner pyrrolic β protons are sensitive to a possible magnetic current. If there is a strong diatropic ring current, the molecule is aromatic. In that case, the chemical shift for the inner β protons is negative (frequently below -5ppm). On the contrary, if there is a paramagnetic ring current, the system is antiaromatic, and the inner β protons will have a large positive chemical shift (20 ppm or more).¹²⁰

Out of the numerous porphyrinoid systems synthesized, we can emphasize the porphyrin nanorings. These systems are macrocycles with only a few nanometers in diameter (around 2.4 nm). Porphyrin nanorings are interesting compounds because they offer an end-free π -conjugated system with remarkable properties such as photophysical and guest-encapsulating.^{1,147-149} As they are large conjugated systems, they are good candidates to present (anti)aromatic species. For this reason, numerous previous studies of porphyrin nanorings have focused on the ground and the excited states (anti)aromaticity.^{1,150,151}

1.4 Photosensitizers

In most of the studies provided in the present dissertation, porphyrinoid systems have been analyzed. However, two families of photosensitizers (PSs) based on copper and iridium have also been examined to design a computational protocol to study the electronic structure of a specific molecule.

Photosensitizers, also called dyes, are molecules that absorb light and transfer the energy from the incident light to another nearby molecule. The absorbed light is often within the visible or infrared part of the electromagnetic spectrum.¹⁵²⁻¹⁵⁴ After transferring the energy, the PS eventually returns to its ground state. Photosensitizers have a wide range of applications in lighting, solar energy conversion, and photocatalysis.¹⁵⁴ For example, PSs are used in Dye-sensitized solar cells (DSSCs) or in the solar-driven water-splitting (WS) process.^{153,155,156} The global process of WS is highly complicated to study as it is a multi-electron transfer coupled with multi-proton transfer process, but it could be divided into the two implied reactions to reduce the complexity and facilitate the analysis of the results. These reactions correspond to the water oxidation

to molecular oxygen and the water reduction to hydrogen molecule.^{156–158} Light-driven water reduction to molecular hydrogen process needs a catalyst, a dye, and a sacrificial electron donor. This process belongs to the photocatalytic processes known as artificial photosynthesis, as they mimic the first step of natural photosynthesis.^{156,159} Interestingly, the process occurring in DSSCs is exactly the opposite one that takes place in organic light-emitting diodes (OLEDs). Often, active-(UV-Vis) molecules are thus tested for both their efficiency as dyes in DSSC and OLEDs.^{160–163}

Photovoltaic solar cells are a common option to produce electricity from solar light. Predominantly, they are based on highly pure silicon. However, this type of cells is costly and complex to produce, and for this reason, there emerge several alternatives such as perovskite photovoltaics, organic photovoltaics, inorganic quantum dot solar, and DSSCs, among others.^{152,164,165}

Dye-sensitized solar cells, also known as Grätzel solar cells.^{166,167} They are one promising alternative to the highly pure silicon cells since they are easier to build, cheaper, more flexible, and thinner.^{152,164,166,167} The first synthesis of a DSSC was in 1972 with chlorophyll sensitized zinc oxide electrode by Helmut Tributsch.¹⁶⁸ The fact that these cells were very inefficient prompted continued research and in 1988, Michael Grätzel and Brian O'Regan co-invented the modern version of DSSC with a titanium dioxide support. Still, it was not until 1991 when the first publication was made.¹⁶⁶ Unfortunately, DSSCs do not have high efficiencies compared to pure silicon cells.^{169,170} While the best commercial silicon cell efficiency is about 23%, DSSC achieved 13% in 2014.¹⁷¹ Moreover, Snaith found that the theoretical maximum efficiency of DSSC is 20.25% due to the electrical and optical losses in the devices.¹⁷² DSSCs' efficiency mainly depends on the dye. Two important parameters that define DSSC efficiency are the dye absorption spectrum and the anchorage to the semiconductor surfaces (TiO₂). Dyes used in devices like DSSC should gather some essential qualities, for instance: strong absorption in the visible range, present the appropriate anchor group to the semiconductor oxide, large energy gap, high stability in different states (oxidized, ground, and excited states), appropriate redox potential, and good efficiency in the charge injection to a transparent semiconducting layer which contains titanium dioxide particles and in the regeneration process.^{152–154,173} Usually, to ensure a high energy gap, molecules with metal-to-ligand charge transfer (MLCT) states are used where an electron is transferred from a metal orbital to a ligand-based orbital.¹⁵⁴

Photosensitizers employed in photovoltaics or photocatalysis are mainly based on novel metals such as ruthenium (Ru^{II})¹⁷⁴ and iridium (Ir^{III})^{175,176} especially as photoredox catalysts.^{155,177,178} Transition metals of the second and the third period are chemically stable, they have long-lived excited states whose density is mostly located in the ligand, and redox potentials that could be optimized.¹⁷⁷ Although complexes based

on the first period transition metals are more abundant and cheaper only copper(I) complexes are commonly used.^{155,177,179,180} Indeed, these latter complexes are more difficult to control due to the presence of excited states centered on the metal with several multiplicities. A strong ligand field strength has been employed to address this problem, leading to the discovery of new Cr, Mn, Fe, and Co metal complexes.^{155,178}

From the theoretical perspective, another topic to be discussed in detail is the computational method to characterize dyes and their chemical properties. Excitation energies and redox potentials are two important properties for DSSCs to improve their efficiency. For this reason, it is important to find a proper computational method to describe both properties. Most of the exchange-correlation functionals used in TDDFT (see Section 2.4) are not suitable to describe CT excitations²⁰⁻²³ due to the self interaction error (*vide supra*). Consequently, range-separated functionals (RSF) are usually used to investigate CT excitations of photosensitizers.²⁰⁻²³ Besides, it has been seen that tuning the attenuating parameter (ω) of RSF and finding the optimal value for each system can improve the obtained excitation energies (see Section 2.3).^{181,182} However, to the best of our knowledge, it has not been tested whether optimally tuned range-separated functionals also improves redox potentials (see Chapter 9).

Chapter 2

Quantum chemistry methods

In the present chapter, approximate methods to solve the electronic Schrödinger equation will be reviewed, starting with Hartree-Fock and post-HF methods. Afterward, we will cover the density functional theory (DFT), discussing the delocalization error present in some DFAs, which plays a crucial role in this thesis. Finally, we briefly review the time-dependent density functional theory (TDDFT).

2.1 Hartree-Fock and a brief overview of post-HF methods

Given the position of atomic nuclei and the total number of electrons in the system, *ab initio* methods aim to compute a solution of the electronic Schrödinger equation to calculate the electronic energy and the wavefunction (within the Born Oppenheimer approximation). The electron density, dipolar moments, and other chemical properties of the system can be obtained from the wavefunction using the appropriate operator. As mentioned before, the electronic Schrödinger equation is a many-body problem whose exact form cannot be solved beyond hydrogen and hydrogenoid atoms as its complexity grows exponentially with the number of electrons.¹⁸³ For this reason, approximate methods are needed.

In this regard, we can highlight one of the most fundamental concepts in quantum chemistry, the molecular orbital (MO). The MO describes the areas of probability of finding an electron in a given region of the space. A great bulk of electronic structure calculations are based on the orbital approximation and the molecular orbitals expression as a linear combination of atomic orbitals (MO-LCAO):¹⁸⁴

$$\phi_i(r) = \sum_{\mu} c_{\mu i} \phi_{\mu}(r) \quad (2.1)$$

where $c_{\mu i}$ is the expansion coefficient of the atomic orbital ϕ_{μ} in the molecular orbital ϕ_i .

One of the main factors determining the accuracy of a calculation is the choice of the set of atomic orbitals (also called basis set) used to build up the MOs. The basis set consists of mono-electronic functions in which the molecular orbitals are expanded. As they are generally nucleus-centered functions, they are a sort of atomic orbitals of the atoms that compose the molecule. There are two main types of atom-centered basis set: Slater-type orbitals (STO)^{185,186} and Gaussian-type orbital (GTO).¹⁸⁷ In this thesis GTO basis sets are used, specifically Pople¹⁸⁸⁻¹⁹⁰ and Dunning basis sets.¹⁹¹ In addition, there are diffusion and polarization basis functions that are not atom-centered. These functions are important to describe accurately, for example, the anions or the polarization of a system. Nowadays, the minimal basis set used is a double zeta precision type with polarization functions. However, in practice, this latter basis is only used for large systems, and for smaller systems, a bigger basis set (at least triple basis set) is generally used.

The simplest wavefunction method is Hartree-Fock. It involves optimizing a single Slater determinant (Eq. 2.2)(preserving the antisymmetry) made of MOs by applying the variational principle,

$$\psi(\mathbf{1}, \mathbf{2}, \dots, N) = (N!)^{-\frac{1}{2}} \begin{vmatrix} \phi_i(\mathbf{1}) & \phi_j(\mathbf{1}) & \cdots & \phi_N(\mathbf{1}) \\ \phi_i(\mathbf{2}) & \phi_j(\mathbf{2}) & \cdots & \phi_N(\mathbf{2}) \\ \vdots & \vdots & & \vdots \\ \phi_i(N) & \phi_j(N) & \cdots & \phi_N(N) \end{vmatrix} \quad (2.2)$$

For the hydrogen atom, the HF method is exact. But it is incapable of providing a full description beyond the hydrogen or hydrogenoid atoms because the wavefunction is no longer exact, and it does not include electron correlation.¹⁹² Although up to 99% of the total energy can be recovered with HF, the *chemistry* lies in this remaining 1%.¹⁹³ Therefore, HF can not be used to study many chemical reactions. A solution is to include electron correlation by the use of post-HF methods. As HF can recover most of the total energy, it is usually the reference of post-HF methods. These methods are more accurate wavefunction-based approaches that expand the electronic wavefunction beyond a single Slater determinant and include electron correlation.

The concept of electron correlation (E_{corr}) comes from the inability of the HF method to correctly describe the coupled motion of electrons. There are several definitions of electron correlation.^{194–196} In 1959, Löwdin defined it as the energy difference between the exact eigenvalue of non-relativistic Hamiltonian (E_{exact}) and its HF expectation value (E_{HF}) in a complete basis:¹⁹⁷

$$E_{corr} = E_{exact} - E_{HF} \quad (2.3)$$

Usually, the exact energy (under the Born-Oppenheimer approximation,⁷ and ignoring relativistic effects) of a molecule is not known as it comes from the full configuration interaction (FCI)¹⁹⁸ energy computed for a complete basis set. For this reason, Pines definition¹⁹⁹ is more commonly used as it employs the energy of a post-HF method instead of the exact energy with a specific basis set. Depending on the context, different terminology for electron correlation is used for atomic and molecular systems:^{200–204} Fermi vs Coulomb correlation (considering spin pairs), weak vs strong correlation (in terms of strength), *etc.* But one of the most relevant ones is the classification of correlation into dynamic and nondynamic.^{205–208}

On the one hand, the dynamic correlation refers to the dynamic character of the electron-electron interactions. In general, all molecules with more than one electron display this type of correlation, *i.e.*, it is a universal feature.²⁰⁹ The dynamic correlation becomes important when the number of electrons increases and the HF method is consistent but incomplete because it cannot correctly describe the electron-electron cusp (when the interelectronic distances are close to zero). Dynamic correlation problems

could only be solved entirely using the FCI method. For a given molecule, FCI is the configuration interaction (CI) method that includes all the possible Slater determinants that consider all possible excitations within a given basis set. The CI wavefunction expands as a linear combination of Slater determinants where the reference is usually the HF determinant:^{192,210}

$$\psi_{CI} = c_0\psi_{HF} + \sum_{ia} c_i^a \psi_i^a + \sum_{\substack{ab \\ ij}} c_{ij}^{ab} \psi_{ij}^{ab} + \dots = \sum_I c_I \psi_I \quad (2.4)$$

where c are the coefficients that determine the importance of each Slater determinant in the CI wavefunction, and the subindex I indicates all the possible excitations. Precisely, c_i^a corresponds to the inclusion of single excitations and c_{ij}^{ab} to the inclusion of double excitations. In practice, FCI is rarely an affordable method because the computational cost grows exponentially with the system size. Accordingly, dynamic correlation is usually partially addressed by adding small amounts of other Slater determinants to the HF wavefunction (the reference wavefunction in the CI expansion) that only produce small changes in the electron density.

On the other hand, nondynamic correlation, often also named static correlation, arises from having similar weights of different determinants due to the near degeneracy of the frontier orbitals (HOMO and LUMO orbitals). The single Slater-determinant HF method is clearly not flexible enough to describe some molecular systems. Molecules with long-range (LR) electronic interactions and systems that require more than one determinant to correctly describe the appropriate spin state or reflect the system's symmetry suffer from nondynamic correlation. This correlation could be almost entirely accounted for by mixing low-lying-energy excited states along with the HF configuration. The molecular dissociations or diradicals systems are two examples where nondynamic correlation plays an important role.

It is worth noticing that a molecule as such is not classified as having dynamic or nondynamic correlation; we consider a molecule in a particular electronic state. Most post-HF methods are designed to tackle one of the correlation types mentioned above.²⁰⁴

Configuration interaction and the subsequent approximate methods, Möller-Plesset perturbation theory (MP),²¹¹ and Coupled cluster methods²¹² (explained in more detail in the following subsection) introduce dynamic correlation. On the contrary, other methods like complete active space self-consistent field (CASSCF),²¹³ correctly treat the nondynamic correlation. Moreover, to include both corrections, dynamic and nondynamic, hybrid methods are often used (e.g., apply a second-order perturbation theory after a CASSCF calculation into what is known as CASPT2).

2.1.1 Coupled-cluster (CC) methods

Coupled-cluster (CC) methods use the HF wavefunction or a Slater determinant reference to expand the total wavefunction through the exponential cluster operator (\hat{T}).^{198,214} These methods provide size-consistent and size-extensive approximations of the ground state. In 1966, Čížek defined CC as an elegant technique to calculate the correlation energy,²¹⁵

$$\Psi = e^{\hat{T}} \Psi_{HF} , \quad (2.5)$$

where the exponential can be extended as a Taylor series:

$$e^{\hat{T}} = 1 + \hat{T} + \frac{1}{2!} \hat{T}^2 + \frac{1}{3!} \hat{T}^3 + \dots \quad (2.6)$$

and the cluster operator could be subdivided as the sum of the order of the different excitations that the system could present (single, double, triple, *etc.* excitations):

$$\hat{T} = \hat{T}_1 + \hat{T}_2 + \hat{T}_3 + \dots + \hat{T}_N . \quad (2.7)$$

The \hat{T} operator could also be expressed as the sum of different excitations using a coefficient named amplitude (t_μ):

$$\hat{T} = \sum_{\mu} t_{\mu} \hat{t}_{\mu} \quad (2.8)$$

where μ are the different excitations, and \hat{t}_{μ} is the excitation operator.

In practice, truncated CC methods are used. The most popular methods are CCSD²¹⁵ and CCSD(T).^{216,217} Beyond these two, the CC approximations are computationally unaffordable for almost all systems. The CCSD wavefunction is expressed as:

$$\begin{aligned} \Psi_{CCSD} &= e^{\hat{T}_1 + \hat{T}_2} \Psi_{HF} \\ &= \left(1 + \hat{T}_1 + \frac{1}{2} \hat{T}_1^2 + \dots \right) \left(1 + \hat{T}_2 + \frac{1}{2} \hat{T}_2^2 + \dots \right) \Psi_{HF} \\ &= \left(1 + \hat{T}_1 + \hat{T}_2 + \frac{1}{2} \hat{T}_1^2 + \hat{T}_1 \hat{T}_2 + \frac{1}{6} \hat{T}_1^3 + \dots \right) \Psi_{HF} , \end{aligned} \quad (2.9)$$

therefore, it ends up with a summation of excitations, where connected ($t_{ij}^{ab} \hat{\Psi}_{ij}^{ab}$) and disconnected ($t_i^a t_j^b \hat{\Psi}_i^a \hat{\Psi}_j^b$) excitations can be distinguished.

To determine the value of the amplitudes, an iterative process is done by solving:

$$\langle \mu | e^{-\hat{T}} \hat{H} | \Psi_{CC} \rangle = 0 . \quad (2.10)$$

Once the amplitudes are known, the CC energy can be obtained,

$$E_{CC} = \langle \Psi_{HF} | \hat{H} | \Psi_{CC} \rangle . \quad (2.11)$$

Coupled Cluster including single, double, and estimated triple excitations (CCSD(T)) is the CC variant where CCSD energy is calculated, and triple excitations are included as an estimation, using perturbation theory. Using CCSD(T) guarantees the addition of enough dynamic correlation for most purposes. Simultaneously, the addition of all the effects of the excitations, ensures an accurate description of systems with some nondynamic correlation. For this reason, CCSD(T) is known as the Gold Standard method to include dynamic correlation in quantum chemistry. It should be noted that if the system is clearly nondynamic, CC will not be a suitable method.²¹⁸

To assess the adequacy of CCSD or CCSD(T) usage, we could employ several measures. One of the most well-known is the T_1 diagnostic²¹⁹ by Lee and Taylor:

$$T_1 = \frac{\|t_\mu\|}{N^{1/2}}, \quad (2.12)$$

where N is the number of electrons included in the correlation procedure. T_1 is evaluated to detect if a system has a large nondynamic character based on the CC wavefunction. In other words, it measures whether a single-reference electron correlation method is appropriate or not. For CCSD, T_1 diagnostic value larger than 0.02 indicates that the results are not to be trusted and the need for a multireference electron correlation procedure. In addition to the T_1 diagnostic there are other measures such as D_1 ,²²⁰ D_2 ²²¹ or I_{ND} .^{206,207}

2.1.2 Domain localized pair natural orbitals (DLPNOs)

Among the great variety of post-HF methods, successive approximations come to light. The main idea behind the approximate methods is lowering the cost of the computational methods already available in the literature. This means applying approximations to the existing methods and reducing the computational cost's scaling with the system size.

Post-HF methods are computationally expensive as the cost scales with the system size and basis set used, soon reaching the limit of computational resources. Apart from long computational time, a fast storage of all the information generated during the calculation, and large disk space are important factors to have at your disposal when doing such calculations with large systems.

HF molecular orbitals, the starting point of most post-HF methods, are significantly delocalized. However, most molecular orbitals are highly delocalized, for instance, Kohn-Sham orbitals. The fundamental idea behind localized methods is exploiting the locality (short interelectronic distances) of dynamic correlation. If the correlation is significant

at short interelectronic distances, where the electrons are already placed by HF, working with localized orbitals will save computational time.

There are diverse localization-based post-HF methods founded on different localization schemes. In this thesis, we will spotlight the domain localized pair natural orbitals method^{222–225} developed by Neese, as it is one of the most popular methods employed nowadays and it has been used in some of the works covered in this thesis (see Section 8).

The DLPNO method emerges as an improvement of an already existent method, the localized pair natural orbital method (LPNO), also developed by Frank Neese.²²⁶ LPNO expands the pair natural orbitals (PNO) employing canonical virtual orbitals (HF virtual orbitals), and it does not truncate the single excitations. At first, it seemed unnecessary to truncate the single excitations because they give the orbital rotations allowing to include some nondynamic correlation.²²⁷ The original LPNO-CCSD method performed outstandingly for molecules smaller than seventy atoms, with a computational cost only from two to four times greater than a HF calculation. For a large system, an LPNO-CCSD calculation could reduce the number of amplitudes to be calculated by a factor of 10^5 - 10^6 compared to a canonical CCSD calculation using the same basis set.²²³ Although these methods are highly reliable and efficient, they become computationally expensive for large molecules (with > 100 atoms) due to the necessity of higher-order scaling steps.

The DLPNO approximation is based on direct local approaches where locality is used to evade the computation of some specific terms. First, it expands the pair natural orbitals in terms of localized virtual orbitals. Neese used the orbitals named projected atomic orbitals (PAO), and truncated the single excitations using single-specific natural orbitals as accurate as the LPNO method.²²³

PAOs are defined using a virtual basis set and a projector (pseudo-identity operator). A linear combination will provide a set of projected atomic orbitals that expand the external space. The coefficient resulting from the linear combination is the overlap between a virtual and an occupied atomic orbital. There will be as many PAOs as atomic orbitals. Virtual orbitals are being localized around a particular atomic orbital. Therefore, we can define zones or domains. Domains are sets of PAOs that are used to determine a localized molecular orbital. Usually, distances and connectivities are the two criteria used to select the series of PAOs. The bigger the domain, the more accurate the calculation. The orbital will be better described, but at the same time, the efficiency will be reduced. However, there are correlation effects that are not so local; dynamic correlation is primarily local but not entirely. Some effects occur at higher interelectronic distances, and those could be missed with all localized orbital methods. A clear case is Van der Waals interactions. Using only PAOs, calculations are highly dependent on the

domain size. For this reason, Neese proposed to use the PAOs as the basis to construct the PNOs.

In summary, in DLPNO, natural orbitals are built using the PAOs, while the latter will define the domains to start the DLPNO calculation. In such a manner, the high compactness of the original LPNO wavefunction remains as long as we take advantage of a greater locality. DLPNO scales almost linearly with the system size. It has been seen that combining the pair natural orbital approach and the concept of orbital domains, it is possible to attain almost entirely linear scaling CC implementations (DLPNO-CCSD and DLPNO-CCSD(T)) relative to system size that recover roughly 99.9% of the total correlation energy.²²⁸

Several thresholds control DLPNO calculations. However, only three cut-off parameters are needed to be modified unless specific questions are addressed: (i) $T_{CutPairs}$, the threshold for electron pairs to be involved in the CC iterations; (ii) T_{CutPNO} , the most crucial parameter which controls how many PNOs are used for a given electron pair; and (iii) the Mulliken population cutoff for domain selection, T_{CutMKN} , which regulates how large the domains are (the domains will later form the PNOs). For the linear-scaling DLPNO calculations, the domain sizes are controlled with the T_{CutDo} parameter.^{223,225}

DLPNO-MP2, DLPNO-CCSD, and DLPNO-CCSD(T) have become popular methods that can be applied to very large molecules. After all, we should be aware that only dynamical correlation is highly local. Therefore, if these methods retrieve some mild nondynamic correlation effects, it is only natural that we will miss these effects by employing the locality of correlation.

2.2 Density Functional Theory (DFT)

Density Functional Theory^{229,230} is an alternative to wavefunction methods. The formal foundations of DFT were introduced by Hohenberg and Kohn (HK) in 1964. Previously, different energy functionals such as the Thomas-Fermi²³¹ had been proposed, but the basis of the theory was not discovered yet. Thomas-Fermi approximation was formulated in terms of the electronic density ($\rho(\mathbf{1})$) to analyze the electronic structure of a many-body system. It was developed semi-classically, and it is only correct in the limit of an infinite nuclear charge.^{232,233}

HK established the theoretical basis of DFT by introducing the HK theorems. According to HK theorems, DFT is, in principle, an exact theory that states that any property of a system can be calculated employing the ground-state electron density, $\rho(\mathbf{1})$. $\rho(\mathbf{1})$ is an observable that only depends on three spatial coordinates and one spin variable ($\mathbf{1} \equiv r, \sigma$). Unlike wavefunction methods that rely on $4N$ variables (N is the total number of electrons in the system), in DFT the problem's dimensionality is reduced

to 4 variables.

The first HK theorem establishes a one-to-one mapping between the exact ground-state electron density and the external potential (up to an additive arbitrary constant), *i.e.*, any property of the system is a unique functional of the ground-state electron density. Up to this point, for the sake of simplicity, the $E[\rho] \equiv E[\rho(\mathbf{1})]$ short-hand notation will be used. The energy functional can be written as:

$$\begin{aligned} E[\rho] &= T[\rho] + V_{ext}[\rho] + V_{ee}[\rho] \\ &= \int \rho(r) \nu_{ext}(r) dr + F_{HK}[\rho], \end{aligned} \quad (2.13)$$

where $T[\rho]$ is the electronic kinetic energy, V_{ext} is the external potential, and V_{ee} is the electron-electron interaction energy. $F_{HK}[\rho]$ is the Hohenberg and Kohn functional, which is an universal energy functional that depends only on the total number of the electrons of the system,

$$F_{HK}[\rho] = T[\rho] + V_{ee}[\rho] . \quad (2.14)$$

The second HK theorem guarantees the existence of a variational principle,²³⁴

$$E[\rho] \geq E[\rho_{exact}] = E_{min} \quad (2.15)$$

Then, the ground-state density can be found by minimizing $E[\rho]$ constraining the search to densities that integrate to the number of electrons,

$$\frac{\delta}{\delta \rho(r)} \left[E[\rho] - \mu \int \rho(r) dr \right] = 0 \quad (2.16)$$

where μ is the Lagrange multiplier. Using equation 2.13, the Euler equation reads:

$$\frac{\delta F_{HK}(r)}{\delta \rho(r)} + \nu_{ext}(r) = \mu \quad (2.17)$$

The bottleneck of DFT is that the F_{HK} universal functional is unknown. Therefore, DFT methods use approximate functionals. In 1965, Kohn and Sham (KS) introduced the fundamental scheme for the general use of DFT (KS-DFT).²³⁵ The KS scheme uses as a reference a non-interacting system (KS system) with the same density as the original system. Hence, $V_{ee} = 0$ and $T = T_s$. The KS system has N electrons that do not interact with each other, but they interact with an external potential (ν_s). For this system, the electronic energy functional is:

$$E[\rho] = \int \rho(r) \nu_s(r) dr + T_s[\rho] \quad (2.18)$$

and thus the Euler equation reads as:

$$\frac{\delta T_s[\rho]}{\delta \rho} + \nu_s(r) = \mu \quad (2.19)$$

The exact wavefunction of a non-interacting system is a Slater determinant. To find the orbitals and the density of the system one has to solve a set of single-particle equations (similar to the Fock secular equations that arise in HF theory):

$$\left(-\frac{\nabla^2}{2} + \nu_s(r) \right) \phi_i(r) = \varepsilon_i \phi_i(r) \quad (2.20)$$

The density of the KS system is written in terms of one-electron functions, the KS orbitals,

$$\rho(r) = \rho^{KS}(r) = \sum_{i=1}^N |\phi_i(r)|^2 \quad (2.21)$$

KS proposed to express the $F_{HK}[\rho]$ (2.14) as:

$$F_{HK}[\rho] = T_s[\rho] + J[\rho] + E_{xc}[\rho] \quad (2.22)$$

where $J[\rho]$ is the classical Coulomb repulsion between charges and E_{xc} is the exchange-correlation energy. This latter term includes the difference between the exact kinetic energy and the kinetic energy of the non-interacting system, as well as all the energetic non-classical terms between electrons (electron-electron repulsion correlation potential and exchange energy):

$$E_{xc}[\rho] = T[\rho] - T_s[\rho] + V_{ee} - J[\rho] \quad (2.23)$$

Inserting equation 2.22 into equation 2.17:

$$\frac{\delta T_s[\rho]}{\delta \rho(r)} + \nu_{ext}(r) + \frac{\rho(r')}{|r - r'|} + \nu_{xc}(r) = \mu \quad (2.24)$$

and comparing with equation 2.19, we find:

$$\nu_s(r) = \nu_{ext}(r) + \frac{\rho(r')}{|r - r'|} + \nu_{xc}(r) \quad (2.25)$$

It seems that the ground-state density of the interacting system can be found by solving single-particle equations (see Equation 2.20). All the complexity of DFT remains in one term, the XC functional, as every energy functional in equation 2.22 can be calculated exactly from the electron density or the KS orbitals except the exchange-correlation functional.

Accordingly, the KS strategy mitigates the problem of the unknown energy functional using the two main ideas already stated: (i) the energy is described as a sum of terms where only one remains unknown, and (ii) the electron density is calculated from a set of new orbitals that is iteratively improved.

Finding an efficient approach for constructing functionals in terms of the electron density that are universally applicable to correctly describe all the properties of a system is a hard problem and remains unsolved. In this sense, several approximations to the $E_{xc}[\rho]$ functional exist in the literature, known as density functional approximations (DFAs). The use of DFAs leads to errors in the property being calculated. Each DFA is characterized by a different approximation of the XC part. *Jacob's ladder*²³⁶ is a simple and visual way to classify the five main groups of the XC functionals according to the ingredients included in the functional. In other words, in *Jacob's ladder* the functionals are ordered in agreement with their computational cost to achieve the best accuracy, namely, the *heaven of chemical accuracy*.

As one climbs the Jacob ladder, one can find firstly the local spin-density approximation (LSDA), which approximates the XC energy using only the information of the electron density. Secondly, generalized gradient approximation (GGA), which besides $\rho(\mathbf{r})$, also includes the gradient of the density ($\nabla\rho$) at that given position. Thirdly, meta-GGA, for which the energy density also depends on the Laplacian of electron density ($\nabla^2\rho$) or the kinetic energy (τ). These first three rungs scale as N^3 . At higher-order approximations, like hyper-GGA or hybrid functionals, the cost increases, and the XC functional includes a certain fraction of HF exchange (ϵ_x^{HF}).

In the fifth rung, we find the non-local or double hybrid functionals, where the XC functional also relies on the information of unoccupied KS orbitals (ϕ_a). The higher the rung, the higher the complexity of the functional and the computational cost are. Nevertheless, higher-rung functionals do not always imply a better performance of the functional.²³⁷

Nowadays, one of the most used rungs of Jacob's ladder is the one that comprises hybrid functionals, especially to study reactivity and thermochemistry because they offer

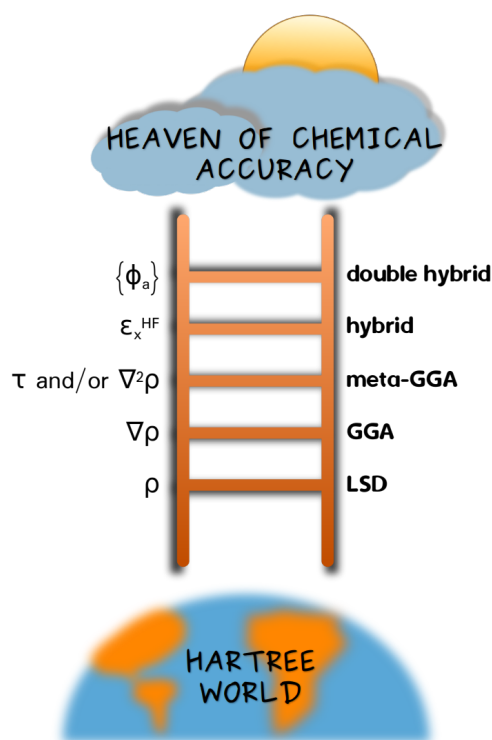


Figure 2.1: Representation of Jacob's Ladder.

a better description of reaction barriers and reaction energies. The energy of the hybrid functionals (E_{XC}^{hyb}) is a summation of GGA/meta-GGA correlation energy (E_C^{GGA}), a fixed fraction of GGA/meta-GGA exchange (E_X^{GGA}) and, a fraction of the exact exchange (E_X^{HF}):

$$E_{XC}^{hyb} = aE_C^{GGA} + bE_X^{GGA} + cE_X^{HF} \quad (2.26)$$

where a , b and c are hybridization coefficients.

Although DFT is among the most popular methods in computational chemistry, especially for big systems, one should keep in mind the main limitations of DFT approximations already mentioned in the introduction (see Section 1.1.1), which can even lead to an erroneous prediction of a particular property.^{238,239}

2.2.1 Delocalization error (DE)

As stated in the previous chapter, the self-interaction and the delocalization errors are a key factor in our studies. In HF, the artificial term corresponding to the Coulomb repulsion energy of an electron with itself is exactly canceled by the corresponding exchange term. Conversely, in DFT, while Coulomb terms are described exactly, the exchange term is expressed by an approximate functional. The SIE is due to the non-cancellation of these two terms. Accordingly, HF does not suffer from this type of error. The DFT XC potential does not decay asymptotically as $-1/r$, as the exact XC potential does.^{240,241} XC potential is the XC energy derivative with respect to the electron density.

Going beyond GGA functionals and introducing non-local HF exchange in the XC potential partially corrects the delocalization error, improving the results using hybrid functionals. Hybrid functionals mix a constant percentage of HF exchange with a semi-local exchange functional (see Eq. 2.26 and B3LYP in Fig. 2.2). However, the use of hybrid functionals is not always sufficient because the decay of XC potential is still incorrect. For this reason, the range-separated functionals were proposed (see Section 2.3). In this context, there are several recent discussions in the literature related to the role of the exact exchange in DFT calculations, especially in large systems.^{17,242–246}

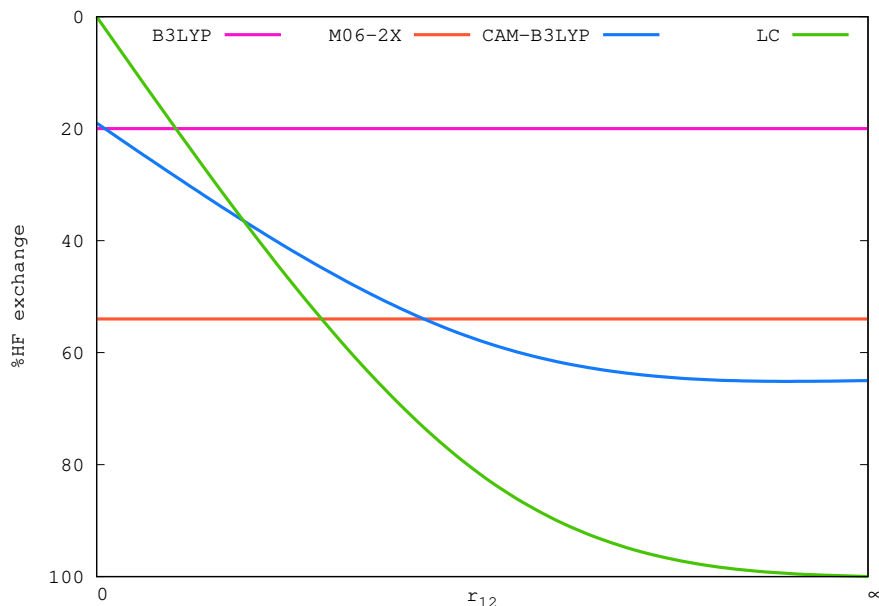


Figure 2.2: Schematic plot of exact exchange percentage included in B3LYP (HF[%]=19), M06-2X (HF[%]=54), CAM-B3LYP (HF[%]=19-65) functionals and LC general scheme (HF[%]=0-100).

For the particular case of aromaticity indices studies, we have seen that the amount of exact exchange included in the functional clearly changes the picture for most of the aromaticity indices, indicating that the percentage of HF-exchange included is highly relevant to obtain an accurate description of the aromaticity character.^{18,19} In most of the projects included in this thesis, we have compared the performance of HF and three different DFAs.

2.3 Range-separated functionals (RSF)

In 1996, Savin proposed a scheme²⁴⁷ to accurately describe the charge transfer states, Rydberg excitations, and polarizabilities of long-chain molecules.²⁴⁸ He suggested splitting the electron repulsion operator, *i.e.*, the classical Coulomb operator, into two terms; one short-range term and one long-range term (eq. 2.27) applying the traditional Ewald approach, which uses the standard error function (*erf*) and treating the two terms with two different methods:

$$\frac{1}{r_{12}} = \frac{\text{erfc}(\omega r_{12})}{r_{12}} + \frac{\text{erf}(\omega r_{12})}{r_{12}}, \quad (2.27)$$

where r_{12} corresponds to the distance between two electrons and ω is the attenuating parameter. In other words, the ω parameter is the one that modifies the percentage of HF exchange included in the XC functional for each interelectronic distance. $\text{erfc}(\omega r)$ is the complementary error function ($\text{erfc}(x) = 1 - \text{erf}(x)$) applied for the short-range term

and $\text{erf}(\omega r)$ is the standard error function which is used for the long-range interaction term. There are more functions that one could apply to this scheme, but the standard error function is the most widely used as it allows the bi-electronic integrals to remain analytically solvable for Gaussian functions. The larger the ω value, the greater role of the long-range method used. If ω tends to zero, then the selected method to describe the long-range term is not being included and all the interelectronic distances are treated with the method used for the short-range (SR) regime (DFT). Conversely, if $\omega=1$, the electron-electron interaction is completely treated with the method selected to describe the LR regime (wave function theory). In DFT, functionals based on this scheme are named range-separated functionals.

Several RSF have come to light over the years. Long-range corrected (LC) functionals, proposed by Hirao,²⁴⁸ were the first type of RSF, including a semi-local method (GGA or LSDA) at a short interelectronic distance and HF for the long-range term. HF exchange exhibits the correct asymptotic behavior for large interelectronic distances, while DFT functionals are usually appropriate for describing interactions at the short-range regime. In fact, at the limit where r_{12} tends to zero, the LDA method is exact.²⁴⁷ Some examples are LC- ω PBE²⁴⁹ or LC-BLYP.²⁴⁸ Yet another group of RSF are the Coulomb-attenuating methods (CAMs), e.g., CAM-B3LYP²⁵⁰ or ω B97X,²⁵¹ that further generalize the LC functionals to couple hybrids at the short-range and increase the HF exchange at long distances.

The first LC functionals presented a static value of the attenuating parameter for general use in thermochemical applications.²⁵² Nevertheless, later, it was suggested to modify this parameter to reach more accurate results.^{253–255} There are different theoretical approaches to modify the attenuating parameter,^{255–257} however, in the following subsection, we will further discuss the scheme proposed by Livshits *et al.*^{253,258–260}

2.3.1 Tuning of the attenuating parameter

The attenuating parameter, also known as the screening or range-separation parameter, changes the relative weight of the two ranges in a RSF as a function of the interelectronic distance. As mentioned before, it has been seen that optimizing the ω parameter for each molecule can improve one-electron excitation energies calculations, such as valence, Rydberg, core and charge-transfer excitations.^{181,261}

There are different methods to proceed with the optimization of the screening parameter. In this thesis, we have employed the so-called Δ SCF method.^{253,258–260} This method is implemented in an in-house script based on Koopmans'-type theorem in Kohn-Sham theory (also known as IP-theorem).²⁶² Within HF theory, Koopmans's theorem stipulates that the first ionization potential (IP) is equal to minus the energy of the highest occupied molecular orbital (HOMO), neglecting orbital relaxation and orbital

correlation. In analogy, it is possible to approximate the electron affinity (EA) to the LUMO orbital energy in the opposite sign. However, in DFT, the exact KS functional satisfies the Koopmans theorem ($\varepsilon_{HOMO} = -IP$) while approximate KS functional does not, which results in an underestimation of the ionization energy.

LC functionals are approximate methods offering KS orbital energies that provide reasonable approximations to the principal IPs according to Koopmans'-type theorem. In Δ SCF method, the IP and the EA can be obtained from the difference between the ground-state energies of the system with N electrons and with $N \pm 1$ electrons:

$$IP(N) = E(N - 1) - E(N) \quad (2.28)$$

$$EA(N) = -IP(N + 1) = E(N + 1) - E(N) \quad (2.29)$$

Then, several functions are defined (Equations 2.30, 2.31, 2.32 and 2.33), their minimization leading to the optimal value of ω .²⁵³

The Koopmans'-type theorem deviation for a system with N and $N + 1$ electrons yield the following tuning conditions:

$$J_0(\omega) = |\varepsilon_{HOMO}^{\omega}(N) + IP(N)| \quad (2.30)$$

$$J_1(\omega) = |\varepsilon_{HOMO}^{\omega}(N + 1) + EA(N)| \quad (2.31)$$

For the purpose of properly describing the fundamental gap, both functions should be minimized simultaneously:

$$J(\omega) = J_0(\omega) + J_1(\omega) \quad (2.32)$$

In general, $J(\omega)$ can be non-zero even for exact functionals as it is defined for systems with different number of electrons. However, it has been seen that the optimal values of ω are very close to the minima of $J_0(\omega)$ or $J_1(\omega)$ subject to the particular form of the ε_{HOMO} and the total energy.^{263,264} To prevent such biased behavior $J^*(\omega)$ function was suggested.²⁵³

$$J^*(\omega) = \sqrt{J_0^2(\omega) + J_1^2(\omega)} \quad (2.33)$$

The script used to optimize the attenuating parameter is based on the minimization of J^* descriptor. First the IP(N) and IP(N+1) calculations were performed at the ω default value ($\omega_{def} = 0.4a.u^{-1}$).²⁴⁹ Although these two calculations depend on the value of ω , for the sake of simplicity, we have only calculated them at the beginning of the optimization process, using the default value of ω . Then, using the golden section search numerical method,²⁶⁵ the J^* minimum is found by constricting the range of values of

ω , where the minimum is supposed to exist. Once the optimal attenuating parameter is found, it is used to perform the required DFT or TDDFT calculation.

We have used this protocol mainly to simulate UV-Vis absorption spectra of different photosensitizers that present CT excitations as well as to compute their redox potential (see Section 9).

2.4 Time dependent density functional theory (TDDFT)

Time-dependent density functional theory is the extension of DFT to study the time-dependent phenomena. TDDFT has become one of the most popular and successful method for computing electronic spectra and non-adiabatic excited dynamics in computational chemistry.²⁶⁶ One of the most frequently calculated properties in this exact approach is the vertical absorption energy as it requires neither the knowledge of the electronic excited-state density nor the energy gradient.²⁶⁷

The building blocks of this theory are the time-dependent equivalent of the first HK theorem (Runge-Gross theorem) and the time-dependent version of the KS theory.^{230,268} The Runge-Gross theorem states a one-to-one mapping exists between the exact electron density and the exact time-dependent external potential aside from a spatial constant that depends on time.^{230,269,270} Furthermore, the availability of a time-dependent KS reference system enables the derivation of the time-dependent KS equations and subsequently reaches the time-dependent one-particle Schrödinger equation.

In the same vein as DFT, where the exact XC functional is not established, in TDDFT, the exact time-dependent XC kernel (Eq. 2.34) is not known, and some approximations are needed. The XC kernel is determined as the second derivative of the XC energy (E_{xc}) with respect to time-dependent density, evaluated at the ground-state density:²³

$$f_{xc}(r_1, t_1, r_2, t_2) = \left. \frac{\delta^2 E_{xc}}{\delta \rho(r_1, t_1) \delta \rho(r_2, t_2)} \right|_{\rho(r)} \quad (2.34)$$

One of the most important approximations is the adiabatic approximation, which allows the utilization of the standard ground-state XC functionals in the context of TDDFT since it is expected that density only varies sluggishly with time. Within this approximation, the exchange-correlation kernel (f_{xc}) is defined as the second derivative of the XC energy with respect to the electron density, and it is assumed to be independent of time:

$$f_{xc}(r_1, r_2) = \frac{\delta^2 E_{xc}}{\delta \rho(r_1) \delta \rho(r_2)} \quad (2.35)$$

After having the time-dependent Kohn-Sham equations, we can use real-time TDDFT or linear-response TDDFT to carry out our calculations. The former consists in propagating the KS wavefunction with respect to the time, while the latter, involves measuring the linear response of the system after applying a weak time-dependent perturbation such as an electromagnetic potential. If, for example, the response to the application of a laser was measured, it would not be possible to use linear response TDDFT and probably it would be necessary to use a quadratic response formalism.

Nowadays, most applications are carried out using linear-response formalism because it is a powerful approach to calculate excitation energies and optical spectra. In all the calculations of this thesis where TDDFT was needed, we have employed this formalism.

Within linear-response TDDFT, the excitation energies of a many-body system are obtained using the so-called Casida's equation or random-phase approximation (RPA):^{23,271,272}

$$\begin{pmatrix} A & B \\ B^* & A^* \end{pmatrix} \begin{pmatrix} X \\ Y \end{pmatrix} = \omega \begin{pmatrix} 1 & 0 \\ 0 & -1 \end{pmatrix} \begin{pmatrix} X \\ Y \end{pmatrix} \quad (2.36)$$

where the matrix elements of A and B are given by:

$$A_{ia,jb} = \delta_{ij}\delta_{ab}(\varepsilon_a - \varepsilon_i) + (ia|jb) - c_{HF}(ij|ab) + (1 - c_{HF})(ia|f_{xc}|jb) \quad (2.37)$$

$$B_{ia,jb} = (ia|bj) - c_{HF}(ib|aj) + (1 - c_{HF})(ia|f_{xc}|bj) \quad (2.38)$$

where ε are the orbital energies. The first term of the A matrix diagonal is the difference between i (occupied) and a (virtual) orbitals energy. The second term of A matrix and the first term of B matrix correspond to the antisymmetrized two-electron integrals (Eq. 2.39) that arise from the linear response of the Coulomb and exchange operators to the first-order changes in the single-particle orbitals,²³⁴

$$(ia|jb) = \int \int dr dr' \frac{\phi_i(r)\phi_a(r)\phi_j(r')\phi_b(r') - \phi_i(r)\phi_j(r)\phi_a(r')\phi_b(r')}{|r - r'|} \quad (2.39)$$

The c_{HF} term in Equations 2.37 and 2.38 is the percentage of HF included in the functional. Therefore, the terms that depend on this parameter correspond to the response of the chosen XC potential (last terms in Equations 2.37 and 2.38) involving the XC kernel.

As a consequence of the adiabatic approximation, the principal limitation of TDDFT approximate functionals inherited from DFT is that they bring in significant errors in the description of some excited states (CT or the Rydberg excited states).²⁰⁻²³ As commented in the previous section, the approximate functionals usually underestimate the

CT excitation energy and they fail to reproduce their potential energy curves due to the SIE. For large interelectronic distances, they do not exhibit the correct $-1/r_{12}$ decay. However, if the approximate functionals include a specific percentage of exact exchange (HF exchange) they improve the description of the above mentioned excited states.

Another important problem of TDDFT is the description of double²⁷³ and triplet^{274,275} excitations. TDDFT does not identify double excitations when the linear response and adiabatic approximations are used. These excitations can be incorporated in TDDFT, for example, by extending the method beyond linear response.^{276,277} On the other hand, triplet excitations energies could be underestimated using TDDFT due to the inclusion of the exact exchange in the XC potential. This limitation of TDDFT is known as triplet instability, and it is usually addressed by using the Tamm-Dancoff approximation.^{23,278} However, in the present dissertation, neither double nor triplet excitations are studied.

Chapter 3

Aromaticity

In this chapter, we will explain which indicators we use to establish bridges between quantum mechanics and classical chemical concepts (*e.g.*, chemical bond or aromaticity), starting with the partition of the molecular space and the definition of an atom in a molecule. Since atoms are composed of electrons and most of the chemistry and reactivity can be explained by distributing the electrons in the molecules, it is natural to take the electron density as the central quantity to define an atomic partition. For this reason, the tools used in this thesis are based on the electron density, the pair density, and the orbitals, among others. Then, we will review the aromaticity descriptors used in the projects of this thesis, giving some examples and paying special attention to the electronic ones.

3.1 Density and high-order density matrices

The electron density ($\rho(\mathbf{1})$) is the central quantity in DFT (*vide infra*) and also to the quantum theory of atoms in molecules (QTAIM, see the following sections). Born's rule²⁷⁹ specifies that the probability of finding one electron within the infinitesimal volume around the position of electron 1 with spin σ_1 (d_1) is determined by the square of the wavefunction that describes the system,

$$P(\mathbf{1})d_1 = \int d_2 \int d_3 \dots \int d_N |\psi(\mathbf{1}, \mathbf{2}, \dots, N)|^2 d_1, \quad (3.1)$$

where N is the total number of electrons in the system, and $P(\mathbf{1})$ is the probability of finding one electron at position $\mathbf{1}$ regardless of the position of the other ($N-1$) electrons. From equation 3.1 the electron density is determined as:

$$\rho(\mathbf{1}) = NP(\mathbf{1}). \quad (3.2)$$

Since the electrons are indistinguishable particles, the electron density accounts for the probability of finding at least one electron at $\mathbf{1}$.

Indeed, electron density is the diagonal part of the first-order reduced density matrix (1-RDM), $\rho(\mathbf{1}) \equiv \rho_1(\mathbf{1}; \mathbf{1})$:

$$\rho_1(\mathbf{1}; \mathbf{1}') = N \int d_2 d_3 \dots \int d_N \psi^*(\mathbf{1}, \mathbf{2}, \dots, N) \psi(\mathbf{1}', \mathbf{2}, \dots, N), \quad (3.3)$$

where different coordinates are used for the first electron of the two wavefunctions that are included in the integral. The 1-RDM will be used to define several chemical bonding tools.

Reduced density matrices (RDM) are lower-rank matrices obtained by integrating the appropriate electronic coordinates of density matrices.^{280,281} Density matrices are a compact form to display the maximum information available about the system, using functions with less variables. In general, the diagonal of the n -order RDM (n -RDM) are named n -electron densities. Another relevant n -electron density is the one derived from the diagonal elements of the second-order RDM (2-RDM), the pair density ($\rho_2(\mathbf{1}, \mathbf{2})$):

$$\rho_2(\mathbf{1}, \mathbf{2}) = N(N-1)P(\mathbf{1}, \mathbf{2}), \quad (3.4)$$

where $P(\mathbf{1}, \mathbf{2})$ is the probability of finding two electrons, one at $\mathbf{1}$ and the other at $\mathbf{2}$, regardless of the position of other $N-2$ electrons.²⁸²

$$P(\mathbf{1}, \mathbf{2}) = \int d_3 \dots \int d_N \psi^*(\mathbf{1}, \mathbf{2}, \dots, N) \psi(\mathbf{1}, \mathbf{2}, \dots, N) d_1 d_2. \quad (3.5)$$

Therefore, the pair density represents the probability of finding at least a pair of electrons, one in d_1 and the other in d_2 .^{229,283}

3.2 An atom in a molecule (AIM)

In 1916, Lewis presented his first definition of a chemical bond when he suggested that atoms remain together by sharing a pair of electrons between them. To characterize the electronic distribution of a molecule we need to define an atom in a molecule (AIM). This will allow to define the type of bonding between atoms and the character of atoms that assemble the bond.

There are several definitions of an atom within a molecule that could be classified according to the atomic partition method, *i.e.*, the scheme used to define the atoms in the molecule. The atomic partition is an arbitrary method used to calculate atomic properties and identify chemical bonds within its limitations. On the one hand, the atomic partition could be defined using the Hilbert space, where the atom in a molecule is defined as an assortment of basis functions localized over the atom. We can highlight the Mulliken population analysis²⁸⁴ which uses the Hilbert space to provide the partial atomic charges. Even though Hilbert space allows an analytically atomic decomposition for some properties, it also presents two main drawbacks: it is a strong basis-set dependent method, and it presents ambiguity in assigning some basis set functions to an atom (*e.g.*, diffuse functions). On the other hand, the atomic partition could be defined by partitioning the real 3D molecular space, where the most well-known method is the quantum theory of atoms in molecules (QTAIM).²⁸⁵ Among the other real-space partitions we can highlight, for example, the Voronoi Cells,²⁸⁶ Hirshfeld Atoms²⁸⁷ fuzzy atom partition,^{288,289} Becke- ρ partition^{290–292} and topological fuzzy Voronoi cells (TFVC).²⁹³ However, it has been demonstrated that QTAIM method is the best one for aromaticity studies.²⁹⁴ Therefore, we have used the QTAIM method in the studies presented herein and it will be briefly discussed hereafter. It has been seen that employing other atomic partitions, the aromaticity indices do not have a correct performance.²⁹⁴ In addition, TFVC method was used to calculate the effective oxidation states in the study presented in Section 8.

3.2.1 Effective oxidation states (EOS)

The topological fuzzy Voronoi cells²⁹³ atomic definition was proposed as an alternative to the QTAIM partitioning to define the atomic boundaries within the molecule. TFVC basins are based on the fuzzy atomic Voronoi cells introduced by Becke.²⁹⁰ TFVC provides, with a lower computational cost, properties that depend on the atomic definition, such as atomic charges or delocalization indexes (*vide infra*), very similar to those obtained with QTAIM.

The effective oxidation states (EOS) method^{295,296} is a new general scheme to cal-

culate oxidation states (OS) from electronic structure calculations. This scheme can be applied to any molecular system and for any level of theory or electronic state. The first step to compute the EOS, is the calculation of the effective atomic orbitals (eff-AOs) for each atom or fragment considered.^{297,298} These are hybrid atomic orbitals that are obtained, for single-determinant methods, by diagonalizing the following matrix,

$$S_{ij}^A = \int \phi_i^{A,\sigma}(r) \phi_j^{A,\sigma}(r) dr \quad , \quad (3.6)$$

were,

$$\phi_i^{A,\sigma}(r) = \begin{cases} \phi_i^{A,\sigma}(r) = \phi_i^\sigma(r), & \text{if } r \in A \\ \phi_i^{A,\sigma}(r) = 0, & \text{otherwise} \end{cases} \quad , \quad (3.7)$$

A is the spatial region belonging to a given atom or fragment, and $\phi^\sigma(r)$ is an occupied molecular orbital. Each eff-AO has an occupation number that indicates whether it is a core/lone pair, valence, or virtual hybrid. In the EOS scheme, this occupation number will be used to list by decreasing order, the eff-AOs of all atoms or fragments treating each spin σ independently. The first N_σ , being N_σ the number of σ electrons of the system, eff-AOs are considered occupied ($\lambda_\nu^{A,\sigma} \rightarrow 1$) while the latter are considered empty ($\lambda_\nu^{A,\sigma} \rightarrow 0$). With the occupied eff-AOs one can build the effective configuration of the atoms or fragments within the molecule, and thus their OS. In addition to the OS assignment, the reliability index ($R \equiv \min(R^\alpha, R^\beta)$) can be calculated from the frontier eff-AOs as,

$$R^\sigma = 100 \times \min(1, \lambda_{LO}^\sigma - \lambda_{FU}^\sigma + 1/2) \quad \text{with} \quad (\lambda_{LO}^\sigma \geq \lambda_{FU}^\sigma) \quad , \quad (3.8)$$

where λ_{LO}^σ and λ_{FU}^σ are the actual occupations of the considered last occupied and first unoccupied eff-AOs, respectively. The worst situation is when $\lambda_{LO}^\sigma = \lambda_{FU}^\sigma$ and it corresponds to a $R = 50\%$.

3.2.2 The quantum theory of atoms in molecules (QTAIM)

The quantum theory of atoms in molecules (originally called the Atoms in Molecules theory) was established by Richard F. W. Bader.²⁹⁹ It defines the atom as a proper open system by partitioning the real space employing the topological properties of the electron density. This theory aims to have a well-defined physical understanding for two fundamental and significant concepts in quantum chemistry: atoms and bonds. The electron density is a scalar field and it can be visualized in a molecular plane (Figure 3.1), where the atoms present the maxima of this function. By carefully analyzing the topology of ρ and its first derivative, we find a set of different critical points (\mathbf{r}_{cp}):

$$\nabla\rho(\mathbf{r}_{cp}) = 0 \quad (3.9)$$

We can characterize them analyzing the second derivative of the ρ collected in the Hessian Matrix (\mathbf{H}):

$$\mathbf{H}[\rho](\mathbf{r}_{cp}) = \nabla_r^T \nabla_r \rho(r)|_{r=r_{cp}} = \begin{pmatrix} \frac{\partial^2 \rho(r)}{\partial x^2} & \frac{\partial^2 \rho(r)}{\partial x \partial y} & \frac{\partial^2 \rho(r)}{\partial x \partial z} \\ \frac{\partial^2 \rho(r)}{\partial y \partial x} & \frac{\partial^2 \rho(r)}{\partial y^2} & \frac{\partial^2 \rho(r)}{\partial y \partial z} \\ \frac{\partial^2 \rho(r)}{\partial z \partial x} & \frac{\partial^2 \rho(r)}{\partial z \partial y} & \frac{\partial^2 \rho(r)}{\partial z^2} \end{pmatrix}_{r=r_{cp}} \quad (3.10)$$

The Hessian matrix is a real symmetric matrix that can be diagonalized via a unitary transformation (\mathbf{L}):

$$\mathbf{H}[\rho]\mathbf{L} = \mathbf{L}\Lambda \quad (3.11)$$

$$\Lambda = \begin{pmatrix} \frac{\partial^2 \rho(r)}{\partial x_1^2} & 0 & 0 \\ 0 & \frac{\partial^2 \rho(r)}{\partial y_1^2} & 0 \\ 0 & 0 & \frac{\partial^2 \rho(r)}{\partial z_1^2} \end{pmatrix}_{r_1=r_c} = \begin{pmatrix} \lambda_1 & 0 & 0 \\ 0 & \lambda_2 & 0 \\ 0 & 0 & \lambda_3 \end{pmatrix} \quad (3.12)$$

We can label a critical point (CP) using its rank (Ω) and signature (α) as $\text{CP}=(\Omega,\alpha)$. The rank is the number of eigenvalues other than zero, and the signature is the sum of the sign of the eigenvalues, *i.e.*, the curvature. Each positive curvature contributes +1 to the signature while a negative curvature adds -1. Assuming non-zero eigenvalues ($\Omega=3$), the critical points can be classified into four groups determined by the value of the signature:

- **(3,-3)**: Attractor or Nuclear Critical Point (ACP). All the curvatures are negative in an ACP, and thus this CP is a maximum of the electron density. These points usually coincide with an atomic position; otherwise, these CPs are called non-nuclear maxima (NNA).
- **(3,-1)**: Bond Critical Point (BCP). A BCP shows two negative curvatures and a positive one. BCP connects two ACP, and it is usually an indicator of the presence of a chemical bond.
- **(3,+1)**: Ring Critical Point (RCP). A RCP has two positive curvatures and a negative one. The presence of a RCP usually indicates a ring structure of the

molecule. If the molecule is planar, the RCP is located in the minimum of the electron density inside the ring structure.

- **(3,+3):** Cage Critical Point (CCP). A CCP has three positive eigenvalues, and it is thus a minimum of the electron density. The CCP indicates a cage structure, and it is usually located near the center of the cage.

The CP are connected between them through gradient lines named bond paths. The gradient lines that connect the RCP with BCP are known as ring paths.

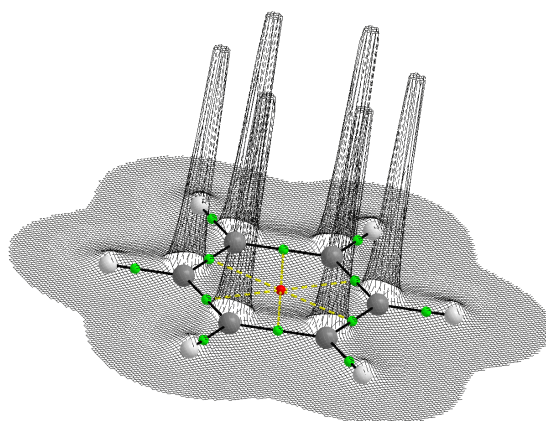


Figure 3.1: QTAIM analysis of benzene. In grey the relief map of electron density (ρ) is plotted. The carbon atoms in grey, hydrogen atoms in white, BCP in green, RCP in red, bond path in black lines and ring path in yellow dashed lines are represented.

The Poincaré-Hopf expression³⁰⁰ gives the relationship between the different number of critical points in a molecule:

$$n_{ACP} - n_{BCP} + n_{rCP} - n_{CCP} = 1 \quad (3.13)$$

The second derivative of the electron density also provides insight on the concentration or depletion of the electron density. If the Laplacian is negative, we have an electron accumulation (localization of electrons). On the other side, if the Laplacian is positive, we have an electron depletion (delocalization of electrons).

3.2.3 Population Analysis

A helpful tool to study the electron distribution within a molecule is the population analysis. This technique uses a specific definition of the AIM to obtain atomic populations and atomic charges. The integration of the electron density over a region A gives the amount of charge located in this atomic domain, N_A :

$$N_A = \int_A \rho(\mathbf{1}) d_1 \quad (3.14)$$

This is a way to distribute the N electrons of the molecule between the atoms that form it. The sum of all atomic populations must give the total number of electrons of the system. Using the atomic population and the atomic number (Z_A), one can obtain the atomic charge (Q_A) as:

$$Q_A = Z_A - N_A \quad (3.15)$$

The resulting Q_A can not be used to calculate the oxidation state of a molecule as it is usually a non-integer number, and oxidation states are always integer values. Atomic charges are very sensitive to the choice of the AIM method.²⁸⁶ For this reason, it is not recommended to draw any conclusion only from the atomic charges calculations.

As it was mentioned before, the most popular population analysis is the Mulliken one that uses the Hilbert space partition and can be obtained from any computational code. Contrarily, AIMS employing a real space partition are more complicated to calculate because they require a numerical integration over the atomic domain A:

$$N_A = \int_A \rho(\mathbf{1})d_1 = \sum_i n_i \int_A |\phi_i(\mathbf{1})|^2 d_1 = \sum_i n_i S_{ii}(A) \quad (3.16)$$

that requires the diagonal part of atomic overlap matrix (AOM):

$$S_{ij}(A) = \int_A \phi_i^*(\mathbf{1})\phi_j(\mathbf{1})d_1, \quad (3.17)$$

where n_i is the orbital occupation.

The analysis based on the real space partition presents a numerical error due to the need to use numerical integration to obtain AOM. In contrast, the ones using the Hilbert space division present no numerical error because they involve analytical integrals for GTOs. QAIM population analysis can be attained from AIMall,³⁰¹ AIM2000,^{302,303} APOST-3D³⁰⁴ or ESI-3D³⁰⁵ (the latter does not perform integrations, AOMs should be provided), among others.

3.2.4 Electron-sharing indices (ESI)

Once we have defined an atom in a molecule, another fundamental chemical concept we can calculate is the bond order (BO). The BO gives the number of chemical bonds between a pair of atoms, and from the very beginning, it was also closely related to aromaticity.³⁰⁶ Coulson was one of the first to quantify the BO employing quantum mechanics calculations, which involved the Hückel molecular orbital theory.³⁰⁷ This measure of BO is known as the Coulson bond order (CBO). Nonetheless, nowadays, CBO is almost not used anymore due to the very approximate nature of the HMO method. A well-known replacement for the CBO is the concept of electron sharing index (ESI) proposed by Fulton,³⁰⁸ which measures to which extent two atoms are sharing the electrons

lying between them. Following some previous works²⁹¹ we will name ESI all quantities that measure the number of electrons shared by a pair of atoms. We can find several definitions of ESI in the literature.²⁹¹ Here we will focus on the ones calculated from the exchange-correlation density (XCD).³⁰⁹ However, it is worth mentioning that Mulliken's analysis²⁸⁴ was also one of the preferred for its simplicity and low computational cost.³¹⁰

The exchange-correlation density compares a fictitious pair density of independent electron pairs ($\rho(1)\rho(2)$) with the real pair density ($\rho_2(1,2)$) as defined in the following equation:

$$\rho_{xc}(1,2) = \rho(1)\rho(2) - \rho_2(1,2), \quad (3.18)$$

The more independent the electrons are, the smaller the XCD should be. The opposite scenario is when the electrons are dependent or coupled; the more coupled, the more significant the difference. One of the most popular ESI derived from QTAIM is the delocalization index (DI):^{311–313}

$$\delta(A,B) = 2 \int_A \int_B d_1 d_2 \rho_{xc}(1,2) = -2cov(N_A, N_B), \quad (3.19)$$

where N_A is the electron population of the atom A and N_B for the atom B (Eq. 3.16).

On the contrary, the localization index (LI) could also be defined using the XCD as:

$$\lambda(A) = \frac{\delta(A,A)}{2} = \int_A \int_A d_1 d_2 \rho_{xc}(1,2) \quad (3.20)$$

The DI measures the number of electrons delocalized or shared between two different atoms (A and B), while the LI informs us about the number of electrons localized in one atomic domain (A). As shown in Eq. 3.19, the DI is related to the covariance of A and B atomic populations since it is also a measure of the fluctuating electrons between this pair of atoms. The DI has been used to define aromaticity indices, and its validation has also been done.^{314–316}

Single, double, and triple bonds usually exhibit DI values close to 1, 2, and 3, respectively, whereas classical aromatic bonds show DI values around 1.5. The less the molecular structure resembles a Lewis-structure, the less predictable the localization indices are.

It is also helpful to define the delocalization of a specific atom, which some authors³¹⁷ relate to the valence of the atom:

$$\delta(A) = \sum_{B \neq A} \delta(A,B) = \frac{1}{2} \sum_{B, A < B} \delta(A,B) \quad (3.21)$$

Since the XCD integrates to the number of electrons, we can classify all the electrons in a molecule as localized, assigning them to atoms, or delocalized, attributing them to the pairs of atoms; the following equation is satisfied:

$$N_A = \int_A \rho(\mathbf{1}) d_1 = \delta(A) + \lambda(A) , \quad (3.22)$$

giving rise to the sum rule:

$$N = \sum_A N_A = \sum_{B, A < B} \delta(A, B) + \sum_A \lambda(A), \quad (3.23)$$

where N is the total number of electrons in the system. An electron localized within an atom contributes 1 to the LI. When a pair of electrons is shared between two atoms, it contributes 0.5 to the LI of each atom and 1 to the DI.³¹¹

In this thesis, the delocalization index will be calculated for single-determinant (SD) wavefunctions such as HF and KS-DFT. For closed-shell SD wavefunctions, the DI and LI (Eqs. 3.19 and 3.20) attain a simple form:

$$\delta(A, B) = 4 \sum_{ij}^{N/2} S_{ij}(A) S_{ij}(B) \quad (3.24)$$

$$\lambda(A) = 2 \sum_{ij}^{N/2} S_{ij}(A)^2 \quad (3.25)$$

where S_{ij} is the AOM of atom A defined as,

$$S_{ij}(A) = \int_A d_1 \phi_i^*(1) \phi_j(1), \quad (3.26)$$

$\phi_i(1)$ being a molecular orbital. DI gives a measure of the number of electron pairs covalently shared between two atoms. However, this index has a relevant limitation: if the atom pair is bonded by electrostatic interactions, the index will not reflect it. If we suspect our bond to be ionic, we should inspect the DI, and the value should be relatively small. We can help ourselves by analyzing electron density at the BCP (*i.e.*, if it is small, it is probably an ionic bond) or perform an energy decomposition analysis (EDA).²⁹²

For correlated wavefunctions, the calculation is tedious and complicated since the pair density is not easy to obtain and computationally expensive. More often than not, one computes an approximation to the DI. Usually, the 2-RDM or pair density in terms of the 1-RDM.²⁹¹ In the literature, there are plenty of different methods to make such approximations,²⁰⁴ but the most used, due to its simplicity, are Ángyán's or HF-like³¹⁸ and Fulton or Müller³¹⁹ approximations. Ángyán approximation does not fulfill the sum rule exposed in equation 3.23. In contrast, Fulton approximation usually gives a better approximation because it does satisfy the equation 3.23.^{291,320}

ESI are not limited to the study of the electron sharing between two entities; they are also employed to investigate to what extent the electrons are shared between more than two regions or atoms, the so-called multicenter indices.

3.2.5 Multicenter indices

The Lewis theory³²¹ is not enough to fully rationalize the electronic structures of the molecules due to the lack of accountability for multicenter bonding. Using the electron pair, one could characterize the bonding between two atoms but not the bond that involve more than two atoms in the chemical bond. In 1990, Giambiagi *et al.* proposed one of the first attempts to use a multicenter index³²² to calculate a multicenter bonding:

$$I(A_1, A_2, \dots, A_n) = \int_{A_1} d_1 \int_{A_2} d_2 \dots \int_{A_n} d_n \rho_1(1;2)\rho_1(2;3) \dots \rho_1(n;1) \quad (3.27)$$

where $N \geq n$ and the expression depends on the 1-RDM, $\rho_1(1,2)$, defined previously. Notice that this index depends on the particular order of the atoms in the string for $n > 3$. Afterward, some authors^{323–325} discovered that the sign of three-center indices was an indicator of the number of electrons involved in the bond. A positive value indicates three-center two-electron (3c-2e) while a negative value points to a three-center four-electron (3c-4e) system.

In 1994, Giambiagi³²⁶ reformulated his definition of I index in terms of the n -RDM, named here n -center ESI (nc -ESI)³²⁷

$$\delta(A_1, \dots, A_n) = \frac{(-2)^{n-1}}{(n-1)!} \left\langle \prod_{i=1}^n (\hat{N}_{A_i} - \bar{N}_{A_i}) \right\rangle \quad (3.28)$$

The last-mentioned index is invariant with respect to the order of the atoms in the ring. It measures the probability of having simultaneously one electron at A_1 , another at A_2 , *etc.*, regardless of the position of the $N-n$ electrons of the system. The regions A_i are usually atoms in the molecule, but one could also use molecular fragments or other relevant regions of the space, *vide supra*. Giambiagi was also the one who later proposed to use the multicenter indices as a measure of aromaticity³²⁸ and denote Eq. 3.27 as an aromaticity index, I_{ring} .³²⁹ After that, several aromaticity indices based on multicenter indices start to be developed by different authors.^{330,331} Besides the use in aromaticity studies, multicenter indices have been used to analyze conjugation and hyperconjugation effects,³³² to distinguish agostic bonds^{333,334} and to account for electron distribution in molecules.³³⁵

In the next section, we will carefully review the different multicenter indices to study aromaticity and other descriptors that are not based on electron delocalization.

3.3 Aromaticity Descriptors

If the definition of *aromaticity* is a troublesome issue, trying to reach an agreement on the description and quantification of the aromatic character of a particular system is even more complicated. In other words, despite having different experimental techniques to characterize this property indirectly and a wide range of diverse theoretical indices, it is expected that all of them will lead to the same conclusions. Nonetheless, Katritzky *et al.* demonstrated that the magnetic manifestations of aromaticity are orthogonal to other electronic or geometric measures.⁷¹

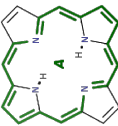




Many authors suggest using a set of descriptors based on different criteria to describe aromaticity, both from an experimental and theoretical perspective.^{71,85,92,336–338} The previous chapters, (see 1.3) have already mentioned some of the experimental techniques or properties used to describe aromaticity, especially in porphyrinoids. In the present section, we will focus on the theoretical criteria to define the aromatic character of molecules.

In computational chemistry, one can measure aromaticity using a sorted variety of descriptors available in the literature. Aromaticity indices could be classified into four primary groups regarding the different manifestations of aromaticity: energetic,⁸¹ magnetic,³³ geometric,⁸³ and electronic.⁸⁵ In the following sections, the ones used in our studies will be described. The articles included in this thesis particularly focus on electronic aromaticity indices and their performance.

For most of the indices explained in this section, we will employ as a reference the indices values of porphin, the simplest aromatic porphyrin known. Isophlorin,¹²¹ by contrast, will be presented as an antiaromatic example. The local aromaticity indices, will correspond to the most aromatic pathway. We will also evaluate more straightforward examples, such as to benzene, cyclohexane, and cyclohexatriene (with a relation between the double bond and simple bond of 0.8). These molecules are known to be aromatic, nonaromatic, and antiaromatic, respectively. All the calculations were done at the CAM-B3YLP level of theory in combination with the 6-311G(d,p) basis set in the gas phase. All aromaticity indices reported are gathered in Table 3.1.

For simplicity, the aromaticity descriptors formula are associated to a molecule with n atoms denoted by the string $\mathcal{A} = \{A_1, A_2, \dots, A_n\}$ whose components are arranged following the connectivity of the atoms in the ring. In addition, for convenience, we adopt $A_{n+p} \equiv A_p (p \geq 0)$.

Table 3.1: Aromaticity descriptors values of porphrin, isophlorin, benzene, cyclohexane, and cyclohexatriene (a/b=0.8) at CAM-B3LYP/6-311G(d,p) level of theory.

Molecule	Structure	HOMA	BLA	FLU	BOA	I_{ring}	$I_{ring}^{1/n}$	MCI	$MCI^{1/n}$	AV1245	AV_{min}	$NICS(0)_{iso}$	$NICS(1)$
Porphrin		0.872	0.035	0.010	0.137	-	-	-	-	2.16	1.28	-15.5	-14.1
Isophlorin		0.465	0.082	0.026	0.374	-	-	-	-	1.12	0.76	13.8	12.2
Benzene		0.000	0.000	0.000	0.000	0.048	0.603	0.072	0.646	10.71	10.71	-8.8	-11.3
Cyclohexane		-4.167	0.000	0.090	0.000	0.000	0.256	0.000	0.260	-0.01	0.01	-2.1	-1.9
Cyclohexatriene (a/b=0.8)		-31.266	0.408	0.087	0.822	0.012	0.478	0.013	0.484	2.99	2.99	-4.1	-4.6

3.3.1 Energetic indices

Energetic criteria are important to identify molecules that benefit from extra energy stabilization. In some molecules, especially organic ones, conjugated-electron circuits along a ring structure cause important energy stabilization, bond-length and bond-order equalization. In recent years, energetic aromaticity descriptors have not been widely used³³⁹ but among the different energetic criteria, the aromatic stabilization energy (ASE)⁸¹ could be highlighted. Despite different versions of ASE exist,¹⁵¹ the original idea is to assess the aromatic stabilization energy using a homodesmotic or isodesmotic reaction. As an aromatic descriptor, ASE is positive for aromatic molecules and negative for antiaromatic ones. The primary limitations of ASE are the difficulty to isolate the aromatic stabilization energy from other effects that could stabilize or destabilize the system, and the arbitrariness of the reference reaction to compute it. To calculate ASE, a reference reaction involving the system of interest is needed, and it is not always a step-forward process to find the most suitable reference. In addition, as we will see with other descriptors, *vide infra*, an aromatic index based on references, does not measure the aromatic character of the system but it measures the similarity with respect to some reference molecule. For all these reasons, energetic descriptors are not used in the present thesis.

3.3.2 Geometric indices

The main idea of the structural aromaticity descriptors is that bond-length equalization and the molecular symmetry are signatures of the aromatic character.

Harmonic oscillator model of aromaticity (HOMA)

One of the most popular and effective geometric aromaticity indices is the so-called harmonic oscillator model of aromaticity developed by Kruszewski and Krygowski in 1972.³⁴⁰ HOMA relies only on geometric data, and it can be calculated using the following formula:

$$\begin{aligned} HOMA(\mathcal{A}) &= 1 - \frac{1}{n} \sum_i^n \alpha_i (r_{opt} - r_{A_i, A_{i+1}})^2 \\ &= 1 - (EN + GEO) \end{aligned} \quad (3.29)$$

where α_i is an empirical constant that depends on the type of bonds in the molecule, and $r_{A,B}$ is the distance between atoms A and B. It is usually assumed that all the bonds present in a molecule are of the same kind. However, it can also be derived for rings with different bonding patterns, but it is a bit more tedious.³⁴¹ HOMA index uses some

reference bond lengths, r_{opt} , for which the compression energy of the double bond and the expansion energy of the single bond are minimal according to the harmonic potential model.

As can be seen in the formula 3.29, HOMA could be decomposed into the energetic (EN) and the geometric (GEO) components. The EN contribution measures the deviation of the bond distances compared to some tabulated data, while the GEO component evaluates the variance of the interatomic distance for the bonded pairs (or bond distance). Both quantities, EN and GEO, are close to zero for aromatic molecules.

HOMA descriptor gives values close to one for aromatic species. Small or negative values indicate a nonaromatic or antiaromatic species. For porphin, HOMA equals 0.872, and for isophlorin, 0.465, whereas the descriptor takes values of 0.000, -4.167, and -31.266 for benzene, cyclohexane, and cyclohexatriene, respectively.

The main advantage of all the structural indices is that with only the bond lengths and some extra reference values, they can tell you whether the system is aromatic, antiaromatic, or nonaromatic. On the contrary, the major limitation of HOMA is its dependence on reference values. This implies that the reference data is limited only to a few numbers of bonds (C–C, C–N, C–O, C–P, C–S, N–N, and N–O). Therefore, HOMA can not be calculated for all molecules, and it is not suitable to study reactivity^{38,92} and new aromatic molecules which contain bonds other than the reference ones.

Bond-length alternation (BLA)

Bond-length alternation is another old structural descriptor^{342,343} which compares the average of bond lengths of consecutive bonds in a ring and it can be expressed as:

$$BLA(\mathcal{A}) = \frac{1}{n_1} \sum_{i=1}^{n_1} r_{A_{2i-1}, A_{2i}} - \frac{1}{n_2} \sum_{i=1}^{n_2} r_{A_{2i}, A_{2i+1}} \quad (3.30)$$

where $n_1 = \lfloor (n+1)/2 \rfloor$ and $n_2 = \lfloor n/2 \rfloor$. $\lfloor x \rfloor$ is the floor function of x , which returns the largest integer less than or equal to x .

The definition expressed in formula 3.30 was originally derived for open chains. Therefore, it does not correctly describe the bond-length alternation of rings with an odd number of atoms. In such cases, two consecutive bonds are averaged together, and its value depends on the order of the atoms in the ring. Accordingly, we have used a modified BLA definition for all cases (odd and even number of atoms):¹⁹

$$BLA(\mathcal{A}) = \frac{1}{2n} \sum_{i=1}^n |r_{A_i, A_{i+1}} - r_{A_{i+1}, A_{i+2}}| \quad (3.31)$$

BLA directly measures the bond-length equalization expected in aromatic paths, and it does not need reference data. The BLA values are close to zero for aromatic species.

As expected for an aromatic and antiaromatic species, it takes values of 0.035 and 0.082 respectively, for porphin and isophlorin. BLA equals 0.000, 0.000, and 0.408 for benzene, cyclohexane, and cyclohexatriene, respectively. As it can be seen, nonaromatic species could also present BLA values close to zero. Cyclohexane, for example, only presents single bonds and if the difference between the bonds length is performed, it will give $BLA=0.000$.

As stated above, it is necessary to choose an expression to correctly characterize the system, leaving aside the number of atoms. For some authors, one of the limitations of BLA is that it assumes the alternation of bond length reflects the distribution of electrons in a conjugated circuit. As we have just seen with cyclohexane, this is not always the case. For this reason, electronic indices are usually preferred.

3.3.3 Electronic indices

In recent times, the aromaticity indicators based on the electronic structure of the molecule are becoming popular. Among a great variety of electronic descriptors,^{330,331,344–346} the ones described in more detail in the following subsections are based on the electron delocalization measures, most of them involving the ESIs (equation 3.19).

Aromatic fluctuation index (FLU)

In 2005, Matito and Solà introduced the electronic analog to HOMA index, the aromatic fluctuation index. FLU is constructed to perform an aromaticity analysis that goes beyond the bond-length information.^{315,316} This electronic descriptor only employs the electronic delocalization of the atoms in the ring and compare them with the cyclic electron delocalization of an aromatic molecule of reference:

$$FLU(A) = \frac{1}{n} \sum_{i=1}^n \left[\left(\frac{\delta(A_i)}{\delta(A_{i-1})} \right)^\alpha \left(\frac{\delta(A_i, A_{i-1}) - \delta_{ref}(A_i, A_{i-1})}{\delta_{ref}(A_i, A_{i-1})} \right) \right]^2 \quad (3.32)$$

where α allows to ensure that the first term of the equation 3.32 is always greater than or equal to 1,

$$\alpha = \begin{cases} 1 & \delta(A_{i-1}) \leq \delta(A_i) \\ -1 & \delta(A_i) < \delta(A_{i-1}) \end{cases}, \quad (3.33)$$

and $\delta_{ref}(A, B)$ is the DI of the aromatic molecule of reference. For instance, for C–C bonds, the reference is benzene, whereas the C–N bond reference is taken from pyridine.

FLU values are close to zero if the molecule is aromatic, while it takes large values for nonaromatic and antiaromatic species. For the simplest aromatic porphyrin, its value

equals to 0.010, albeit for isophlorin is 0.026. Thus, the FLU value of isophlorin is slightly higher than the porhin one, as it is expected because it is an antiaromatic molecule. In the six-membered ring examples, the FLU values are 0.000, 0.090, and 0.087, corresponding to benzene, cyclohexane, and cyclohexatriene, respectively. Cyclohexatriene's FLU value lies in the middle of the other two six-membered rings because it is slightly antiaromatic and the others are aromatic (benzene) and nonaromatic (cyclohexane).

Similar to HOMA, FLU does not measure aromaticity itself. Instead, it compares the values with an aromatic reference molecule. Thus, it cannot be used to describe reactivity^{38,92} because it will always underestimate the aromaticity character. Additionally, FLU is an index that relies on two-center measures of delocalization. Consequently, it could fail to describe the aromatic character of the molecules where the aromaticity involves multicenter conjugation patterns.

Bond-order alternation (BOA)

The bond-order alternation (BOA) index is the electronic counterpart of BLA as was FLU the electron-structure equivalent descriptor of HOMA. BOA utilizes the bond order or electron-sharing index as opposed to the bond length, and the equivalent expressions of 3.30 and 3.31 are:

$$BOA(\mathcal{A}) = \frac{1}{n_1} \sum_{i=1}^{n_1} \delta(A_{2i-1}, A_{2i}) - \frac{1}{n_2} \sum_{i=1}^{n_2} \delta(A_{2i}, A_{2i+1}) \quad (3.34)$$

$$BOA(\mathcal{A}) = \frac{1}{2n} \sum_{i=1}^n |\delta(A_i, A_{i+1}) - \delta(A_{i+1}, A_{i+2})| \quad (3.35)$$

Similarly to BLA (*cf.* equation 3.30 vs. 3.31), equation 3.34 is not suitable for molecules with an odd number of atoms, and we prefer to use equation 3.35.

Accordingly, BOA assumes values close to zero for aromatic molecules. Porphin's BOA equals 0.137 while isophlorin's value is much more significant, 0.374. BOA values of benzene, cyclohexane, and cyclohexatriene are 0.000, 0.000, and 0.822, respectively.

To qualitatively differentiate whether a molecule is aromatic or nonaromatic, BLA and BOA indices may not be a good alternative. Especially for highly aromatic molecules as bond length or bond orders of single and double bonds might compensate each other. For example, the values of benzene and cyclohexane, could be equal or somewhat similar to each other (*vide infra*). On the other hand, an advantage of BOA is that bond orders are much less dependent on the method and basis set used and hence on the level of theory applied.^{347,348} Nonetheless, the delocalization error present in some DFAs with low percentage of HF exchange must be taken into account¹⁸ (see Sections 1.1.1 and 2.2.1).

A multicenter based index: I_{ring}

As previously seen, Giambiagi *et al.* generalized the DI concept to various atomic centers³²² and later, in 2000, they proposed to use it as a measure of aromaticity under the well-known name of I_{ring} .^{329,349} I_{ring} is a multicenter index that quantifies the electron delocalization along the ring (the Kekulé structures contribution). For a single-determinant wavefunction applied to a ring structure, it is expressed as:

$$I_{ring}(\mathcal{A}) = \sum_{i_1 i_2 \dots i_n}^{occ} S_{i_1 i_2}(A_1) S_{i_2 i_3}(A_2) \dots S_{i_n, i_1}(A_n) \quad (3.36)$$

where $S_{ij}(A)$ is the overlap of molecular orbitals i and j in the atom A (see Eq. 3.17). I_{ring} gets large values for aromatic species while nonaromatic species exhibit values close to zero. For instance, I_{ring} has values of 0.048, 0.000, and 0.012 for benzene, cyclohexane, and cyclohexatriene, respectively. Benzene, as an aromatic molecule, presents the highest value and cyclohexane, a nonaromatic ring, the lowest one, while cyclohexatriene's value lies in the middle as expected from its antiaromaticity.

It is worth noting that I_{ring} is ring-size dependent together with the multicenter index (MCI) described hereafter.³³¹ As a consequence, to be able to compare values between species with a different number of atoms, Cioslowski *et al.* established the normalized versions of I_{ring} and MCI, called I_{NG} and I_{NB} , respectively.³³¹ For the sake of simplicity, in the studies of this thesis, we have used the normalized version that is just obtained from taking the $1/n$ power of equations 3.36 and 3.37 ($I_{ring}^{1/n}$ and $MCI^{1/n}$), n being the total number of atoms. If I_{ring} or MCI values are negative and n is odd, to compute the normalized version of the index, we will take the power of the absolute value and multiply it by minus one. $I_{ring}^{1/n}$ equals 0.603, 0.256, and 0.478 for benzene, cyclohexane, and cyclohexatriene, respectively. Normalizing I_{ring} higher values are obtained but the trend remains the same, *i.e.*, aromatic molecules present higher values of $I_{ring}^{1/n}$ like benzene. As seen with I_{ring} values, cyclohexane exhibits the lowest value due to its nonaromatic character, while cyclohexatriene displays an intermediate value.

The multicenter index (MCI)

Beyond the I_{ring} , the multicenter index of aromaticity was reported in 2005. Bultinck and coworkers, in addition to take into account I_{ring} 's information, proposed to sum the contributions of all the delocalization patterns across the ring and combine them. In other words, to consider the contribution of all the structures that arise from taking into account all possible permutations of the atomic positions in the ring. Considering the cross-ring delocalizations is very important for molecules that include metals in their structure (all-metal clusters) because they are the most important delocalizations

within these systems. Other authors already addressed a similar option.^{325,349} The MCI expression is as follows:³³¹

$$MCI(\mathcal{A}) = \frac{1}{2n} \sum_{\mathcal{P}(\mathcal{A})} I_{ring}(\mathcal{A}) = \frac{1}{2n} \sum_{\mathcal{P}(\mathcal{A})} \sum_{i_1, i_2, \dots, i_n}^{occ} S_{i_1 i_2}(A_1) S_{i_2 i_3}(A_2) \dots S_{i_n, i_1}(A_n) \quad (3.37)$$

where $\mathcal{P}(\mathcal{A})$ connotes the $n!$ permutations of the elements in the string \mathcal{A} .

MCI yields large numbers for aromatic species, and the authors state negative values correspond to antiaromatic species.³⁵⁰ However, the latter statement does not hold for rings of arbitrary size. MCI values for benzene, cyclohexane, and cyclohexatriene are 0.072, 0.000, and 0.013, respectively. Like I_{ring} , MCI is a ring-size-dependent index, and we can calculate a proper normalized version of MCI by raising to the inverse number of total atoms. In this case, $MCI^{1/n}$ gives 0.646, 0.260 and 0.484, respectively. For this particular case, if we want to compare the different MCI values, it is unnecessary to compute the normalized version as all the reference molecules have six members.

Despite I_{ring} and MCI indices are among the most popular and reliable electronic descriptors of aromaticity^{84,85,91,92,351} they present a serious limitation if we want to use them for large systems. Their computational cost and numerical error grow factorially with the number of atoms due to the numerical integration of AOMs. Their calculation becomes very complex if the ring presents more than twelve atoms.⁸⁶

AV1245 and AV_{min}

Trying to solve the main drawback of I_{ring} and MCI, in 2006, Matito designed a new electronic aromaticity index, especially for large circuits, AV1245.⁸⁶ As MCI is known to give accurate results, the original idea was to study a small fragment of a ring, mimicking the performance of MCI, and extend it to describe the aromaticity of the system. This electronic index is an arithmetic average of four-center MCI between relative positions 1–2 and 4–5,³⁵² constructed from each five-atom fragment along the perimeter of a ring (see Figure 3.2). AV1245 can be calculated for molecules with six or more atoms and preferably for an even number of atoms in the studied path. Experience shows that for an even-member circuit, there is an excellent correlation with MCI values but, with odd-member circuits, the correlation showed some outliers.

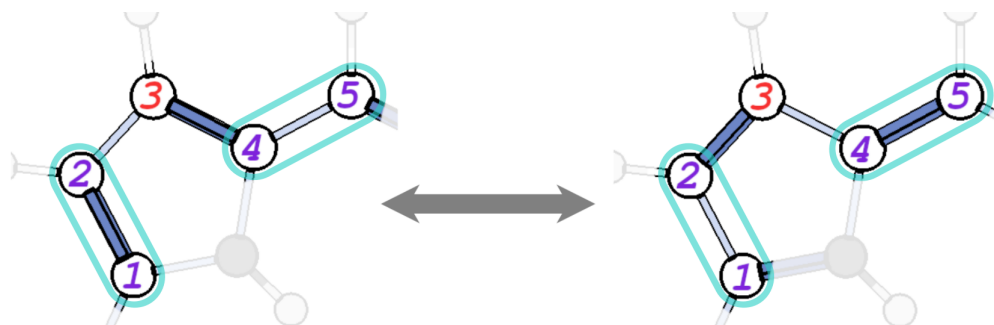


Figure 3.2: Schematic representation of bonds used in AV1245 index.

Large values of AV1245 will identify aromatic species. Contrarily, small values will point out nonaromatic and antiaromatic species. For example, for porphin, AV1245 is equal to 2.16, and for isophlorin, 1.12. If we also look at BOA values, they confirm that porphin is aromatic and isophlorin is antiaromatic since the latter has a more significant BOA value (0.137 vs 0.374). For the smaller rings, the values are 10.71, -0.01, and 2.99 for benzene, cyclohexane, and cyclohexatriene, respectively. Indeed, the examples given are in line with the aforementioned statement, aromatic molecules present the highest values, while nonaromatic and antiaromatic ones present lower values. In addition, it can be seen that the small classical organic molecules present higher values than the porphyrins presented. Index values of AV1245 are expected to decrease with the system size, regardless of the aromatic character. Moreover, in classic organic systems all values are equal because they are really symmetric structures. For this reason, the average reflects well the situation. On the contrary, porphyrins are large molecules and the symmetry is lost, that is why the values are not longer equal.

Concerning the previously described electronic descriptors, we can point out a few advantages of AV1245: (i) it does not rely on reference values, (ii) it does not suffer from large numerical precision errors, (iii) it does not present any limitation on the nature of the atoms, the molecular geometry or the level of calculation, and (iv) it has low computational cost as it grows linearly with the number of ring members. To the best of our knowledge, it is one of the first electronic-based indices available for large non-planar systems.

After some experience using AV1245, we have realized that the average value of the index could hinder some crucial values to describe the aromatic character of a system. Indices based on averages conceal the large and low values that some ring fragments may have. In aromaticity, low values of electronic delocalization are essential to characterize the system as aromatic, antiaromatic, or nonaromatic. If a molecule presents one fragment with really poor electronic delocalization, the molecule will be less aromatic than one with the same average value but larger delocalization of the least delocal-

ized fragment. Likewise, the FLU, BOA, HOMA, and BLA aromaticity indices can also present this limitation because they are based on average values. Consequently, we have started to use its minimal absolute value, AV_{min} .^{18,87} The minimum absolute value of AV1245 indicates the five-atom fragment of the ring with less electron delocalization or less conjugation, *i.e.*, where the electrons will have more difficulties going through. AV_{min} identifies the weakest link in the ring structure, which in most cases it is responsible for the loss of aromaticity in the ring. The larger AV_{min} , the more favorable the electron mobility in the circuit, *i.e.*, the molecules will be aromatic ($AV_{min} > 1$). Small values will indicate a nonaromatic character, while antiaromatic molecules usually exhibit intermediate AV_{min} values and are more challenging to identify.

Porphin and isophlorin AV_{min} values are 1.28 and 0.76, respectively. In the smaller examples, AV_{min} is equal to 10.71, 0.01, and 2.99 for benzene, cyclohexane, and cyclohexatriene, respectively. As we have seen in these examples, the aromaticity of porphyrins is considerably reduced compared to small annulenes. The larger the system, the smaller the AV_{min} in an aromatic molecule ($AV_{min} > 0.5$ in expanded porphyrins). Porphyrins and expanded porphyrins are not as aromatic as their aromatic annulene analogs.

It is not easy to distinguish antiaromatic and nonaromatic molecules with AV1245 or AV_{min} . To perform such differentiation in small molecules, BOA values can be used. On the other hand, for larger systems, where the aromatic character is smaller, we can also examine the behavior of the individual MCI(1,2,4,5) for each five-atoms fragment of the studied path that gives rise to the AV1245 index. We can plot the individual MCI(1,2,4,5) in a distribution along the studied path to more easily interpret the results.³⁵³ Using the four-atom MCI profiles along the perimeter (1245-index distribution profile) could help us differentiate the compounds that are in an intermediate situation between two different characters (*e.g.*, between aromatic and antiaromatic compounds). In Figure 3.3 the 1245-index distribution profile of porphin and isophlorin is represented.

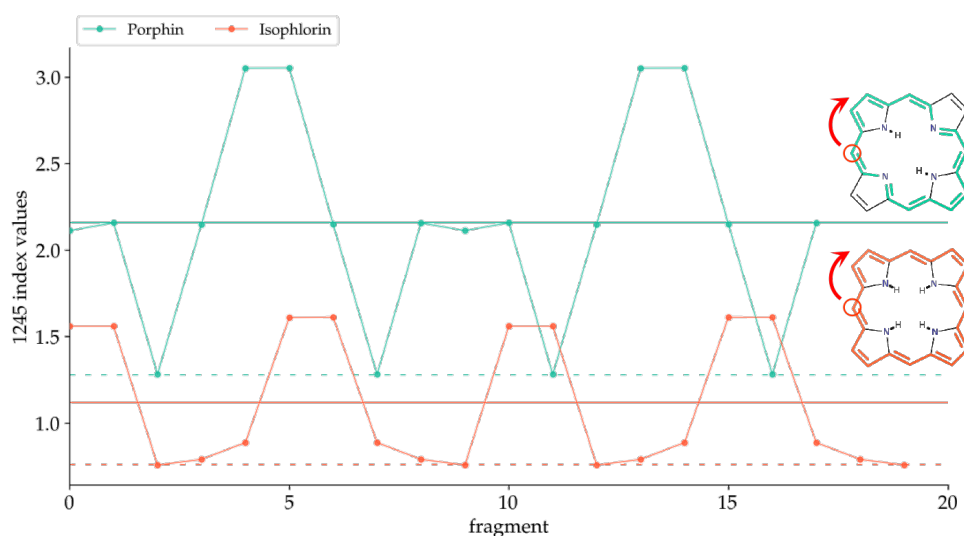


Figure 3.3: 1245-index distribution profile of porphyrin and isophlorin along the most aromatic path. This path corresponds to the annulene one for porphyrin and to the outer one for isophlorin. Horizontal solid line corresponds to the AV_{1245} value and dashed line to the AV_{min} value (see Table 3.1).

In porphyrin and isophlorin there is a clear difference in the value of AV_{min} , and the individual MCI(1,2,4,5) individual representations would not be needed. However, they serve as a simple example of this type of plot and, we can see that isophlorin always presents smaller values than porphyrin. Additionally, in some cases, the visualization of the most and least aromatic fragments of the ring with respect to the AV_{1245} value could also help to understand the aromatic character of the molecule (see Section 10.2.3).⁹⁰

Despite all our efforts in trying to make a clear distinction between aromatic, antiaromatic and nonaromatic character using AV_{min} , we have to accept that this electronic index is a delocalization measure. If the AV_{min} value is large, the molecule is aromatic. In contrast, if it is small, the molecule is nonaromatic. However, it is not straightforward to distinguish between aromatic and antiaromatic systems. This happens when we have to study large π -conjugated systems like expanded porphyrins or porphyrin nanorings, where the electronic delocalization is really small making in turn AV_{min} value small (see Chapter 7 and 8).

3.3.4 Magnetic indices

Applying an external magnetic field perpendicular to the molecular plane of an (anti)aromatic molecule will induce a π -electron ring current that can be measured and used to describe aromaticity. Several indices based on magnetic properties have been developed,⁸² such as the Gauge-including magnetically induced currents (GIMIC)^{354,355}, NICS,³⁵⁶ and ACID.^{357,358} The latter two are discussed in detail in the following sub-

sections. It is worth mentioning that magnetic descriptors are a response property of the molecule, not a ground-state property as structural, electronic, or energetic indices. This means that the ground-state wavefunction no longer serves for this type of descriptors. There is no straightforward physical basis for a direct relation between response properties and ground-state properties.³⁵⁹

Nucleus independent chemical shift (NICS)

Michael Buhl and Christoph van Wullen first employed the Nucleus-independent chemical shift in 1995 for studying the electronic currents in fullerenes.³⁵⁶ However, it was Paul Schleyer and coworkers who named this descriptor as NICS in 1996.³⁶⁰ The NICS is the negative value of the absolute shielding computed at the center of the ring or other relevant point of the system, also labeled $\text{NICS}(0)$ or $\text{NICS}(0)_{iso}$. The "0" denotes that NICS is calculated in the plane of the molecule, and "iso" means that isotropic magnetic shielding is considered.

Schleyer *et al.* predicted that aromatic molecules present negative values of NICS and antiaromatic molecules provide positive NICS values. The more negative the NICS values, the more aromatic the rings are. For instance, the $\text{NICS}(0)_{iso}$ values for porphin and isophlorin are -15.5 and 13.8, accordingly. For benzene, cyclohexane, and cyclohexatriene it takes values of -8.8, -2.1 and -4.1, respectively.

NICS presents some advantages compared with other aromaticity indices: (i) it is easy to compute (ii) it can be used to describe local and global aromaticity (iii) like many others, it does not use reference data. However, its computational cost is elevated. The NICS criticism led to the appearance of numerous NICS variants: $\text{NICS}(1)$, which is calculated at one Ångstrom above or below the ring plane, $\text{NICS}(0)_{zz}$ and $\text{NICS}(1)_{zz}$ calculated only taking into account the out-of-plane tensor component, and NICS scan or profile that is obtained by calculating NICS values in the direction perpendicular to the molecular plane or in the molecular plane.³⁶¹⁻³⁶⁴ Moreover, some authors prefer to calculate $\text{NICS}(0)$ not at the geometrical center but in the ring critical point,³⁶⁵ the lowest density point in the ring plane (especially significant for heterocyclic or metalloaromatic compounds) as sometimes the geometrical center is displaced.³⁶² Some other limitations that NICS can present are related to ring size dependence^{72,366} or relativistic effects inclusion dependencies in the presence of heavy elements,^{367,368} and it is highly dependent on the level of theory employed.³⁶⁹

The $\text{NICS}(1)$ values for porphin and isophlorin are -14.1 and 12.2, respectively. For benzene, cyclohexane, and cyclohexatriene takes values of -11.3, -1.9 and -4.6, respectively. Calculating $\text{NICS}(1)$ at 1 Å above the ring plane is intended to characterize the density of the p orbitals, therefore those that will form the π orbitals. With the examples shown, we can clearly see that the aromatic molecules (porphyrin and benzene) present

the largest negative values while antiaromatic molecules present positive values (isophlorine) or smaller negative values (cyclohexatriene). Cyclohexane, as a nonaromatic ring, presents a value close to zero. In addition, we can see that the ring size dependence of NICS^{92,362,363} is clearly reflected on benzene's and porphin's values (-11.3 and -14.1, respectively).

Anisotropy of the induced current density (ACID)

Herges and Geuenich developed a method based on the anisotropy of the current-induced density to study the delocalization in molecules in 2001.^{357,358} Analogous to the square of the wavefunction, which defines the total electron density, the ACID scalar field describes the density of delocalized electrons. In other words, ACID provides a straightforward manner to quantify the conjugated effects. The ACID method is a versatile and descriptive tool implemented in a software package developed in the group of Prof. R. Herges that provides visualization of the ACID scalar field isosurfaces and the current density vectors.

For the visualization of the ACID scalar field, isosurfaces are plotted similarly to the total electron density representations. Small ACID values indicate the absence of delocalized electrons, while larger values denote the presence of delocalized electrons. Current density vectors are plotted into the ACID isosurface to distinguish between anisotropies caused by diatropic or paratropic ring currents. The presence of clockwise current density vectors is indicative of diatropic currents related with aromatic systems. In contrast, counterclockwise currents will indicate paratropic ring currents associated with antiaromatic molecules. The length of the arrows indicates the absolute value of current density at the point of its origin.

In Figure 3.4, the ACID plot with the corresponding current density vectors of porphin and isophlorin is represented.

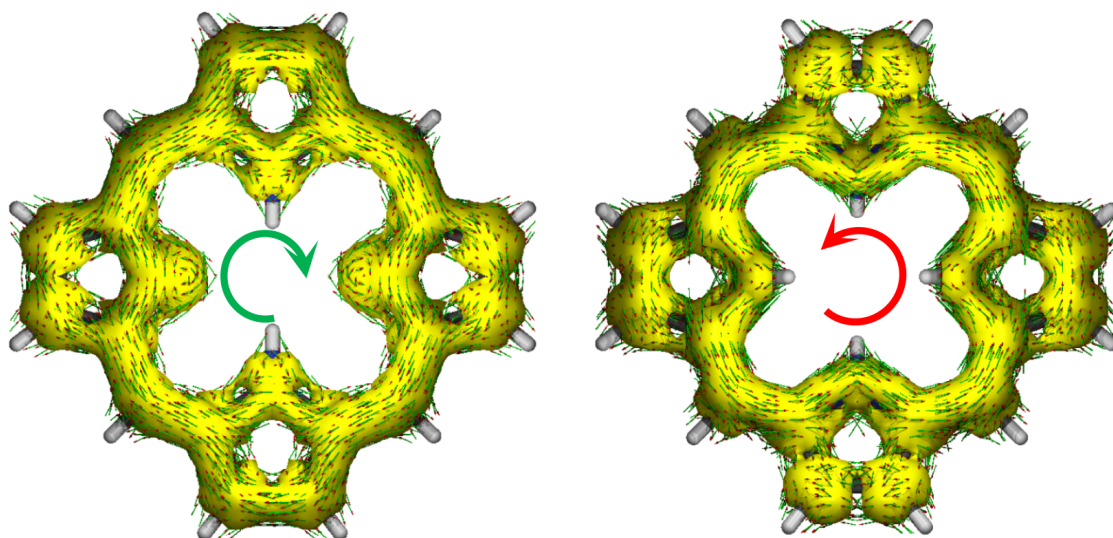


Figure 3.4: ACID isosurface plots (isocontour value 0.06) for (left) porphin and (right) isophlorin.

The porphin's ACID isosurface indicates that the delocalized system is mainly confined in the annulene path. Besides, it exhibits a strong diamagnetic ring current as it is an aromatic molecule. Oppositely, we have the example of isophlorin, an antiaromatic porphyrin. In its ACID isosurface we can see more disconnections than in porphin. The current density vectors show a paramagnetic ring current typical of an antiaromatic molecule. According to ACID, the most aromatic path is the inner path (the one that goes through all nitrogen atoms). However, following the annulene model the most aromatic path would have to be the outer one (the one that passes for the C–C bonds in the imine ring). This path is only recognized as the most aromatic one by AV_{1245} and AV_{min} . BOA and BLA indices, like ACID, recognizes the inner path as the most aromatic one, while FLU and HOMA identify another path. In Section 10.2.2 we will further discuss the case of porphyn.

Chapter 4

Objectives

There are **two main goals** in the present thesis; the **first one** is the study of the aromatic character of large conjugated systems, and the **second one** is the discussion of the computational method used in the electronic characterization, specifically for large conjugated molecules and systems with charge-transfer excitations.

This thesis is divided into two different blocks. The first block is related to aromaticity studies in an annulene series and large conjugated systems, while the second one is based on the study of medium to large photosensitizers to design a complete protocol to obtain the structures, UV-Vis spectra, and redox potentials. Within the blocks, **several specific objectives** have been defined to achieve the general goals.

We want to focus on analyzing the large (anti)aromatic systems employing electron delocalization measures. There are many aromaticity indices already available in the literature to study the aromatic character of a molecule. However, the most reliable electronic indices are computationally inaccessible for large molecular rings. To overcome this limitation, in our research group, two new electronic aromatic indices were proposed, AV_{1245} and AV_{min} . Consequently, the **first specific objective** is to test AV_{1245} and AV_{min} in large conjugated systems. By comparing them with some other electronic and geometric indices, the **second specific objective** is to find the best index to figure out the most aromatic pathway in large non-planar systems. We will first study simple expanded porphyrins in Chapter 5 and a set of annulenes in Chapter 6 to calibrate AV_{1245} and AV_{min} indices, to then use this knowledge in the study of a controversial porphyrin nanoring (Chapter 8).

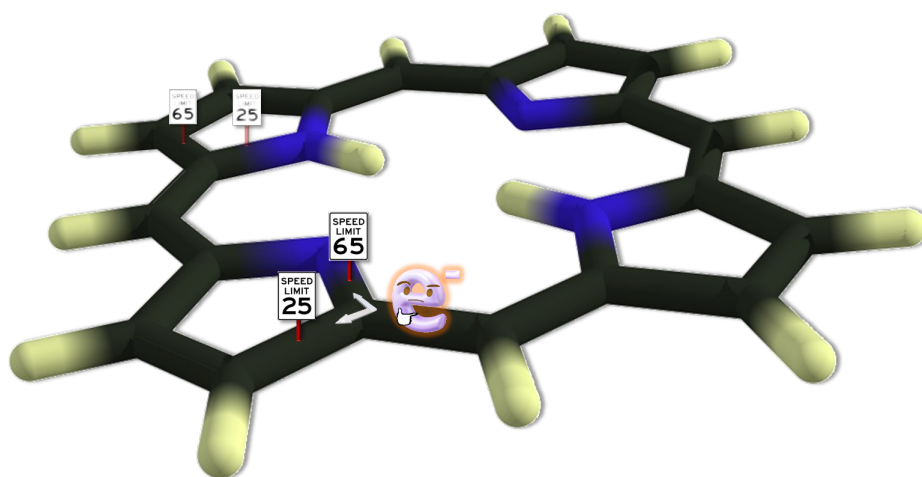
To the best of our knowledge, there have been a limited number of studies based on quantifying how the aromaticity rules fade away with the ring size. Hence, the **third specific objective** is to perform a deep analysis of two well-known aromaticity rules, Hückel's and Baird's. Beginning with an investigation of how these rules are expected to change with the ring size as predicted by the Hückel molecular orbital model, we then evaluate the trend using different density functionals approximations.

The **fourth specific objective** of this manuscript arises from the need to describe the electronic structure of the systems correctly. As mentioned in the previous sections, the delocalization error is a well-known failure of some density functionals approximations. For this reason, it is essential to choose an acceptable computational method to correctly describe the minimal structure of large conjugated systems and medium to large complexes with CT excitations.

It has been shown that charge-transfer excitations are misdescribed using DFAs with a low percentage of HF exchange, and range-separated functionals were proposed to overcome this limitation. In the spirit of the previous objective, we will tune the attenuating parameter of a long-range corrected functional using a method available in the literature to reproduce the UV-Vis absorption experimental spectra more accurately. The **fifth specific objective** is to apply the same optimally tuned long-range corrected functional to the redox potential calculation and analyze if it also improves this quantity. All this may help in the future to propose new complexes with improved properties for applications in DSSCs, LEDs, and in the water-splitting process.

Chapter 5

New electron delocalization tools to describe the aromaticity in porphyrinoids





New electron delocalization tools to describe the aromaticity in porphyrinoids†

Cite this: *Phys. Chem. Chem. Phys.*, 2018, 20, 2787

Irene Casademont-Reig,^{‡a} Tatiana Woller,^{‡b} Julia Contreras-García,^{‡c} Mercedes Alonso,^{‡*b} Miquel Torrent-Sucarrat^{‡*ad} and Eduard Matito^{‡*ad}

The role of aromaticity in porphyrinoids is a current subject of debate due to the intricate structure of these macrocycles, which can adopt Hückel, Möbius and even figure-eight conformers. One of the main challenges in these large π -conjugated structures is identifying the most conjugated pathway because, among aromaticity descriptors, there are very few that can be applied coherently to this variety of conformers. In this paper, we have investigated the conjugated pathways in nine porphyrinoid compounds using several aromaticity descriptors, including BLA, BOA, FLU and HOMA, as well as the recently introduced AV1245 and AV_{\min} indices. All the indices agree on the general features of these compounds, such as the fulfillment of Hückel's rule or which compounds should be more or less aromatic from the series. However, our results evince the difficulty of finding the most aromatic pathway in the macrocycle for large porphyrinoids. In fact, only AV_{\min} is capable of recognizing the annulene pathway as the most aromatic one in the nine studied structures. Finally, we study the effect of the exchange in DFT functionals on the description of the aromaticity of the porphyrinoids. The amount of exact exchange quantitatively changes the picture for most aromaticity descriptors, AV_{\min} being the only exception that shows the same qualitative results in all cases.

Received 9th November 2017,
Accepted 19th December 2017

DOI: 10.1039/c7cp07581b

rsc.li/pccp

1 Introduction

Aromaticity is a ubiquitous concept in chemistry that covers a large number of properties including energy stabilization, bond-length equalization, exalted magnetic properties and electron conjugation and delocalization.^{1–6} As many other chemical concepts (chemical bonding, electronegativity, bond order, hardness, electron population, *etc.*), aromaticity is not a quantum observable and it lacks a physical rigorous definition. This fact results in a plethora of aromaticity indices (energetic, structural, magnetic and electronic) reported in the literature,^{2–4,6,7} which have been successfully applied to explain countless chemical phenomena. For this reason, it is recommended to study the multidimensional phenomenon of aromaticity with a set of descriptors based on different criteria.^{6,8–12}

However, the multidimensional character of aromaticity should not prevent critical analysis of aromaticity descriptors

from being undertaken.^{10,13–15} Recently, Feixas *et al.*^{10,15} have designed a series of tests to evaluate the performance of aromaticity indices in organic and inorganic molecules, but the study of macrocycles was not among the tests suggested. In this regard, porphyrinoids can be considered one of the most stringent test beds for the aromaticity descriptors along three main different lines: (a) identifying the most aromatic pathway; (b) describing aromaticity in non-planar compounds; (c) computational method dependency. In the following paragraphs, these three factors are addressed in detail.

Porphyrinoids contain several heterocycles and many multiple π -conjugation pathways can be defined. Then, one of the main issues to describe the aromaticity in porphyrinoids concerns the selection of the macrocyclic conjugation pathway (or pathways) to study. To this aim, porphyrinoids were traditionally interpreted as annulenes, *e.g.* porphine was considered as a tetraaza[18]annulene system.^{16,17} This approximation is called the annulene model; *i.e.* the pathway is selected avoiding NH in pyrrole and the outer CH=CH groups of imine rings (see some examples of annulene pathways in Fig. 1, illustrated in bold). Conversely, several authors^{18–27} have concluded that all the π electrons of the macrocycles are necessary for a correct description of aromaticity in porphyrinoids and that the individual pyrrolic subunits (and not the imine rings) determine the global aromatic character of the macrocycle. For instance, in the case of porphine, it has been reported that it is necessary to consider all the 22 π electrons, and

^a Kimika Fakultatea, Euskal Herriko Unibertsitatea (UPV/EHU), and Donostia International Physics Center (DIPC), P.K. 1072, 20080 Donostia, Euskadi, Spain. E-mail: miqueltorrentsucarrat@gmail.com, ematito@gmail.com

^b Eenheid Algemene Chemie (ALGC), Vrije Universiteit Brussel (VUB), Pleinlaan 2, 1050 Brussels, Belgium. E-mail: Mercedes.alonso.giner@vub.be

^c Sorbonne Universités, UPMC Univ. Paris, UMR 7616 Laboratoire de Chimie Théorique, CNRS, UMR 7616, LCT 75005, Paris, France

^d Ikerbasque, Basque Foundation for Science, María Díaz de Haro 3, 6, 48013 Bilbao, Euskadi, Spain

† Electronic supplementary information (ESI) available. See DOI: 10.1039/c7cp07581b

‡ These authors contributed equally to this work.

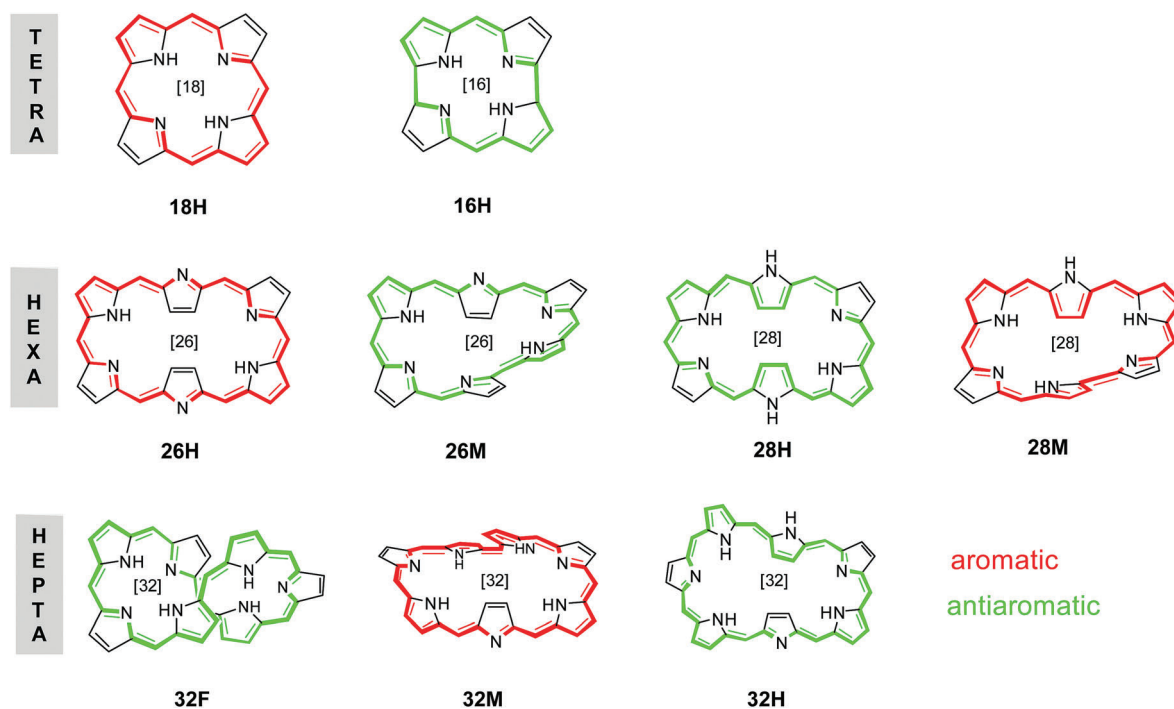


Fig. 1 Hückel (H), Möbius (M) and figure-eight (F) conformations of selected porphyrinoids and their expected aromatic character according to the annulene model. The annulene-type conjugation pathway is depicted with bold colored bonds (red stands for aromatic and green for antiaromatic).

not only the 18 π electrons of the annulene pathway, for a correct description of its aromaticity.²⁸ From these discrepancies, it is possible to conclude that it is essential to search for new aromaticity descriptors that are able to select in an accurate way (ideally also unambiguous) the most aromatic pathway from a π -electron macrocyclic structure.

It is important to keep in mind that most of the aromaticity indices, such as the harmonic oscillator model of aromaticity (HOMA) and the nuclear-independent chemical shifts (NICS), have been conceived to describe the aromaticity of planar structures. Thus, an additional problem appears when the porphyrinoid structure shows a nonplanar geometry.^{29,30} Within this context, it is necessary to put a special emphasis on expanded porphyrins. These systems present a conformational flexibility that allows them to achieve different π -conjugation topologies (namely, Möbius, Hückel and twisted-Hückel) with distinct aromaticities, as well as different electric, magnetic and conductance properties.^{31–35} For instance, the switch between different topologies (*e.g.* the Hückel planar, single twisted Möbius, figure eight, and triply twisted Möbius) can be achieved by changing the external conditions, such as the temperature, the solvent, the redox potential or through metalation and photoexcitation.^{36–41}

According to the Hückel rule, a planar (or with an even number of half-twists) singlet π -conjugated system with $(4N + 2)\pi$ electrons is aromatic, whereas it is antiaromatic with $4N$ π electrons. On the other hand, Heilbronner⁴² predicts that the Hückel rule is reversed for a planar π -conjugated system with an odd number of half-twists; *i.e.* a singlet Möbius system with $4N + 2$ ($4N$) π electrons is antiaromatic (aromatic). This diversity of aromatic patterns with different topologies can be increased

by a factor of two if one considers triplet states because, according to Baird's rule,^{43,44} the aromaticity/antiaromaticity electron counting rule of the singlet ground state is reversed for the lowest $\pi\pi^*$ triplet state. Expanded porphyrins (and to a minor degree annulenes) present all these features.^{45–54} In this sense, it is not unexpected that expanded porphyrins are among the most challenging test beds for aromaticity descriptors. It should be pointed out that several works^{20,55–62} have recently analyzed the aromaticity of expanded porphyrins with different topologies and the number of π electrons using various aromaticity indices based on the energetic, magnetic, structural, and reactivity criteria.

The last problem to describe the aromaticity of porphyrinoids is the critical role of the selected density functional approximations (DFAs) to evaluate geometric, energetic and magnetic properties.^{63–66} For instance, it has been reported for expanded porphyrins that some DFAs overemphasize the delocalization of conjugated systems, which results in more stable and bond-equalized structures.⁶⁶ In this regard, it is worth noting that this phenomenon has also been observed in annulenes.^{67–70} The effect of the method in aromaticity descriptors remains thus far unexplored and will be addressed in this work.

Many of the current aromaticity indices cannot be easily applied in macrocycles, motivating the definition of new aromaticity descriptors.^{71,72} One of us⁷¹ has recently proposed the AV1245 index, which consists on the average of the 4-center multicenter index (MCI) values along the ring that keeps a positional relationship of 1, 2, 4, 5. It measures the extent of transferability of the delocalized electrons between bonds 1–2 and 4–5, which is expected to be large in aromatic molecules. The main

advantages of AV1245 are that it does not rely on reference values, it does not suffer from large numerical precision errors and it does not present any limitation on the nature of atoms, the molecular geometry or the level of calculation.

Herein, we report a theoretical investigation on the aromaticity of nine porphyrinoid compounds (see Fig. 1) using three DFAs (B3LYP, M06-2X and CAM-B3LYP) and six aromaticity descriptors (AV1245, AV_{\min} , BLA, BOA, FLU and HOMA). In order to test the new electron delocalization tools (AV1245 and AV_{\min}), and to provide deeper insights into the evaluation of porphyrinoids' aromaticity and their three major challenges (*vide supra*), three different studies have been performed. Firstly, all the possible pathways in porphine have been evaluated using the six aromaticity descriptors and the most aromatic pathway has been identified. Secondly, the values of the aromatic indices for the annulene pathway of all the studied molecules are analyzed. Finally, the influence of the exchange–correlation functional on different aromaticity index values has been discussed.

2 Methodology

In this section, we will review several aromaticity measures that can be applied to find the most conjugated pathway in porphyrins. Many other popular measures of aromaticity such as the NICS,⁷³ the aromatic stabilization energies,⁷ the magnetic susceptibility exaltation⁷⁴ or the relative hardness⁶⁵ provide global measures of aromaticity and cannot be employed to find the most aromatic pathway in a macrocycle.

Hereafter, we will indicate the coordinates of the electron using the short-hand notation $\mathbf{1} \equiv (\vec{r}_1, \sigma_1)$ and $d\mathbf{1} \equiv d\vec{r}_1 d\sigma_1$ for the electron positions and their derivatives and we will assume a single-determinant wavefunction (for a more general approach we suggest ref. 75). Let us consider a ring structure consisting of n atoms, represented by the string $\mathcal{A} = \{\mathcal{A}_1, \mathcal{A}_2, \dots, \mathcal{A}_n\}$, whose elements are ordered according to the connectivity of the atoms in the ring. In order to illustrate the performance of electron delocalization indices, we select three archetype molecules: benzene, cyclohexane and three geometries of cyclohexatriene with variable bond-length alternation.

First of all, we will review the concepts of an *atom in a molecule* (AIM), electron delocalization and bond orders, which

are employed in the definition of the electronic indices of aromaticity. In order to estimate the aromaticity of molecules, we need to define an AIM, so as to measure the electron delocalization among the atoms in the ring. In this work, we will define the AIM using the quantum theory of atoms in molecules (QTAIM)⁷⁶ that defines the boundaries of an atom using the topology of the electron density. The QTAIM is among the most reliable definitions of an AIM, providing good estimates of bond orders in difficult cases^{77–83} and trustworthy results for aromaticity indices.⁸⁴ As a measure of electron delocalization, we will employ Bader's definition⁸⁵ that estimates the electron delocalization as the variance of the atomic population, $\delta(A)$. From this definition, one can provide a measure of the bond order based on the covariance of the populations of atoms A and B ,^{78,86} commonly known as the delocalization index (DI),



$$\delta(A, B) = 2 \int_A \int_B d\mathbf{1} d\mathbf{2} \rho_{xc}(\mathbf{1}, \mathbf{2}) = -2 \text{cov}(N_A, N_B), \quad (1)$$

where $\rho_{xc}(\mathbf{1}, \mathbf{2})$ is the exchange–correlation density and N_A is the atomic population of atom A . $\delta(A)$ is the variance of the atomic population and it is given by $\delta(A) = N_A - \delta(A, A)/2$. For single-determinant wave functions (Hartree–Fock or Kohn–Sham DFT), the calculation of N_A and $\delta(A, B)$ only requires the atomic-overlap matrices (AOMs),

$$S_{ij}(A) = \int_{A_1} d\mathbf{1} \phi_i^*(\mathbf{1}) \phi_j(\mathbf{1}), \quad (2)$$

where $\phi_i(\mathbf{1})$ is the orbital i of the set of orbitals in terms of which we expand the density and the exchange–correlation density. Some authors have found a link between the DI and the interaction energy of two atoms.^{87–89} In Table 1, the DI values of several molecules are collected. Cyclohexane shows the typical value of $\delta(C, C)$ of a non-aromatic molecule which equals 1, as the bond involves only sigma orbitals. The structures of cyclohexatriene show some $\delta(C, C)$ close to one, and others close to two, indicating an alternation of single and double bonds, typical of antiaromatic molecules, whereas benzene gives $\delta(C, C) = 1.4$, which is halfway between single and double bonds and it is the typical signature of the conjugated bonds present in aromatic molecules.

Table 1 DI values and aromaticity indices of benzene, cyclohexane and three structures of cyclohexatriene calculated at the B3LYP/6-311G(d,p) level of theory

		$\delta(C_1, C_2)$	$\delta(C_2, C_3)$	FLU	BOA	HOMA	BLA	MCI	AV1245	AV_{\min}
Benzene		1.39	1.39	0.000	0.000	0.991	0.000	0.073	10.72	10.72
Cyclohexane		0.98	0.98	0.092	0.000	−4.637	0.000	0.000	−0.01	0.01
Cyclohexatriene	$a/b = 0.9$	1.12	1.59	0.029	0.472	−18.024	0.204	0.050	8.16	8.16
	$a/b = 0.8$	0.97	1.76	0.082	0.797	−31.266	0.408	0.017	3.70	3.70
	$a/b = 0.7$	0.86	1.89	0.138	1.037	−50.540	0.622	0.009	2.18	2.18

One of the most popular indicators of aromaticity is the bond-length alternation (BLA), which compares the average of bond lengths of consecutive bonds in a ring,

$$\text{BLA}(\mathcal{A}) = \frac{1}{n_1} \sum_{i=1}^{n_1} r_{A_{2i-1}, A_{2i}} - \frac{1}{n_2} \sum_{i=1}^{n_2} r_{A_{2i}, A_{2i+1}}, \quad (3)$$

where $n_1 = \lfloor (n+1)/2 \rfloor$, $n_2 = \lfloor n/2 \rfloor$; the symbol $\lfloor x \rfloor$ stands for the floor function of x , which returns the largest integer less than or equal to x . The BLA directly measures the bond-length equalization expected in aromatic circuits and it does not rely on reference values. In Table 1, we see that benzene and cyclohexane do not exhibit bond-length alternation, whereas the value of BLA for cyclohexatriene increases with bond-length alternation. However, the BLA is built upon the premise that the bond-length alternation (*i.e.* a geometrical feature) reflects the distribution of electron pairs on the conjugated circuit. For this reason, some people prefer an electronic-structure formulation equivalent of the BLA, the bond-order alternation (BOA), which uses the bond order (or electron-sharing index⁷⁸) instead of the bond length,

$$\text{BOA}(\mathcal{A}) = \frac{1}{n_1} \sum_{i=1}^{n_1} \delta(A_{2i-1}, A_{2i}) - \frac{1}{n_2} \sum_{i=1}^{n_2} \delta(A_{2i}, A_{2i+1}), \quad (4)$$

where $\delta(A, B)$ is a given measure of the bond order between atoms A and B . Unlike the atomic charges,⁹⁰ the bond orders are much less dependent on the method and the basis set used⁹¹ and, therefore, aromaticity indices based on bond orders⁹² are not highly dependent on the level of theory employed. The values of the BOA are collected in Table 1 and show the same trend as the BLA values of these systems.

An alternative geometry-based index is the widely used harmonic oscillator model of aromaticity (HOMA) proposed by Kruszewski and Krygowski.⁹³ The HOMA uses some reference bond lengths, R_{opt} , for which the compression energy of the double bond and expansion energy of the single bond are minimal according to the harmonic potential model. The expression of the HOMA is based on the differences between the reference and the actual bond lengths within the ring structure,

$$\text{HOMA}(\mathcal{A}) = 1 - \frac{1}{n} \sum_i \alpha_i (R_{\text{opt}} - R_{A_i, A_{i+1}})^2, \quad (5)$$

where α_i is an empirical constant fixed to give values close to one for aromatic species, and small or large negative values for non-aromatic and antiaromatic molecules (see Table 1). For C–C bonds, $\alpha_i = 257.7$ and $R_{\text{opt}} = 1.388 \text{ \AA}$, whereas $\alpha_i = 93.52$ and $R_{\text{opt}} = 1.334 \text{ \AA}$ for C–N bonds.⁹⁴

Just as BOA is the quantum-chemical equivalent of BLA, the aromatic fluctuation index (FLU) is constructed to perform an aromaticity analysis that goes beyond the bond-length information.^{95,96} The FLU expression only employs the electron delocalization of the atoms in the ring,

$$\text{FLU}(\mathcal{A}) = \frac{1}{n} \sum_{i=1}^n \left[\left(\frac{\delta(A_i)}{\delta(A_{i-1})} \right)^\alpha \left(\frac{\delta(A_i, A_{i-1}) - \delta_{\text{ref}}(A_i, A_{i-1})}{\delta_{\text{ref}}(A_i, A_{i-1})} \right) \right]^2, \quad (6)$$

where $\delta_{\text{ref}}(A_i, A_j)$ are taken from some reference aromatic molecules where the bonding pattern A_i-A_j occurs in the aromatic ring (for instance, the C–C delocalization is taken from benzene and the C–N delocalization is taken from pyridine), and

$$\alpha = \begin{cases} 1 & \delta(A_{i-1}) \leq \delta(A_i) \\ -1 & \delta(A_i) < \delta(A_{i-1}) \end{cases}. \quad (7)$$

The FLU is close to zero in aromatic molecules and takes large values in non-aromatic and antiaromatic molecules (see Table 1). It is worth mentioning that the FLU has been already used to account for the aromaticity in porphyrins.⁹⁷ Unfortunately, the aromaticity indices based on references do not actually measure aromaticity but the similarity with respect to some aromatic molecules (or patterns found in aromatic molecules). In this sense, the HOMA and FLU are not adequate to describe reactivity because they will always predict a loss of aromaticity when the bond distance or the delocalization, respectively, change with respect to the reference value.¹⁴ For instance, in the case of the Diels–Alder reaction they cannot recognize the transition state (TS) as the most aromatic point along the reaction path because the product, cyclohexene, is more similar to benzene (the reference molecule for C–C bonds) than the TS, which shows large C–C distances and small DIs in the bonds that will be formed.¹³ In addition, several studies pointed out that the HOMA index needs to be applied with caution in expanded porphyrins because the HOMA differences between aromatic and antiaromatic conformations are very small and the HOMA index behaves qualitatively different for aromatic and antiaromatic species.^{62,98}

The most reliable indices of aromaticity are actually based on multicenter electron delocalization measures.^{10,15} The first such measure is due to Giambiagi and it quantifies the electron delocalization along the ring,⁹⁹

$$I_{\text{ring}}(\mathcal{A}) = \sum_{i_1, i_2, \dots, i_n}^{\text{occ}} S_{i_1 i_2}(A_1) S_{i_2 i_3}(A_2) \dots S_{i_n i_1}(A_n). \quad (8)$$

This measure was extended to include all the delocalization patterns across the ring (*i.e.* it uses not only the Kekulé structure but all the possible arrangements of the atoms in the string \mathcal{A}),¹⁰⁰

$$\text{MCI}(\mathcal{A}) = \sum_{\mathcal{P}(\mathcal{A})} I_{\text{ring}}(\mathcal{A}) = \sum_{\mathcal{P}(\mathcal{A})} \sum_{i_1, i_2, \dots, i_n}^{\text{occ}} S_{i_1 i_2}(A_1) S_{i_2 i_3}(A_2) \dots S_{i_n i_1}(A_n), \quad (9)$$

where $\mathcal{P}(\mathcal{A})$ stands for the $n!$ permutations of the elements in the string \mathcal{A} . Both I_{ring} and MCI produce large values for aromatic molecules, small values for non-aromatic molecules and negative values for some antiaromatic molecules (see Table 1).¹⁰¹ These indices are ring-size dependent but proper normalization has been recently suggested.¹⁰² Unfortunately, the cost and the numerical error associated with these quantities grow with the ring size and their calculation for rings of more than twelve atoms poses a serious computational challenge.⁷¹

Recently, we have made some efforts in overcoming these drawbacks, resulting in the definition of a new electronic

aromaticity index for large circuits, the AV1245 index.⁷¹ Based on the study of long-range delocalization patterns in aromatic molecules,^{103,104} the AV1245 index measures the average delocalization in bonds 1–2 and 4–5 along a ring of more than six members. To this aim, we average out the four-center MCI values (including atoms in positions 1, 2, 4 and 5) of each consecutive five-atom fragment in the circuit. In the framework of intermolecular conjugation, we have found that AV_{\min} (the minimal absolute value of the aforementioned four-center MCI values along the ring) can be used to characterize the highly dispersive bands in conjugated polymers.¹⁰⁵ Both AV_{\min} and AV1245 show large numbers for aromatic molecules ($AV_{1245} \approx 11$ for benzene) and small numbers for antiaromatic and non-aromatic molecules. In this sense, the combined information of BOA and AV_{1245}/AV_{\min} helps distinguishing the latter situations.

Finally, we should also mention that the electron density of delocalized bonds has been recently used as an additional electronic criterion to account for aromaticity in large circuits.⁷²

3 Computational methods

The geometries of the selected porphyrinoids (see the structures in Fig. 1) have been fully optimized and characterized using harmonic vibrational frequency calculations with B3LYP,^{106,107} M06-2X¹⁰⁸ and CAM-B3LYP¹⁰⁹ functionals in combination with the 6-311G(d,p) basis set.^{110,111} The initial structures of the Hückel, Möbius and figure-eight topologies of [26]- and [28]-hexaphyrins and [32]-heptaphyrin¹¹² have been obtained from our previous works (notice that the meso substituents in Fig. 1 are hydrogen atoms).^{58,63,64,66} The geometry optimizations and frequencies, calculated within the DFT framework, were performed with the Gaussian 09 software package.¹¹³ The calculation of the electronic aromaticity indices (AV_{1245} , AV_{\min} , BOA and FLU) uses a QTAIM atomic partition performed by the AIMAll software.¹¹⁴ The AOM resulting from this partition (see eqn (2)) and the molecular geometries are input in the in-house ESI-3D code,^{78,92,115} which provides AV_{1245} , AV_{\min} , BLA, BOA, DIs, FLU, HOMA and MCI values. The ESI-3D code is available upon request (ematito@gmail.com).

4 Results and discussion

We have performed calculations on nine porphyrinoid systems, collected in Fig. 1. First of all, we will analyze the simplest system, the porphine molecule (**18H** in Fig. 1), to illustrate the performance of the different measures of aromaticity studied in this work. We will choose CAM-B3LYP optimized structures to analyze the aromaticity of all porphyrinoid structures considered, however, in the last part of this section, we will also comment on the influence of the exchange–correlation functional on the values of the aromaticity descriptors. All the results obtained with B3LYP and M06-2X can be found in the ESI† (see Tables S1 and S2).

In Table 2, the results for all the possible pathways in **18H** are collected. **18H** is composed of imine and pyrrole rings. The pathways differ on the route they follow upon passing through

five-membered rings (5-MRs): they can pass through the C–N–C bonds (inner path, hereafter) or through the C–C bonds (outer path). We label the pathways using as many letters as 5-MRs the porphyrinoid structure has. These letters are ‘i’ for inner paths and ‘o’ for outer paths. We take the top left 5-MR of the structures in Fig. 1 and follow the clockwise direction to define the order of the 5-MRs in the molecule. According to this convention, the classical or annulene path in the **18H** system is labeled as ‘oioi’ (see the red pathway in Fig. 1). See Fig. S1 (ESI†) for all possible pathways in **18H**. The first entry in Table 2 displays the results for the annulene pathway in **18H**, showing that all aromaticity indices recognize this circuit as highly aromatic. However, by comparison with other pathways, we observe that only some indices (AV_{1245} , AV_{\min} , BLA and BOA) recognize the annulene pathway as the most aromatic one. In addition, we notice that BLA and BOA recognize the opposite path to the annulene model (*i.e.* ‘ioio’) as aromatic as the annulene pathway itself, which is somehow contradictory. On the other hand, AV_{1245} and AV_{\min} identify the ‘ioio’ as the least aromatic pathway in **18H**. We have also computed the delocalization indices (DIs) for all the bonds in **18H** (see Fig. S2, ESI†) and the DIs with largest values follow the annulene pathway.

In order to identify the second most conjugated pathway, we should take the one predicted by the annulene model and choose a different route in one of the 5-MRs. The most reasonable choice consists of changing the route in the most aromatic 5-MR in the macrocycle, where the change of route is expected to be less important. Taking into account that our current MCI calculations predict that the imine rings within **18H** (MCI = 0.024) are somewhat more aromatic than the pyrrole rings (MCI = 0.022), we assume that the second most aromatic pathway corresponds to ‘oooi’ (see Table S3 of the ESI†). Both AV_{\min} and AV_{1245} predict this one as the second most aromatic pathway. If we follow this rule for choosing an alternative route on the next most aromatic 5-MR, we order the pathways as they are presented in Table 2. AV_{1245} and AV_{\min} follow the same order, suggesting that the local aromaticity of the 5-MRs calculated from MCI values is consistent with the description provided by these indices, which are based on four-center MCI calculations along the macrocyclic ring.

We observe that AV_{\min} provides the same value for some pathways because they share a given five-center fragment for

Table 2 Aromaticity indices for different pathways in **18H**, calculated at the CAM-B3LYP/6-311G(d,p) level of theory

Pathway ^a	FLU	BOA	HOMA	BLA	AV_{1245}	AV_{\min}
oioi	0.010	0.000	0.872	0.000	2.16	1.28
oooi (2)	0.016	0.309	0.734	0.288	1.91	0.49
oooo	0.022	0.041	0.610	0.011	1.70	0.49
iooi (2)	0.008	0.367	0.917	0.313	1.57	0.13
ooii (4)	0.015	0.023	0.769	0.006	1.36	0.13
ooio (2)	0.021	0.372	0.637	0.270	1.17	0.13
iiii	0.006	0.000	0.968	0.000	0.91	0.13
iiio (2)	0.013	0.388	0.808	0.307	0.73	0.13
ioio	0.019	0.000	0.666	0.000	0.57	0.13

^a The number in brackets indicates the number of equivalent pathways.

which the four-center MCI absolute value turns out to be minimal. In such cases, since the AV_{\min} value is identical, we assume that the pathways are rather similar and if a distinction between them needs to be done, we suggest using AV1245 as a way to differentiate them.

However, the order of pathways we have just described for **18H** is not completely followed by either the topological or magnetic indices of aromaticity.^{19–23,25,116} While these indices agree on the annulene pathway being, by far, the most conjugated one, their values for the second and third most aromatic pathways correspond to 'iioi' and 'oioo', respectively.¹⁹ The latter puts forward that these indices prefer to choose alternative routes for the pyrrole rings rather than for imine ones, as it was the case of AV1245 and AV_{\min} . Interestingly, this fact is also in agreement with the aromaticity of 5-MRs predicted by the topological and magnetic indices, which predict the pyrrole ring within **18H** as more aromatic than the imine ring. This rather simple example illustrates the difficulty of ordering the pathways in a porphyrinoid system according to their aromaticity. While most indices agree on the most aromatic pathway, the next most aromatic ones are quite difficult to classify and it seems that the aromaticity of the 5-MRs determines the aromaticity of the pathways. After all, aromaticity is a multi-dimensional phenomenon of which we are only measuring indirect consequences. We are not necessarily measuring the very same thing when we are comparing geometrical, electronic and magnetic indices of aromaticity and, therefore, some discrepancies can be expected.¹²

In the following, we will be only concerned with the annulene pathway of the structures. Table 3 collects the values of the aromaticity indices for the annulene pathway of all selected porphyrinoids (Fig. 1). The indices that do not recognize the annulene pathway as the most aromatic one also include in parentheses the values of the pathway they find as most aromatic for comparison. First of all, we check whether the values of the indices reflect the global aromatic character expected in these systems. According to all the indices hereby studied, **18H** is the system with the most aromatic pathway and for **16H** the annulene pathway is predicted as having low aromaticity (as expected for a nonplanar antiaromatic system). In addition, all indices also agree on the finding that the annulene pathway in Hückel aromatic systems is more aromatic than the annulene pathway in the corresponding Möbius antiaromatic systems

(*i.e.* **26H** vs. **26M**) and *vice versa*: attributing a more aromatic character to the annulene pathway in Möbius aromatic systems than in the corresponding Hückel antiaromatic system (*i.e.* **28M** vs. **28H**, and **32M** vs. **32H**). Interestingly, the figure-eight structure of **32F** is predicted as an intermediate situation between **32H** and **32M**. Hence, in general, all the indices provide a reasonable description of the (anti)aromaticity among the different conformers. However, when comparing the most aromatic pathway in the macrocycle many differences arise (*vide infra*).

The annulene model works fairly well in identifying the most aromatic pathway in simple free-base porphyrinoid systems, which are not protonated or deprotonated.²¹ In addition, for these systems, the global aromatic character coincides with the aromaticity of the most conjugated pathway and, from a qualitative point of view, it can be determined by the number of π -electrons in this circuit.²¹ In this sense, the systems selected in this work are expected to have the annulene pathway as the most aromatic one in the porphyrinoid structure. We have examined the DIs along the different pathways and we have found that in all cases except **16H**, the annulene path is the one with the largest DIs (see the ESI[†]). However, when we examine the aromaticity indices (see Table 3), we observe that only AV_{\min} predicts the annulene pathway as the most aromatic one in all the studied porphyrinoids. In some cases, the most aromatic pathway presents values close to the annulene pathway and, therefore, one could argue that the indices perform qualitatively well. Nevertheless, as the size of the porphyrinoid increases, the differences between the most conjugated pathway and the annulene one become larger. For instance, **32H**, **32M** and **32F** present pathways with very small BLA and BOA, suggesting that these circuits are more aromatic than the annulene pathway. However, as we examine in greater detail the bond lengths and the DI patterns we realize that the small BLA and BOA values are due to the compensation of deviations from the average values between odd and even bonds (see eqn (3) and (4), respectively). In this sense, small values of BOA and BLA should be taken with caution, as they do not always indicate a lack of bond-length or bond-order alternation. Another important problem occurs in other indices based on averages, such as AV1245, FLU or HOMA. Some large specific deviations in multicenter indices, bond orders and bond lengths, which could hinder the conjugation along the pathway (and therefore, aromaticity), can be concealed as they are averaged with the rest of the values. If the number of

Table 3 Aromaticity indices for the annulene pathway of the nine porphyrinoid structures, calculated at the CAM-B3LYP/6-311G(d,p) level of theory. The numbers in parenthesis are the minimum values of BLA, BOA and FLU, and the maximum values of AV1245, AV_{\min} and HOMA among all possible pathways

Porphyrin	Pathway	FLU	BOA	HOMA	BLA	AV1245	AV_{\min}
16H	oioi	0.021	0.227 (0.000)	0.547	0.063 (0.000)	1.19 (1.58)	0.13
18H	oioi	0.010 (0.006)	0.000	0.872 (0.968)	0.000	2.16	1.28
26H	oioioi	0.019 (0.016)	0.256 (0.000)	0.716 (0.797)	0.062 (0.001)	1.58	0.61
26M	oioioi	0.028 (0.025)	0.340 (0.011)	0.542 (0.633)	0.083 (0.002)	1.02 (1.12)	0.04
28H	oioioi	0.021 (0.017)	0.286 (0.000)	0.617 (0.759)	0.066 (0.000)	1.32 (1.46)	0.42
28M	oioioi	0.018 (0.013)	0.250 (0.000)	0.682 (0.824)	0.058 (0.000)	1.48 (1.50)	0.60
32H	oioioi	0.023 (0.018)	0.314 (0.006)	0.594 (0.734)	0.073 (0.002)	1.18 (1.24)	0.45
32M	oioioi	0.020 (0.015)	0.263 (0.006)	0.666 (0.793)	0.062 (0.000)	1.41 (1.48)	0.55
32F	oioioi	0.021 (0.015)	0.277 (0.000)	0.632 (0.780)	0.065 (0.001)	1.26 (1.38)	0.46

atoms in the pathway is relatively small, as it occurs in small organic rings, large individual deviations are easily spotted and, quite often, they have a significant effect on the average value. However, in large samples, *i.e.* in large expanded porphyrins, a few specific deviations are easily hidden. For these reasons, we believe that AV_{\min} is a better descriptor of the aromaticity than the other quantities considered in Table 3.

Finally, we focus on the effect of the density functional in the calculation of these electronic and structural aromaticity indices. There have been recent discussions in the literature concerning the role of the amount of the exact exchange in the density functional theory (DFT) calculations of large conjugated molecules.^{62–64,66,69,117} It is beyond the scope of the present manuscript deciding for the best exchange–correlation functional to characterize the electronic structure and geometry of porphyrinoids, but we believe a study of the effect of the amount of exact exchange of the aromaticity indicators is in order. Due to the relevance of the delocalization error in these measures, we will focus on the role of the exchange. To this aim, we compare the results of two popular global hybrid functionals, B3LYP and M06-2X, including 20% and 54% of exact exchange, respectively, against the performance of a popular range-separated functional, CAM-B3LYP, which adds variable amounts of exchange according to the interelectronic distance considered (from 19% at short-range distances to 65% at long-range distances). In Fig. 2 and 3, we have plotted the values of AV_{1245} and AV_{\min} calculated with B3LYP and M06-2X against CAM-B3LYP values for all the conjugation pathways of the nine studied systems. There is an excellent agreement between M06-2X and CAM-B3LYP for both indices. However, the correlation of AV_{1245} values computed with B3LYP and CAM-B3LYP presents some outliers and there is no clear correlation between the AV_{\min} values predicted by both methods. In Fig. 4 and 5, we show the same correlations but only for the annulene pathway. According to these results, the correlations are not improved when only the annulene pathway is considered. Now, we will analyze these results in greater detail.

To this aim, we have replicated the results of Table 3 with B3LYP and M06-2X in Tables S4 and S5 of the ESI.† Again, we find an excellent agreement between M06-2X and CAM-B3LYP

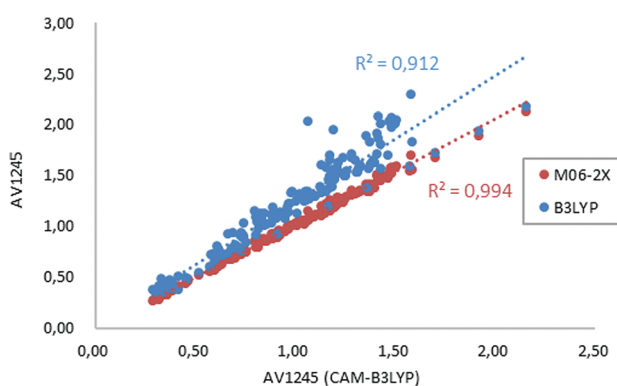


Fig. 2 Relationship of AV_{1245} among nine porphyrinoid compounds computed with M06-2X and B3LYP against CAM-B3LYP values for all the conjugation pathways in these structures.

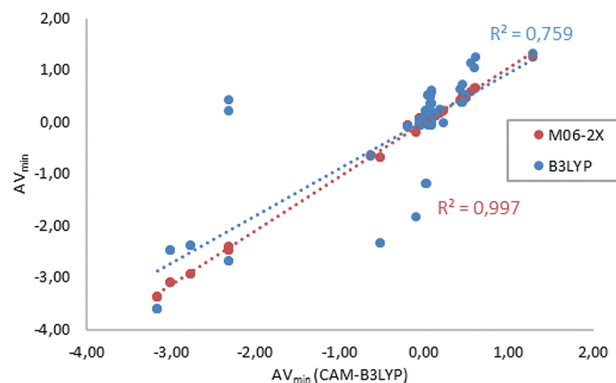


Fig. 3 Relationship of AV_{\min} among nine porphyrinoid compounds computed with M06-2X and B3LYP against CAM-B3LYP values for all the conjugation pathways in these structures.

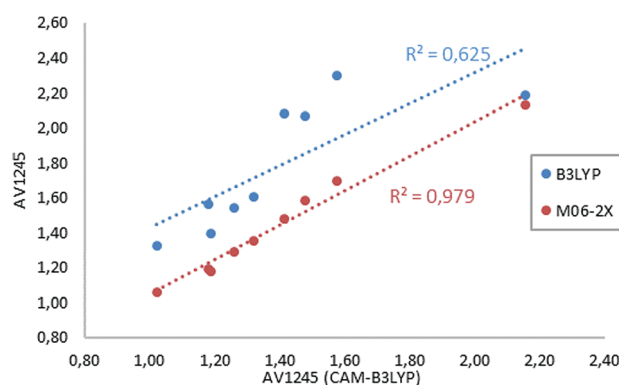


Fig. 4 Relationship of AV_{1245} among nine porphyrinoid compounds computed with M06-2X and B3LYP against CAM-B3LYP values for the annulene conjugation pathway in these structures.

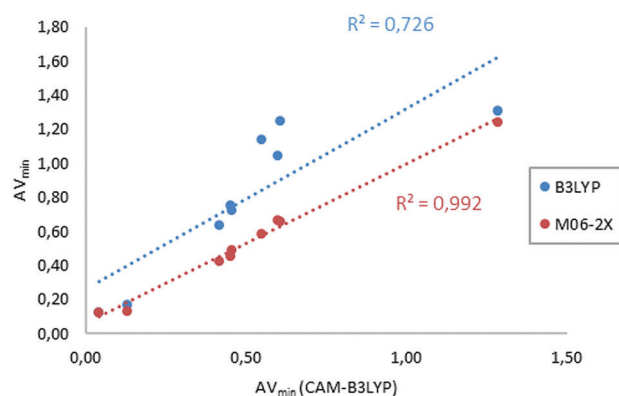


Fig. 5 Relationship of AV_{\min} among nine porphyrinoid compounds computed with M06-2X and B3LYP against CAM-B3LYP values for the annulene conjugation pathway in these structures.

results, suggesting that the long-range part of the exact exchange has a dominant role in the assessment of aromaticity. This finding is in line with the recent results reported by Szczepanik *et al.*¹¹⁷ Hereafter, we only discuss the differences between B3LYP and CAM-B3LYP. The analysis of specific porphyrinoid structures

shows that the agreement between methods for species such as **18H** is quantitative, whereas for some other systems, such as **16H**, **26H**, **26M** and **32F**, only a qualitative agreement is observed, *i.e.*, the values are quite different between B3LYP and CAM-B3LYP but the conclusions are the same. However, there is another set of systems, including **28H**, **28M**, **32H** and **32M**, for which there is no qualitative agreement between these functionals. Indeed, B3LYP presents larger differences between aromatic and antiaromatic compounds than CAM-B3LYP and M06-2X. These results are in agreement with the recent finding that the functionals with small amounts of exact exchange tend to generate structures with bond-length equalization as opposed to the functionals with a larger admixture of exact exchange (say, greater than 50%), which produce structures with bond-length alternation.⁶⁶ Not unexpectedly, this disagreement occurs for the most complicated systems including large porphyrinoid structures that admit Hückel, Möbius and eight-figure conformers. We have confirmed that there are non-negligible differences between the geometries predicted using B3LYP and CAM-B3LYP (or M06-2X) methods, which we speculate could be responsible for the aforementioned disagreements. These results advise some caution concerning the amount of exact exchange used in the calculation of aromatic species. Research in this line is currently underway in our laboratories.

5 Conclusions

We have investigated the conjugated pathways in nine porphyrinoid compounds of varying ring sizes and topologies using several aromaticity descriptors, including BLA, BOA, FLU and HOMA, as well as the recently introduced AV1245 and AV_{min} indices. In particular, the latter has been proposed to yield low aromaticity values for pathways with disconnected fragments that prevent a full conjugation around the macrocycle.

All the indices agree on the general features of these compounds, such as the fulfillment of Hückel's rule or which compounds should be more or less aromatic from the series. However, our results evince the difficulty in finding the most aromatic pathway in the macrocycle for large porphyrinoids. A careful examination of the data shows that some indices overestimate the aromaticity in the pathways because they are based on average values and, therefore, conceal disconnected fragments that are responsible for the loss of aromaticity. AV_{min} does not suffer from this drawback and it is actually the only index capable of recognizing the annulene pathway as the most aromatic one in the nine studied structures.

Finally, we study the effect of the exchange of DFT functionals on the description of the aromaticity of porphyrinoids. The amount of exact exchange at long range quantitatively changes the picture for most aromaticity descriptors. In line with previous findings,⁶⁶ we find that functionals with a small amount of long-range exact exchange tend to identify the macrocycles as more aromatic than functionals that include a larger percentage of exact exchange. Interestingly, regardless of the method employed, AV_{min} shows the same qualitative results in all studied cases.

Conflicts of interest

There are no conflicts to declare.

Acknowledgements

Financial support was provided by the Ministerio de Economía y Competitividad (MINECO) of Spain (MINECO/FEDER projects CTQ2016-80375-P, CTQ2014-52525-P and EUIN2017-88605) and by the Eusko Jaurlaritz (Basque Government) Consolidated Group Project No. IT588-13. I. C. R. acknowledges the Basque Government for funding through a predoctoral fellowship (PRE_2016_1_0159). The authors acknowledge the computational resources and technical and human support provided by DIPC and the SGI/IZO-SGIker UPV/EHU. M. A. thanks the Fund for Scientific Research–Flanders (FWO-12F4416N) for a postdoctoral fellowship and the Free University of Brussels (VUB) for financial support.

References

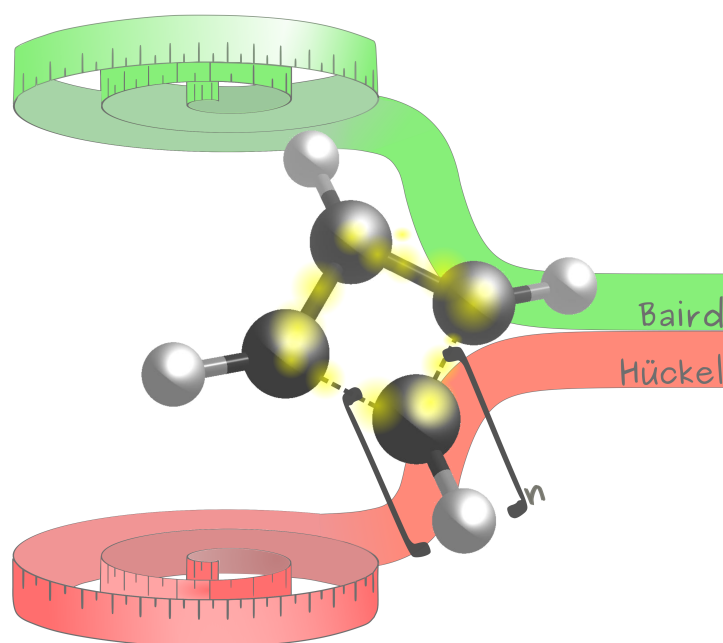
- P. V. R. Schleyer and H. Jiao, *Pure Appl. Chem.*, 1996, **68**, 209–218.
- Z. F. Chen, C. S. Wannere, C. Corminboeuf, R. Puchta and P. V. R. Schleyer, *Chem. Rev.*, 2005, **105**, 3842–3888.
- J. Poater, M. Duran, M. Solà and B. Silvi, *Chem. Rev.*, 2005, **105**, 3911–3947.
- T. M. Krygowski, H. Szatyłowicz, O. A. Stasyuk, J. Dominikowska and M. Palusiak, *Chem. Rev.*, 2014, **114**, 6383–6422.
- F. Feixas, E. Matito, J. Poater and M. Solà, *Wiley Interdiscip. Rev.: Comput. Mol. Sci.*, 2013, **3**, 105–122.
- F. Feixas, E. Matito, J. Poater and M. Solà, *Chem. Soc. Rev.*, 2015, **44**, 6434–6451.
- M. K. Cyrański, *Chem. Rev.*, 2005, **105**, 3773–3811.
- A. R. Katritzky, P. Barczynski, G. Musumarra, D. Pisano and M. Szafran, *J. Am. Chem. Soc.*, 1989, **111**, 7–15.
- M. Torrent-Sucarrat, J. M. Luis and M. Solà, *Chem. – Eur. J.*, 2005, **11**, 6024–6031.
- F. Feixas, E. Matito, J. Poater and M. Solà, *J. Comput. Chem.*, 2008, **29**, 1543–1554.
- M. Alonso and B. Herradón, *J. Comput. Chem.*, 2010, **31**, 917–928.
- L. Zhao, R. Grande-Aztatzzi, C. Foroutan-Nejad, J. M. Ugalde and G. Frenking, *ChemistrySelect*, 2017, **2**, 863–870.
- E. Matito, J. Poater, M. Duran and M. Solà, *THEOCHEM*, 2005, **727**, 165–171.
- F. Feixas, E. Matito, J. Poater and M. Solà, *J. Phys. Chem. A*, 2007, **111**, 4513–4521.
- F. Feixas, J. O. C. Jiménez-Halla, E. Matito, J. Poater and M. Solà, *J. Chem. Theory Comput.*, 2010, **6**, 1118–1130.
- E. Vogel, *Pure Appl. Chem.*, 1993, **65**, 143–152.
- E. Vogel, *Angew. Chem., Int. Ed.*, 2011, **50**, 4278–4287.
- M. K. Cyrański, T. M. Krygowski, M. Wisiorowski, N. J. R. van Eikema Hommes and P. V. R. Schleyer, *Angew. Chem., Int. Ed.*, 1998, **37**, 177–180.

- 19 J. Aihara, E. Kimura and T. M. Krygowski, *Bull. Chem. Soc. Jpn.*, 2008, **81**, 826–835.
- 20 H. Fliegl, D. Sundholm, S. Taubert and F. Pichierri, *J. Phys. Chem. A*, 2010, **114**, 7153–7161.
- 21 J. Aihara, Y. Nakagami, R. Sekine and M. Makino, *J. Phys. Chem. A*, 2012, **116**, 11718–11730.
- 22 J. I. Wu, I. Fernández and P. V. R. Schleyer, *J. Am. Chem. Soc.*, 2013, **135**, 315–321.
- 23 A. S. Ivanov and A. I. Boldyrev, *Org. Biomol. Chem.*, 2014, **12**, 6145–6150.
- 24 R. R. Valiev, H. Fliegl and D. Sundholm, *Phys. Chem. Chem. Phys.*, 2015, **17**, 14215–14222.
- 25 H. Fliegl, J. Jusélius and D. Sundholm, *J. Phys. Chem. A*, 2016, **120**, 5658–5664.
- 26 I. Benkyi, H. Fliegl, R. R. Valiev and D. Sundholm, *Phys. Chem. Chem. Phys.*, 2016, **18**, 11932–11941.
- 27 Y. J. Franzke, D. Sundholm and F. Weigend, *Phys. Chem. Chem. Phys.*, 2017, **19**, 12794–12803.
- 28 M. Bröring, *Angew. Chem., Int. Ed.*, 2011, **50**, 2436–2438.
- 29 H. S. Rzepa, *Chem. Rev.*, 2005, **105**, 3697–3715.
- 30 C. S. Wannere, H. S. Rzepa, B. C. Rinderspacher, A. Paul, C. S. M. Allan, H. F. Schaefer and P. V. R. Schleyer, *J. Phys. Chem. A*, 2009, **113**, 11619–11629.
- 31 J. M. Lim, Z. S. Yoon, J. Y. Shin, K. S. Kim, M. C. Yoon and D. Kim, *Chem. Commun.*, 2009, 261–273.
- 32 M. Torrent-Sucarrat, J. M. Anglada and J. M. Luis, *J. Chem. Theory Comput.*, 2011, **7**, 3935–3943.
- 33 T. Woller, N. Ramos-Berdullas, M. Mandado, M. Alonso, F. de Proft and J. Contreras-Garcia, *Phys. Chem. Chem. Phys.*, 2016, **18**, 11829–11838.
- 34 M. Torrent-Sucarrat, J. M. Anglada and J. M. Luis, *J. Chem. Phys.*, 2012, **137**, 1184306.
- 35 M. Torrent-Sucarrat, S. Navarro, E. Marcos, J. M. Anglada and J. M. Luis, *J. Phys. Chem. C*, 2017, **121**, 19348–19357.
- 36 J. Y. Shin, K. S. Kim, M. C. Yoon, J. M. Lim, Z. S. Yoon, A. Osuka and D. Kim, *Chem. Soc. Rev.*, 2010, **39**, 2751–2767.
- 37 S. Saito and A. Osuka, *Angew. Chem., Int. Ed.*, 2011, **50**, 4342–4373.
- 38 M. Stepień, N. Sprutta and L. Latos-Grażyński, *Angew. Chem., Int. Ed.*, 2011, **50**, 4288–4340.
- 39 T. Tanaka and A. Osuka, *Chem. Rev.*, 2017, **117**, 2584–2640.
- 40 B. Szyszko, M. J. Bialek, E. Pacholska-Dudziak and L. Latos-Grażyński, *Chem. Rev.*, 2017, **117**, 2839–2909.
- 41 Y. M. Sung, J. Oh, W. Y. Cha, W. Kim, J. M. Lim, M. C. Yoon and D. Kim, *Chem. Rev.*, 2017, **117**, 2257–2312.
- 42 E. Heilbronner, *Tetrahedron Lett.*, 1964, **5**, 1923–1928.
- 43 N. C. Baird and R. M. West, *J. Am. Chem. Soc.*, 1971, **93**, 4427–4432.
- 44 N. C. Baird, *J. Am. Chem. Soc.*, 1972, **94**, 4941–4948.
- 45 D. Ajami, O. Oeckler, A. Simon and R. Herges, *Nature*, 2003, **426**, 819–821.
- 46 M. Stepień, L. Latos-Grażyński, N. Sprutta, P. Chwalisz and L. Sztarenberg, *Angew. Chem., Int. Ed.*, 2007, **46**, 7869–7873.
- 47 J. Sankar, S. Mori, S. Saito, H. Rath, M. Suzuki, Y. Inokuma, H. Shinokubo, K. S. Kim, Z. S. Yoon, J. Y. Shin, J. M. Lim, Y. Matsuzaki, O. Matsushita, A. Muranaka, N. Kobayashi, D. Kim and A. Osuka, *J. Am. Chem. Soc.*, 2008, **130**, 13568–13579.
- 48 Y. Tanaka, S. Saito, S. Mori, N. Aratani, H. Shinokubo, N. Shibata, Y. Higuchi, Z. S. Yoon, K. S. Kim, S. B. Noh, J. K. Park, D. Kim and A. Osuka, *Angew. Chem., Int. Ed.*, 2008, **47**, 681–684.
- 49 S. Tokuji, J. Y. Shin, K. S. Kim, J. M. Lim, K. Youfu, S. Saito, D. Kim and A. Osuka, *J. Am. Chem. Soc.*, 2009, **131**, 7240–7241.
- 50 M. Stepień, B. Szyszko and L. Latos-Grażyński, *J. Am. Chem. Soc.*, 2010, **132**, 3140–3152.
- 51 T. Yoneda, Y. M. Sung, J. M. Lim, D. Kim and A. Osuka, *Angew. Chem., Int. Ed.*, 2014, **53**, 13169–13173.
- 52 G. R. Schaller, F. Topic, K. Rissanen, Y. Okamoto, J. Shen and R. Herges, *Nat. Chem.*, 2014, **6**, 609–614.
- 53 Y. M. Sung, M. C. Yoon, J. M. Lim, R. Rath, K. Naoda, A. Osuka and D. Kim, *Nat. Chem.*, 2015, **7**, 418–422.
- 54 Y. Hong, J. Oh, Y. M. Sung, Y. Tanaka, A. Osuka and D. Kim, *Angew. Chem., Int. Ed.*, 2017, **56**, 2932–2936.
- 55 H. S. Rzepa, *Org. Lett.*, 2008, **10**, 949–952.
- 56 C. S. M. Allan and H. S. Rzepa, *J. Org. Chem.*, 2008, **73**, 6615–6622.
- 57 H. Fliegl, D. Sundholm and F. Pichierri, *Phys. Chem. Chem. Phys.*, 2011, **13**, 20659–20665.
- 58 M. Alonso, P. Geerlings and F. de Proft, *Chem. – Eur. J.*, 2012, **18**, 10916–10928.
- 59 M. Alonso, P. Geerlings and F. De Proft, *J. Org. Chem.*, 2013, **78**, 4419–4431.
- 60 E. Marcos, J. M. Anglada and M. Torrent-Sucarrat, *J. Org. Chem.*, 2014, **79**, 5036–5046.
- 61 M. Alonso, B. Pinter, P. Geerlings and F. De Proft, *Chem. – Eur. J.*, 2015, **21**, 17631–17638.
- 62 T. Woller, J. Contreras-Garcia, P. Geerlings, F. De Proft and M. Alonso, *Phys. Chem. Chem. Phys.*, 2016, **18**, 11885–11900.
- 63 E. Marcos, J. M. Anglada and M. Torrent-Sucarrat, *J. Phys. Chem. C*, 2012, **116**, 24358–24366.
- 64 M. Alonso, P. Geerlings and F. de Proft, *Chem. – Eur. J.*, 2013, **19**, 1617–1628.
- 65 M. Alonso, P. Geerlings and F. De Proft, *Phys. Chem. Chem. Phys.*, 2014, **16**, 14396–14407.
- 66 M. Torrent-Sucarrat, S. Navarro, F. P. Cossio, J. M. Anglada and J. M. Luis, *J. Comput. Chem.*, 2017, **38**, 2819–2828.
- 67 R. A. King, T. D. Crawford, J. F. Stanton and H. F. Schaefer, *J. Am. Chem. Soc.*, 1999, **121**, 10788–10793.
- 68 C. S. Wannere and P. v. R. Schleyer, *Org. Lett.*, 2004, **5**, 865–868.
- 69 C. S. Wannere, K. W. Sattelmeyer, H. F. Schaefer and P. v. R. Schleyer, *Angew. Chem., Int. Ed.*, 2004, **43**, 4200–4206.
- 70 C. Castro, W. L. Karney, M. A. Valencia, C. M. H. Vu and R. P. Pemberton, *J. Am. Chem. Soc.*, 2005, **127**, 9704–9705.
- 71 E. Matito, *Phys. Chem. Chem. Phys.*, 2016, **18**, 11839–11846.
- 72 D. W. Szczepanik, M. Andrzejak, K. Dyduch, E. Zak, M. Makowski, G. Mazur and J. Mrozek, *Phys. Chem. Chem. Phys.*, 2014, **16**, 20514–20523.
- 73 P. V. R. Schleyer, C. Maerker, A. Dransfeld, H. J. Jiao and N. Hommes, *J. Am. Chem. Soc.*, 1996, **118**, 6317–6318.
- 74 H. J. Dauben Jr., J. D. Wilson and J. L. Laity, *J. Am. Chem. Soc.*, 1968, **90**, 811–813.

- 75 F. Feixas, M. Solà, J. M. Barroso, J. M. Ugalde and E. Matito, *J. Chem. Theory Comput.*, 2014, **10**, 3055–3065.
- 76 R. F. W. Bader, *Atoms in Molecules: A Quantum Theory*, Clarendon, Oxford, 1990.
- 77 E. Matito, J. Poater, F. M. Bickelhaupt and M. Solà, *J. Phys. Chem. B*, 2006, **110**, 7189–7198.
- 78 E. Matito, M. Solà, P. Salvador and M. Duran, *Faraday Discuss.*, 2007, **135**, 325–345.
- 79 C. Foroutan-Nejad, S. Shahbazian and R. Marek, *Chem. – Eur. J.*, 2014, **20**, 10140–10152.
- 80 C. Foroutan-Nejad, J. Vicha, R. Marek, M. Patzschke and M. Straka, *Phys. Chem. Chem. Phys.*, 2015, **17**, 24182–24192.
- 81 Z. Badri, C. Foroutan-Nejad, J. Kozelka and R. Marek, *Phys. Chem. Chem. Phys.*, 2015, **17**, 26183–26190.
- 82 M. Rodríguez-Mayorga, E. Ramos-Cordoba, P. Salvador, M. Solà and E. Matito, *Mol. Phys.*, 2016, **114**, 1345–1355.
- 83 P. L. Bora, M. Novák, J. Novotný, C. Foroutan-Nejad and R. Marek, *Chem. – Eur. J.*, 2017, **23**, 7315–7323.
- 84 W. Heyndrickx, P. Salvador, P. Bultinck, M. Solà and E. Matito, *J. Comput. Chem.*, 2011, **32**, 386–395.
- 85 R. F. W. Bader and M. E. Stephens, *J. Am. Chem. Soc.*, 1975, **97**, 7391–7399.
- 86 X. Fradera, M. A. Austen and R. F. W. Bader, *J. Phys. Chem. A*, 1999, **103**, 304–314.
- 87 M. Rafat and L. A. Popelier, in *The quantum theory of atoms in molecules: from solid state to DNA and drug design*, ed. C. F. Matta and R. J. Boyd, Wiley-VCH, Weinheim, 2007, pp. 121–140.
- 88 E. Francisco, D. Menéndez Crespo, A. Costales and Á. Martín Pendás, *J. Comput. Chem.*, 2017, **38**, 816–829.
- 89 Z. Badri and C. Foroutan-Nejad, *Phys. Chem. Chem. Phys.*, 2016, **18**, 11693–11699.
- 90 C. Fonseca Guerra, J.-W. Handgraaf, E. J. Baerends and F. M. Bickelhaupt, *J. Comput. Chem.*, 2004, **25**, 189–210.
- 91 E. Matito, J. Poater, M. Solà, M. Duran and P. Salvador, *J. Phys. Chem. A*, 2005, **109**, 9904–9910.
- 92 E. Matito, P. Salvador, M. Duran and M. Solà, *J. Phys. Chem. A*, 2006, **110**, 5108–5113.
- 93 J. Kruszewski and T. M. Krygowski, *Tetrahedron Lett.*, 1972, **13**, 3839–3842.
- 94 T. M. Krygowski and M. K. Cyranski, *Chem. Rev.*, 2001, **101**, 1385–1419.
- 95 E. Matito, M. Duran and M. Solà, *J. Chem. Phys.*, 2005, **122**, 014109.
- 96 E. Matito, M. Duran and M. Solà, *J. Chem. Phys.*, 2006, **125**, 059901.
- 97 F. Feixas, M. Solà and M. Swart, *Can. J. Chem.*, 2009, **87**, 1063–1073.
- 98 R. Herges, *Chem. Rev.*, 2006, **106**, 4820–4842.
- 99 M. Giambiagi, M. S. de Giambiagi, C. D. dos Santos and A. P. de Figueiredo, *Phys. Chem. Chem. Phys.*, 2000, **2**, 3381–3392.
- 100 P. Bultinck, R. Ponec and S. Van Damme, *J. Phys. Org. Chem.*, 2005, **18**, 706–718.
- 101 X. Min, I. A. Popov, F.-X. Pan, L.-J. Li, E. Matito, Z.-M. Sun, L.-S. Wang and A. I. Boldyrev, *Angew. Chem., Int. Ed.*, 2016, **55**, 5531–5535.
- 102 J. Cioslowski, E. Matito and M. Solà, *J. Phys. Chem. A*, 2007, **111**, 6521–6525.
- 103 E. Matito, F. Feixas and M. Solà, *THEOCHEM*, 2007, **811**, 3–11.
- 104 F. Feixas, E. Matito, M. Solà and J. Poater, *Phys. Chem. Chem. Phys.*, 2010, **12**, 7126–7137.
- 105 C. García-Fernández, E. Sierda, M. Abadía, B. Bugenhagen, M. H. Prosenc, R. Wiesendanger, M. Bazarnik, J. E. Ortega, J. Brede, E. Matito and A. Arnau, *J. Phys. Chem. C*, 2017, **121**, 27118–27125.
- 106 A. D. Becke, *J. Chem. Phys.*, 1993, **98**, 5648–5652.
- 107 P. J. Stephens, F. J. Devlin, C. F. Chabalowski and M. J. Frisch, *J. Phys. Chem.*, 1994, **98**, 11623–11627.
- 108 Y. Zhao and D. G. Truhlar, *Theor. Chem. Acc.*, 2008, **120**, 215–241.
- 109 T. Yanai, D. P. Tew and N. C. Handy, *Chem. Phys. Lett.*, 2004, **393**, 51–57.
- 110 W. J. Hehre, R. Ditchfield and J. A. Pople, *J. Chem. Phys.*, 1972, **56**, 2257–2261.
- 111 W. J. Hehre, L. Radom, P. V. R. Schleyer and J. A. Pople, *Ab Initio Molecular Orbital Theory*, Wiley, New York, 1986.
- 112 In the case of the hydrogen as *meso*-substituent it is worth noting that the figure eight structure has almost no twist.
- 113 M. J. Frisch, G. W. Trucks, H. B. Schlegel, G. E. Scuseria, M. A. Robb, J. R. Cheeseman, G. Scalmani, V. Barone, B. Mennucci, G. A. Petersson, H. Nakatsuji, M. Caricato, X. Li, H. P. Hratchian, A. F. Izmaylov, J. Bloino, G. Zheng, J. L. Sonnenberg, M. Hada, M. Ehara, K. Toyota, R. Fukuda, J. Hasegawa, M. Ishida, T. Nakajima, Y. Honda, O. Kitao, H. Nakai, T. Vreven, J. A. Montgomery Jr., J. E. Peralta, F. Ogliaro, M. Bearpark, J. J. Heyd, E. Brothers, K. N. Kudin, V. N. Staroverov, R. Kobayashi, J. Normand, K. Raghavachari, A. Rendell, J. C. Burant, S. S. Iyengar, J. Tomasi, M. Cossi, N. Rega, J. M. Millam, M. Klene, J. E. Knox, J. B. Cross, V. Bakken, C. Adamo, J. Jaramillo, R. Gomperts, R. E. Stratmann, O. Yazyev, A. J. Austin, R. Cammi, C. Pomelli, J. W. Ochterski, R. L. Martin, K. Morokuma, V. G. Zakrzewski, G. A. Voth, P. Salvador, J. J. Dannenberg, S. Dapprich, A. D. Daniels, Ö. Farkas, J. B. Foresman, J. V. Ortiz, J. Cioslowski and D. J. Fox, *Gaussian 09, revision E.01*, Gaussian, Inc., Wallingford, CT, 2009.
- 114 AIMAll (Version 14.11.23) *aim.tkgristmill.com*, Keith, T. A., TK Gristmill Software, Overland Park KS, USA, 2014.
- 115 E. Matito, *ESI-3D: Electron Sharing Indexes Program for 3D Molecular Space Partitioning*, Institute of Computational Chemistry and Catalysis, University of Girona, Catalonia, Spain, 2014.
- 116 H. Fliegl, S. Taubert, O. Lehtonen and D. Sundholm, *Phys. Chem. Chem. Phys.*, 2011, **13**, 20500–20518.
- 117 D. W. Szczepanik, M. Solà, M. Andrzejak, B. Pawełek, J. Dominikowska, M. Kukulka, K. Dyduch, T. M. Krygowski and H. Szatyłowicz, *J. Comput. Chem.*, 2017, **38**, 1640–1654.

Chapter 6

How do the Hückel and Baird Rules Fade away in Annulenes?



Article

How do the Hückel and Baird Rules Fade away in Annulenes?

Irene Casademont-Reig ^{1,2}, Eloy Ramos-Cordoba ^{1,2}, Miquel Torrent-Sucarrat ^{1,2,3} and Eduard Matito ^{1,3*}

- ¹ Donostia International Physics Center (DIPC), 20018 Donostia, Euskadi, Spain; irenecasre@gmail.com (I.C.-R.); eloy.raco@gmail.com (E.R.-C.); miqueltorrentsucarrat@gmail.com (M.T.-S.)
² Kimika Fakultatea, Euskal Herriko Unibertsitatea (UPV/EHU), 20080 Donostia, Euskadi, Spain
³ IKERBASQUE, Basque Foundation for Science, 48013 Bilbao, Euskadi, Spain
* Correspondence: ematito@gmail.com; Tel.: +34-943018513

Academic Editors: Diego Andrada and Israel Fernández

Received: 20 December 2019; Accepted: 29 January 2020; Published: 7 February 2020



Abstract: Two of the most popular rules to characterize the aromaticity of molecules are those due to Hückel and Baird, which govern the aromaticity of singlet and triplet states. In this work, we study how these rules fade away as the ring structure increases and an optimal overlap between p orbitals is no longer possible due to geometrical restrictions. To this end, we study the lowest-lying singlet and triplet states of neutral annulenes with an even number of carbon atoms between four and eighteen. First of all, we analyze these rules from the Hückel molecular orbital method and, afterwards, we perform a geometry optimization of the annulenes with several density functional approximations in order to analyze the effect that the distortions from planarity produce on the aromaticity of annulenes. Finally, we analyze the performance of three density functional approximations that employ different percentages of Hartree-Fock exchange (B3LYP, CAM-B3LYP and M06-2X) and Hartree-Fock. Our results reveal that functionals with a low percentage of Hartree-Fock exchange at long ranges suffer from severe delocalization errors that result in wrong geometrical structures and the overestimation of the aromatic character of annulenes.

Keywords: annulenes; aromaticity; antiaromaticity; Hückel rule; Baird rule; density functional theory; delocalization error

1. Introduction

Aromaticity is one of the most important concepts in chemistry, and it is associated with cyclic electron delocalization (or conjugation) in closed circuits giving rise to bond-length equalization, energy stabilization, large magnetic anisotropies and abnormal chemical shifts, among other well-known effects [1–3]. Despite the multidimensional character of aromaticity and the recent proliferation of aromatic compounds that extend beyond the organic chemistry realm [4,5], several simple but predictive models have been designed to characterize aromaticity [6–10]. From these models, *rules of aromaticity* [11] have been obtained that are commonly used in assessing the aromatic character of molecules. Among these rules, the Hückel rule was the first and remains the most widely employed [12–15].

According to the Hückel rule, annulenes with $4n + 2 \pi$ electrons (n being an integer number) are more stable than the corresponding open-chain polyenes and, therefore, considered *aromatic*. Although this prediction is met for the first elements of the annulenes series, the rule is soon broken due to out-of-plane geometrical distortions that are more energetically favorable but disrupt the optimal overlaps between p orbitals that give rise to conjugated circuits [16]. These geometrical distortions cannot be considered by the Hückel rule which, inevitably, overestimates the aromaticity of $4n + 2$

annulenes that are described as planar structures having bond equalization. Conversely, the Hückel rule also predicts that $4n$ π electron annulenes are unstable with respect to their open-chain analogues, exhibit bond length alternation, and are considered *antiaromatic*. The application of this rule has not been limited to annulenes and it is currently used in all sorts of molecules, including non-organic molecules [4,5].

Another important rule of aromaticity, complementary to Hückel's, is the Baird rule [17]. While the Hückel rule is limited to singlet ground states, the Baird rule applies to the lowest-lying triplet and excited singlet states and predicts $4n(4n + 2)$ π -electron molecules to be aromatic (antiaromatic). Aihara calculated the resonance energies of singlet and triplet annulenes, concluding that Baird's rule was satisfied, i.e., that the lowest-lying excited state of annulenes presented the opposite aromatic character to that in the ground state [18]. Baird's rule has been called the *photochemistry analogue of Hückel's rule* [19] because it has been used to tailor molecules with enhanced photochemical activity [20–22].

The most (anti)aromatic molecules do not usually have many atoms in the ring. The optimal overlap between orbitals that favors electron conjugation calls for a particular arrangement of the atoms in the ring that cannot be sustained as the ring size increases. Therefore, both aromaticity and antiaromaticity are expected to decrease with the ring size. Although there is evidence of large aromatic nanorings [23], studies on annulenes have led to the conclusion that systems with more than 30π electrons are nonaromatic [24].

In his seminal paper, Baird studied the velocity at which the antiaromaticity (measured through Dewar resonance energy, DRE) diminished with increasing ring size [17]. Based on a few examples, he found that $4n + 2$ triplets lost their antiaromaticity with the ring size as fast as $4n$ singlets [17]. To the best of our knowledge, thus far, there have been very few attempts to actually quantify how the aromaticity rules fade away with the ring size and they were limited to $4n + 2$ annulenes [25,26]. This is the goal of this paper. We will first perform an analysis of how these rules are expected to change with the ring size as predicted by the model from which they originated. Second, we will study how the geometry distorts these molecules from the optimal (planar) geometry assumed in the model and how it affects the aromaticity. Finally, we will analyze the effect of the computational method in the description of these systems by taking into account several density functional approximations (DFAs) with a varying percentage of Hartree Fock (HF) exchange.

2. Methodology

2.1. Aromaticity Indices

In this section, we will review the expressions of several aromaticity indices based on electron delocalization [2]. In the following, we will assume a molecule having at least one ring structure, which consists of N atoms represented by the string $\mathcal{A} = \{A_1, A_2, \dots, A_N\}$, whose elements are ordered according to the connectivity of the atoms in the ring. For convenience, we adopt $A_{N+p} \equiv A_p$ and $A_0 \equiv A_N$.

2.1.1. The Aromatic Fluctuation Index: FLU

The FLU index measures aromaticity by comparison with the cyclic electron delocalization of some reference aromatic molecules [27]. Its expression depends on the delocalization index (DI) [28–31], $\delta(A, B)$, which measures the electron sharing between atoms A and B ,

$$FLU(\mathcal{A}) = \frac{1}{N} \sum_{i=1}^N \left[\left(\frac{\delta(A_i)}{\delta(A_{i-1})} \right)^\alpha \left(\frac{\delta(A_i, A_{i-1}) - \delta_{ref}(A_i, A_{i-1})}{\delta_{ref}(A_i, A_{i-1})} \right) \right]^2, \quad (1)$$

where $\delta(A)$ is the atomic valence for a closed-shell system [32], and α is a simple function to ensure that the first term in Equation (1) is always greater or equal to 1,

$$\alpha = \begin{cases} 1 & \delta(A_{i-1}) \leq \delta(A_i) \\ -1 & \delta(A_i) < \delta(A_{i-1}) \end{cases} \quad (2)$$

$\delta_{ref}(A, B)$ is the DI corresponding to an aromatic molecule which has the pattern of bonding $A - B$. For example, the aromatic reference for C-C bonds is benzene. FLU is close to zero for aromatic species, and greater than zero for non-aromatic or antiaromatic species.

Aromaticity indices based on references, such as FLU or HOMA [33,34], do not measure aromaticity but the similarity with respect to some aromatic molecule. Therefore, they are not adequate to describe reactivity [35,36].

2.1.2. The Bond-Length and Bond-Order Alternation Indices

Two popular indicators of aromaticity are the bond-length (BLA) and the bond-order alternation (BOA), which compare the average of bond lengths and bond orders, respectively, of consecutive bonds in a ring:

$$\frac{1}{n_1} \sum_{i=1}^{n_1} x_{A_{2i-1}, A_{2i}} - \frac{1}{n_2} \sum_{i=1}^{n_2} x_{A_{2i}, A_{2i+1}'} \quad (3)$$

where $n_1 = \lfloor (N + 1) / 2 \rfloor$ and $n_2 = \lfloor N / 2 \rfloor$, $\lfloor y \rfloor$ being the floor function of y , that returns the largest integer less than or equal to y , and x is either the bond length or the bond order. Unlike the atomic charges [37], the bond orders are much less dependent on the computational method and the basis set used [38] and, therefore, aromaticity indices based on bond orders [39] are not highly dependent on the level of theory employed. An exception to this rule is the delocalization error that is present in some DFAs [40] with a low percentage of Hartree-Fock exchange, which causes an overestimation of the aromaticity of some compounds (see Section 3.4).

The definition of Equation (3) presents a serious drawback: it is not well defined for a ring of an odd number of members because its value depends on the order of the atoms in the ring. For the sake of generality, in this paper we adopt an alternative definition of BLA/BOA:

$$\frac{1}{2N} \sum_{i=1}^N |x_{A_i, A_{i+1}} - x_{A_{i+1}, A_{i+2}}|. \quad (4)$$

and we choose the delocalization index [28–31] as a measure of bond order.

2.1.3. A Many-Center Electron Delocalization Index: I_{ring}

Giambiagi and coworkers suggested to use the multicenter index, which was previously defined by them to account for the simultaneous electron sharing among various centers [41], as a measure of aromaticity [42]. This index was named I_{ring} and its formulation for single-determinant wavefunctions reads as follows:

$$I_{\text{ring}}(\mathcal{A}) = \sum_{i_1, i_2, \dots, i_n}^{\text{occ}} S_{i_1 i_2}(A_1) S_{i_2 i_3}(A_2) \dots S_{i_n i_1}(A_n), \quad (5)$$

where $S_{ij}(A)$ is the overlap of molecular orbitals i and j in the atom A , i.e.,

$$S_{ij}(A) = \int_A \phi_i^*(\mathbf{r}) \phi_j(\mathbf{r}) d\mathbf{r}. \quad (6)$$

I_{ring} will provide large values for aromatic molecules. Although it will not be considered in this paper, it is worth to mention that Bultinck and co-workers generalized I_{ring} considering also the delocalization of a non-Kekule arrangement of the atoms in the ring; the index is known as MCI [43]. Some of us have shown that both I_{ring} and MCI are ring-size dependent [44] and, therefore, for convenience, we will calculate the multicenter *electron delocalization per atom* that can be obtained as $I_{\text{ring}}^{1/N}$.

2.1.4. AV1245 and AV_{\min}

Both I_{ring} and MCI are among the less fallible aromaticity indices available in the literature [2,36,45] and, therefore, they have been used in a plethora of cases involving a difficult assessment of aromaticity [46–54]. However, these indices present some drawbacks that prevent their use in large rings [55] and, therefore, we have recently designed [55] and tested [40,56] a new electronic aromaticity index, AV1245, based on MCI but free of the shortcomings of this index. AV1245 is defined as the average value of the four-atom MCI index between relative positions 1–2 and 4–5 constructed from each five-atom fragment (five consecutive atoms) along the perimeter of the ring [55]. The latter gives an *average picture* of the electron delocalization among the atoms in the ring. However, for the purpose of measuring aromaticity, it has been found more adequate to use the minimum absolute MCI value evaluated along the perimeter, AV_{\min} [56]. AV_{\min} identifies the *weakest link*, i.e., the fragment with the lowest electron delocalization which is usually responsible for the loss of aromaticity in the ring. A detailed study of all the MCI values along the perimeter has been recently shown to be useful in identifying electron delocalization patterns and it will be the topic of discussion in a forthcoming work. Aromatic molecules are thus identified by large values of AV_{\min} ($AV_{\min} \gg 1$) and non-aromatic molecules exhibit very low AV_{\min} values. Antiaromatic molecules usually exhibit intermediate AV_{\min} values and are more difficult to identify. To this end, the analysis is complemented by the examination of either four-atom MCI profiles along the perimeter of the ring or the BOA, which help differentiate between aromatic and antiaromatic compounds.

2.2. Hückel Molecular Orbital Method

Despite the drastic approximations inherent in the Hückel Molecular Orbital (HMO) approach [12–15], organic aromatic molecules are usually well described within the HMO method. It is thus usual to learn the HMO method at the same time as $4n + 2$ Hückel's rule and other aromaticity measures given by the HMO method, such as the resonance energy (RE), the RE per electron (REPE) or the topological REPE (TREPE) [57]. Some recent works have studied Hückel's rule from the perspective of electron delocalization [58,59]. Since the studies of Hückel on organic molecules, the concept of aromaticity has extended importantly including all sorts of new aromatic molecules such as metalloaromatic molecules [4,51,52,60,61], fullerenes [62], nanotubes [63], porphyrins [64,65] with a Möbius-like structure [66–73], and all-metal clusters [4,5], among others.

For a cyclic polyene of n carbon atoms and N π electrons, the Hückel molecular orbital (HMO) method provides a general formulation for its orbitals:

$$\phi_l = \sum_{\mu=1}^N \chi_{\mu} c_{\mu l} = \frac{1}{\sqrt{N}} \sum_{\mu=1}^N \chi_{\mu} e^{2\pi i(\mu-1)l/N}, \quad (7)$$

where χ_{μ} is the atomic orbital $2p_z$ of the μ^{th} carbon atom and $l = 0 \pm 1, \dots, \pm(N-1)/2, N/2$. Excepting for the first (ϕ_0) and the last ($\phi_{N/2}$), these orbitals are complex and degenerate by pairs ($\phi_{\pm 1}, \phi_{\pm 2}, \dots$). From these equations, one can easily calculate the atomic overlap matrices (AOMs), the bond orders, as well as many aromaticity indices (see Section 2.1), obtaining analytical expressions [74].

The typical way to assess the aromaticity within the framework of HMO theory is through the study of stabilization or resonance energy. Since the computational chemistry study of resonance energies puts severe limitations to analyze more complicated molecules, especially those containing atoms other than carbon, we prefer to study electron delocalization to assess the aromatic character of compounds [2,55]. In particular, we focus here on the study of I_{ring} which, in the case of HMO theory, takes a very simple form (compare to Equation (5)),

$$I_{\text{ring}}^{\text{HMO}}(\mathcal{A}) = P_{A_1 A_2} P_{A_2 A_3} \cdots P_{A_n A_1}, \quad (8)$$

where P_{AB} is the bond-order between atoms A and B and it is related to the DI: $\delta(A, B) = P_{AB}P_{BA}$ [74].

In order to compare annulenes of different sizes among them, we will study the normalized quantity $I_{\text{ring}}^{1/N}$ [44]. The calculation of the bond orders takes a very simple form for singlet annulenes with $4n + 2\pi$ electrons [74]. The study of other multiplicities or number of π electrons is less evident. The HMO theory does not distinguish between alpha and beta electrons (beyond the fact of permitting only one electron of each kind to populate each orbital) and, therefore, the study of triplets is not entirely satisfactory. However, to a reasonable extent, one can analyze the $4n + 2$ triplets as cases where one electron is promoted from a l orbital to a $l + 1$ orbital. If the orbitals obtained from HMO are those of Equation (7), the results are the same regardless the electrons are promoted from l or $-l$ orbitals (or whether they are promoted to $l + 1$ or $-l - 1$ orbitals). Hence, the study of $4n + 2$ triplets can be done without ambiguity. However, the study of neutral $4n$ singlets, which are expected to exhibit localized structures of symmetry $D_{N/2h}$, cannot be conducted because both l and $-l$ orbitals contribute the same amount to all the bond orders in the perimeter of the ring. In order to enforce the appearance of mesomeric structures, we should obtain a different set of orbitals from the HMO theory. Since degenerate orbitals can be freely combined without altering the energy of the system, it is convenient to recombine each pair of degenerate orbitals among themselves to produce this set of orbitals:

$$\bar{\phi}_l = (1 + i)\phi_l + (1 - i)\phi_{-l}, \quad (9)$$

for $l = \pm 1, \dots, \pm(N - 1)/2$. Unlike those in Equation (7), these orbitals are real and produce one of the two mesomeric structures that one can expect in neutral $4n$ annulenes, depending on whether the last two electrons occupy a l or $-l$ orbital. Finally, we find that the study of neutral $4n$ triplets within the HMO theory is far from obvious because both the singlet-open and the triplet states would be actually described by the same orbital occupancies. For the sake of completeness, we have also included this case in our study. To this end, we have employed the original set of orbitals (Equation (7)) and these results are labeled as $4n D_{Nh}$. (We could have also chosen the second set of orbitals that lead to mesomeric structures. In such case, we would have obtained different I_{ring} values but the same qualitative trend (see Section 3.1)).

3. Results

3.1. Aromaticity from the HMO Method

First of all, we will study Hückel's and Baird's rules from the simple HMO theory [12,14]. Although we cannot expect this theory to provide a reliable description of annulenes (especially the large ones), the results we obtain will provide a high bound to the aromaticity/antiaromaticity expected in these species.

All the values of I_{ring} (Equation (8)) are collected in Figure 1. Interestingly, all the curves conform to the same general expression: $a + b/N^2$, where N is the number of ring members. The values of a do not differ significantly among the four cases giving values very close to the theoretical limit for annulenes, $2/\pi$, whereas the values of b present large differences among them: -2.1867 , 1.0822 , -5.1151 , and -5.5910 for $4n D_{Nh}$, $4n + 2$ singlet, $4n + 2$ triplet, and $4n$ singlet $D_{N/2h}$ structures, respectively. These results are in agreement with the chemical intuition: (i) for very large annulenes both Hückel and Baird rules break and all the species become equally aromatic, (ii) the initial (anti)aromatic character decreases smoothly with the annulene size. We can also see that $4n + 2$ singlets, which are aromatic, display values above the $2/\pi$ limit, whereas $4n + 2$ triplets and $4n$ singlets, which are expected to be antiaromatic, present values below this limit. On the other hand, $4n D_{Nh}$ annulenes also behave like antiaromatic molecules, which does not conform with the aromaticity expected in $4n$ triplets and, therefore, these species are not well described from the delocalization measures we can obtain from the HMO theory. Finally, we can compare the velocity with which the (anti)aromaticity decreases according to Hückel's and Baird's rule. The values of b show that the velocity at which the aromaticity decreases with the ring size is about five times smaller for $4n + 2$ singlet annulenes than

the corresponding decrease of antiaromaticity for $4n + 2$ triplets. Interestingly, the latter is very close to the decrease of antiaromaticity found in $4n$ singlets, in agreement with the study of Baird on cyclic hydrocarbons using DRE [17]. We have also studied the HMO method forcing bond-length alternation by employing two different resonance integrals for each bond type (single and double) [75,76], finding that the antiaromaticity of $4n$ singlets decreases more rapidly when the annulenes are forced to exhibit bond alternation. Since we cannot compare $4n$ singlets and triplets, we cannot extract any relevant conclusion about which rule, Hückel's or Baird's, is broken more quickly with the ring size. We can, however, conclude from this data that molecules are more resilient to the loss of aromaticity than to the loss of antiaromaticity, as one would expect from purely energetic grounds.

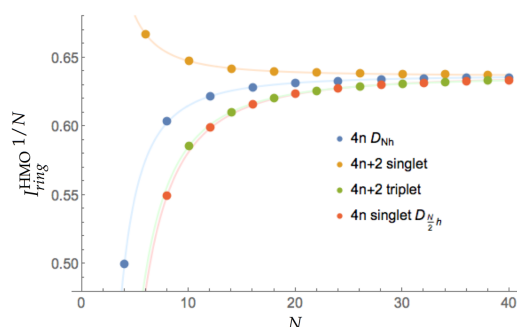


Figure 1. Values of $I_{\text{ring}}^{1/N}$ for the annulenes series against the number of C atoms (N) for different singlets and triplets. The species have been divided according to the number of electrons ($4n$ and $4n + 2$) and the spin multiplicity (singlet and triplet).

3.2. Geometrical Relaxation

Thus far, we have studied ideally planar annulenes within the HMO method. In this section, we employ quantum chemistry methods to study the geometry of annulenes, which often do not attain a planar conformation in their ground state configuration [77] (see Figure 2). We will employ HF and three DFAs: B3LYP, M06-2X and CAM-B3LYP. These results will be compared against the benchmark data available in the literature. We will split the results into two blocks: $4n + 2$ and $4n$ π -electron annulenes.

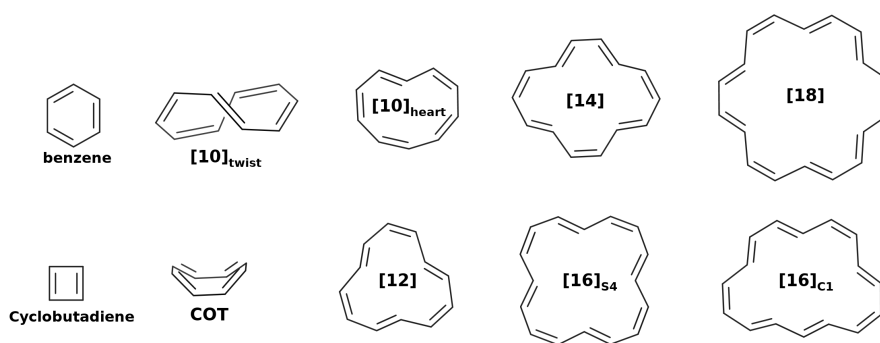


Figure 2. Geometrical structures of the studied annulenes.

3.2.1. $4n + 2$ Annulenes

First of all, we have studied the lowest-lying structures of singlet and triplet benzene. The ground state of benzene has been largely studied and its characterization does not present a challenge for DFAs. The molecule is identified by all the aromaticity measures as the most aromatic molecule among the studied annulenes. Conversely, the triplet state of benzene has a more elusive character, presenting two D_{2h} conformations which are very close in energy, the quinoidal (Q) and antiquinoidal (AQ) one [17].

The former is characterized by two clear double bonds separated by two radical C atoms, whereas the AQ shows two allylic structures merged by two single C-C bonds. The energy difference between the two conformations is below 1 kcal/mol and they are connected by a transition state with an energy barrier of 2.5 kcal/mol [78]. Both conformers are expected to be antiaromatic, displaying an energy destabilization that is responsible for their prominent photochemical reactivity [79]. The lowest-lying triplet state of benzene has been identified by HF, B3LYP, and CAM-B3LYP as AQ-like, whereas the Q structure could not be located with these methods. Conversely, M06-2X provides a Q-like structure. The aromaticity indices display values which are much smaller than those of benzene and the BOA index reveals a bond-order alternation that is characteristic of antiaromatic molecules. AV_{\min} values are small, which in conjunction with the oscillating pattern displayed by the dissected index profile (see Supplementary Material), agrees with the antiaromatic character anticipated in this species.

Singlet [10]annulene presents several low-energy isomers, which are difficult to sort energetically from the results of computational calculations. Most ab initio methods find the *twist* conformation to be the lowest in energy, the exception being B3LYP, which predicts the *heart* conformation to be the ground state [16]. Our calculations agree with these results. The most delocalized structure, corresponding to a D_{10h} symmetry, lies more than 30kcal/mol above the ground state geometry [16] and, hence, the isomer expected to be the most aromatic it is actually not stable. On the contrary, the twist isomer (which does not exhibit a planar conformation) presents a very modest aromatic/antiaromatic character according to all the aromaticity indices. In fact, the molecule could be easily classified as nonaromatic from the AV_{\min} value, which is very close to zero and, as the dissected index profile shows (see Supplementary Material), the twisted bonds are those that prevent an optimal overlap of *p* orbitals. Conversely, the heart configuration (lying 0.6 and 2.3 kcal/mol above the ground state according to CAM-B3LYP and M06-2X) is an aromatic molecule as stated by all aromaticity indices. To the best of our knowledge, triplet [10]annulene has been much less studied and there are only examples of triplet dicationic [10]annulene structures on the literature [20,21]. The lowest-lying triplet state of [10]annulene displays *naphthalene* (B3LYP, CAM-B3LYP and M06-2X) and *twist* (HF) configurations. Following the Baird rule, this molecule should be antiaromatic. The naphthalene conformation is indeed mildly antiaromatic but the twist conformation is rather nonaromatic (see Table 1).

The ground-state [14]annulene geometry corresponds to a distorted pyrene perimeter [16] that can undergo a facile isomerization reaction through a Möbius antiraromatic transition state [80]. At the B3LYP level of theory, we locate a minimal structure with C_{2h} symmetry that is aromatic according to all criteria of aromaticity. However, the CAM-B3LYP and M06-2X C_{2h} configurations correspond to a transition state (TS) that through a small energy barrier (ca. 2.5 kcal/mol) connects two C_s -symmetry antiaromatic energy minima with complementary bond-length alternation. The triplet conformer leads to an energy minimum that is only mildly antiaromatic at all the levels of theory.

The Hückel rule predicts that [18]annulene is an aromatic molecule but the situation is similar to [14]annulene. B3LYP finds the molecule to be a highly symmetric (D_{6h}) structure that is also aromatic from all aromaticity indices. However, both CAM-B3LYP and M06-2X predict that this structure is actually a transition state that connects two identical structures that exhibit bond-order alternation and, therefore, are antiaromatic. This discrepancy has been attributed to the delocalization error of DFAs with a low percentage of Hartree-Fock exchange, a fact that has been confirmed through the comparison of experimental proton chemical shifts [81]. A detailed study of the delocalization error is done in Section 3.4 of this manuscript. The lowest-lying triplet displays a D_2 symmetry (HF) or a C_{2h} symmetry (CAM-B3LYP, B3LYP, and M06-2X). DFAs agree on the triplet [18]annulene being weakly antiaromatic, whereas HF predicts it to be rather nonaromatic.

Table 1. Aromaticity indices for $4n + 2$ annulenes calculated with HF, B3LYP, CAM-B3LYP, and M06-2X and the 6-311G(d,p) basis set. ^a I_{ring} values were too small for an accurate calculation of $I_{\text{ring}}^{1/N}$.

Structure	Multiplicity	Functional	FLU	$\overline{I_{\text{ring}}}^{1/N}$	BOA	BLA	$I_{\text{ring}}^{1/N}$	$ \text{AV}_{\text{min}} $
C ₆ H ₆	S	HF	0.000	0.624	0.000	0.000	0.597	10.25
		B3LYP	0.000	0.625	0.000	0.000	0.603	10.72
		CAM-B3LYP	0.000	0.628	0.000	0.000	0.603	10.71
		M06-2X	0.000	0.626	0.000	0.000	0.603	10.73
C ₆ H ₆	T	HF	0.024	0.393	0.246	0.089	0.341	0.39
		B3LYP	0.025	0.399	0.275	0.090	0.353	1.51
		CAM-B3LYP	0.025	0.408	0.276	0.091	0.363	1.20
		M06-2X	0.041	0.467	0.281	0.056	0.380	0.28
C ₁₀ H ₁₀ (twist)	S	HF	0.068	0.421	0.728	0.157	0.339	0.00
		B3LYP	0.052	0.480	0.639	0.128	0.322	0.03
		CAM-B3LYP	0.059	0.466	0.677	0.137	0.341	0.03
		M06-2X	0.058	0.463	0.670	0.136	0.325	0.05
C ₁₀ H ₁₀ (heart)	S	HF	0.065	0.436	0.712	0.153	0.380	0.01
		B3LYP	0.000	0.610	0.007	0.009	0.579	5.19
		CAM-B3LYP	0.000	0.614	0.009	0.010	0.579	5.13
		M06-2X	0.000	0.611	0.010	0.010	0.579	5.11
C ₁₀ H ₁₀ (naphthalene)	T	HF	0.030	0.470	0.364	0.085	0.353	0.14
		B3LYP	0.023	0.531	0.328	0.064	0.460	0.91
		CAM-B3LYP	0.027	0.524	0.364	0.072	0.446	0.68
		M06-2X	0.028	0.522	0.367	0.073	0.444	0.63
C ₁₀ H ₁₀ (twist)	T	HF	0.020	0.478	0.266	0.068	0.295	0.05
		B3LYP	0.020	0.517	0.305	0.066	0.352	0.08
		CAM-B3LYP	0.022	0.513	0.324	0.071	0.347	0.07
		M06-2X	0.022	0.511	0.328	0.072	0.337	0.10
C ₁₄ H ₁₄	S	HF	0.050	0.497	0.626	0.136	- ^a	0.49
		B3LYP	0.001	0.605	0.010	0.008	- ^a	4.24
		CAM-B3LYP	0.026	0.561	0.449	0.091	- ^a	1.80
		M06-2X	0.025	0.561	0.438	0.088	- ^a	1.89
C ₁₄ H ₁₄ (TS)	S	CAM-B3LYP	0.000	0.609	0.007	0.007	-	4.29
		M06-2X	0.001	0.606	0.007	0.007	- ^a	4.27
C ₁₄ H ₁₄	T	HF	0.021	0.502	0.282	0.069	- ^a	0.01
		B3LYP	0.017	0.554	0.302	0.060	- ^a	0.13
		CAM-B3LYP	0.023	0.544	0.348	0.071	- ^a	0.08
		M06-2X	0.022	0.544	0.349	0.071	- ^a	0.04
C ₁₈ H ₁₈	S	HF	0.049	0.504	0.616	0.133	0.472	0.57
		B3LYP	0.001	0.606	0.026	0.011	0.573	4.27
		CAM-B3LYP	0.026	0.563	0.446	0.090	0.530	1.80
		M06-2X	0.025	0.561	0.444	0.089	0.529	1.81
C ₁₈ H ₁₈ (TS)	S	CAM-B3LYP	0.001	0.609	0.022	0.010	0.572	4.29
		M06-2X	0.001	0.607	0.022	0.010	0.572	4.28
C ₁₈ H ₁₈	T	HF	0.018	0.514	0.257	0.060	0.411	0.12
		B3LYP	0.013	0.570	0.265	0.053	0.533	0.58
		CAM-B3LYP	0.019	0.559	0.324	0.066	0.513	0.30
		M06-2X	0.019	0.559	0.324	0.065	0.517	0.46

3.2.2. $4n$ Annulenes

The photochemical formation of $4n$ annulenes is very important in excited-state aromaticity [19]. Cyclobutadiene is often used as the paradigmatic example of an antiaromatic molecule following the $4n$ rule. Although (anti)aromaticity can be easily overestimated with a single-determinant wavefunction [82–84], cyclobutadiene is the molecule with the largest bond-length and bond-order alternation and all indicators of aromaticity clearly confirm its antiaromatic character. Baird was first to suggest that triplet $4n$ π -electron annulenes should be regarded as aromatic and confirm it through DRE calculations [17]. In particular, the DRE confirmed that triplet cyclobutadiene is an aromatic

molecule. A fact that is further substantiated by its symmetric D_{4h} geometry and the values of the aromaticity indices gathered in Table 2.

Unlike cyclobutadiene, cycloocta-1,3,5,7-tetraene (COT) is not a planar molecule in its ground state. COT shows a boat-like D_{2d} geometry that, although presents bond-length and bond-order alternation, is not a very antiaromatic molecule [16,85]. The aromaticity indices reveal that this molecule could be classified as mildly antiaromatic. Conversely, the lowest-lying triplet state of COT presents D_{8h} symmetry and values of the aromaticity indices that confirm the aromatic character anticipated by the Baird rule. Interestingly, the realization of planar triplet COT in some substituted annulenes has been studied as an acceleration path for the photochemical inversion of the ring [22].

In contrast to smaller annulenes, [12]annulene presents several energy minima in the potential energy surface, five of which lie within 5 kcal/mol according to CCSD(T) calculations [86]. The instability and the easy isomerization [87] of this species explain the difficulty in characterizing it experimentally. All DFAs and HF predict a CTCTCT (C_1) geometry with a large bond-order alternation, where C and T stand for the arrangement of C-C bonds that can be either cis (C) or trans (T). Nevertheless, the molecule presents very small AV_{\min} values that indicate a nonaromatic character. The lowest-lying triplet state of [12]annulene shows a very similar geometry in agreement with a CTCTCT arrangement of the atoms but corresponding to a CTCTCT (C_s) geometry, according to all DFAs. The HF lowest-lying triplet also presents a CTCTCT geometry (C_1) but it is severely distorted with respect to the latter one. Regardless of the method used, AV_{\min} value is small, prompting us to also classify the triplet state as a nonaromatic species.

As in the previous case, a large number of [16]annulene isomers have been found [88] and, therefore, this species also easily undergoes isomerization [87] even through quantum mechanical tunneling [89]. According to all the methods, the ground state structure can be classified as CTCTCTCT (S_4). Interestingly, there is another structure, which presents a distorted CTCTTCTT structure (C_1) lying 5-8 kcal/mol above the ground state structure. The lowest-lying triplet presents a conformation very close to the latter one. Although the singlet is less antiaromatic than COT or cyclobutadiene, we find that both S_4 and C_1 present a similar character and are more antiaromatic than [12]annulene. Therefore, [16]annulene could be classified as weakly antiaromatic. Likewise, the triplet provides values of the indices that indicate a more aromatic character than [12]annulene triplet. Although AV_{\min} values oscillate between 0.35 and 1.16, these values indicate a mild aromatic character in between triplet [12]annulene and triplet cyclobutadiene, which agrees with the fact that this molecule displays a more symmetric structure (C_s) than its singlet counterpart (C_1).

3.3. Aromaticity from DFAs

The HMO cannot take into account the geometrical relaxation from a planar structure (permitting an optimal overlap of p orbitals) and, therefore, the results obtained in the Section 3.1 are upper bounds to aromaticity and antiaromaticity in annulenes. In this section, we will consider the optimization of several singlet and triplet annulenes and how it affects the aromaticity of these compounds. As an improvement over HMO results, we will calculate an approximate version of I_{ring} that consists in using only the two-center bond orders of bonded atoms to estimate the N -center delocalization. In particular, we will employ the equivalent of Equation (8) in the framework of quantum mechanics. To this end, we will take $\delta(A, B)$ and subtract 1.00 to (approximately) remove the sigma contribution to the C-C bond, and multiply all resulting DIs of the bonds around the perimeter of the ring,

$$\overline{I_{\text{ring}}}(\mathcal{A}) = \sqrt{(\delta(A_1, A_2) - 1) (\delta(A_2, A_3) - 1) \dots (\delta(A_n, A_1) - 1)}, \quad (10)$$

where we have taken the square root to account for the fact that at the HMO level the DI corresponds to the square of the Hückel bond-order [74]. One can consider the latter as a rough approximation that bridges the HMO definition (Equation (8)) and the actual I_{ring} value (Equation (5)). We have collected the results of $\overline{I_{\text{ring}}}^{1/N}$ in Figure 3.

Table 2. Aromaticity indices for the studied $4n$ annulenes calculated with HF, B3LYP, CAM-B3LYP, and M06-2X and the 6-311G(d,p) basis set. ^a I_{ring} values were too small for an accurate calculation of $I_{\text{ring}}^{1/N}$. ^b AV_{min} cannot be calculated for rings with less than six members.

Structure	Multiplicity	Method	FLU	$\overline{I_{\text{ring}}}^{1/N}$	BOA	BLA	$I_{\text{ring}}^{1/N}$	$ AV_{\text{min}} $
C ₄ H ₄	S	HF	0.101	0.391	0.888	0.249	0.262	- ^b
		B3LYP	0.104	0.416	0.900	0.247	0.266	- ^b
		CAM-B3LYP	0.103	0.398	0.898	0.245	0.264	- ^b
		M06-2X	0.103	0.405	0.898	0.242	0.268	- ^b
C ₄ H ₄	T	HF	0.010	0.507	0.000	0.000	0.433	- ^b
		B3LYP	0.012	0.499	0.000	0.000	0.440	- ^b
		CAM-B3LYP	0.011	0.504	0.000	0.000	0.439	- ^b
		M06-2X	0.011	0.505	0.000	0.000	0.438	- ^b
C ₈ H ₈	S	HF	0.067	0.436	0.726	0.156	0.406	0.30
		B3LYP	0.056	0.477	0.664	0.134	0.441	0.72
		CAM-B3LYP	0.061	0.468	0.693	0.140	0.428	0.52
		M06-2X	0.062	0.460	0.694	0.141	0.427	0.51
C ₈ H ₈	T	HF	0.001	0.590	0.000	0.000	0.534	4.07
		B3LYP	0.001	0.589	0.000	0.000	0.540	4.31
		CAM-B3LYP	0.001	0.593	0.000	0.000	0.539	4.29
		M06-2X	0.001	0.591	0.000	0.000	0.539	4.29
C ₁₂ H ₁₂	S	HF	0.063	0.445	0.698	0.153	- ^a	0.04
		B3LYP	0.042	0.511	0.565	0.115	- ^a	0.01
		CAM-B3LYP	0.050	0.494	0.624	0.128	- ^a	0.02
		M06-2X	0.050	0.488	0.624	0.128	- ^a	0.06
C ₁₂ H ₁₂	T	HF	0.021	0.487	0.280	0.067	- ^a	0.07
		B3LYP	0.002	0.590	0.033	0.012	- ^a	0.07
		CAM-B3LYP	0.015	0.562	0.288	0.056	- ^a	0.21
		M06-2X	0.008	0.577	0.208	0.039	- ^a	0.13
C ₁₆ H ₁₆ (S ₄)	S	HF	0.054	0.486	0.651	0.139	0.440	0.33
		B3LYP	0.029	0.551	0.476	0.095	0.513	0.96
		CAM-B3LYP	0.041	0.529	0.564	0.113	0.484	0.64
		M06-2X	0.040	0.526	0.562	0.113	0.484	0.63
C ₁₆ H ₁₆ (C ₁)	S	HF	0.053	0.488	0.643	0.139	0.452	0.25
		B3LYP	0.029	0.548	0.474	0.096	0.512	0.78
		CAM-B3LYP	0.040	0.530	0.555	0.113	0.487	0.55
		M06-2X	0.039	0.526	0.553	0.112	0.487	0.58
C ₁₆ H ₁₆ (C _s)	T	HF	0.001	0.598	0.013	0.005	- ^a	1.08
		B3LYP	0.002	0.596	0.057	0.013	- ^a	1.16
		CAM-B3LYP	0.015	0.568	0.294	0.059	- ^a	0.35
		M06-2X	0.011	0.576	0.252	0.050	- ^a	0.74

The results show some differences with respect to the HMO values we have shown earlier. $4n + 2$ singlet compounds show a similar trend to the HMO results except for [10]annulene, which exhibits a smaller aromaticity than expected. This molecule undergoes important geometrical distortions that disrupt the overlap of p orbitals and causes the apparent loss of aromaticity. $4n$ singlets are expected to be antiaromatic, as is confirmed by the large BOA values (see Tables 1 and 2), and they become less and less antiaromatic as they increase the ring size (see the increasing $\overline{I_{\text{ring}}}^{1/N}$ values of Figure 3). $4n + 2$ triplet annulenes follow a very similar trend in agreement with Baird's rule. Finally, we examine the $4n$ triplet annulenes that are expected to be aromatic and for which there is no clear trend. On one hand, COT, which displays a planar structure, is actually among the most aromatic compounds, even more aromatic than cyclobutadiene in its lowest-lying triplet state, which actually shows the smallest value among the molecules that are expected to be aromatic. On the other hand, neither [12] nor [16]annulene present a planar structure and, therefore, they exhibit larger BOA values, suggesting

that these molecules are rather nonaromatic or slightly antiaromatic. Interestingly, all the aromaticity trends are similar to those found for pure HMO calculations for $4n + 2$ annulenes and $4n$ singlets with the only mentioned exception of [10]annulene.

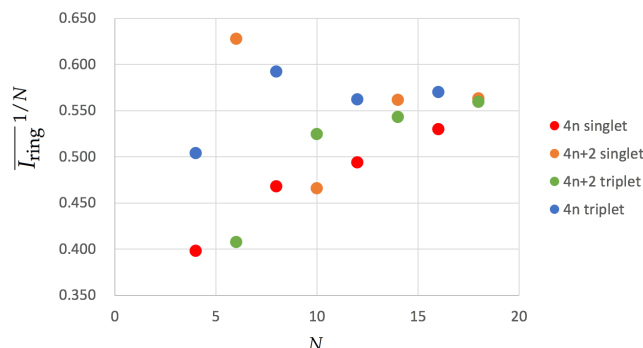


Figure 3. Values of $\overline{I}_{\text{ring}}^{1/N}$ for the annulenes series in terms of the number of C atoms (N) for the lowest-lying singlets and triplets. The species have been divided according to the number of electrons ($4n$ and $4n + 2$) and the spin multiplicity (singlet and triplet). Calculations were performed with CAM-B3LYP/6-311G(d,p).

Tables 1 and 2 also include the actual values of $I_{\text{ring}}^{1/N}$ but we have not discussed them because they mostly corroborate the trends we have found with $\overline{I}_{\text{ring}}^{1/N}$ and some of the values for large annulenes could not be obtained with enough precision. This is one of the main shortcomings of I_{ring} for large rings [55], the values become so small that they conflict with the numerical precision of the calculation and, consequently, we cannot obtain a reliable normalization ($I_{\text{ring}}^{1/N}$) which permits the comparison among rings of different sizes.

In order to remedy this problem, AV_{min} was recently designed [55]. AV_{min} values for the annulenes series are collected in Figure 4. Although the trends are not so clear as in HMO calculations or the approximate account of aromaticity with $\overline{I}_{\text{ring}}^{1/N}$, the picture we can extract from AV_{min} does not differ entirely from that we obtained from $\overline{I}_{\text{ring}}^{1/N}$. The four most aromatic molecules are the same according to both indices and each single-triplet pair shows the same order of aromaticity, e.g., singlet benzene is more aromatic than triplet benzene. The only apparent exception to this rule is [10]annulene that has a larger AV_{min} value for the lowest-lying triplet than for the ground state singlet. The latter is due to the fact that the ground state configuration of [10]annulene is found to be nonaromatic (the second lowest-lying structure, the *heart* configuration, is actually quite aromatic) whereas the triplet configuration is antiaromatic.

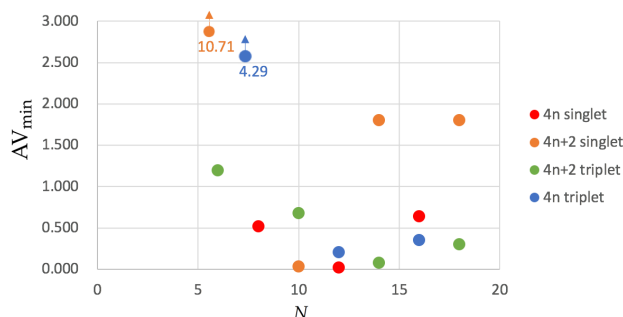


Figure 4. Values of AV_{min} for the annulenes series (lowest-lying singlets and triplets) in terms of the number of C atoms (N). The species have been divided according to the number of electrons ($4n$ and $4n + 2$) and the spin multiplicity (singlet and triplet). Calculations were performed with CAM-B3LYP/6-311G(d,p).

Finally, we find that FLU, BOA, and BLA give a similar qualitative trend to $\overline{I}_{\text{ring}}^{1/N}$ (see Tables 1 and 2, and also the Supplementary Material) with the exception of large $4n + 2$ annulenes ([14]annulene and [18]annulene) that are found to be more aromatic in their triplet state than in their ground state. One should bear in mind that these indices are based on pairwise interactions (FLU is also based on fixed ground-state aromatic references) and they are not as reliable as indices based on multicenter calculations [36].

3.4. The Delocalization Error in DFAs

DFAs suffer the so-called delocalization error [90–92], which tends to give delocalized electronic structures. This is the exact opposite behavior of HF, which tends to overestimate the localization of the electronic structures. DFAs with a low percentage of HF exchange are more prone to delocalization errors. This effect has been observed in conjugate systems [93] and aromatic systems [40,81,94,95] including singlet annulenes [81]. Recently, Contreras-García, et al. [96] have suggested that the exact result is often bracketed between two extreme situations, the highly localized one (HF) and a highly delocalized one (LDA, which does not include HF exchange). They have used this result to construct error bars for the calculation of some solid-state properties. Likewise, Burke, et al. [97] have defined the sensitivity of DFAs to the density as the energy difference between DFA calculations from LDA and HF densities.

In this section, we investigate how the delocalization error affects the aromaticity measures in the studied annulene series through the analysis of $\overline{I}_{\text{ring}}^{1/N}$ calculated with four methods that use a different amount of HF exchange. In our study, LDA is ruled out because it is not reliable for gas-phase calculations [98] and B3LYP is used as the most *delocalizing* method (includes 19% of HF exchange). As the most *localizing* method we employ HF (that obviously uses 100% of HF exchange), and, as DFA with a large percentage of HF exchange, we have selected M06-2X (54%) and a range-separation functional [91], CAM-B3LYP, which presents a variable amount of HF exchange that goes from 19% at short ranges to 65% at large interelectronic separations.

$\overline{I}_{\text{ring}}^{1/N}$ values for different methods are collected in Figure 5. Our results confirm that in the large majority of cases B3LYP and HF are giving the most and the less aromatic species, respectively, among the DFA studied. In some cases (see, singlet benzene, triplet cyclobutadiene or triplet COT) there are no large differences among the DFAs because these species do not suffer from the delocalization error. However, in many other cases (see $4n + 2$ singlet annulenes larger than benzene) B3LYP clearly overestimates electron delocalization, sometimes even favoring a different geometrical arrangement of the atoms in the ring that permits larger electron delocalization (see Section 3.2). As expected, HF tends to overestimate electron localization whereas CAM-B3LYP and M06-2X provide very similar results lying between HF and B3LYP values. There is only two exceptions to this rule: the triplet states of benzene and [16]annulene. Unlike other DFAs and HF, the M06-2X geometry optimization of triplet benzene leads to a non-planar structure that does not correspond to the AQ structure [17] and, therefore, it is not as antiaromatic as one would expect. A careful examination of the potential energy surface of the triplet state of benzene confirms that M06-2X does not identify the AQ conformation as a minimum of energy at this level of theory. In the case of [16]annulene, the exception is that HF $\overline{I}_{\text{ring}}^{1/N}$ value is actually larger than that of CAM-B3LYP or M06-2X because, according to HF, the structure is more planar than predicted by these DFAs.

Interestingly, $4n + 2$ singlet molecules (with the exception of benzene) and $4n$ singlets tend to suffer the most from electron delocalization errors, whereas $4n + 2$ triplet molecules barely exhibit differences between B3LYP and other DFAs with higher percentage of HF exchange. The fact that M06-2X and CAM-B3LYP present very similar values for most molecules corroborates that it is actually the long-range part of Hartree-Fock exchange the one which is relevant to decrease the delocalization error [40]. In this sense, we recommend the use of a range-separation functional, such as CAM-B3LYP, to study aromatic and antiaromatic compounds.

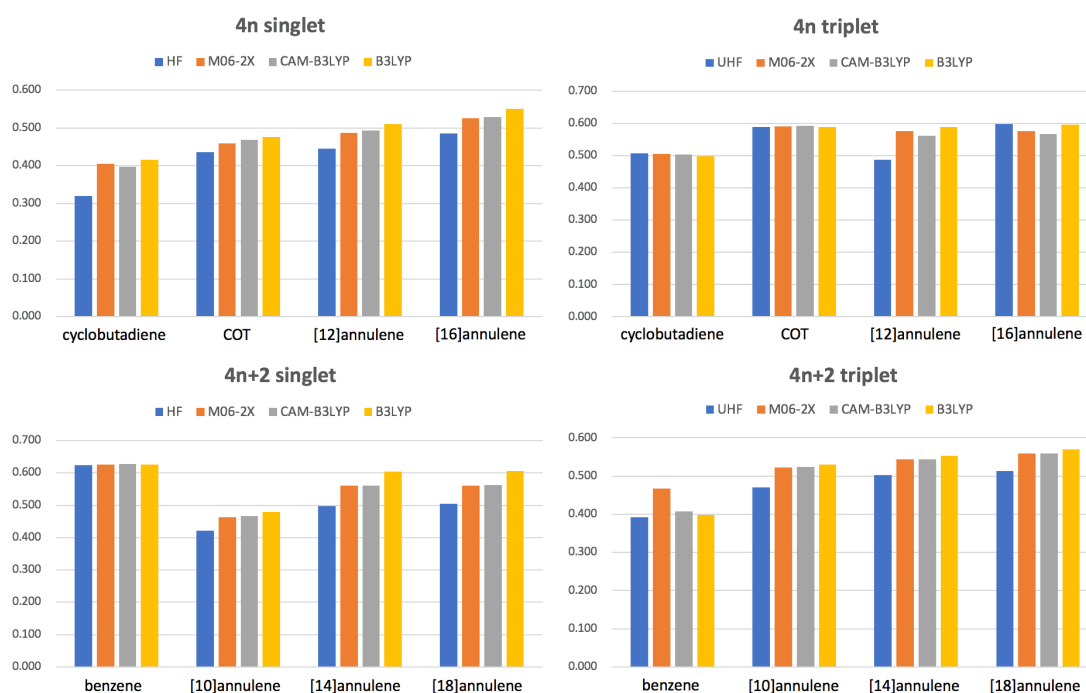


Figure 5. Values of $\overline{I_{\text{ring}}}^{1/N}$ for the lowest-lying states of the studied annulenes obtained with methods using a different percentage of Hartree Fock (HF) exchange: HF (100%), M06-2X (54%), CAM-B3LYP (19–65%) and B3LYP (19%).

4. Materials and Methods

The singlet ground state and the first triplet excited state of all the studied structures have been fully characterized. The optimizations have been performed with the Gaussian16 software package [99] using B3LYP [100,101], CAM-B3LYP [102], M06-2X [103] DFAs, and HF in combination with the 6-311G(d,p) basis set [104]. The harmonic vibrational frequencies were calculated at the corresponding level of theory in order to verify the nature of the stationary points of their potential energy surface (minima or transition states).

The calculation of the electronic aromaticity indices (AV_{1245} , AV_{min} , BOA and FLU) uses a QTAIM atomic partition [105] performed by the AIMAll software [106]. The AOM resulting from the QTAIM partition and the molecular geometries are the input for the in-house ESI-3D program [27,31,107], which provides AV_{1245} [55], AV_{min} [56], BLA, BOA, DIs [29,30], FLU [27], HOMA [33] (included in the Supplementary Material), I_{ring} [42], $\overline{I_{\text{ring}}}$ and MCI [43] values. The numerical accuracy of the QTAIM calculations has been assessed using two criteria: (i) The integration of the Laplacian of the electron density ($\nabla^2\rho(r)$) within an atomic basin must be close to zero; (ii) the number of electrons in a molecule must be equal to the sum of all the electron populations of the molecule, and also equal to the sum of all the localization indices and half of the delocalization indices in the molecule. For all atomic calculations, integrated absolute values of $\nabla^2\rho(r)$ were always lower than 0.001 a.u. For all molecules, errors in the calculated number of electrons were always lower than 0.01 a.u. From our experience, these errors provide sufficient accuracy for all the indices here calculated except for the *normalized* multicenter indices of large rings, which require a numerical precision of the AOM well beyond the accuracy that one can obtain with AIMAll or any other similar software available in the literature. For the latter and other reasons commented in Ref. [55], multicenter indices (MCI and I_{ring}) cannot be used in large rings.

We have employed Mathematica [108] to perform all Hückel calculations, fittings and extrapolations presented in this manuscript.

5. Conclusions

In this paper, we have studied how the Hückel and Baird rules fade away in cyclic polyenes. According to pure HMO calculations and the seminal Baird study [17], antiaromatic annulenes lose their antiaromatic character at the same speed as the ring size increases, regardless of their multiplicity. However, a two-resonance parameter HMO method, permitting bond-order alternation, shows that the antiaromaticity of $4n$ singlets decreases more rapidly with the ring size. The conclusion is far less clear from calculations that consider the geometry relaxation because the potential energy surface of annulenes with more than eight carbon atoms often shows several configurations close in energy that display disparate aromatic characters. Nevertheless, density functional approximations reveal that the rules fade away much more quickly than it would be expected from the HMO method; they just do not follow a smooth trend.

The study of the level of theory employed in the calculation of annulenes reveals a clear tendency of density functional approximations with a low-percentage of HF exchange at long ranges to exhibit delocalization errors that lead to the overestimation of the aromatic character of the molecule and sometimes even to wrong geometries. Molecules with large ring structures are more prone to this kind of errors. These results are in line with previous findings [40,81,94] and suggest caution in choosing an appropriate density functional approximation to study aromatic and antiaromatic molecules. In particular, we recommend the use of a range-separation density functional approximation such as CAM-B3LYP.

Supplementary Materials: The Cartesian coordinates of the molecules as well as full tables and supplementary graphics are available online at <http://www.mdpi.com/1420-3049/25/3/711/s1>.

Author Contributions: Conceptualization, E.M.; methodology, E.R.-C. and E.M.; validation, E.R.-C., M.T.-S. and E.M.; formal analysis, I.C.-R., E.R.-C., M.T.-S. and E.M.; data curation, I.C.-R., E.R.-C., M.T.-S. and E.M.; writing—original draft preparation, E.M.; writing—review and editing, I.C.-R., E.R.-C., M.T.-S. and E.M.; supervision, E.R.-C., M.T.-S. and E.M.; funding acquisition, E.R.-C., M.T.-S. and E.M. All authors have read and agreed to the published version of the manuscript.

Funding: This research was funded by Spanish MINECO grant numbers PGC2018-098212-B-C21, CTQ2016-80375-P, EUIN2017-88605 and EUR2019-103825, the Basque Government/Eusko Jaurlaritza (GV/EJ) grant numbers IT1346-19, IT1254-19, PIBA19-0004, and 2019-CIEN-000092-01, and the doctoral grant PRE_2016_1_0159. E.R.C. acknowledges funding from the Juan de la Cierva program IJCI-2017-34658.

Acknowledgments: The authors acknowledge the computational resources and technical and human support provided by DIPC and the SGI/IZO-SGIker UPV/EHU.

Conflicts of Interest: The authors declare no conflict of interest.

Abbreviations

The following abbreviations are used in this manuscript:

AOM	Atomic overlaps matrix
AV1245	Aromaticity index for large rings [55]
AV _{min}	Minimal value of 12-45 delocalizations [56]
BLA	Bond-length alternation
BOA	Bond-order alternation
DFA	Density Functional Approximation
DI	Delocalization index [28]
FLU	Fluctuation aromaticity index [27]
HF	Hartree-Fock
HMO	Hückel Molecular Orbital
HOMA	Harmonic Oscillator Model of Aromaticity [33]

LDA	Local density approximation [109]
MCI	Multicenter index [43]
RE	Resonance energy
TREPE	Topological resonance energy per π electron
I_{ring}	Giambiagi's multicenter index [42]
\overline{I}_{ring}	Approximation to I_{ring} (Equation (8))

References

1. von Ragué Schleyer, P.; Jiao, H. What is aromaticity. *Pure Appl. Chem.* **1996**, *68*, 209–218.
2. Feixas, F.; Matito, E.; Poater, J.; Solà, M. Quantifying aromaticity with electron delocalisation measures. *Chem. Soc. Rev.* **2015**, *44*, 6389–6646. [[CrossRef](#)] [[PubMed](#)]
3. Solà, M. Why aromaticity is a suspicious concept? Why? *Front. Chem.* **2017**, *5*, 22. [[CrossRef](#)] [[PubMed](#)]
4. Boldyrev, A.I.; Wang, L.S. All-metal aromaticity and antiaromaticity. *Chem. Rev.* **2005**, *105*, 3716–3757. [[CrossRef](#)]
5. Feixas, F.; Matito, E.; Poater, J.; Solà, M. Metalloaromaticity. *WIREs Comput. Mol. Sci.* **2013**, *3*, 105–122. [[CrossRef](#)]
6. Wade, K. The structural significance of the number of skeletal bonding electron-pairs in carboranes, the higher boranes and borane anions, and various transition-metal carbonyl cluster compounds. *J. Chem. Soc. D: Chem. Commun.* **1971**, 792–793. [[CrossRef](#)]
7. Mingos, D.M. Polyhedral Skeletal Electron Pair Approach. *Acc. Chem. Res.* **1984**, *17*, 311–319. [[CrossRef](#)]
8. Hirsch, A.; Chen, Z.; Jiao, H. Spherical aromaticity in Ih symmetrical fullerenes: the $2(N + 1)2$ rule. *Angew. Chem. Int. Ed.* **2000**, *39*, 3915–3917. [[CrossRef](#)]
9. Poater, J.; Solà, M. Open-shell spherical aromaticity: The $2N^2 + 2N + 1$ (with $S = N + 1/2$) rule. *Chem. Commun.* **2011**, *47*, 11647–11649. [[CrossRef](#)]
10. Poater, J.; Solà, M. Open-shell jellium aromaticity in metal clusters. *Chem. Commun.* **2019**, *55*, 5559–5562. [[CrossRef](#)]
11. Feixas, F.; Matito, E.; Poater, J.; Solà, M. Rules of aromaticity. In *Applications of Topological Methods in Molecular Chemistry*; Springer: Cham, Switzerland, 2016; pp. 321–335.
12. Hückel, E. Quantentheoretische Beiträge zum Benzolproblem, I: Die Elektronenkonfiguration des Benzols und verwandter Verbindungen. *Z. Physik* **1931**, *70*, 104–186. [[CrossRef](#)]
13. Hückel, E. Quantentheoretische Beiträge zum Benzolproblem, II: Quantentheorie der induzierten Polaritäten. *Z. Physik* **1931**, *72*, 310–337. [[CrossRef](#)]
14. Hückel, E. Beiträge zum Problem der aromatischen und ungesättigten Verbindungen. III. *Z. Physik* **1932**, *76*, 628–648. [[CrossRef](#)]
15. Hückel, E. Grundzüge der Theorie ungesättigter und aromatischer Verbindungen. *Z. Elektrochem.* **1937**, *43*, 752–788, 827–849.
16. Gellini, C.; Salvi, P.R. Structures of annulenes and model annulene systems in the ground and lowest excited states. *Symmetry* **2010**, *2*, 1846–1924. [[CrossRef](#)]
17. Baird, N.C. Quantum organic photochemistry. II. Resonance and aromaticity in the lowest $3\pi\pi^*$ state of cyclic hydrocarbons. *J. Am. Chem. Soc.* **1972**, *94*, 4941–4948. [[CrossRef](#)]
18. Aihara, J.I. Aromaticity-based theory of pericyclic reactions. *Bull. Chem. Soc. Jpn.* **1978**, *51*, 1788–1792. [[CrossRef](#)]
19. Ottosson, H. Organic photochemistry: exciting excited-state aromaticity. *Nat. Chem.* **2012**, *4*, 969–971. [[CrossRef](#)]
20. Streifel, B.C.; Zafra, J.L.; Espejo, G.L.; Gómez-García, C.J.; Casado, J.; Tovar, J.D. An Unusually Small Singlet–Triplet Gap in a Quinoidal 1, 6-Methano [10]annulene Resulting from Baird's $4n\pi$ -Electron Triplet Stabilization. *Angew. Chem. Int. Ed.* **2015**, *54*, 5888–5893. [[CrossRef](#)]
21. Jorner, K.; Feixas, F.; Ayub, R.; Lindh, R.; Solà, M.; Ottosson, H. Analysis of a compound class with triplet states stabilized by potentially Baird aromatic [10]annulenylic dicationic rings. *Chem. Eur. J.* **2016**, *22*, 2793–2800. [[CrossRef](#)]

22. Ueda, M.; Jorner, K.; Sung, Y.M.; Mori, T.; Xiao, Q.; Kim, D.; Ottosson, H.; Aida, T.; Itoh, Y. Energetics of Baird aromaticity supported by inversion of photoexcited chiral $[4n]$ annulene derivatives. *Nat. Chem.* **2017**, *8*, 346–354. [[CrossRef](#)] [[PubMed](#)]
23. Peeks, M.D.; Claridge, T.D.; Anderson, H.L. Aromatic and antiaromatic ring currents in a molecular nanoring. *Nature* **2017**, *541*, 200–205. [[CrossRef](#)] [[PubMed](#)]
24. Choi, C.H.; Kertesz, M. Bond length alternation and aromaticity in large annulenes. *J. Chem. Phys.* **1998**, *108*, 6681–6688. [[CrossRef](#)]
25. Soncini, A.; Fowler, P.W.; Jenneskens, L.W. Ring currents in large $[4n + 2]$ -annulenes. *Phys. Chem. Chem. Phys.* **2004**, *6*, 277–284. [[CrossRef](#)]
26. Wannere, C.S.; Schleyer, P.v.R. How Aromatic Are Large $(4n + 2) \pi$ Annulenes? *Org. Lett.* **2003**, *5*, 865–868. [[CrossRef](#)]
27. Matito, E.; Duran, M.; Solà, M. The aromatic fluctuation index (FLU): A new aromaticity index based on electron delocalization. *J. Chem. Phys.* **2005**, *122*, 014109; Erratum in **2006**, *125*, 059901. [[CrossRef](#)]
28. Bader, R.F.W.; Stephens, M.E. Fluctuation and correlation of electrons in molecular systems. *Chem. Phys. Lett.* **1974**, *26*, 445–449. [[CrossRef](#)]
29. Bader, R.F.W.; Stephens, M.E. Spatial localization of the electronic pair and number distributions in molecules. *J. Am. Chem. Soc.* **1975**, *97*, 7391–7399. [[CrossRef](#)]
30. Fradera, X.; Austen, M.A.; Bader, R.F.W. The Lewis Model and Beyond. *J. Phys. Chem. A* **1999**, *103*, 304–314. [[CrossRef](#)]
31. Matito, E.; Solà, M.; Salvador, P.; Duran, M. Electron sharing indexes at the correlated level. Application to aromaticity calculations. *Faraday Discuss.* **2007**, *135*, 325–345. [[CrossRef](#)]
32. Mayer, I. Charge, Bond Order, and Valence in the ab initio SCF Theory. *Chem. Phys. Lett.* **1983**, *97*, 270–274. [[CrossRef](#)]
33. Kruszewski, J.; Krygowski, T.M. Definition of aromaticity basing on the harmonic oscillator model. *Tetrahedron Lett.* **1972**, *13*, 3839–3842. [[CrossRef](#)]
34. Krygowski, T.M.; Cyranski, M.K. Structural aspects of aromaticity. *Chem. Rev.* **2001**, *101*, 1385–1420. [[CrossRef](#)] [[PubMed](#)]
35. Matito, E.; Poater, J.; Duran, M.; Solà, M. An analysis of the changes in aromaticity and planarity along the reaction path of the simplest Diels–Alder reaction. Exploring the validity of different indicators of aromaticity. *J. Mol. Struct. (Theochem)* **2005**, *727*, 165–171. [[CrossRef](#)]
36. Feixas, F.; Matito, E.; Poater, J.; Solà, M. On the performance of some aromaticity indices: A critical assessment using a test set. *J. Comput. Chem.* **2008**, *29*, 1543–1554. [[CrossRef](#)]
37. Fonseca Guerra, C.; Handgraaf, J.W.; Baerends, E.J.; Bickelhaupt, F.M. Voronoi deformation density (VDD) charges: Assessment of the Mulliken, Bader, Hirshfeld, Weinhold, and VDD methods for charge analysis. *J. Comput. Chem.* **2004**, *25*, 189–210. [[CrossRef](#)]
38. Matito, E.; Poater, J.; Solà, M.; Duran, M.; Salvador, P. Comparison of the AIM Delocalization Index and the Mayer and Fuzzy Atom Bond Orders. *J. Phys. Chem. A* **2005**, *109*, 9904–9910. [[CrossRef](#)]
39. Matito, E.; Solà, M.; Duran, M.; Salvador, P. Aromaticity Measures from Fuzzy-Atom Bond Orders (FBO). The Aromatic Fluctuation (FLU) and the para-Delocalization (PDI) Indexes. *J. Phys. Chem. A* **2006**, *110*, 5108–5113. [[CrossRef](#)]
40. Casademont-Reig, I.; Woller, T.; Contreras-García, J.; Alonso, M.; Torrent-Sucarrat, M.; Matito, E. New electron delocalization tools to describe the aromaticity in porphyrinoids. *Phys. Chem. Chem. Phys.* **2018**, *20*, 2787–2796. [[CrossRef](#)]
41. Giambiagi, M.; de Giambiagi, M.S.; Mundim, K.C. Definition of a multicenter bond index. *Struct. Chem.* **1990**, *1*, 423–427. [[CrossRef](#)]
42. Giambiagi, M.; de Giambiagi, M.S.; dos Santos Silva, C.D.; de Figueiredo, A.P. Multicenter bond indices as a measure of aromaticity. *Phys. Chem. Chem. Phys.* **2000**, *2*, 3381–3392. [[CrossRef](#)]
43. Bultinck, P.; Ponec, R.; Van Damme, S. Multicenter bond indices as a new measure of aromaticity in polycyclic aromatic hydrocarbons. *J. Phys. Org. Chem.* **2005**, *18*, 706–718. [[CrossRef](#)]
44. Cioslowski, J.; Matito, E.; Solà, M. Properties of Aromaticity Indices Based on the One-electron Density Matrix. *J. Phys. Chem. A* **2007**, *111*, 6521–6525. [[CrossRef](#)] [[PubMed](#)]

45. Feixas, F.; Jiménez-Halla, J.; Matito, E.; Poater, J.; Solà, M. A Test to Evaluate the Performance of Aromaticity Descriptors in All-Metal and Semimetal Clusters. An Appraisal of Electronic and Magnetic Indicators of Aromaticity. *J. Chem. Theory Comput.* **2010**, *6*, 1118–1130. [[CrossRef](#)]
46. Feixas, F.; Vandebussche, J.; Bultinck, P.; Matito, E.; Solà, M. Electron delocalization and aromaticity in low-lying excited states of archetypal organic compounds. *Phys. Chem. Chem. Phys.* **2011**, *13*, 20690–20703. [[CrossRef](#)]
47. Mercero, J.M.; Matito, E.; Ruipérez, F.; Infante, I.; Lopez, X.; Ugalde, J.M. The Electronic Structure of the Al_3^- Anion: Is it Aromatic? *Chem. Eur. J.* **2015**, *21*, 9610–9614. [[CrossRef](#)]
48. Fortenberry, R.C.; Novak, C.M.; Layfield, J.P.; Matito, E.; Lee, T.J. Overcoming the Failure of Correlation for Out-of-Plane Motions in a Simple Aromatic: Rovibrational Quantum Chemical Analysis of $c-C_3H_2$. *J. Chem. Theory Comput.* **2018**, *14*, 2155–2164. [[CrossRef](#)]
49. Grande-Aztatzi, R.; Mercero, J.M.; Matito, E.; Frenking, G.; Ugalde, J.M. The aromaticity of dicupra [10]annulenes. *Phys. Chem. Chem. Phys.* **2017**, *19*, 9669–9675. [[CrossRef](#)]
50. López, R.V.; Faza, O.N.; Matito, E.; López, C.S. Cycloreversion of the CO_2 trimer: A paradigmatic pseudopericyclic [2+2+2] cycloaddition reaction. *Org. Biomol. Chem.* **2017**, *15*, 435–441. [[CrossRef](#)]
51. Popov, I.A.; Pan, F.X.; You, X.R.; Li, L.J.; Matito, E.; Liu, C.; Zhai, H.J.; Sun, Z.M.; Boldyrev, A.I. Peculiar All-Metal σ -Aromaticity of the $[Au_2Sb_{16}]^{4-}$ Anion in the Solid State. *Angew. Chem. Int. Ed.* **2016**, *128*, 15570–15572. [[CrossRef](#)]
52. Min, X.; Popov, I.A.; Pan, F.X.; Li, L.J.; Matito, E.; Sun, Z.M.; Wang, L.S.; Boldyrev, A.I. All-Metal Antiaromaticity in Sb_4 -Type Lanthanocene Anions. *Angew. Chem. Int. Ed.* **2016**, *55*, 5531–5535. [[CrossRef](#)] [[PubMed](#)]
53. Jiménez-Halla, J.O.C.; Matito, E.; Solà, M.; Braunschweig, H.; Hörl, C.; Krummenacher, I.; Wahler, J. A theoretical study of the aromaticity in neutral and anionic borole compounds. *Dalton Trans.* **2015**, *44*, 6740–6747. [[CrossRef](#)] [[PubMed](#)]
54. Castro, A.C.; Osorio, E.; Cabellos, J.L.; Cerpa, E.; Matito, E.; Solà, M.; Swart, M.; Merino, G. Exploring the Potential Energy Surface of E_2P_4 Clusters (E= Group 13 Element): The Quest for Inverse Carbon-Free Sandwiches. *Chem. Eur. J.* **2014**, *20*, 4583–4590. [[CrossRef](#)] [[PubMed](#)]
55. Matito, E. Electronic Aromaticity Index for Large Rings. *Phys. Chem. Chem. Phys.* **2016**, *18*, 11839–11846. [[CrossRef](#)] [[PubMed](#)]
56. García-Fernández, C.; Sierda, E.; Abadia, M.; Bugenhagen, B.E.C.; Proscenc, M.H.; Wiesendanger, R.; Bazarnik, M.; Ortega, J.E.; Brede, J.; Matito, E.; et al. Exploring the Relation Between Intramolecular Conjugation and Band Dispersion in One-Dimensional Polymers. *J. Phys. Chem. C* **2017**, *121*, 27118–27125. [[CrossRef](#)]
57. Gutman, I.; Milun, M.; Trinajstić, N. Graph theory and molecular orbitals. 19. Nonparametric resonance energies of arbitrary conjugated systems. *J. Am. Chem. Soc.* **1977**, *99*, 1692–1704. [[CrossRef](#)]
58. Feixas, F.; Matito, E.; Solà, M.; Poater, J. Analysis of Hückel's $[4n+2]$ Rule through Electronic Delocalization Measures. *J. Phys. Chem. A* **2008**, *112*, 13231–13238. [[CrossRef](#)]
59. Feixas, F.; Matito, E.; Solà, M.; Poater, J. Patterns of π -electron delocalization in aromatic and antiaromatic organic compounds in the light of Hückel's $4n+2$ rule. *Phys. Chem. Chem. Phys.* **2010**, *12*, 7126–7137. [[CrossRef](#)]
60. Li, X.; Kuznetsov, A.E.; Zhang, H.F.; Boldyrev, A.I.; Wang, L.S. Observation of all-metal aromatic molecules. *Science* **2001**, *291*, 859–861. [[CrossRef](#)]
61. Jiménez-Halla, J.O.C.; Matito, E.; Blancafort, L.; Robles, J.; Solà, M. Tuning aromaticity in trigonal alkaline earth metal clusters and their alkali metal salts. *J. Comput. Chem.* **2009**, *30*, 2764–2776. [[CrossRef](#)]
62. Garcia-Borràs, M.; Osuna, S.; Swart, M.; Luis, J.M.; Solà, M. Maximum aromaticity as a guiding principle for the most suitable hosting cages in endohedral metallofullerenes. *Angew. Chem. Int. Ed.* **2013**, *52*, 9275–9278. [[CrossRef](#)]
63. Lu, X.; Chen, Z. Curved π -conjugation, aromaticity, and the related chemistry of small fullerenes. *Chem. Rev.* **2005**, *105*, 3643–3696. [[CrossRef](#)]
64. Osuka, A.; Saito, S. Expanded porphyrins and aromaticity. *Chem. Commun.* **2011**, *47*, 4330–4339. [[CrossRef](#)] [[PubMed](#)]
65. Feixas, F.; Solà, M.; Swart, M. Chemical bonding and aromaticity in metalloporphyrins 1, 2. *Can. J. Chem.* **2009**, *87*, 1063–1073. [[CrossRef](#)]

66. Sung, Y.M.; Oh, J.; Cha, W.Y.; Kim, W.; Lim, J.M.; Yoon, M.C.; Kim, D. Control and switching of aromaticity in various all-aza-expanded porphyrins: spectroscopic and theoretical analyses. *Chem. Rev.* **2017**, *117*, 2257–2312. [[CrossRef](#)] [[PubMed](#)]
67. Tanaka, T.; Osuka, A. Conjugated porphyrin arrays: synthesis, properties and applications for functional materials. *Chem. Soc. Rev.* **2015**, *44*, 943–969. [[CrossRef](#)] [[PubMed](#)]
68. Stępień, M.; Latos-Grażyński, L.; Sprutta, N.; Chwalisz, P.; Szterenber, L. Expanded porphyrin with a split personality: a Hückel–Möbius aromaticity switch. *Angew. Chem. Int. Ed.* **2007**, *46*, 7869–7873. [[CrossRef](#)]
69. Marcos, E.; Anglada, J.M.; Torrent-Sucarrat, M. Theoretical study of the switching between Hückel and Möbius topologies for expanded porphyrins. *J. Phys. Chem. C* **2012**, *116*, 24358–24366. [[CrossRef](#)]
70. Liu, Z.; Tian, Z.; Li, W.; Meng, S.; Wang, L.; Ma, J. Chiral Interconversions of Pd and/or Au Bis-Metalated [32]Octaphyrins(1,0,1,0,1,0,1,0) Involving Hückel and Möbius Macrocyclic Topologies: A Theoretical Prediction. *J. Org. Chem.* **2012**, *77*, 8124–8130. [[CrossRef](#)]
71. Marcos, E.; Anglada, J.M.; Torrent-Sucarrat, M. Effect of the Meso-Substituent in the Hückel-to-Möbius Topological Switches. *J. Org. Chem.* **2014**, *79*, 5036–5046. [[CrossRef](#)]
72. Alonso, M.; Geerlings, P.; De Proft, F. Exploring the structure–aromaticity relationship in Hückel and Möbius N-fused pentaphyrins using DFT. *Phys. Chem. Chem. Phys.* **2014**, *16*, 14396–14407. [[CrossRef](#)] [[PubMed](#)]
73. Alonso, M.; Pinter, B.; Geerlings, P.; De Proft, F. Metalated Hexaphyrins: From Understanding to Rational Design. *Chem. Eur. J.* **2015**, *21*, 17631–17638. [[CrossRef](#)] [[PubMed](#)]
74. Matito, E.; Feixas, F.; Solà, M. Electron delocalization and aromaticity measures within the Hückel molecular orbital method. *J. Mol. Struct. (Theochem)* **2007**, *811*, 3–11. [[CrossRef](#)]
75. Karadakov, P.; Castaño, O.; Ftatev, F.; Enchev, V. Some contributions and generalizations to the electronic theory of even polyenes and annulenes. *Chem. Phys. Lett.* **1981**, *78*, 560–565. [[CrossRef](#)]
76. Ftatev, F.; Enchev, V.; Polansky, O.; Bonchev, D. A theoretical—information study on the electron delocalization (aromaticity) of annulenes with and without bond alternation. *J. Mol. Struct. (Theochem)* **1982**, *88*, 105–118. [[CrossRef](#)]
77. Spitler, E.L.; Johnson, C.A.; Haley, M.M. Renaissance of annulene chemistry. *Chem. Rev.* **2006**, *106*, 5344–5386. [[CrossRef](#)]
78. Koseki, S.; Toyota, A. Energy component analysis of the Pseudo-Jahn-Teller effect in the ground and electronically excited states of the cyclic conjugated hydrocarbons: Cyclobutadiene, benzene, and cyclooctatetraene. *J. Phys. Chem. A* **1997**, *101*, 5712–5718. [[CrossRef](#)]
79. Papadakis, R.; Ottosson, H. The excited state antiaromatic benzene ring: A molecular Mr Hyde? *Chem. Soc. Rev.* **2015**, *44*, 6472–6493. [[CrossRef](#)]
80. Moll, J.F.; Pemberton, R.P.; Gutierrez, M.G.; Castro, C.; Karney, W.L. Configuration change in [14] annulene requires Möbius antiaromatic bond shifting. *J. Am. Chem. Soc.* **2007**, *129*, 274–275. [[CrossRef](#)]
81. Wannere, C.S.; Sattelmeyer, K.W.; Schaefer III, H.F.; Schleyer, P.v.R. Aromaticity: The Alternating C-C Bond Length Structures of [14]-, [18]-, and [22] Annulene. *Angew. Chem. Int. Ed.* **2004**, *43*, 4200–4206. [[CrossRef](#)]
82. Feixas, F.; Solà, M.; Barroso, J.M.; Ugalde, J.M.; Matito, E. New Approximation to the Third-Order Density. Application to the Calculation of Correlated Multicenter Indices. *J. Chem. Theory Comput.* **2014**, *10*, 3055–3065. [[CrossRef](#)] [[PubMed](#)]
83. Feixas, F.; Rodríguez-Mayorga, M.; Matito, E.; Solà, M. Three-center bonding analyzed from correlated and uncorrelated third-order reduced density matrices. *Comput. Theor. Chem.* **2015**, *1053*, 173–179. [[CrossRef](#)]
84. Mandado, M.; Graña, A.M.; Pérez-Juste, I. Aromaticity in spin-polarized systems: Can rings be simultaneously alpha aromatic and beta antiaromatic? *J. Chem. Phys.* **2008**, *129*, 164114. [[CrossRef](#)]
85. Karadakov, P.B. Aromaticity and antiaromaticity in the low-lying electronic states of cyclooctatetraene. *J. Phys. Chem. A* **2008**, *112*, 12707–12713. [[CrossRef](#)] [[PubMed](#)]
86. Braten, M.N.; Castro, C.; Herges, R.; Köhler, F.; Karney, W.L. The [12]annulene global minimum. *J. Org. Chem.* **2008**, *73*, 1532–1535. [[CrossRef](#)]
87. Castro, C.; Karney, W.L. Mechanisms and Möbius strips: Understanding dynamic processes in annulenes. *J. Phys. Org. Chem.* **2012**, *25*, 612–619. [[CrossRef](#)]
88. Lee, H.L.; Li, W.K. Computational study on the electrocyclic reactions of [16]annulene. *Org. Biomol. Chem.* **2003**, *1*, 2748–2754. [[CrossRef](#)]
89. Arbitman, J.K.; Michel, C.S.; Castro, C.; Karney, W.L. Calculations Predict That Heavy-Atom Tunneling Dominates Möbius Bond Shifting in [12]- and [16] Annulene. *Org. Lett.* **2019**, *21*, 8587–8591. [[CrossRef](#)]

90. Merkle, R.; Savin, A.; Preuss, H. Singly ionized first-row dimers and hydrides calculated with the fully-numerical density-functional program numol. *J. Chem. Phys.* **1992**, *97*, 9216–9221. [[CrossRef](#)]
91. Savin, A. On degeneracy, near-degeneracy and density functional theory. In *Recent Developments of Modern Density Functional Theory*; Seminario, J.M., Ed.; Elsevier: Amsterdam, The Netherlands, 1996; p. 327.
92. Cohen, A.J.; Mori-Sánchez, P.; Yang, W. Insights into Current Limitations of Density Functional Theory. *Science* **2008**, *321*, 792–794. [[CrossRef](#)]
93. Sancho-García, J.; Pérez-Jiménez, A. Improved accuracy with medium cost computational methods for the evaluation of bond length alternation of increasingly long oligoacetylenes. *Phys. Chem. Chem. Phys.* **2007**, *9*, 5874–5879. [[CrossRef](#)]
94. Torrent-Sucarrat, M.; Navarro, S.; Cossío, F.P.; Anglada, J.M.; Luis, J.M. Relevance of the DFT method to study expanded porphyrins with different topologies. *J. Comput. Chem.* **2017**, *38*, 2819–2828. [[CrossRef](#)] [[PubMed](#)]
95. Szczepanik, D.W.; Solà, M.; Andrzejak, M.; Pawełek, B.; Dominikowska, J.; Kukułka, M.; Dyduch, K.; Krygowski, T.M.; Szatylowicz, H. The role of the long-range exchange corrections in the description of electron delocalization in aromatic species. *J. Comput. Chem.* **2017**, *38*, 1640–1654. [[CrossRef](#)] [[PubMed](#)]
96. Peccati, F.; Laplaza, R.; Contreras-García, J. Overcoming Distrust in Solid State Simulations: Adding Error Bars to Computational Data. *J. Phys. Chem. C* **2019**, *123*, 4767–4772. [[CrossRef](#)]
97. Sim, E.; Song, S.; Burke, K. Quantifying density errors in DFT. *J. Phys. Chem. Lett.* **2018**, *9*, 6385–6392. [[CrossRef](#)]
98. Parr, R.G.; Yang, W. *Density-Functional Theory of Atoms and Molecules*; Oxford University Press: New York, NY, USA, 1989.
99. Frisch, M.J.; Trucks, G.W.; Schlegel, H.B.; Scuseria, G.E.; Robb, M.A.; Cheeseman, J.R.; Scalmani, G.; Barone, V.; Petersson, G.A.; Nakatsuji, H.; et al. *Gaussian-16 Revision C.01*; Gaussian Inc.: Wallingford, CT, USA, 2016.
100. Becke, A.D. Density-functional thermochemistry. III. The role of exact exchange. *J. Chem. Phys.* **1993**, *98*, 5648–5652. [[CrossRef](#)]
101. Stephens, P.J.; Devlin, F.J.; Chabalowski, C.F.; Frisch, M.J. Ab initio calculation of vibrational absorption and circular dichroism spectra using density functional force fields. *J. Phys. Chem.* **1994**, *98*, 11623–11627. [[CrossRef](#)]
102. Yanai, T.; Tew, D.P.; Handy, N.C. A new hybrid exchange–correlation functional using the Coulomb-attenuating method (CAM-B3LYP). *Chem. Phys. Lett.* **2004**, *393*, 51–57. [[CrossRef](#)]
103. Zhao, Y.; Truhlar, D.G. The M06 suite of density functionals for main group thermochemistry, thermochemical kinetics, noncovalent interactions, excited states, and transition elements: Two new functionals and systematic testing of four M06-class functionals and 12 other functionals. *Theor. Chem. Acc.* **2008**, *120*, 215–241.
104. Krishnan, R.; Binkley, J.S.; Seeger, R.; Pople, J.A. Self-consistent molecular orbital methods. XX. A basis set for correlated wave functions. *J. Chem. Phys.* **1980**, *72*, 650–654. [[CrossRef](#)]
105. Bader, R.F.W. *Atoms in Molecules: A Quantum Theory*; Oxford University Press: Oxford, UK, 1990.
106. Keith, T.A. *AIMAll (Version 14.11.23)*; TK Gristmill Software: Overland Park, KS, USA, 2014.
107. Matito, E. *ESI-3D*; IQCC and DIPC: Donostia, Euskadi, Spain, 2015.
108. Wolfram, S. *Mathematica 10*; Wolfram Research Inc.: Champaign, IL, USA, 2014.
109. Vosko, S.H.; Wilk, L.; Nusair, M. Accurate spin-dependent electron liquid correlation energies for local spin density calculations: A critical analysis. *Can. J. Phys.* **1980**, *58*, 1200–1211. [[CrossRef](#)]



Chapter 7

Aromaticity descriptors based on electron delocalization

Aromaticity descriptors based on electron delocalization

7

Irene Casademont-Reig^{a,b}, Eloy Ramos-Cordoba^{a,b}, Miquel Torrent-Sucarrat^{a,b,c},
Eduard Matito^{a,c}

^aDonostia International Physics Center (DIPC), Donostia, Euskadi, Spain. ^bPolimero eta Material Aurreratuak: Fisika, Kimika eta Teknologia, Kimika Fakultatea, Euskal Herriko Unibertsitatea UPV/EHU, Donostia, Euskadi, Spain. ^cIKERBASQUE, Basque Foundation for Science, Bilbao, Euskadi, Spain

Introduction

Aromaticity is an *ill-defined* concept. It does not correspond to a physical observable like many other properties that populate the world of tools used in the routine analysis of chemical reactions [1,2]. Bond orders [3], bond ionicity [4], reaction concertedness, oxidation states [5,6], local spin [7–10], and atomic contributions to the optical property of a molecule [11,12] are also properties that cannot be directly measured and unambiguously assigned. However, aromaticity is still more controverted than the latter because it refers not to one, but to several properties that are not necessarily mutually related. Despite its fuzziness, this concept is still widely used to elucidate phenomena such as chemical stability and reactivity [13–15]. In this sense, aromaticity is a concept used by chemists world-wide and it cannot be so easily ignored or put aside [16].

Despite aromaticity has not found (and most likely cannot find) a solid root in the quantum theory, there have been numerous attempts to define aromaticity measures. These *aromaticity indices* quantify to some extent the typical manifestations of aromaticity in molecules: energy stabilization, bond-length equalization, large magnetic anisotropies, abnormal chemical shifts, electron delocalization, etc. [17]. As a result, nowadays, there is a number of different indices available in the literature, sometimes offering disparate results about the aromaticity of certain chemical species [18]. The multidimensional character of aromaticity [19] calls for the use of various indices to assert the true nature of a given species. Moreover, the use of several measures is highly recommended because most indices fail to pass some aromaticity tests [18,20].

First of all, we should identify which is the actual feature of aromaticity that we want to analyze because not all aforementioned manifestations occur simultaneously in all molecules. The latter is particularly relevant in new aromatic species that extend beyond the realm of organic chemistry and show some aromatic features that are not due to the π -electron delocalization [21–28], but we also have some examples among organic molecules [18,29]. Aromaticity criteria based on electron delocalization [15] are adequate to identify conjugated-electron circuits [30–32], which might play important roles in the distribution of the electrons in a ring, the mobility of the electron cloud, or the assignment of electronic spectrum transitions. On the other hand,

energetic criteria [33] are important to identify molecules that benefit from extra energy stabilization. In some molecules, conjugated-electron circuits along a ring structure cause bond-length and bond-order equalization as well as an important energy stabilization in the molecule. However, the transition state (TS) of the Diels–Alder reaction is the most aromatic point along the intrinsic reaction coordinate and there is no bond-length or bond-order equalization [29]. In fact, this point is the most energetic point along the intrinsic reaction coordinate. One could argue that the energy stabilization should be compared with the TS of similar reactions. Nevertheless, pseudopericyclic reactions are essentially barrierless and produce similar products through a nonaromatic TS [34,35].

Several manifestations of aromaticity are related to the whole molecular structure, whereas others are specific of a given annular structure within the molecule. The former are known as *global properties* and the latter concern only specific regions of the molecule and, therefore, are *local properties* of the molecule. Global aromaticity indicators include the HOMO–LUMO gap that is often directly related with the ability of the molecule to undergo chemical reactions. The larger the gap, the least (energetically) accessible the LUMO orbital is and, thus, the least reactive the molecule is expected to be. This stabilization is characteristic of aromatic molecules. In general, energetic measures of aromaticity are global properties. On the other hand, geometrical features (e.g., bond-length equalization and bond distances halfway between single and double bonds), electronic ring currents (induced by an external magnetic field perpendicular to the ring plane), or multicenter electronic delocalization along the atoms in the ring are typical features of the annular structures within the molecule and are regarded as *local aromaticity* features. In this chapter, we will only consider indices of local aromaticity.

In the literature, there are many indices of aromaticity and they can be classified as energetic [33], magnetic [13], geometric [14], and electronic indices [15], corresponding to the different manifestations of aromaticity, i.e., energetic stabilization, exalted magnetic susceptibilities [36], particular geometrical features (such as bond-length equalization or planarity) or electron delocalization along the aromatic ring, respectively. Although in this chapter we focus on aromaticity indices based on electron delocalization, for the sake of comparison, we have also included bond-length alternation (BLA) and the harmonic oscillator model of aromaticity (HOMA) [37]. In the following section, we give the necessary background to introduce the electronic aromaticity indices, which we review in the next section. Finally, we include a select list of examples that will help us illustrate the usage of the indices.

Methodology

Since the indices of aromaticity covered in this work are based on electron delocalization, we first need to retrieve information about electron delocalization from the wavefunction. To this end, we resort to the pair density, which contains information about the relative motion of an electron pair and it is straightforwardly obtained from the wavefunction $\Psi(\mathbf{1}, \mathbf{2}, \dots, \mathbf{N})$:

$$\rho_2(\mathbf{1}, \mathbf{2}) = N(N - 1)P(\mathbf{1}, \mathbf{2}), \quad (7.1)$$

with

$$P(\mathbf{1}, \mathbf{2})d_1d_2 = \int d_3 \dots \int d_N \Psi^*(\mathbf{1}, \mathbf{2}, \dots, \mathbf{N})\Psi(\mathbf{1}, \mathbf{2}, \dots, \mathbf{N})d_1d_2, \quad (7.2)$$

where N is the number of electrons and $\mathbf{i} = \mathbf{1}, \mathbf{2}, \dots$ stands for the combined space and spin coordinates of the i th electron. $P(\mathbf{1}, \mathbf{2})d_1d_2$ is the probability of finding two electrons, one at d_1 and the other at d_2 , regardless of the position of the other $N - 2$ electrons [38]. A popular function in density functional theory is the exchange-correlation density (XCD) [39], which captures electron exchange and correlation effects, and it is defined as

$$\rho_{xc}(\mathbf{1}, \mathbf{2}) = \rho(\mathbf{1})\rho(\mathbf{2}) - \rho_2(\mathbf{1}, \mathbf{2}), \quad (7.3)$$

where $\rho(\mathbf{1})$ is the electron density. In the present context, it will be used to define the so-called electron-sharing indices (ESIs) [40–42].

The electron-sharing indices

The concept of *bond order* is crucial to understand the bonding in molecules. It measures the number of chemical bonds between a pair of atoms. In his seminal work, Coulson [3] put forward a measure of the *order of a bond*, which he applied within Hückel molecular orbital (HMO) theory to explain the electronic structure of some polyenes and aromatic molecules. This measure of the order of a bond, more commonly known as Coulson bond order, has been connected with the HMO calculations.

Nowadays, very few calculations are performed within the HMO method, as more sophisticated (and now computational affordable) methods are easily available. As a consequence, the Coulson bond order has been replaced by the concept of ESIs, which measure to which extent two atoms are sharing the electrons lying between them [42].

The XCD compares a fictitious pair density of independent electron pairs [$\rho(\mathbf{1})\rho(\mathbf{2})$] with the real pair density, $\rho_2(\mathbf{1}, \mathbf{2})$ [see Eq. (7.3)]. The smaller the difference, the more independent the electrons in these positions are. The larger the difference, the more dependent, i.e., the more *coupled* they are. Therefore, for pairs of electrons shared between points belonging to two different atoms we expect a large XCD value. The XCD can thus give rise to the concept of ESI [41–44]. The XCD between points belonging to two different atoms A and B is used to define the delocalization index (DI),

$$\delta(A, B) = 2 \int_A \int_B d_1d_2 \rho_{xc}(\mathbf{1}, \mathbf{2}) = -2cov(N_A, N_B), \quad (7.4)$$

whereas the localization index arises from the consideration of two points that pertain to atom A ,

$$\lambda(A) = \int_A \int_A d_1d_2 \rho_{xc}(\mathbf{1}, \mathbf{2}). \quad (7.5)$$

As we can see from Eq. (7.4), the DI is actually related to the covariance of the populations of atoms A and B , N_A and N_B , respectively, and it is thus a measure of the number of electrons simultaneously fluctuating between these atoms. The atom population is defined from the electron density,

$$N_A = \int_A d\mathbf{1} \rho(\mathbf{1}). \quad (7.6)$$

It is also worth defining the total delocalization in a given atom,

$$\delta(A) = \sum_{B \neq A} \delta(A, B), \quad (7.7)$$

which some authors [45] relate to the valence of an atom. Since the XCD integrates to the number of electrons, we can classify the electrons as localized and delocalized and assign them to atoms (localized) and pairs of atoms (delocalized):

$$N_A = \delta(A) + \lambda(A), \quad (7.8)$$

the following sum rule being satisfied:

$$N = \sum_A N_A = \sum_{B, A < B} \delta(A, B) + \sum_A \lambda(A). \quad (7.9)$$

The calculation of the DI and localization index requires the knowledge of the pair density and the density. In the case of multideterminantal wavefunctions, the calculation of the pair density carries a large computational cost that hampers the computation of quantities related to the electron-pair delocalization. In this chapter, we will restrict ourselves to single-determinant wavefunctions such as Hartree–Fock and Kohn–Sham density functional theory. The reader interested in ESIs or population covariances for many-body wavefunctions can consult other sources [20,42,46–48]. For closed-shell single-determinant wavefunctions, Eqs. (7.4) and (7.5) simplify significantly:

$$\delta(A, B) = 4 \sum_{ij} S_{ij}(A) S_{ij}(B), \quad (7.10)$$

$$\lambda(A) = 2 \sum_{ij} S_{ij}(A)^2, \quad (7.11)$$

where the latter summations run over occupied molecular orbitals and $S_{ij}(A)$ is the *atomic overlap matrix* (AOM) of atom A ,

$$S_{ij}(A) = \int_A d\mathbf{1} \phi_i^*(\mathbf{1}) \phi_j(\mathbf{1}), \quad (7.12)$$

$\phi_i(\mathbf{1})$ being a molecular orbital.

Aromaticity indices

In this section, we will study the aromaticity of a molecular ring consisting of n atoms represented by the string $A = \{A_1, A_2, \dots, A_n\}$, whose elements are ordered according to the connectivity of the atoms in the ring. For convenience, we adopt $A_{n+p} \equiv A_p$ ($p \geq 0$).

Geometrical aromaticity indices

In this subsection, we will analyze the so-called HOMA as defined by Kruszewski and Krygowski [37]. The HOMA relies only on geometrical data and it can be computed using the following expression:

$$\begin{aligned} \text{HOMA}(\mathcal{A}) &= 1 - 257.7 \frac{1}{n} \sum_i^n (R_{\text{opt}} - R_{A_i, A_{i+1}})^2 \\ &= 1 - 257.7 \left((R_{\text{opt}} - \bar{R})^2 + \frac{1}{n} \sum_i^n (R_{A_i, A_{i+1}} - \bar{R})^2 \right) \\ &= 1 - (\text{EN} + \text{GEO}) \end{aligned} \quad (7.13)$$

where the reference bond lengths, R_{opt} , are chosen so that the compression energy of the double bond and expansion energy of the single bond are minimal according to the harmonic potential model and $R_{A_i, A_{i+1}}$ are calculated from the distances of atoms A_i and A_{i+1} (see ref. [49]). In the derivation of Eq. (7.13), we assume that all bonds are of the same type. The expression for rings with different bonding patterns can also be decomposed into EN and GEO terms but its derivation is less straightforward [50]. The closer to one the index, the more aromatic the molecule. The formula depends on some reference bond distances and, unfortunately, there is a limited number of bonds for which these references have been tabulated (C–C, C–N, C–O, C–P, C–S, N–N, and N–O). This set suffices to calculate most organic molecules but imposes a serious drawback to extend the use of HOMA to new aromatic molecules.

The EN component of HOMA measures the deviation of the interatomic distances as compared to some tabulated numbers. GEO measures the variance of the interatomic distance, which for aromatic molecules is usually a small number because, unlike antiaromatic molecules, they do not present BLA. Both quantities, EN and GEO, are close to zero for aromatic molecules.

Another popular geometrical indicator of aromaticity is the BLA, which compares the average of bond lengths of consecutive bonds in a ring:

$$\text{BLA}(\mathcal{A}) = \frac{1}{n_1} \sum_{i=1}^{n_1} r_{A_{2i-1}, A_{2i}} - \frac{1}{n_2} \sum_{i=1}^{n_2} r_{A_{2i}, A_{2i+1}} \quad (7.14)$$

where $n_1 = \lfloor (n+1)/2 \rfloor$ and $n_2 = \lfloor n/2 \rfloor$, $\lfloor x \rfloor$ being the floor function of x , which returns the largest integer less than or equal to x . This expression of the BLA is not well defined

for rings of an odd number of members and, therefore, we have recently opt for a modified BLA definition [51]:

$$\text{BLA}(\mathcal{A}) = \frac{1}{2n} \sum_{i=1}^n |r_{A_i, A_{i+1}} - r_{A_{i+1}, A_{i+2}}|. \quad (7.15)$$

Electronic aromaticity indices

Lately, aromaticity indicators based on the electronic structure of molecules are becoming popular, and several research groups have designed new electronic aromaticity indices [15]. Among others, we can mention the I_{ring} [52] of Giambiagi et al., the multicenter index (MCI) [53] of Bultinck et al., the θ index [54] of Matta or the Shannon entropy [55] at the bond critical point [56] as suggested by Noorizadeh and Shakerzadeh [57]. The group of Miquel Solà and collaborators have also contributed with the fluctuation index (FLU) [58] and para-delocalization index (PDI) [59] as well as the normalized versions of I_{ring} and MCI [60]. More recently, Szczepanik et al. have contributed with an index capable of accounting for multicenter bonding [61,62] and Matito et al. have defined AV1245 [30] and AV_{min} [31,32] for large rings. Here we will focus on FLU, PDI, MCI, I_{ring} , AV1245, and AV_{min}.

Bond-order alternation

The bond-length alternation index (BLA) is built upon the premise that the bond-length alternation reflects the distribution of electron pairs on a conjugated circuit. Since some people are skeptical about the use of an aromaticity measure that only reflects a geometrical feature, they prefer the electronic-structure counterpart of the BLA, the bond-order alternation (BOA), which uses the bond order—or any equivalent concept such as the ESI [42]—instead of the bond length,

$$\text{BOA}(\mathcal{A}) = \frac{1}{2n} \sum_{i=1}^n |\delta(A_i, A_{i+1}) - \delta(A_{i+1}, A_{i+2})|. \quad (7.16)$$

Unlike the atomic charges [63], the bond orders are much less dependent on the method and the basis set used [64] and, therefore, aromaticity indices based on bond orders [65] are not highly dependent on the level of theory employed.

Aromatic fluctuation index

The FLU index measures aromaticity by comparison with the cyclic electron delocalization of a typical aromatic molecule [58,66],

$$\text{FLU}(\mathcal{A}) = \frac{1}{n} \sum_{i=1}^n \left[\left(\frac{\delta(A_i)}{\delta(A_{i-1})} \right)^\alpha \left(\frac{\delta(A_i, A_{i-1}) - \delta_{\text{ref}}(A_i, A_{i-1})}{\delta_{\text{ref}}(A_i, A_{i-1})} \right) \right]^2, \quad (7.17)$$

where α is a simple function to ensure the first term in Eq. (7.17) is always greater or equal to 1,

$$\alpha = \begin{cases} 1 & \delta(A_{i-1}) \leq \delta(A_i) \\ -1 & \delta(A_i) < \delta(A_{i-1}) \end{cases} \quad (7.18)$$

and $\delta_{ref}(A,B)$ is the DI corresponding to a reference aromatic ring which has the bond $A-B$. The aromatic reference for C–C bonds is benzene, whereas C–N bond reference is taken from pyridine. FLU is close to zero for aromatic species, and greater than zero for nonaromatic or antiaromatic species.

The aromaticity indices based on references actually measure the similarity with respect to some aromatic molecule. Hence, HOMA and FLU are not adequate to describe reactivity [18,29]. For instance, in the case of the Diels–Alder reaction they cannot recognize the TS as the most aromatic point along the reaction path because the product, cyclohexene, is more similar to benzene (the reference molecule for C–C bonds) than the TS, which shows large C–C distances and small DIs in the bonds that will be formed [29].

Para-delocalization index

Fulton [40] and Bader et al. [67] showed that benzene exhibits larger DI between the atoms in *para* position than in *meta* position. This finding was used by Poater et al. [59] to define the *para*-delocalization index (PDI), which consists in the average DI between the atoms in *para* position of a six-membered ring,

$$\text{PDI}(\mathcal{A}) = \frac{\delta(A_1, A_4) + \delta(A_2, A_5) + \delta(A_3, A_6)}{3}. \quad (7.19)$$

The larger the index, the greater the aromaticity. Obviously, the index cannot be used in rings with more or less than six members. The PDI is less reliable for heterocycles and rings made of highly polarizable atoms [18] because it can increase the delocalization across the ring without a substantial increase of the peripheral delocalization.

I_{ring}

A generalization of the DI concept to various atomic centers was provided by Giambiagi et al. [68] in 1990. The concept has been used to account for multicenter bonding and it is commonly known in the literature as the MCI [69]. Some years later, Giambiagi et al. suggested to use the MCI as a measure of aromaticity. In the context of aromaticity the index was called I_{ring} and its formulation for single-determinant wavefunctions reads [52]:

$$I_{\text{ring}}(\mathcal{A}) = \sum_{i_1, i_2, \dots, i_n}^{occ} S_{i_1 i_2}(A_1) S_{i_2 i_3}(A_2) \dots S_{i_n i_1}(A_n). \quad (7.20)$$

I_{ring} provides large values for aromatic molecules and values close to zero for nonaromatic species.

Multicenter index

Bultinck et al. [53] proposed to sum not only the contribution from the Kekule structures (as I_{ring} does), but also the contributions of all structures generated by permuting the position of all the atoms in the ring. Such possibility was already discussed by Ponec et al. [69,70] among others [71]. The resulting index was named multicenter index (MCI) and its expression is as follows:

$$\begin{aligned} \text{MCI}(\mathcal{A}) &= I_{\text{ring}}(\mathcal{A}) \\ &= \sum_{\mathcal{P}(\mathcal{A})} \sum_{i_1, i_2, \dots, i_n}^{\text{occ}} S_{i_1 i_2}(A_1) S_{i_2 i_3}(A_2) \dots S_{i_n i_1}(A_n), \end{aligned} \quad (7.21)$$

where $\mathcal{P}(\mathcal{A})$ stands for the $n!$ permutations of the elements in the string \mathcal{A} . Although the original proposal of MCI differs from this one by a numerical factor, we will skip it for the reasons already commented in ref. [60]. Like I_{ring} , MCI produces large numbers for aromatic species, and the authors claim negative numbers identify antiaromatic species [72]. To our knowledge, this fact has only been proven for three-member rings [69] and heuristically for six-member rings [73].

Normalized versions of I_{ring} and MCI

I_{ring} and MCI have been shown to be ring-size dependent [60] and, therefore, for convenience, we often calculate the multicenter electron delocalization per atom that can be simply obtained as $I_{\text{ring}}^{1/n}$ and $\text{MCI}^{1/n}$.

AV1245 and AV_{min}

I_{ring} and MCI are among the best-performing aromaticity indices available in the literature [15,18,20]. In fact, they have been used to assert the aromaticity of a large number of nontrivial cases, including new aromatic molecules [25, 26,74–80]. Unfortunately, for large rings, these indices carry a prohibitively large cost and present large numerical errors derived from the numerical integration of the AOMs. For this reason, we have recently designed two indices of aromaticity, AV1245 [30] and AV_{min} [31,32], which are free of these shortcomings. AV1245 gives an average electron delocalization along the ring and it is defined as the average value of the four-atom MCI index between relative positions 1–2 and 4–5 constructed from each five consecutive atoms along the perimeter of the ring. Lately, we have found that for the purpose of measuring aromaticity it is more adequate to use the minimum absolute MCI value evaluated along the perimeter, AV_{min} [31,32], which identifies the least delocalized five-atom fragment in the ring. Aromatic molecules are identified by large values of AV_{min} ($AV_{\text{min}} > 1$), whereas nonaromatic molecules are characterized by very low

AV_{\min} values. Antiaromatic molecules usually exhibit intermediate AV_{\min} values and are more difficult to identify. For this reason, the BOA is often used in conjunction with AV_{\min} to differentiate between nonaromatic and antiaromatic compounds. One should mention here that, according to AV_{\min} and AV_{1245} , the aromaticity of porphyrins is substantially reduced with respect to small annulenes. Typically, for aromatic porphyrins up to 32 atoms, we have found that $AV_{\min} > 0.5$, whereas antiaromatic porphyrins show $AV_{\min} < 0.5$. However, these numbers are likely to decrease if larger macrocycles are considered [81]. In this sense, we believe AV_{\min} is reflecting that, while porphyrin and extended porphyrins can be aromatic and antiaromatic, they are not as aromatic as their smaller-ring annulene counterparts.

Computational details

All the calculations have been performed with the Gaussian16 software package using CAM-B3LYP [82] and the 6-311G(d,p) basis set [83]. CAM-B3LYP has been employed to minimize the delocalization errors that plague DFAs calculations on aromatic molecules [31,51,84–87]. For the optimized geometries, the harmonic vibrational frequencies were calculated at the same level of theory in order to verify that the stationary points of the potential energy surface correspond to energy minima.

The atomic partition employed to calculate the aromaticity indices is the quantum theory of atoms in molecules (QTAIM) [56] for the reasons commented elsewhere [88]. The QTAIM AOMs were obtained from the AIMAll software [89], whereas the aromaticity indices were calculated with the in-house ESI-3D program [42,58,90]. This program provides AV_{1245} [30], AV_{\min} [32], BLA [51], BOA [51], PDI [59], FLU [58], HOMA [37], I_{ring} [52], and MCI [53] values. The numerical accuracy of the QTAIM calculations has been assessed using two criteria: (i) the integration of the Laplacian of the electron density ($\nabla^2\rho(r)$) within an atomic basin must be close to zero; (ii) the number of electrons in a molecule must be equal to the sum of all the electron populations of the molecule, and also equal to the sum of all the localization indices and half of the delocalization indices in the molecule (see Eqs. (7.8) and (7.9)). For all atomic calculations, integrated absolute values of $\nabla^2\rho(r)$ were lower than 0.001 a.u. For all molecules, errors in the calculated number of electrons were lower than 0.01 a.u. From our experience, these errors provide sufficient accuracy for all the indices here calculated except for the *normalized* MCIs of large rings, which require a numerical precision of the AOM well beyond the accuracy that one can obtain with AIMAll or any other similar software available in the literature. For the latter and other reasons commented in ref. [30], MCIs (I_{ring}) cannot be used in large rings.

Discussion

We have considered a small but assorted collection of molecules to illustrate the performance of the aromaticity indices (see Fig. 7.1). First of all, we consider benzene, cyclohexane, and three geometries of cyclohexatriene with various degrees of bond-length alternation. This small set will be used to analyze the transition of aromaticity

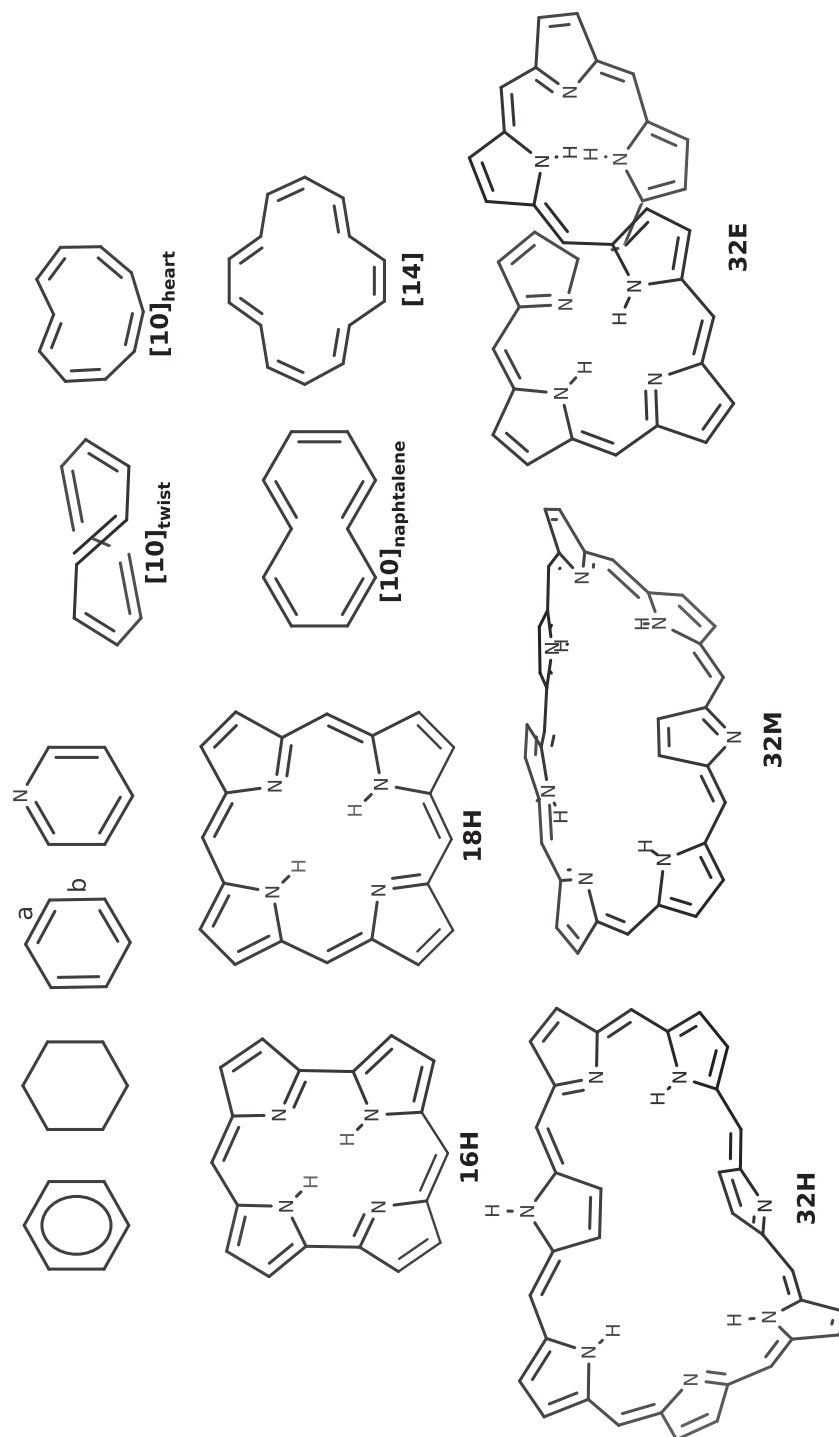


Fig. 7.1 Molecules studied in this work.

(benzene) to antiaromaticity (cyclohexatriene with small a/b ratio, a and b being the bond lengths of the short and the long bond, respectively) and a nonaromatic molecule (cyclohexane). We have also included pyridine, whose ring is not a pure skeleton of carbon atoms, and five porphyrinic structures, **16H**, **18H**, **32H**, **32M**, and **32E**, to assess the capability of the indices in recognizing the most aromatic pathway [31]. Finally, two different conformations of $C_{10}H_{10}$ for two spin multiplicities, and two conformations of $C_{14}H_{14}$ and a TS are considered [51], to check the reliability of these aromaticity measures for different spin states (Table 7.1).

Six-membered rings

All the aromaticity indices recognize benzene as the most aromatic six-membered ring and consistently show that the aromaticity of the ring is lost as one forces BLA in cyclohexatriene. However, the indices do not coincide on where to place the aromaticity of cyclohexane with respect to the latter molecules. According to PDI, AV1245, AV_{min}, MCI, and I_{ring} , the least aromatic molecule is cyclohexane. Therefore, these indices identify nonaromaticity as the completely opposite situation with respect to aromaticity. This is not completely unexpected because each of these indices measures, in a different way, the degree of electron delocalization in the ring. HOMA and FLU, which in this case measure to some extent the degree of similarity with respect to benzene, identify cyclohexane as more similar to benzene than any of the constrained cyclohexatriene structures considered in this study. This situation is reminiscent of the failure of these indices to recognize the most aromatic point in the reaction path of the Diels–Alder reaction [29], suggesting caution in employing these indices to assess the aromaticity of certain molecules. BOA and BLA only measure the degree of BOA or BLA and, therefore, are deemed to fail to differentiate between benzene and cyclohexane. Although BOA and BLA provide useful information about the electron delocalization character in aromatic rings, these results reveal that they cannot be blindly used to assess aromaticity. Finally, all the indices recognize pyridine as a molecule with an aromatic character very close to benzene.

Porphyrinic systems

In these porphyrinic systems, **16H**, **18H**, **32H**, **32M**, and **32E**, we will consider the annulene pathway [91], which contains as many π -electrons as the name of the system indicates, and the internal pathway (called *iiii* in ref. [31]), which are represented in Figs. 7.2 and 7.3. Since we are dealing with singlet ground-state configurations, **16H** and **18H** are expected to be antiaromatic and aromatic, respectively, whereas **32H**, **32M**, and **32E** are antiaromatic, aromatic, and antiaromatic, respectively, according to Hückel's [92] and Heilbronner's [93] rules.

All the indices correctly identify the annulene pathway of **18H** as more aromatic than the **16H** annulene pathway, although they also coincide in giving it a much less aromatic character than benzene. However, it is apparent that the antiaromaticity of the annulene pathway of **16H** is clearly very different from the antiaromaticity we had found for alternated cyclohexatriene. FLU and HOMA identify the annulene pathway of **16H** as much more similar to the annulene pathway of **18H** than to cyclohexatriene

Table 7.1 Aromaticity indices for a selected set of molecules (see the text) calculated at the CAM-B3LYP/6-311G(d,p) level of theory. S and T stand for singlet and triplet spin states, respectively.

Structure	FLU	BOA	HOMA	BLA	PDI	AV1245	AV _{min}	MCI	MCI ^{1/n}	I _{ring}	I _{ring} ^{1/n}
Benzene	0.000	0.000	1.000	0.000	0.103	10.71	10.71	0.072	0.646	0.048	0.603
Cyclohexane	0.090	0.000	-4.167	0.000	0.009	-0.01	0.01	0.000	0.260	0.000	0.256
Cyclohexatriene (<i>a/b</i> = 0.9)	0.034	0.511	-18.024	0.204	0.079	7.43	7.43	0.044	0.594	0.032	0.564
Cyclohexatriene (<i>a/b</i> = 0.8)	0.087	0.822	-31.266	0.408	0.051	2.99	2.99	0.013	0.484	0.012	0.478
Cyclohexatriene (<i>a/b</i> = 0.7)	0.138	1.038	-50.540	0.622	0.042	1.76	1.76	0.007	0.438	0.007	0.436
Pyridine	0.005	0.027	1.000	0.020	0.103	10.17	9.89	0.068	0.639	0.046	0.598
16H (annulene path)	0.021	0.246	0.547	0.063	-	1.19	0.13	-	-	-	-
16H (inner path)	0.025	0.227	0.505	0.084	-	0.62	0.07	-	-	-	-
18H (annulene path)	0.010	0.137	0.872	0.035	-	2.16	1.28	-	-	-	-
18H (inner path)	0.006	0.081	0.968	0.016	-	0.91	0.13	-	-	-	-
32H (annulene path)	0.023	0.319	0.594	0.073	-	1.18	0.45	-	-	-	-
32H (inner path)	0.022	0.267	0.698	0.059	-	0.32	0.06	-	-	-	-
32M (annulene path)	0.020	0.287	0.666	0.064	-	1.41	0.55	-	-	-	-
32M (inner path)	0.018	0.238	0.767	0.051	-	0.33	0.02	-	-	-	-
32E (annulene path)	0.021	0.296	0.632	0.066	-	1.26	0.46	-	-	-	-
32E (inner path)	0.017	0.240	0.756	0.054	-	0.38	0.03	-	-	-	-
C ₁₀ H ₁₀ (twist) S	0.059	0.677	-0.285	0.137	-	0.12	0.03	0.000	0.353	0.000	0.341
C ₁₀ H ₁₀ (heart) S	0.000	0.008	0.923	0.009	-	5.41	5.13	0.013	0.649	0.004	0.579
C ₁₀ H ₁₀ (naphthalene) T	0.027	0.364	0.411	0.072	-	0.36	0.68	0.000	0.401	0.000	0.446
C ₁₀ H ₁₀ (twist) T	0.022	0.324	0.407	0.071	-	0.56	0.07	0.000	0.382	0.000	0.347
C ₁₄ H ₁₄ S	0.026	0.449	0.437	0.091	-	2.11	1.80	-	-	-	-
C ₁₄ H ₁₄ TS	0.000	0.007	0.983	0.007	-	4.43	4.29	-	-	-	-
C ₁₄ H ₁₄ T	0.023	0.348	0.486	0.071	-	0.81	0.08	-	-	-	-

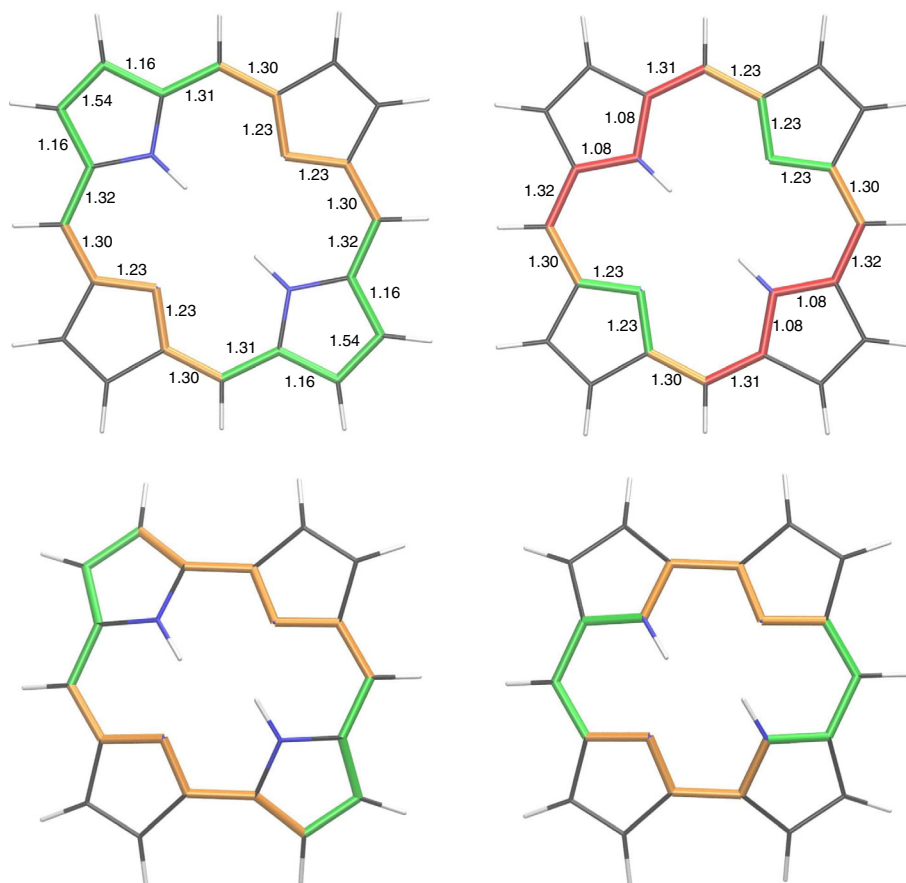


Fig. 7.2 AV1245 colored representations for the annulene (left) and inner (right) pathways of **18H** (top) and **16H** (bottom). The color of every bond is determined by the sum of the contributions to AV1245 that pass through this bond. In green, we represent bonds whose contribution is at least 75% the value of the highest bond, in red, bonds whose contribution is below 25% of this value, and the other bonds are colored in orange. This graph is useful to detect the most (green) and the least (red) aromatic fragments and it should be interpreted taking into account the actual value of AV1245 for the molecule. The numerical values above the bonds correspond to the DIs.

because the C–C distances and bond orders of the annulene pathway of **16H** are much more similar to the ones of benzene than to the bond-alternation patterns that we find in the constrained structures of cyclohexatriene. Again, we attribute this result to the use of benzene as a reference molecule. Also note that, according to AV1245 and AV_{\min} , porphyrinic systems are much less aromatic than small annulenes, and **18H** aromatic pathway exhibits a value of AV_{\min} not much larger than 1.

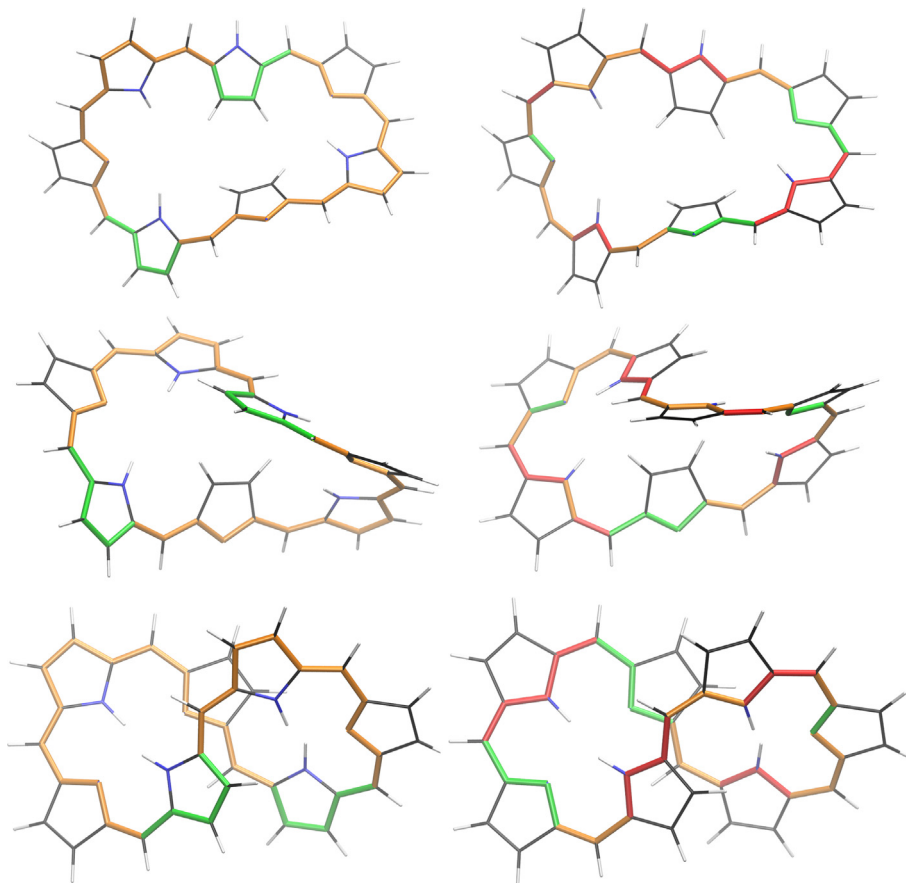


Fig. 7.3 AV1245 colored representations for the annulene (left) and inner (right) pathways of **32H** (top), **32M** (middle), and **32E** (bottom). See the caption of Fig. 7.2.

BOA is the only index that fails to find that the most aromatic pathway in **16H** corresponds to the annulene pathway. Unfortunately, not all indices can recognize the annulene pathway as the most aromatic pathway in **18H**. Indeed, FLU, BOA, BLA, and HOMA identify the inner path of **18H** (which takes always the shortest pathway going through all pyrrole and imidazole rings) as more aromatic than the annulene path. Using the EDDB technique [61], Szczepanik [94] has found a rationale for this result. However, our results suggest that FLU, BOA, BLA, and HOMA results are not consistent with the electronic distribution of **18H**. AV_{\min} shows a very small value for the inner path (0.13) due to the small delocalization of the C–C–NH–C–C fragment of the pyrrole rings (see the red fragments in the top-right picture of Fig. 7.2). In fact, the DIs of the C–NH bond (see Fig. 7.2) are the smallest ones in the circuit, further confirming C–C–NH–C–C as the least delocalized fragment of the pathway. FLU is

smaller for the inner circuit than for the annulene one because the DI of the C–N bonds of the pyrrole ring are closer to the reference values (taken from pyridine), than the DIs of the C–C bonds of the pyrrole are to the corresponding reference values (taken from benzene). However, the DI of the latter C–C bonds (1.16) is larger than the DI of the C–N bonds (1.08) and, therefore, we expect a higher electron delocalization in the annulene path. BOA and BLA are measuring the degree of homogeneity along the circuit of the DIs and the bond lengths, respectively—which does not necessarily reflect the most aromatic pathway. The CH–CH bond of the pyrrole ring of **18H** is shorter than the other C–C bonds and has the highest DI (1.54), contributing to break the homogeneity and giving larger BOA and BLA values for the annulene path. However, the DI of CH–CH of the pyrrole is halfway between a double and single bond, as one would expect for a bond in an aromatic circuit and the bond length (1.36 Å) is half way between a pure double bond and the C–C bond length of benzene. Hence, neither BOA nor BLA seem to favor the most delocalized pathway. It is worth to mention that the ring current analysis also agrees with AV_{\min} in giving the annulene pathway as the most aromatic one in **18H** [95].

Finally, we analyze the aromaticity of three [32]-heptaphyrin conformers: **32H**, **32M**, and **32E** [31,96]. Unlike AV_{\min} and AV1245 (which show large differences between the inner and annulene paths), FLU, HOMA, BOA, and BLA fail to identify the annulene path as the most aromatic circuit and give smaller differences between the two pathways. When we compare annulene pathways of the three conformers, we find that AV_{\min} and AV1245 identify **32M** as the most aromatic compound (in line with Heilbronner's aromaticity rule). However, the latter values are much smaller than those obtained for **18H** and the differences among the conformers are rather small, suggesting that Hückel and Heilbronner's rules fade away with the size of the macrocycle [51]. In Fig. 7.3, we collect the colored AV1245 representations, which show that the regions of maximal torsion correspond to the lowest AV1245 values.

$C_{10}H_{10}$ and $C_{14}H_{14}$

In ref. [51], we studied various singlet and triplet conformations of some annulenes. [10]annulene and [14]annulene presented a rich variety of conformations and aromatic characters and, therefore, we have chosen these species to illustrate the performance of the indices for different spin states. At the CAM-B3LYP/6-311g(d,p) level of theory, the most stable singlet conformation of [10]annulene is the *twist*, which lies only 0.6 kcal/mol below the *heart* conformation, which is highly delocalized. One expects that this molecule, which satisfies the $4N + 2 \pi$ -electron rule, should be aromatic. However, as its name suggests, the *twist* conformation is far from planar and, according to AV_{\min} , is rather nonaromatic. As we can confirm in Fig. 7.4, it is actually around the more twisted bonds that the aromaticity is lost. Conversely, all the indices agree on the large aromatic character of the *heart* conformation.

The lowest-lying triplet [10]annulene displays a *naphthalene-like* conformation with a large BOA value and rather low but non-negligible AV_{\min} value, which suggest this molecule is mildly antiaromatic, as predicted by the Baird rule [97]. On the contrary, the *twist* conformation of [10]annulene (lying only 0.9 kcal/mol above

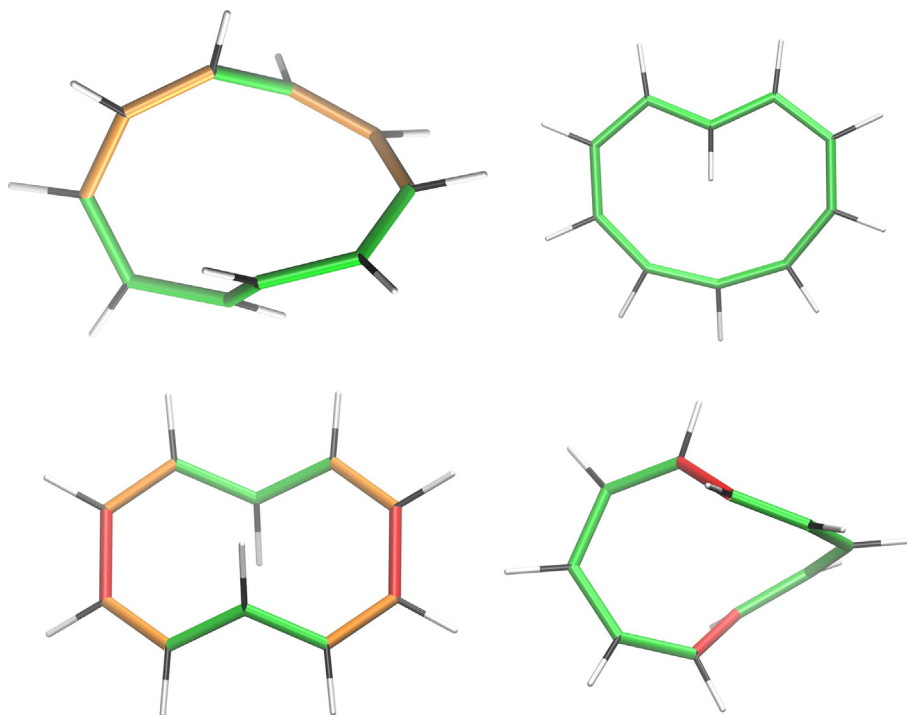


Fig. 7.4 AV1245 colored representation. Top: singlet [10]annulene (left: *twist*, right: *heart*). Bottom: triplet [10]annulene (left: *naphthalene*, right: *twist*).

the naphthalene conformation) displays very small AV_{\min} values which suggest that, despite the large BOA value, this molecule is nonaromatic. Note that FLU, BOA, BLA, and HOMA give a very similar value for both conformers. However, it is hard to assess from FLU or HOMA whether these two triplet conformers of [10]annulene correspond to nonaromatic or antiaromatic species. For a ring of this size, we cannot trust the very small values of MCI and I_{ring} because these indices suffer from ring-size dependence [60]. Instead, we resort to $MCI^{1/n}$ and $I_{\text{ring}}^{1/n}$, according to which the values lie between those of cyclohexane and cyclohexatriene. All in all, it is thus difficult to clearly confirm if these molecules are antiaromatic or nonaromatic. Given the fact that BOA values are rather high, we are inclined to classify them with mildly antiaromatic.

We have studied three [14]annulene conformers: the C_s -symmetry singlet conformer with bond-length alternation (the energy minimum), a TS that connects the latter structure with an analogous structure with complementary bond-length alternation, and the triplet [14]annulene (see Fig. 7.5). The large BOA values of the singlet and the triplet energy minima suggest that these molecules are antiaromatic, however, only the singlet displays a significant AV_{\min} that confirms this antiaromatic character. Despite the different nature of singlet and triplet [14]annulene, HOMA and FLU give rather similar values for both species. Conversely, all the indices agree on the fact that the TS is a quite aromatic molecule.

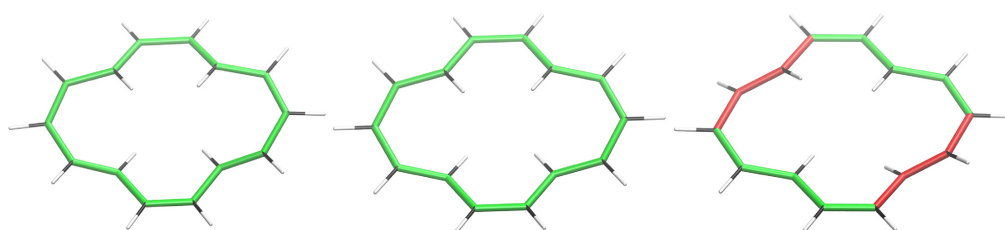


Fig. 7.5 AV1245 colored representation (see Fig. 7.2). From left to right: singlet, singlet transition state, and triplet [14]annulene.

Conclusions

In this book chapter, we have reviewed various aromaticity indices based on the concept of electron delocalization. Starting from the definition of an atom in a molecule, we can calculate two-center or multicenter electron delocalization indices that are used to construct the electronic aromaticity indices. In particular, we have covered three indices based on the two-center delocalization: FLU, PDI, and BOA, and four indices based on multicenter delocalization: I_{ring} , MCI, AV1245, and AV_{min} . We have compared the results of these indices with those obtained with BLA and HOMA. We have considered a small but assorted collection of molecules (see Fig. 7.1) to illustrate the performance of these indices in different challenging situations. Aromatic, antiaromatic, and nonaromatic molecules have been studied and we have shown that some indices struggle in identifying antiaromatic species from nonaromatic ones.

For this work, we have chosen the CAM-B3LYP functional that, as we have recently shown [31,51], significantly decreases the delocalization error that is present in other density functional approximations with a lower percentage of Hartree–Fock exchange, such as B3LYP. The delocalization error results in more delocalized electronic distribution clouds which could easily lead to the overestimation of the aromaticity of the molecule. A simple test to discard the presence of the delocalization error is to compare the electronic distributions obtained with B3LYP and CAM-B3LYP methods. In practice, if the errors are large, the differences are often obvious comparing both optimized geometries.

Our results show that BOA and BLA measure the degree of homogeneity of the DIs and the bond lengths of the ring, which do not necessarily reflect the aromaticity of the molecule. However, they can be used in conjunction with other methods like AV_{min} to distinguish between aromatic and antiaromatic species. FLU and HOMA have a strong dependence on reference values that hinder the abilities of these descriptors. There is enough evidences that suggest that these indices should not be used to study reaction mechanisms [29] but we have seen in this work how they can also provide spurious results in the study of porphyrinoids. MCI and I_{ring} are probably the most reliable indices of aromaticity [18,20] but they suffer from a ring-size dependency [60] that can be partially remedied by taking $1/n$ power of the index. Unfortunately, these indices present a large computational cost and numerical error [30] that prevents its use in large rings such as those present in porphyrinic systems. AV1245 and AV_{min} were introduced to overcome the latter problems and have been shown to provide a very good performance in porphyrinoids [31]. In Fig. 7.6, we show that there is an excellent correlation between AV1245 and AV_{min} against $MCI^{1/n}$ for the systems of Fig. 7.1. In particular, AV_{min} is the only index that can unambiguously identify the annulene pathway [91] as the most aromatic circuit in aromatic extended porphyrins. However, neither AV_{min} , AV1245, I_{ring} , or MCI can clearly distinguish aromatic from antiaromatic species in borderline situations. For this reason, we recommend to employ AV_{min} or MCI in conjunction with the BOA.

Although aromaticity rules are mostly preserved in large circuits [51], AV_{min} values suggest that there is a progressive homogenization of the systems as the rings grow in

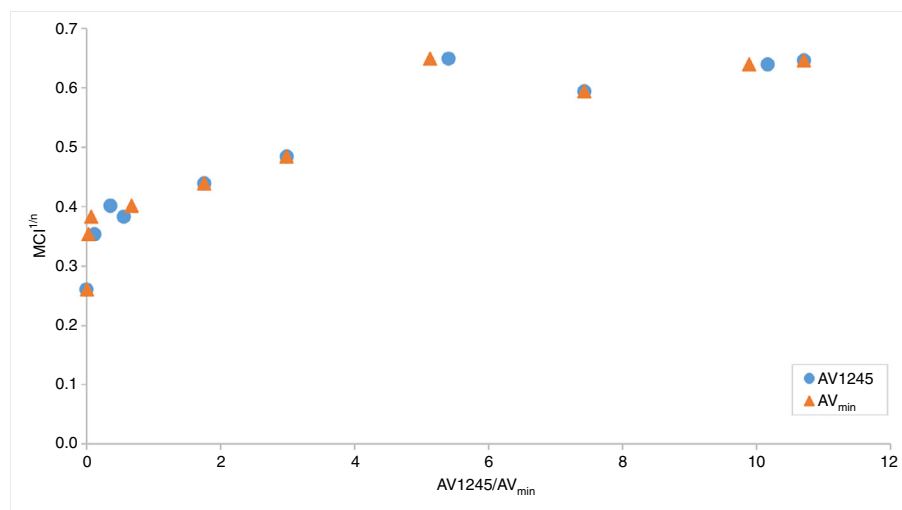


Fig. 7.6 AV₁₂₄₅ and AV_{min} against MCI^{1/n} for the systems reported in Table 7.1.

size. In other words, the electronic distribution of aromatic and antiaromatic species shows smaller differences for large conjugated circuits that are more difficult to capture by the aromaticity indices.

Acknowledgments

We thank our colleagues Mercedes Alonso, Julia Contreras-García, Tatiana Woller, Dariusz W. Szczepanik, and Miquel Solà with whom we have had fruitful discussions on the aromaticity of annulenes and porphyrinic systems.

This research was funded by Spanish MINECO grant numbers PGC2018-098212-B-C21, CTQ2016-80375-P, and EUR2019-103825, the Basque Government/Eusko Jaurlaritza (GV/EJ) grant number IT1254-19, IT-324-07, PIBA19-0004, and 2019-CIEN-000092-01, and the doctoral grant PRE_2016_1_0159. The authors acknowledge the computational resources and technical and human support provided by DIPC and the SGI/IZO-SGIker UPV/EHU. E.R.C. acknowledges funding from the Juan de la Cierva program IJCI-2017-34658.

References

- [1] G. Frenking, A. Krapp, Unicorns in the world of chemical bonding models, *J. Comput. Chem.* 28 (2007) 15–24.
- [2] J. Andrés, P.W. Ayers, R.A. Boto, R. Carbó-Dorca, H. Chermette, J. Cioslowski, J. Contreras-García, D.L. Cooper, G. Frenking, C. Gatti, et al., Nine questions on energy decomposition analysis, *J. Comput. Chem.* 40 (2019) 2248–2283.

- [3] C.A. Coulson, The electronic structure of some polyenes and aromatic molecules. VII. Bonds of fractional order by the molecular orbital method, *Proc. R. Soc. London Ser. A* 169 (1939) 413–428.
- [4] L. Pauling, *The Nature of the Chemical Bond*, Cornell University Press, Ithaca, 1948.
- [5] E. Ramos-Cordoba, V. Postils, P. Salvador, Oxidation states from wave function analysis, *J. Chem. Theory Comput.* 11 (2015) 1501–1508.
- [6] V. Postils, C. Delgado-Alonso, J.M. Luis, P. Salvador, An objective alternative to IUPAC's approach to assign oxidation states, *Angew. Chem. Int. Ed.* 130 (2018) 10685–10689.
- [7] A.E. Clark, E.R. Davidson, Local spin, *J. Chem. Phys.* 115 (2001) 7382–7392.
- [8] I. Mayer, E. Matito, Calculation of local spins for correlated wave functions, *Phys. Chem. Chem. Phys.* 10 (2010) 11308–11314.
- [9] E. Ramos-Cordoba, E. Matito, I. Mayer, P. Salvador, Toward a unique definition of the local spin, *J. Chem. Theory Comput.* 8 (2012) 1270–1279.
- [10] E. Ramos-Cordoba, E. Matito, P. Salvador, I. Mayer, Local spins: improved Hilbert-space analysis, *Phys. Chem. Chem. Phys.* 14 (2012) 15291–15298.
- [11] S.P. Sitkiewicz, M. Rodríguez-Mayorga, J.M. Luis, E. Matito, Partition of optical properties into orbital contributions, *Phys. Chem. Chem. Phys.* 21 (2019) 15380–15391.
- [12] N. Otero, P. Karamanis, M. Mandado, A new method to analyze and understand molecular linear and nonlinear optical responses via field-induced functions: a straightforward alternative to sum-over-states (SOS) analysis, *Phys. Chem. Chem. Phys.* 21 (2019) 6274–6286.
- [13] Z. Chen, C.S. Wannere, C. Corminboeuf, R. Puchta, P.V.R. Schleyer, Nucleus-independent chemical shifts (NICS) as an aromaticity criterion, *Chem. Rev.* 105 (2005) 3842–3888.
- [14] T.M. Krygowski, H. Szatyłowicz, O.A. Stasyuk, J. Dominikowska, M. Palusiak, Aromaticity from the viewpoint of molecular geometry: application to planar systems, *Chem. Rev.* 114 (2014) 6383–6422.
- [15] F. Feixas, E. Matito, J. Poater, M. Solà, Quantifying aromaticity with electron delocalisation measures, *Chem. Soc. Rev.* 44 (2015) 6389–6646.
- [16] M. Solà, Why aromaticity is a suspicious concept? Why? *Front. Chem.* 5 (2017) 22.
- [17] P.V.R. Schleyer, H. Jiao, What is aromaticity, *Pure Appl. Chem.* 68 (1996) 209–218.
- [18] F. Feixas, E. Matito, J. Poater, M. Solà, On the performance of some aromaticity indices: a critical assessment using a test set, *J. Comput. Chem.* 29 (2008) 1543–1554.
- [19] A.R. Katritzky, P. Barczynski, G. Musumarra, D. Pisano, M. Szafran, Aromaticity as a quantitative concept. 1. A statistical demonstration of the orthogonality of classical and magnetic aromaticity in five- and six-membered heterocycles, *J. Am. Chem. Soc.* 111 (1989) 7–15.
- [20] F. Feixas, J. Jiménez-Halla, E. Matito, J. Poater, M. Solà, A test to evaluate the performance of aromaticity descriptors in all-metal and semimetal clusters. An appraisal of electronic and magnetic indicators of aromaticity, *J. Chem. Theory Comput.* 6 (2010) 1118–1130.
- [21] X. Li, A.E. Kuznetsov, H.-F. Zhang, A.I. Boldyrev, L.-S. Wang, Observation of all-metal aromatic molecules, *Science* 291 (2001) 859–861.
- [22] A.I. Boldyrev, L.-S. Wang, All-metal aromaticity and antiaromaticity, *Chem. Rev.* 105 (2005) 3716–3757.
- [23] R. Islas, T. Heine, G. Merino, The induced magnetic field, *Acc. Chem. Res.* 45 (2011) 215–228.
- [24] F. Feixas, E. Matito, J. Poater, M. Solà, Metalloaromaticity, *WIREs, Comput. Mol. Sci.* (3) (2013) 105–122.

- [25] X. Min, I.A. Popov, F.-X. Pan, L.-J. Li, E. Matito, Z.-M. Sun, L.-S. Wang, A.I. Boldyrev, All-metal antiaromaticity in Sb₄-type lanthanocene anions, *Angew. Chem. Int. Ed.* 55 (2016) 5531–5535.
- [26] I.A. Popov, F.-X. Pan, X.-R. You, L.-J. Li, E. Matito, C. Liu, H.-J. Zhai, Z.-M. Sun, A.I. Boldyrev, Peculiar all-metal σ -aromaticity of the [Au₂Sb₁₆]⁴⁻ anion in the solid state, *Angew. Chem. Int. Ed.* 128 (2016) 15570–15572.
- [27] H. Braunschweig, R.D. Dewhurst, J.O.C. Jiménez-Halla, E. Matito, J.H. Muessig, Transition-metal π -ligation of a tetrahalodiborane, *Angew. Chem. Int. Ed.* 57 (2018) 412–416.
- [28] Z. Wang, N.V. Tkachenko, L. Qiao, E. Matito, A. Muñoz-Castro, A. Boldyrev, Z. Sun, All-metal σ -antiaromaticity in dimeric cluster anion {[CuGe₉Mes]₂}⁴⁻, *Chem. Commun.* 56 (2020) 6583–6586.
- [29] E. Matito, J. Poater, M. Duran, M. Solà, An analysis of the changes in aromaticity and planarity along the reaction path of the simplest Diels–Alder reaction. Exploring the validity of different indicators of aromaticity, *J. Mol. Struct. (Theochem)* 727 (2005) 165–171.
- [30] E. Matito, Electronic aromaticity index for large rings, *Phys. Chem. Chem. Phys.* 18 (2016) 11839–11846.
- [31] I. Casademont-Reig, T. Woller, J. Contreras-García, M. Alonso, M. Torrent-Sucarrat, E. Matito, New electron delocalization tools to describe the aromaticity in porphyrinoids, *Phys. Chem. Chem. Phys.* 20 (2018) 2787–2796.
- [32] C. García-Fernández, E. Sierda, M. Abadía, B.E.C. Bugenhagen, M.H. Prosenc, R. Wiesendanger, M. Bazarnik, J.E. Ortega, J. Brede, E. Matito, A. Arnau, Exploring the relation between intramolecular conjugation and band dispersion in one-dimensional polymers, *J. Phys. Chem. C* 121 (2017) 27118–27125.
- [33] M.K. Cyranski, Energetic aspects of cyclic pi-electron delocalization: evaluation of the methods of estimating aromatic stabilization energies, *Chem. Rev.* 105 (2005) 3773–3811.
- [34] E. Matito, M. Solà, M. Duran, J. Poater, Comment on the “Nature of bonding in the thermal cyclization of (z)-1,2,4,6-heptatetraene and its heterosubstituted analogues”, *J. Phys. Chem. B* 109 (2005) 7591–7593.
- [35] E. Matito, J. Poater, M. Duran, M. Solà, Electron fluctuation in pericyclic and pseudopericyclic reactions, *Chem. Phys. Chem.* 7 (2006) 111–113.
- [36] H.J. Dauben Jr, J.D. Wilson, J.L. Laity, Diamagnetic susceptibility exaltation as a criterion of aromaticity, *J. Am. Chem. Soc.* 90 (1968) 811–813.
- [37] J. Kruszewski, T.M. Krygowski, Definition of aromaticity basing on the harmonic oscillator model, *Tetrahedron Lett.* 13 (1972) 3839–3842.
- [38] P.-O. Löwdin, Quantum theory of many-particle systems. I. Physical interpretations by means of density matrices, natural spin-orbitals, and convergence problems in the method of configurational interaction, *Phys. Rev.* 97 (1955) 1474–1489.
- [39] K. Ruedenberg, The physical nature of the chemical bond, *Rev. Mod. Phys.* 34 (1962) 326–376.
- [40] R.L. Fulton, Sharing of electrons in molecules, *J. Phys. Chem.* 97 (1993) 7516–7529.
- [41] R.F.W. Bader, M.E. Stephens, Fluctuation and correlation of electrons in molecular systems, *Chem. Phys. Lett.* 26 (1974) 445–449.
- [42] E. Matito, M. Solà, P. Salvador, M. Duran, Electron sharing indexes at the correlated level. Application to aromaticity calculations, *Faraday Discuss.* 135 (2007) 325–345.

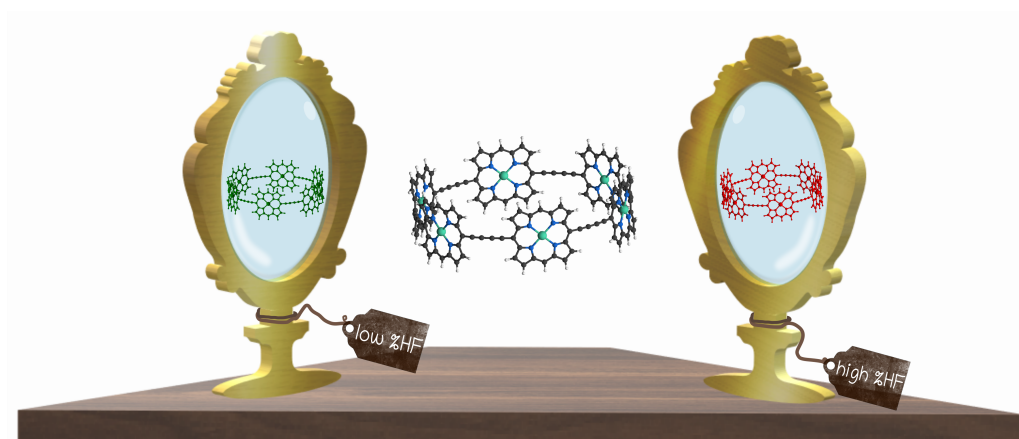
- [43] R.F.W. Bader, M.E. Stephens, Spatial localization of the electronic pair and number distributions in molecules, *J. Am. Chem. Soc.* 97 (1975) 7391–7399.
- [44] X. Fradera, M.A. Austen, R.F.W. Bader, The Lewis Model and Beyond, *J. Phys. Chem. A* 103 (1999) 304–314.
- [45] I. Mayer, Charge, bond order, and valence in the ab initio SCF theory, *Chem. Phys. Lett.* 97 (1983) 270–274.
- [46] E. Matito, B. Silvi, M. Duran, M. Solà, Electron localization function at the correlated level, *J. Chem. Phys.* 125 (2006) 024301.
- [47] F. Feixas, M. Solà, J.M. Barroso, J.M. Ugalde, E. Matito, New approximation to the third-order density. Application to the calculation of correlated multicenter indices, *J. Chem. Theory Comput.* 10 (2014) 3055–3065.
- [48] M. Rodríguez-Mayorga, E. Ramos-Cordoba, F. Feixas, E. Matito, Electron correlation effects in third-order densities, *Phys. Chem. Chem. Phys.* 19 (2017) 4522–4529.
- [49] T.M. Krygowski, M.K. Cyranski, Structural aspects of aromaticity, *Chem. Rev.* 101 (5) (2001) 1385–1420.
- [50] T.M. Krygowski, Crystallographic studies of inter- and intramolecular interactions reflected in aromatic character of π -electron systems, *J. Chem. Inf. Comput. Sci.* 33 (1993) 70–78.
- [51] I. Casademont-Reig, E. Ramos-Cordoba, M. Torrent-Sucarrat, E. Matito, How do the Hückel and Baird rules fade away in annulenes? *Molecules* 25 (2020) 711.
- [52] M. Giambiagi, M.S. de Giambiagi, C.D. dos Santos Silva, A.P. de Figueiredo, Multicenter bond indices as a measure of aromaticity, *Phys. Chem. Chem. Phys.* 2 (2000) 3381–3392.
- [53] P. Bultinck, R. Ponec, S. Van Damme, Multicenter bond indices as a new measure of aromaticity in polycyclic aromatic hydrocarbons, *J. Phys. Org. Chem.* 18 (2005) 706–718.
- [54] C.F. Matta, J. Hernández-Trujillo, Bonding in polycyclic aromatic hydrocarbons in terms of the electron density and of electron delocalization, *J. Phys. Chem. A* 107 (2003) 7496–7504.
- [55] C.E. Shannon, W. Weaver, *The Mathematical Theory of Communication*, The University of Illinois Press, Urbana, IL, USA, 1949.
- [56] R.F.W. Bader, *Atoms in Molecules: A Quantum Theory*, Oxford University Press, Oxford, U.K., 1990.
- [57] S. Noorizadeh, E. Shakerzadeh, Shannon entropy as a new measure of aromaticity, *Shannon aromaticity*, *Phys. Chem. Chem. Phys.* 12 (2010) 4742–4749.
- [58] E. Matito, M. Duran, M. Solà, The aromatic fluctuation index (FLU): a new aromaticity index based on electron delocalization, *J. Chem. Phys.* 122 (2005) 014109.
- [59] J. Poater, X. Fradera, M. Duran, M. Solà, The delocalization index as an electronic aromaticity criterion: application to a series of planar polycyclic aromatic hydrocarbons, *Chem. Eur. J.* 9 (2003) 400–406.
- [60] J. Cioslowski, E. Matito, M. Solà, Properties of aromaticity indices based on the one-electron density matrix, *J. Phys. Chem. A* 111 (2007) 6521–6525.
- [61] D.W. Szczepanik, E. Żak, K. Dyduch, J. Mrozek, Electron delocalization index based on bond order orbitals, *Chem. Phys. Lett.* 593 (2014) 154–159.
- [62] D.W. Szczepanik, M. Andrzejak, K. Dyduch, E. Żak, M. Makowski, G. Mazur, J. Mrozek, A uniform approach to the description of multicenter bonding, *Phys. Chem. Chem. Phys.* 16 (2014) 20514–20523.
- [63] C. Fonseca Guerra, J.-W. Handgraaf, E.J. Baerends, F.M. Bickelhaupt, Voronoi deformation density (VDD) charges: assessment of the mulliken, bader, hirshfeld, weinhold, and VDD methods for charge analysis, *J. Comput. Chem.* 25 (2004) 189–210.

- [64] E. Matito, J. Poater, M. Solà, M. Duran, P. Salvador, Comparison of the aim delocalization index and the mayer and fuzzy atom bond orders, *J. Phys. Chem. A* 109 (2005) 9904–9910.
- [65] E. Matito, M. Solà, M. Duran, P. Salvador, Aromaticity measures from fuzzy-atom bond orders (FBO). The aromatic fluctuation (FLU) and the para-delocalization (PDI) indexes, *J. Phys. Chem. A* 110 (2006) 5108–5113.
- [66] E. Matito, M. Duran, M. Solà, Erratum: “The aromatic fluctuation index (FLU): a new aromaticity index based on electron delocalization [*J. Chem Phys.* 122 (2005) 014109],” *J. Chem. Phys.* 125 (2006) 059901.
- [67] R.F.W. Bader, A. Streitwieser, A. Neuhaus, K.E. Laidig, P. Speers, Electron delocalization and the fermi hole, *J. Am. Chem. Soc.* 118 (1996) 4959–4965.
- [68] M. Giambiagi, M.S. de Giambiagi, K.C. Mundim, Definition of a multicenter bond index, *Struct. Chem.* 1 (1990) 423–427.
- [69] R. Ponec, I. Mayer, Investigation of some properties of multicenter bond indices, *J. Phys. Chem. A* 101 (1997) 1738–1741.
- [70] R. Ponec, F. Uhlík, Multicentre bond indices from the generalized population analysis of higher order densities, *Croat. Chem. Acta* 69 (1996) 941–954.
- [71] C.G. Bollini, M. Giambiagi, M.S.D. Giambiagi, A.P. de Figueiredo, Graphical linking of MO multicenter bond index and VB structures. II-5-c rings and 6-c heterocyclic rings, *Struct. Chem.* 12 (2001) 113–120.
- [72] R. Ponec, P. Bultinck, A.G. Saliner, Multicenter bond indices as a new means for the quantitative characterization of homoaromaticity, *J. Phys. Chem. A* 109 (2005) 6606–6609.
- [73] P. Bultinck, M. Rafat, R. Ponec, B. Van Gheluwe, R. Carbo-Dorca, P. Popelier, Electron delocalization and aromaticity in linear polyacenes: Atoms in molecules multicenter delocalization index, *J. Phys. Chem. A* 110 (2006) 7642–7648.
- [74] J.M. Mercero, E. Matito, F. Ruipérez, I. Infante, X. Lopez, J.M. Ugalde, The electronic structure of the Al_3^- Anion: Is it aromatic? *Chem. Eur. J.* 21 (2015) 9610–9614.
- [75] R.C. Fortenberry, C.M. Novak, J.P. Layfield, E. Matito, T.J. Lee, Overcoming the failure of correlation for out-of-plane motions in a simple aromatic: Rovibrational quantum chemical analysis of $c-C_3H_2$, *J. Chem. Theory Comput.* 14 (2018) 2155–2164.
- [76] R. Grande-Aztatzi, J.M. Mercero, E. Matito, G. Frenking, J.M. Ugalde, The aromaticity of dicupra [10]annulenes, *Phys. Chem. Chem. Phys.* 19 (2017) 9669–9675.
- [77] R.V. López, O.N. Faza, E. Matito, C.S. López, Cycloreversion of the CO_2 trimer: a paradigmatic pseudopericyclic [2+ 2+ 2] cycloaddition reaction, *Org. Biomol. Chem.* 15 (2017) 435–441.
- [78] J.O.C. Jimenez-Halla, E. Matito, M. Solà, H. Braunschweig, C. Hörl, I. Krummenacher, J. Wahler, A theoretical study of the aromaticity in neutral and anionic borole compounds, *Dalton Trans* 44 (2015) 6740–6747.
- [79] A.C. Castro, E. Osorio, J.L. Cabellos, E. Cerpa, E. Matito, M. Solà, M. Swart, G. Merino, Exploring the potential energy surface of E_2P_4 clusters (E = Group 13 Element): the quest for inverse carbon-free sandwiches, *Chem. Eur. J.* 20 (2014) 4583–4590.
- [80] T. Woller, P. Geerlings, F. De Proft, B. Champagne, M. Alonso, Aromaticity as a guiding concept for spectroscopic features and nonlinear optical properties of porphyrinoids, *Molecules* 23 (2018) 1333.
- [81] I. Casademont-Reig, R. Guerrero-Avilés, E. Ramos-Cordoba, M. Torrent-Sucarrat, E. Matito, How aromatic are molecular nanorings? The case of a six-porphyrin nanoring, submitted.

- [82] T. Yanai, D.P. Tew, N.C. Handy, A new hybrid exchange–correlation functional using the coulomb-attenuating method (CAM-B3LYP), *Chem. Phys. Lett.* 393 (2004) 51–57.
- [83] R. Krishnan, J.S. Binkley, R. Seeger, J.A. Pople, Self-consistent molecular orbital methods. XX. A basis set for correlated wave functions, *J. Chem. Phys.* 72 (1980) 650–654.
- [84] C.S. Wannere, K.W. Sattelmeyer, H.F. Schaefer III, P.V.R. Schleyer, Aromaticity: the alternating C-C bond length structures of [14]-, [18]-, and [22]annulene, *Angew. Chem. Int. Ed.* 43 (2004) 4200–4206.
- [85] M. Torrent-Sucarrat, S. Navarro, F.P. Cossío, J.M. Anglada, J.M. Luis, Relevance of the DFT method to study expanded porphyrins with different topologies, *J. Comput. Chem.* 38 (2017) 2819–2828.
- [86] M. Torrent-Sucarrat, S. Navarro, E. Marcos, J.M. Anglada, J.M. Luis, Design of Huckel–Möbius topological switches with high nonlinear optical properties, *J. Phys. Chem. C* 121 (2017) 19348–19357.
- [87] T. Woller, A. Banerjee, N. Sylvetsky, G. Santra, X. Deraet, F. De Proft, J.M. Martin, M. Alonso, Performance of electronic structure methods for the description of Huckel–Möbius interconversions in extended π -systems, *J. Phys. Chem. A* 124 (2020) 2380–2397.
- [88] W. Heyndrickx, P. Salvador, P. Bultinck, M. Solà, E. Matito, Performance of 3d-space-based atoms-in-molecules methods for electronic delocalization aromaticity indices, *J. Comput. Chem.* 32 (2011) 386–395.
- [89] T.A. Keith, AIMAll (Version 14.11.23), tK Gristmill Software, Overland Park KS, USA, 2014. <https://aim.tkgristmill.com>.
- [90] E. Matito, ESI-3D: Electron Sharing Indices Program for 3D Molecular Space Partitioning, Institute of Computational Chemistry and Catalysis, University of Girona, Catalonia, Spain, 2015.
- [91] J.-I. Aihara, Y. Nakagami, R. Sekine, M. Makino, Validity and limitations of the bridged annulene model for porphyrins, *J. Phys. Chem. A* 116 (2012) 11718–11730.
- [92] E. Hückel, Quantentheoretische Beiträge zum benzolproblem, I: Die elektronenkonfiguration des benzols und verwandter verbindungen, *Z. Physik* 70 (1931) 104–186.
- [93] E. Heilbronner, Hückel molecular orbitals of Möbius-type conformations of annulenes, *Tetrahedron Lett.* 5 (1964) 1923–1928.
- [94] D.W. Szczepanik, personal communication.
- [95] H. Fliegl, D. Sundholm, Aromatic pathways of porphyrins, chlorins, and bacteriochlorins, *J. Org. Chem.* 77 (2012) 3408–3414.
- [96] M. Alonso, P. Geerlings, F. De Proft, Topology switching in [32]heptaphyrins controlled by solvent, protonation, and meso substituents, *Chem. Eur. J.* 19 (2013) 1617–1628.
- [97] N.C. Baird, Quantum organic photochemistry. II. Resonance and aromaticity in the lowest $^3\pi\pi^*$ state of cyclic hydrocarbons, *J. Am. Chem. Soc.* 94 (1972) 4941–4948.

Chapter 8

How aromatic are molecular nanorings? The case of a six-porphyrin nanoring



How aromatic are molecular nanorings? The case of a six-porphyrin nanoring[†]

Irene Casademont-Reig, Raúl Guerrero-Avilés,
Eloy Ramos-Cordoba,* Miquel Torrent-Sucarrat,* Eduard Matito*

June 1, 2021

Abstract

Large conjugated rings that can sustain persistent currents are novel promising structures in molecular-scale electronics. One of the most interesting such molecules was recently synthesized [*Nature*, 2017, **541**, 3512] in the form of a six-porphyrin nanoring structure, which, according to the authors, in its +6-oxidation state sustained an aromatic ring current involving 78π electrons; one of the largest aromatic rings ever produced. This paper provides compelling evidence that this molecule is not aromatic, contrary to what was inferred from the analysis of ¹H-NMR experimental data and computational calculations that suffer from large delocalization errors. A thorough analysis of four oxidation states of the six-porphyrin nanoring reveals that the main reason behind the absence of an aromatic ring current in these nanorings is the low delocalization in the transition from the porphyrins to the bridging butadiyne linkers, which disrupts the overall conjugated circuit. These results highlight the importance of choosing a suitable computational method to study large conjugated molecules and the appropriate aromaticity descriptors to identify the part of the molecule responsible for the loss of aromaticity. The strategy employed here holds the promise to help design new large aromatic molecular nanorings.

[†]Dedication: We dedicate this paper to the memory of our friend and colleague, Prof. István Mayer, whose works have been a continuous inspiration.

* I. Casademont-Reig, R. Guerrero-Avilés, E. Ramos-Cordoba, M. Torrent-Sucarrat, E. Matito
Donostia International Physics Center (DIPC), 20018 Donostia, Euskadi, Spain.
E-mail: eloy.raco@gmail.com, miqueltorrentsucarrat@gmail.com, ematito@gmail.com

I. Casademont-Reig, E. Ramos-Cordoba
Polimero eta Material Aurreratuak: Fisika, Kimika eta Teknologia, Kimika Fakultatea, Euskal Herriko Unibertsitatea UPV/EHU, P.K. 1072, 20080 Donostia, Euskadi, Spain.

R. Guerrero-Avilés
Centro de Física de Materiales, CFM-MPC CSIC-UPV/EHU, 20018 Donostia, Euskadi, Spain.

M. Torrent-Sucarrat, E. Matito
Ikerbasque, Basque Foundation for Science, Plaza Euskadi 5, 48009 Bilbao, Euskadi, Spain.

M. Torrent-Sucarrat
Department of Organic Chemistry I, Universidad del País Vasco/Euskal Herriko Unibertsitatea (UPV/EHU), 20018 Donostia, Euskadi, Spain.

Supporting information and the ORCID identification number(s) for the author(s) of this article can be found under: <https://doi.org/anie.xxxxxxxx>.
A previous version of this manuscript has been deposited on a preprint server (<https://doi.org/10.26434/chemrxiv.14035919.v2>)

Introduction

Benzene is the paradigm of an organic aromatic molecule, exhibiting bond-length equalization, cyclic electron delocalization, and exalted magnetic susceptibility. As such, benzene is just the smallest neutral annulene that presents π -conjugated aromaticity; other annulenes possessing $4n + 2$ π electrons are also considered aromatic. It is well established that large annulenes suffer out-of-plane distortions and exhibit a poor overlap between π orbitals, thus favoring non-symmetric conformations that are much less aromatic.¹⁻³ The larger the annulene, the less aromatic the molecule is expected to be. For this reason, it is difficult to find large aromatic macrocycles.^{2,4,5} Hence, geometrical constraints are imposed in some large macrocyclic structures with the hope to preserve conjugation, aromaticity, and quantum coherence.

Among the molecules with the largest aromatic rings, it is worth highlighting the dodecaphyrin structures synthesized by Osuka and co-workers,^{6,7} which adopt twisted Möbius and Hückel conformations, the annulene-with-an-annulene aromatic super-ring structure of Wu *et al.*,⁸ and the π -conjugated six-porphyrin nanoring of Anderson and co-workers (see Figure 1).⁹ The latter work synthesized and analyzed the aromaticity of a six-porphyrin nanoring (c-P6 · T6) in four different oxidation states (c-P6 · T6, c-P6 · T6⁴⁺, c-P6 · T6⁶⁺, and c-P6 · T6¹²⁺), concluding from ¹H-NMR, NICS, and ACID analyses that the neutral and the c-P6 · T6¹²⁺ species are non-aromatic, whereas c-P6 · T6⁴⁺ and c-P6 · T6⁶⁺ are, respectively, antiaromatic and aromatic.^{9,10} These molecules were the first of a series of similar large macrocyclic structures exhibiting (anti)aromaticity.^{9,11-14}

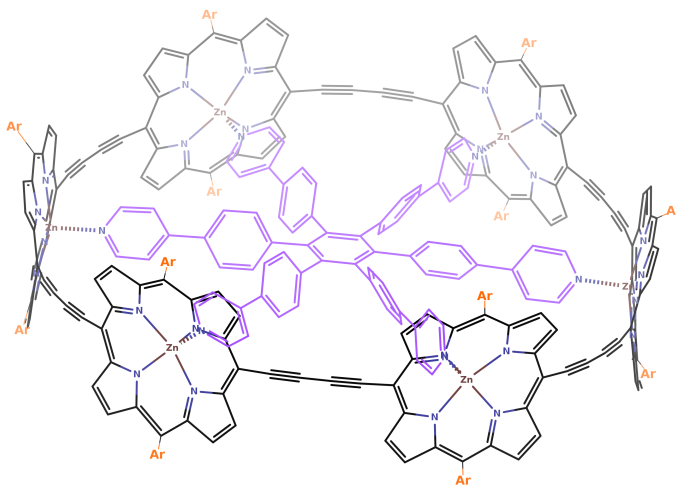


Figure 1: Structure of c-P6. For the nanoring structure with the aryl group substituents (orange) and the encapsulated template (purple) we will use the notation c-P6 · T6. In Ref. 9, they synthesized the compound with Ar=(3,5-bis(trihexylsilyl))phenyl, whereas the computational studies used Ar=Ph for c-P6 · T6 and Ar=H for c-P6.

Porphyrin nanorings are very attractive compounds because they offer an end-free π -conjugated system with remarkable properties such as photophysical and guest-encapsulating, which might lead to a myriad of applications in the field of single-molecule electronics,^{15,16} serve as light-harvesting antennas,¹⁷ or investigate energy transfer in biomimetic systems,¹⁸ among others.^{9,13,19-25} In this sense, the interest and the utility of the compounds synthesized by the group of Anderson are beyond question. However, in this work, we demonstrate that the aromaticity of this large macrocycle is questionable. We perform a throughout analysis of these species using several density functional approximations (DFAs) and various tools to analyze the aromaticity, providing compelling evidence that the conclusions are highly sensitive to the level of calculation employed. In particular, B3LYP presents large delocalization errors that artificially enhance the aromaticity of c-P6⁶⁺, whereas CAM-B3LYP provides an excellent agreement with the experimental data available. Through careful computational analysis and the judicious examination of the ¹H-NMR data, we conclude that c-P6⁶⁺ is not aromatic.

Additionally, we perform a complete electronic structure study of the four oxidation states of the nanoring and analyze the aromaticity of these molecules. By studying the local aromaticity of the six porphyrins that compose the belt structure and the conjugated linkers (the butadiyne fragments linking the porphyrins), we identify the parts of the molecule that are responsible for the absence of the global aromatic ring current. Finally, we provide some hints that might aid in the synthesis of large aromatic nanorings.

Geometry assessment

The synthesized molecules consist of a belt nanoring structure of six porphyrins with aryl groups and an encapsulated template (c-P6 · T6, see Figure 1).⁹ In the original manuscript, Anderson *et al.* computationally analyzed the aromaticity of the nanoring structure without the aryl groups and the template (*i.e.*, c-P6) because the nanoring belt structure is the one responsible for the aromaticity of these compounds. In this work, we have also analyzed the effect of adding the encapsulated template and the aryl groups to the c-P6⁶⁺ structure.

Table 1: Comparison of CAM-B3LYP and M06-2X ground state geometries against the B3LYP one. All root mean square deviations (RMSD)²⁶ are given with respect to the B3LYP minimum. TS c-P6⁶⁺ corresponds to the transition state of c-P6⁶⁺ connecting two energy minima (see Figure 2).

Species	RMSD(CAM-B3LYP)	RMSD (M06-2X)
c-P6	0.05	0.04
c-P6 ⁴⁺	0.66	0.20
c-P6 ⁶⁺	0.22	0.21
c-P6 ¹²⁺	0.04	0.04
TS c-P6 ⁶⁺	0.06	0.07

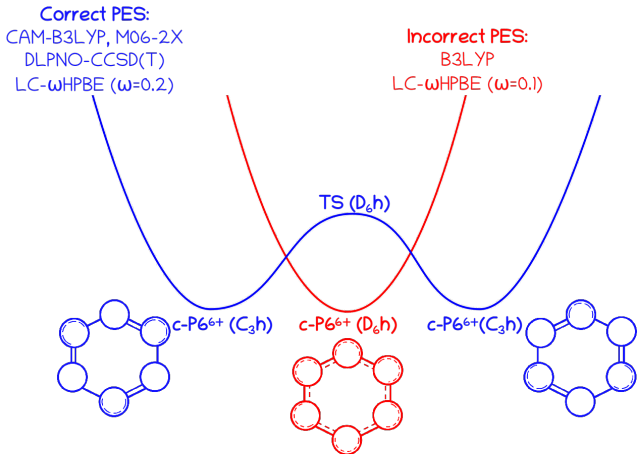


Figure 2: Sketch of the potential energy surface of c-P6⁶⁺ around the energy minimum as described by different DFAs.

DFAs with a low percentage of Hartree-Fock (HF) exchange (typically, HF[%] \ll 50) at long interelectronic ranges are prone to present large delocalization errors,²⁷ leading to the unphysical overdelocalization of electrons, the underestimation of reaction barriers and charge-transfer excitation energies,²⁷ the overestimation of the conductance of molecular junctions, optical responses,^{28,29} the magnetizability of strong antiaromatic molecules,³⁰ electron conjugation,³¹ and aromaticity,^{32,33} especially in large conjugated macrocycles.^{2,3,34-37} Anderson *et al.*⁹ performed B3LYP (HF[%]=20), M06-2X (HF[%]=54), and ω B97X (HF[%]=0-100) calculations with the 6-31G* basis set but mostly employed the B3LYP results to analyze the aromaticity of these compounds. We have performed additional calculations with CAM-B3LYP (HF[%]=19-65) and LC- ω HPBE (HF[%]=0-100), ω being 0.1 and 0.2 (the larger ω , the larger HF[%] at long range). Although all methods give qualitatively the same structure for the neutral and the c-P6¹²⁺ species, c-P6⁴⁺, and c-P6⁶⁺ present significantly different geometries depending on the amount of long-range HF exchange present in the DFA. While CAM-B3LYP, M06-2X, and LC- ω HPBE($\omega=0.2$) give a less symmetric structure for c-P6⁶⁺, B3LYP and LC- ω HPBE($\omega=0.1$) yield a symmetric aromatic species (see Tables 1 and S2). The first group of DFAs has a large percentage of HF exchange at long range, indicating that the latter DFAs may be suffering from delocalization errors. This is further reinforced by single-point DLPNO-CCSD(T)/def-SVP-C calculations that attribute much lower energy to the less symmetric c-P6⁶⁺ structures of M06-2X and CAM-B3LYP geometries compared to the B3LYP one (see Table 2), and the fact that CAM-B3LYP identifies the symmetric structure as a transition state (TS) connecting to equivalent minimal structures with non-equivalent linkers (see Figure 2). Indeed, the

B3LYP minimal geometry has a great resemblance with the geometry of this TS (see Table 1). The situation is reminiscent of the error committed by B3LYP in the potential energy surface of extended-porphyrins,³⁴ and casts a shadow of doubt over the conclusions obtained using this B3LYP geometry.⁹ In the case of c-P6⁴⁺, single-point DLPNO-CCSD(T)/def-SVP-C calculations identify the B3LYP geometry as the lowest-lying one. Although, in the latter case, the energy differences are so small with respect to other DFAs (2–8 kcal/mol), that one cannot unequivocally draw any conclusion about the geometries (see below for an assessment of the aromaticity of c-P6⁴⁺ calculated with different geometries).

Table 2: c-P6⁴⁺ and c-P6⁶⁺ DLPNO-CC/Def-SVP/C relative energy values with respect to the corresponding lowest value. All T₁ diagnostic³⁸ values are below 0.017. DFT calculations employed the 6-31G* basis set. Energy in kcal/mol.

Species	Optimization	Geometry	ΔE_{CCSD}	$\Delta E_{\text{CCSD(T)}}$
c-P6 ⁴⁺	B3LYP	min	0.0	0.0
	CAM-B3LYP	min	-5.2	7.8
	M06-2X	min	-1.8	5.5
c-P6 ⁶⁺	M06-2X	min	0.0	0.0
	B3LYP	min	81.9	68.4
	CAM-B3LYP	min	8.3	10.9
	CAM-B3LYP	TS	32.4	25.0
	M06-2X	TS	28.2	18.8

Thus far, we have analyzed the isolated nanoring model. At the B3LYP level of theory, the addition of the template and the aryl groups breaks the D_{6h} symmetry that was originally predicted by the naked nanoring, providing an overall geometry that is much closer to the CAM-B3LYP C_{3h} geometry. For B3LYP, M06-2X, and CAM-B3LYP geometries, the root mean square deviations (RSMD) of the ¹H-NMR chemical shifts of various relevant hydrogen atoms are collected in Table 3 (see Figure S1). Reproducing experimental ¹H-NMR values is a very challenging computational task because they depend not only on the molecule’s geometry but also on the solvent and the temperature.³⁹ However, CAM-B3LYP geometry provides the closest agreement with the experiment for all compounds tested, whereas B3LYP’s provides the worst agreement (see Table 3), especially in the case c-P6⁶⁺. Hence, we can safely conclude that CAM-B3LYP geometries and the ¹H-NMR of c-P6, c-P6⁶⁺, and c-P6¹²⁺ conform to the experimental data, whereas, in the case of c-P6⁴⁺, there are large discrepancies between the experimental data and all the examined DFAs. As we shall see in the following sections, obtaining the right geometry is crucial to correctly assess the aromaticity of c-P6⁶⁺. Hereafter, unless otherwise explicitly indicated, we will refer to the results obtained from CAM-B3LYP geometries.

Table 3: Selected ¹H-NMR chemical shift differences (in ppm). RMSD are based on nine ¹H-NMR differences with respect to the experimental data available in Ref. 9. Data for c-P6 · T6⁴⁺ is taken from Ref. 13. α^{temp} and β^{temp} are the corresponding data calculated on the isolated template (see Figure 1). See Figure S1 and Tables S3 and S4 for computational details, proton labels, and all ¹H-NMR values.

Method	data	c-P6 · T6	c-P6 · T6 ⁴⁺	c-P6 · T6 ⁶⁺	c-P6 · T6 ¹²⁺
CAM-B3LYP	β - α	2.40	0.09	-0.79	-2.15
	o'-o	0.09	0.41	-0.19	-0.91
	α - α^{temp}	-6.34	-1.92	-0.97	1.88
	β - β^{temp}	-2.54	-0.44	-0.36	1.13
	RMSD	0.16	-	1.35	0.45
B3LYP	β - α	1.95	-12.75	0.99	-4.37
	o'-o	0.31	36.36	-7.23	-2.67
	α - α^{temp}	-5.34	60.43	-12.26	5.63
	β - β^{temp}	-1.97	49.10	-9.85	2.68
	RMSD	0.30	-	5.36	1.41
Experimental	β - α	2.58	-2.80	-0.44	-2.48
	o'-o	0.26	-	-1.87	-0.74
	α - α^{temp}	-6.31	14.16	-2.83	2.77
	β - β^{temp}	-2.34	12.57	-2.06	1.50

Local aromaticity of the porphyrins

We focus now on the local aromaticity of the porphyrins, which is assessed by studying the circular conjugation pathways that go through C-C or C-N bonds around each porphyrin. The pathway going through the C-N bonds of the imine group is labeled as 'i', whereas the one following the C-C bonds of the imine group is labeled as 'o'. There are 16 pathways for each porphyrin but some of them are equivalent by symmetry. We cannot use NICS to study the local aromaticity because there is a Zn atom in the center of the porphyrin, where we should evaluate the effect of the current strength. Instead of NICS, we employ ACID plots as a magnetic criterion of aromaticity, as well as several electron-delocalization measures of aromaticity.⁴⁰

Table 4: Aromaticity indices for the different pathways within the porphyrins of c-P6 calculated at the CAM-B3LYP/6-31G* level of theory. The number in brackets indicates the number of equivalent pathways.

pathway	FLU	BOA	HOMA	BLA	AV1245	AV _{min}
oooo	0.023	0.235	0.658	0.050	1.64	0.57
iiii	0.007	0.071	0.927	0.017	0.92	0.52
ioio (2)	0.016	0.162	0.778	0.036	1.32	0.52
iiio (4)	0.012	0.119	0.848	0.027	1.13	0.52
iioo (2)	0.016	0.162	0.778	0.036	1.32	0.52
iooi (2)	0.016	0.162	0.778	0.036	1.32	0.52
oooi (4)	0.020	0.200	0.715	0.043	1.49	0.52

In Table 4, the results for all the possible pathways in the porphyrins of the neutral species are collected. The delocalization indices⁴¹ do not show significant differences between neighboring C-N and C-C bonds in the imine group, indicating no clear preferential pathway in the porphyrins of c-P6 (see Figure S3). AV_{min}, which measures the least delocalized fragment along the pathway, does not find significant differences among the paths either, a fact which is further confirmed by the ACID plot of Figure 3a. Other aromaticity measures like FLU or HOMA find some differences between the pathways, but one should keep in mind that, unlike AV_{min}, these indices failed to identify the most aromatic pathway in simple porphyrins.^{3,35}

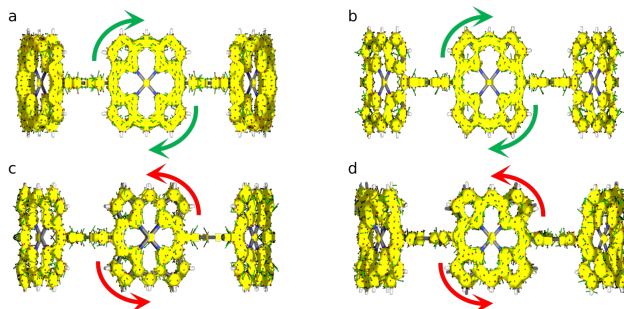


Figure 3: ACID isosurface plots (isocontour value 0.06) for a) c-P6, b) c-P6⁴⁺, c) c-P6⁶⁺, and d) c-P6¹²⁺ at the CAM-B3LYP/6-31G* level of theory.

In Table 5, we collect the results of the most aromatic pathway of the porphyrins for all the oxidation states of the nanoring according to different aromaticity descriptors. All the indices find that the porphyrins of c-P6 are less aromatic than those of porphyrin (see Table S6) but aromatic nonetheless. Although the indices do not agree on the most aromatic pathway of the porphyrins (see Tables S7 and S9), there is a consensus among the descriptors concerning the aromatic character of the porphyrins in c-P6 and the fact that c-P6⁴⁺'s, c-P6⁶⁺'s, and c-P6¹²⁺'s porphyrins are much less aromatic than those of c-P6. ACID plots (see Figure 3) concur with these results, even though they identify the porphyrins in c-P6⁴⁺ as aromatic.

¹H-NMR results were also used by Anderson *et al.*⁹ to assess the aromaticity of the porphyrins. According to the experiment (see Table 3), the differences between the shielding of α and β protons of the template (see Figure S1) are 2.58, -2.80, -0.44, and -2.48 ppm for c-P6 · T6, c-P6 · T6⁴⁺, c-P6 · T6⁶⁺, and

Table 5: Aromaticity indices for the most aromatic pathway of porphyrins calculated at the CAM-B3LYP/6-31G* level of theory.

Species	FLU	HOMA	AV1245	$ \text{AV}_{\min} $	ACID
c-P6	0.007	0.927	1.64	0.57	A
c-P6 ⁴⁺	0.016	0.784	1.45	0.32	A
c-P6 ⁶⁺	0.017	0.760	1.33	0.24	NA
c-P6 ¹²⁺	0.027	0.426	0.63	0.04	NA/AA
porphin	0.006	0.968	2.16	1.28	A

c-P6 · T6¹²⁺, respectively. The latter values are associated with aromatic, antiaromatic, non-aromatic, and antiaromatic porphyrins. CAM-B3LYP values are 2.40, 0.09, -0.79, and -2.15 ppm, in good agreement with the experimental values, whereas the B3LYP values for c-P6 · T6⁴⁺, c-P6 · T6⁶⁺, and c-P6 · T6¹²⁺ show larger discrepancies.

Finally, we study how the constituent parts of the compound change upon oxidation of the nanoring. We have performed an effective oxidation state (EOS)^{42,43} analysis of three different fragments of the nanoring: the zinc atoms (Zn), the porphyrins (P), and the linkers (L). The carbon shared by the porphyrin and the linkers is assigned to the porphyrin. The results of this analysis are collected in Table 6. In all species, the Zn atom has an EOS of +2, indicating that the oxidized electrons never come from the Zn atom. In c-P6⁴⁺, the electrons are subtracted from the butadiyne linkers, distorting the overall symmetry that the linkers had in the neutral species. Interestingly, in compounds with higher oxidation states, c-P6⁶⁺ and c-P6¹²⁺, the electrons are subtracted from the porphyrins, restoring the symmetry of the neutral species. These results agree with the decrease of local aromaticity we have found with the aromaticity descriptors and help to explain the loss of symmetry in the case of c-P6⁴⁺.

Table 6: Effective oxidation States (EOS) of several fragments of the nanoring at the CAM-B3LYP/6-31G* level of theory.

Species	Zn	Porphyrins	Linkers
c-P6	+2	0	-2
c-P6 ⁴⁺	+2	0	(-1)×4 (-2)×2
c-P6 ⁶⁺	+2	+1	-2
c-P6 ¹²⁺	+2	+2	-2

Global aromaticity of the nanoring

In this section, we assess the global aromatic character of the nanoring structure, *i.e.*, we focus on finding a closed conjugation pathway that goes around the nanoring belt. This pathway involves both the porphyrins and the linkers that bridge them. Since we have already studied the aromaticity of the porphyrins, we first focus on the butadiyne linkers and, afterward, we analyze the whole conjugated pathway involving both structures.

In Table 7, we collect the MCI of the six carbons that compose each linker. MCI values measure the extent of electron delocalization along the carbon atoms in the linker,⁴⁴ which is rather small for c-P6 and c-P6¹²⁺, indicating that the linkers cannot contribute to forming a completely delocalized circuit along the nanoring belt (hence, c-P6 and c-P6¹²⁺ cannot be considered aromatic molecules). MCI values for c-P6⁴⁺ and c-P6⁶⁺ exhibit an alternated pattern, *i.e.*, an uneven delocalization of the linkers, which also precludes the appearance of a global conjugated pathway that can be connected with aromaticity. This picture is corroborated by ACID plots shown in Figure 4, where we can see disconnected sections around the position of the linkers for all the oxidation states. From this analysis and the local aromaticity of the porphyrins, we can construct the schematic model of the four nanorings' aromaticity that we collect in the first row of Figure 5.

The global aromaticity of the nanoring can be further analyzed using several aromaticity criteria (for further details see the Supporting Information). We rely here on AV_{\min} ,⁴⁵ which measures the electron

Table 7: MCI ($\times 1000$) values for the six carbon atoms that form the linker bridging two porphyrins.

Species/Linker	L ₁	L ₂	L ₃	L ₄	L ₅	L ₆
c-P6	1	1	1	1	1	1
c-P6 ⁴⁺	20	4	4	20	4	4
c-P6 ⁶⁺	1	21	1	21	1	21
c-P6 ¹²⁺	1	1	1	1	1	1

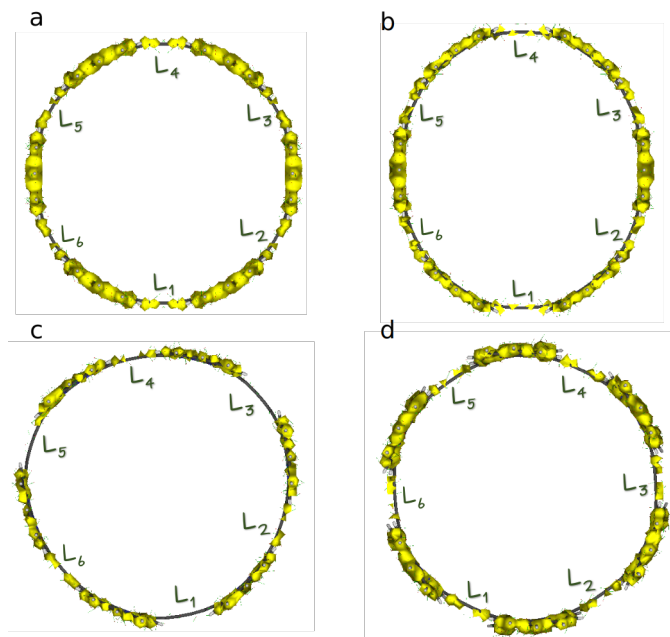


Figure 4: ACID isosurface plots (isocontour value 0.06) for a) c-P6, b) c-P6⁴⁺, c) c-P6⁶⁺, and d) c-P6¹²⁺.

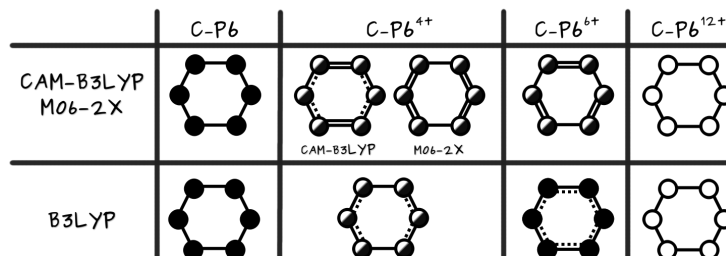


Figure 5: Schematic picture of the global aromatic character of the nanoring from its constituent parts according to the optimized geometries obtained with different DFAs. Full, half-full, and empty circles represent aromatic, weakly aromatic, and non-aromatic porphyrins, respectively. The electron delocalization in the linkers increases from single solid lines (no delocalization) to solid-dashed lines and, finally, double lines.

delocalization along the different aromatic pathways of the nanoring.^{2,35} For c-P6¹²⁺, AV_{\min} is negligible for all the conjugation pathways, clearly establishing the non-aromatic character of this molecule. For c-P6, c-P6⁴⁺, and c-P6⁶⁺, the values of AV_{\min} are negligible for most pathways except the one that passes through the nitrogen atoms of imine groups of each porphyrin. In this pathway, AV_{\min} is also low but not negligible, which is reminiscent of some expanded porphyrin structures, which were considered very weakly aromatic or antiaromatic.³⁵ There is, however, an important difference concerning the latter case: in aromatic expanded porphyrins, the minimal value of electron delocalization was achieved twice or three times during the whole pathway (see Figure S4), whereas in the case of c-P6⁴⁺ and c-P6⁶⁺ there are multiple (over twenty) low-delocalization fragments, as we can see in the delocalization profile of Figure 6. For this reason, all the nanorings in the present study are considered non-aromatic, according

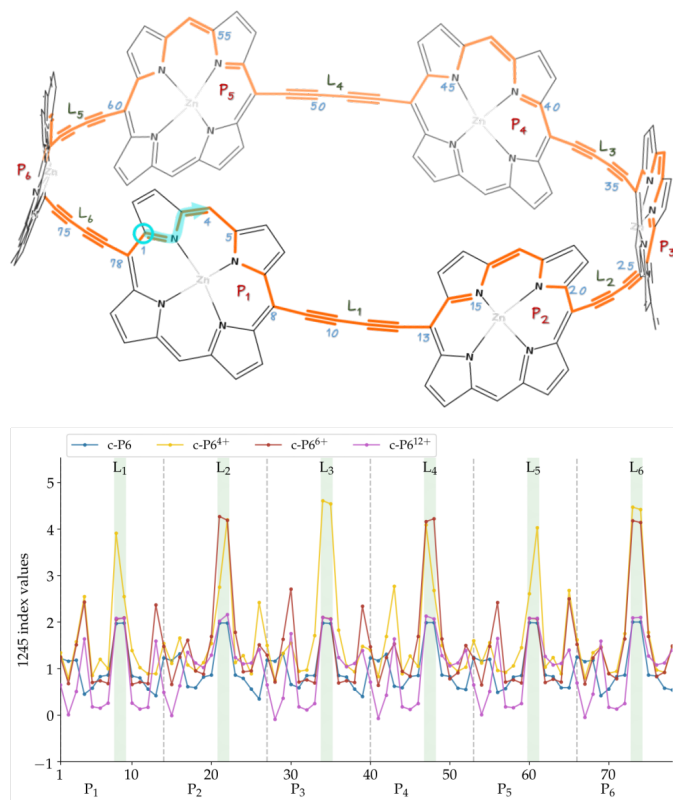


Figure 6: The 1245-index distribution along the most aromatic path.

to AV_{\min} . Interestingly, for $c\text{-P6}^{4+}$, $c\text{-P6}^{6+}$, and $c\text{-P6}^{12+}$, the vast majority of these disconnection points occur in the transition from the porphyrin to the linker, whereas for $c\text{-P6}$, the least delocalized fragment corresponds to an internal fragment inside the porphyrin. ACID confirms the most aromatic pathway indicated by AV_{\min} , and its discontinuous isosurfaces (see Figure 4) also suggest that the molecules are non-aromatic, especially $c\text{-P6}^{6+}$, for which large discontinuities also occur in the vicinity of the linkers. Finally, we have performed two-dimensional NICS profiles^{46,47} and collected them in l.h.s. of Figure 7. In all cases, the values of the NICS inside and outside the nanoring belt are very close to zero, further confirming the global non-aromatic character of these molecules.

Figure 5, provides a qualitative comparison of the aromaticity analyses performed on CAM-B3LYP (or M06-2X) and B3LYP geometries. There are no significant differences for $c\text{-P6}$ and $c\text{-P6}^{12+}$, as expected from the similarity of these geometries regardless of the DFA employed for the optimization. In fact, only for $c\text{-P6}^{6+}$, we obtain a completely different picture of the aromaticity from different methods. The large negative number of the two-dimensional NICS profile in the vicinity of the nanoring center (see the r.h.s. of Figure 7) and the continuous ACID plots (Figure S14) indicate that the B3LYP geometry is globally aromatic. This is further corroborated by the larger AV_{\min} value and, most importantly, by the 1245-index distribution profiles (Figure 8), where we observe the drastic reduction in the number of fragments with a low delocalization. The comparison of the aromaticity measures between B3LYP and CAM-B3LYP $c\text{-P6}^{4+}$ geometries also suggests that B3LYP overestimates the global antiaromaticity of this molecule, as the NICS (see Figure 7 and Table S14) shows a large positive value in the center of the ring and the ACID plots exhibit a continuous paratropic ring current (Figure S14). These results align with the recent results of Sundholm and co-workers, which identify CAM-B3LYP as a good method to calculate magnetizabilities⁴⁸ and the fact that B3LYP tends to overestimate the paramagnetic ring currents.⁴⁹ On the other hand, AV_{\min} and the 1245-index distribution profiles (Figure S8) are consistent with $c\text{-P6}^{4+}$ being a rather antiaromatic or a weakly aromatic molecule, regardless of the geometry. Since the results of no DFA satisfactorily conform to the experimental data, the results of $c\text{-P6}^{4+}$ should be taken with caution.

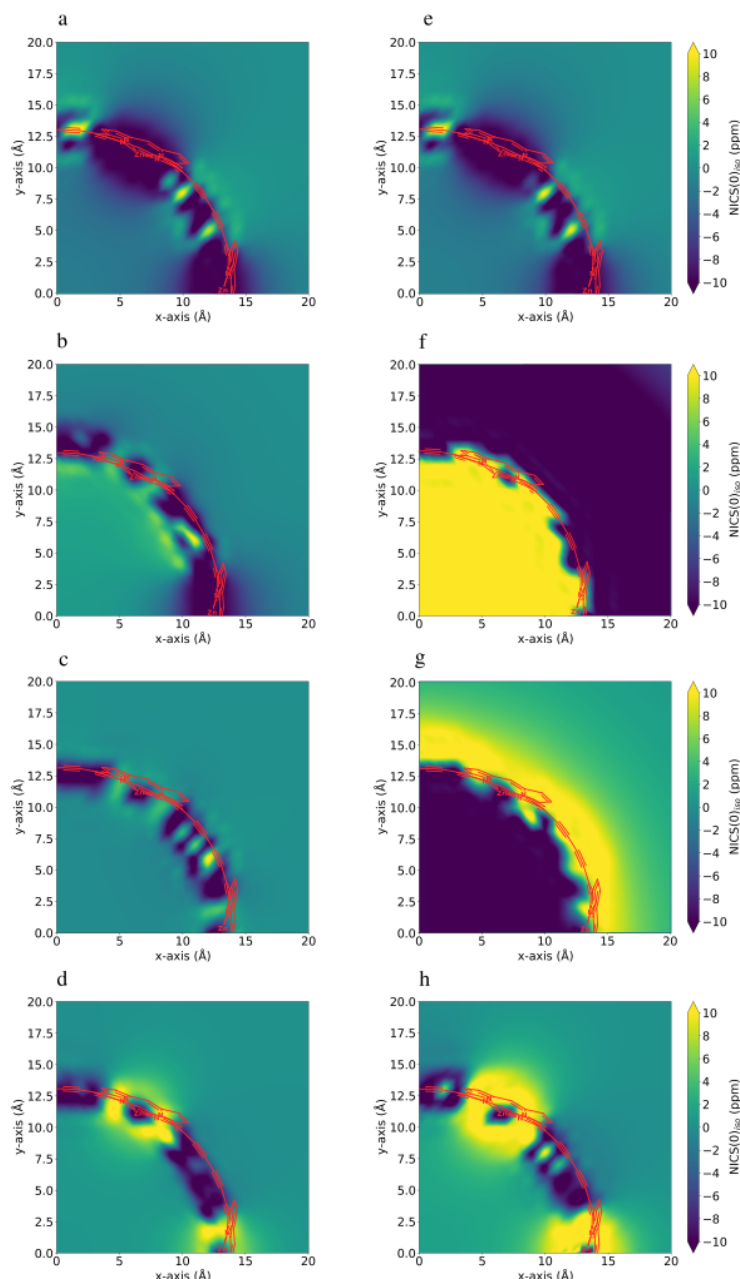


Figure 7: NICS(0)_{iso} grid plots for c-P6, c-P6⁴⁺, c-P6⁶⁺, and c-P6¹²⁺ species from top to bottom respectively. (a-d) corresponding to the CAM-B3LYP optimized geometries and (e-h) to the B3LYP ones. See Figure S15 and Table S14 for further details of this computation.

Anderson and co-workers' strongest experimental evidence to assess the global aromaticity of c-P6⁶⁺ comes from the ¹H-NMR data. They study the (de)shielding of the trihexylsilyl groups (see Figure 1), the *ortho* protons (*o* and *o'*) in the aryl groups (see Figure S1), and the shielding difference between the α (or β) proton of the bound template and the free template, $\Delta\delta_\alpha = \delta_\alpha - \delta_{\alpha\text{temp}}$ ($\Delta\delta_\beta = \delta_\beta - \delta_{\beta\text{temp}}$).¹³ The former data cannot be studied in the present paper due to the computational limitations that pose such large structure. However, we can analyze α , β and *ortho* protons. The B3LYP geometry finds that $\delta_{o'} - \delta_o$ is -7.23 ppm, whereas CAM-B3LYP and M06-2X results are -0.19 ppm and -0.36 ppm, respectively, which are in closer agreement with the experiment,⁹ 1.87 ppm (see Tables 3 and S3). The CAM-B3LYP values of $\Delta\delta_\alpha$ and $\Delta\delta_\beta$ are in much better agreement with the experimental data than the B3LYP ones. Rikhaus *et al.*¹³ argue that $\Delta\delta_\alpha < 0$ and $\Delta\delta_\beta < 0$ are an indication of the presence of a global aromatic current (while the opposite is evidence of an antiaromatic current). However, this would indicate not only that c-P6·T6⁶⁺ is globally aromatic, but also that c-P6·T6 is even more aromatic than the former,

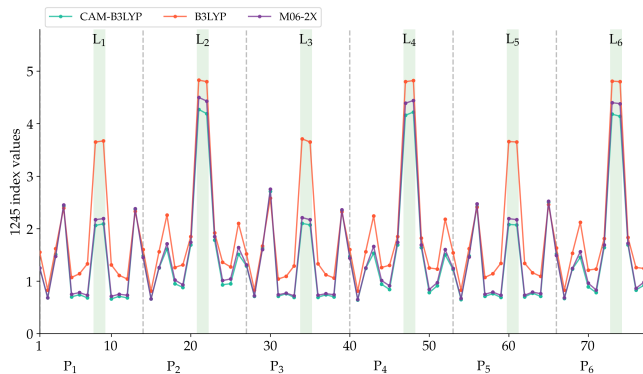


Figure 8: The 1245-index distribution along the most aromatic path of $c\text{-P6}\cdot\text{T6}^{6+}$. See Figure 6 to locate the points of the molecule represented in the x-axis.

which is not supported by any other experimental or computational data. We have also calculated $\Delta\delta_\alpha$ and $\Delta\delta_\beta$ in a bound template in which we have eliminated the alleged current (by removing the bridging butadiyne linkers), and we have found negative and positive $\Delta\delta_\alpha$ and $\Delta\delta_\beta$, which would support the presence of a ring current even in the absence of connectivity among the porphyrins (see Supporting Information). These results bring about two important conclusions. First of all, it reinforces the idea that CAM-B3LYP (or M06-2X) are more adequate methods to obtain the geometry of potential aromatic molecules than B3LYP, which incurs large delocalization errors. Second, through various aromaticity probes, we have shown that the B3LYP geometry of $c\text{-P6}^{6+}$ corresponds to a quite aromatic molecule with $\delta_{o'} - \delta_o = -7.23$ ppm, and $\Delta\delta_\alpha = -12.26$ ppm. Hence, if the corresponding experimental values are only -1.87 ppm and -2.83 ppm, respectively, this is clearly suggesting that $c\text{-P6}\cdot\text{T6}^{6+}$ is either very weakly aromatic or non-aromatic, as the CAM-B3LYP results indicate. This result is further reinforced by a recent finding⁵⁰ that the experimental aromatic stabilization energy of $c\text{-P6}\cdot\text{T6}^{6+}$ is ca. 1.2 kcal/mol, which is relatively small for an aromatic molecule.

Conclusions

We have provided compelling evidence that the B3LYP description of $c\text{-P6}^{6+}$ suffers from severe delocalization errors that result in the overestimation of the aromaticity of this species. This is yet another proof^{2,3,31-35} that DFAs with a low percentage of long-range HF exchange should not be used to analyze aromatic compounds, especially large conjugated circuits. Computational results at the CAM-B3LYP level comfort with the experimental data for $c\text{-P6}$, $c\text{-P6}^{6+}$, and $c\text{-P6}^{12+}$, whereas, for $c\text{-P6}^{4+}$, none of the DFAs we have employed provides a satisfactory agreement with the experiment. Through careful computational analysis and the judicious examination of the $^1\text{H-NMR}$ data, unlike Refs. 9 and 13, we conclude that $c\text{-P6}^{6+}$ is not aromatic and that $^1\text{H-NMR}$ data cannot be used to unequivocally assess the aromaticity of this species. Hence, none of the large nanorings studied can be considered aromatic, and the quest for large aromatic nanorings should be continued. Although enhanced aromaticity of the porphyrin units would help to increase the global aromaticity of these nanorings, our results show that the main reason behind the absence of an aromatic ring current in these nanorings is the low delocalization in the transition from the porphyrins to the bridging butadiyne linkers, which disrupts the overall conjugated circuit.

Computational Details

Geometry optimizations have been performed with B3LYP-D3,^{51,52} CAM-B3LYP-D3,⁵³ and M06-2X⁵⁴ DFAs in combination with the 6-31G* basis set. The geometry minima of all the oxidation states of $c\text{-P6}$ and the transition state of $c\text{-P6}^{6+}$ have been confirmed by analyzing the harmonic frequencies. For $c\text{-P6}^{6+}$, additional geometry optimizations with LC- ω HPBE ($\omega=0.1$ and $\omega=0.2$)⁵⁵ have been performed. For $c\text{-P6}^{6+}$ and $c\text{-P6}^{4+}$, single-point domain-based local pair natural orbital coupled cluster (DLPNO-CCSD(T))⁵⁶ calculations have been performed with the ORCA software⁵⁷ to assess the validity of the geometry optimization with the aforementioned DFAs.

The aromaticity was analyzed with nuclear-independent chemical shift (NICS),⁵⁸ the anisotropy of the induced current density (ACID) plots,⁵⁹ the harmonic oscillator model of aromaticity (HOMA),⁶⁰ and different electronic aromaticity indices.⁴⁰ Namely, FLU,^{61,62} MCI,⁶³ AV1245,⁶⁴ and AV_{min}⁴⁵ com-

putations were performed with the AIMall⁶⁵ and ESI-3D^{41,61,66} suites of programs. We also dissected AV1245 values and assigned a delocalization value to each atom in the corresponding pathway by splitting the MCI(1,2,4,5) of each five-atom fragment among the atoms in the fragment.⁶⁴ These profiles are called 1245-index distribution plots and help detect the fragments responsible for the loss of aromaticity.

Acknowledgments

This work has been supported by grants from the Spanish government MICINN (PGC2018-098212-B-C21, CTQ2016-80375-P, EUR2019-103825, PID2019-105488GB-I00, and PCI2019-103657), Diputación Foral de Gipuzkoa (2019-CIEN-000092-01), and Gobierno Vasco (IT1346-19, IT1254-19, PRE_2016_1_0159, and PIBA19-0004). E.R.C. acknowledges funding from the Juan de la Cierva program IJCI-2017-34658.

Conflicts of interest

The authors declare no conflicts of interest.

Keywords: aromaticity · nanoring · delocalization error

References

- [1] C. Gellini, P. R. Salvi, *Symmetry* **2010**, *2*, 1846–1924.
- [2] I. Casademont-Reig, E. Ramos-Cordoba, M. Torrent-Sucarrat, E. Matito, *Molecules* **2020**, *25*, 711.
- [3] I. Casademont-Reig, E. Ramos-Cordoba, M. Torrent-Sucarrat, E. Matito, *Aromaticity: Modern Computational Methods and Applications* Aromaticity descriptors based on electron delocalization, S. 235–258, Elsevier, The Netherlands, **2021**.
- [4] E. Matito, F. Feixas, M. Solà, *J. Mol. Struct. (Theochem)* **2007**, *811*, 3–11.
- [5] C. S. Wannere, D. Moran, N. L. Allinger, B. A. Hess, L. J. Schaad, P. v. R. Schleyer, *Org. Lett.* **2003**, *5*, 2983–2986.
- [6] T. Soya, W. Kim, D. Kim, A. Osuka, *Chem. Eur. J.* **2015**, *21*, 8341–8346.
- [7] T. Soya, H. Mori, A. Osuka, *Angew. Chem. Int. Ed.* **2018**, *130*, 16108–16112.
- [8] C. Liu, M. E. Sandoval-Salinas, Y. Hong, T. Y. Gopalakrishna, H. Phan, N. Aratani, T. S. Heng, J. Ding, H. Yamada, D. Kim, D. Casanova, J. Wu, *Chem* **2018**, *4*, 1586–1595.
- [9] M. D. Peeks, T. D. Claridge, H. L. Anderson, *Nature* **2017**, *541*, 200–205.
- [10] P. Kowalska, M. D. Peeks, T. Roliński, H. L. Anderson, J. Waluk, *Phys. Chem. Chem. Phys.* **2017**, *19*, 32556–32565.
- [11] M. D. Peeks, J. Q. Gong, K. McLoughlin, T. Kobatake, R. Haver, L. M. Herz, H. L. Anderson, *J. Phys. Chem. Lett.* **2019**, *10*, 2017–2022.
- [12] S. M. Kopp, H. Gotfredsen, J.-R. Deng, T. D. Claridge, H. L. Anderson, *J. Am. Chem. Soc.* **2020**, *142*, 19393–19401.
- [13] M. Rickhaus, M. Jirasek, L. Tejerina, H. Gotfredsen, M. D. Peeks, R. Haver, H.-W. Jiang, T. D. Claridge, H. L. Anderson, *Nat. Chem.* **2020**, *12*, 236–241.
- [14] J. K. Sprafke, D. V. Kondratuk, M. Wykes, A. L. Thompson, M. Hoffmann, R. Drevinskas, W.-H. Chen, C. K. Yong, J. Karnbratt, J. E. Bullock, et al., *J. Am. Chem. Soc.* **2011**, *133*, 17262–17273.
- [15] P. Parkinson, D. V. Kondratuk, C. Menelaou, J. Q. Gong, H. L. Anderson, L. M. Herz, *J. Phys. Chem. Lett.* **2014**, *5*, 4356–4361.
- [16] M. D. Peeks, C. E. Tait, P. Neuhaus, G. M. Fischer, M. Hoffmann, R. Haver, A. Cnossen, J. R. Harmer, C. R. Timmel, H. L. Anderson, *J. Am. Chem. Soc.* **2017**, *139*, 10461–10471.
- [17] C. Maeda, S. Toyama, N. Okada, K. Takaishi, S. Kang, D. Kim, T. Ema, *J. Am. Chem. Soc.* **2020**, *142*, 15661–15666.

- [18] P. Parkinson, C. E. Knappke, N. Kamonsutthipajjit, K. Sirithip, J. D. Matichak, H. L. Anderson, L. M. Herz, *J. Am. Chem. Soc.* **2014**, *136*, 8217–8220.
- [19] M. Rickhaus, A. Vargas Jentzsch, L. Tejerina, I. Grübner, M. Jirasek, T. D. W. Claridge, H. L. Anderson, *J. Am. Chem. Soc.* **2017**, *139*, 16502–16505.
- [20] M. D. Peeks, M. Jirasek, T. D. Claridge, H. L. Anderson, *Angew. Chem. Int. Ed.* **2019**, *58*, 15717–15720.
- [21] R. Haver, L. Tejerina, H.-W. Jiang, M. Rickhaus, M. Jirasek, I. Grübner, H. J. Eggimann, L. M. Herz, H. L. Anderson, *J. Am. Chem. Soc.* **2019**, *141*, 7965–7971.
- [22] J. Cremers, R. Haver, M. Rickhaus, J. Q. Gong, L. Favereau, M. D. Peeks, T. D. Claridge, L. M. Herz, H. L. Anderson, *J. Am. Chem. Soc.* **2018**, *140*, 5352–5355.
- [23] P. Motloch, P. S. Bols, H. L. Anderson, C. Hunter, *Chem. Sci.* **2021**, *12*, 1427–1432.
- [24] G. Bressan, M. D. Peeks, H. L. Anderson, S. R. Meech, I. A. Heisler, *J. Phys. Chem. C* **2019**, *123*, 27222–27229.
- [25] C. Roche, Q. Luo, G. Gil-Ramírez, H.-W. Jiang, D. R. Kohn, Y. Xiong, A. L. Thompson, H. L. Anderson, *J. Org. Chem.* **2017**, *82*, 7446–7462.
- [26] J. Charnley, L. Bratholm, „Calculate Root-mean-square deviation (RMSD) of Two Molecules Using Rotation“, gitHub, v.1.3.2.
- [27] P. Mori-Sánchez, A. J. Cohen, W. Yang, *Phys. Rev. Lett.* **2008**, *100*, 146401.
- [28] R. Zalesny, M. Medved’, S. P. Sitkiewicz, E. Matito, J. M. Luis, *J. Chem. Theory Comput.* **2019**, *15*, 3570–3579.
- [29] P. Besalú-Sala, S. P. Sitkiewicz, P. Salvador, E. Matito, J. M. Luis, *Phys. Chem. Chem. Phys.* **2020**, *22*, 11871–11880.
- [30] R. R. Valiev, I. Benkyi, Y. V. Konyshov, H. Fliegl, D. Sundholm, *J. Phys. Chem. A* **2018**, *122*, 4756–4767.
- [31] J. Sancho-García, A. Pérez-Jiménez, *Phys. Chem. Chem. Phys.* **2007**, *9*, 5874–5879.
- [32] C. S. Wannere, K. W. Sattelmeyer, H. F. Schaefer III, P. v. R. Schleyer, *Angew. Chem. Int. Ed.* **2004**, *43*, 4200–4206.
- [33] D. W. Szczepanik, M. Solà, M. Andrzejak, B. Pawełek, J. Dominikowska, M. Kukułka, K. Dyduch, T. M. Krygowski, H. Szatyłowicz, *J. Comput. Chem.* **2017**, *38*, 1640–1654.
- [34] M. Torrent-Sucarrat, S. Navarro, F. P. Cossío, J. M. Anglada, J. M. Luis, *J. Comput. Chem.* **2017**, *38*, 2819–2828.
- [35] I. Casademont-Reig, T. Woller, J. Contreras-García, M. Alonso, M. Torrent-Sucarrat, E. Matito, *Phys. Chem. Chem. Phys.* **2018**, *20*, 2787–2796.
- [36] M. Torrent-Sucarrat, S. Navarro, E. Marcos, J. M. Anglada, J. M. Luis, *J. Phys. Chem. C* **2017**, *121*, 19348–19357.
- [37] T. Woller, A. Banerjee, N. Sylvetsky, G. Santra, X. Deraet, F. De Proft, J. M. Martin, M. Alonso, *J. Phys. Chem. A* **2020**, *124*, 2380–2397.
- [38] T. J. Lee, *Chem. Phys. Lett.* **2003**, *372*, 362–367.
- [39] C. Benzi, O. Crescenzi, M. Pavone, V. Barone, *Magn. Reson. Chem.* **2004**, *42*, S57–S67.
- [40] F. Feixas, E. Matito, J. Poater, M. Solà, *Chem. Soc. Rev.* **2015**, *44*, 6389–6646.
- [41] E. Matito, M. Solà, P. Salvador, M. Duran, *Faraday Discuss.* **2007**, *135*, 325–345.
- [42] E. Ramos-Cordoba, V. Postils, P. Salvador, *J. Chem. Theory Comput.* **2015**, *11*, 1501–1508.

- [43] V. Postils, C. Delgado-Alonso, J. M. Luis, P. Salvador, *Angew. Chem. Int. Ed.* **2018**, *130*, 10685–10689.
- [44] F. Feixas, E. Matito, J. Poater, M. Solà, *J. Phys. Chem. A* **2011**, *115*, 13104–13113.
- [45] C. García-Fernández, E. Sierda, M. Abadia, B. E. C. Bugenhagen, M. H. Prosenc, R. Wiesendanger, M. Bazarnik, J. E. Ortega, J. Brede, E. Matito, A. Arnau, *J. Phys. Chem. C* **2017**, *121*, 27118–27125.
- [46] J. O. C. Jiménez-Halla, E. Matito, J. Robles, M. Solà, *J. Organomet. Chem.* **2006**, *691*, 4359–4366.
- [47] A. Stanger, *J. Org. Chem.* **2006**, *71*, 883–893.
- [48] S. Lehtola, M. Dimitrova, H. Fliegl, D. Sundholm, *J. Chem. Theory Comput.* **2021**, *17*, 1457–1468.
- [49] R. R. Valiev, H. Fliegl, D. Sundholm, *Chem. Commun.* **2017**, *53*, 9866–9869.
- [50] M. Jirásek, M. Rickhaus, L. Tejerina, H. L. Anderson, *J. Am. Chem. Soc.* **2021**, *143*, 2403–2412.
- [51] A. D. Becke, *J. Chem. Phys.* **1993**, *98*, 5648–5652.
- [52] P. J. Stephens, F. J. Devlin, C. F. Chabalowski, M. J. Frisch, *J. Phys. Chem.* **1994**, *98*, 11623–11627.
- [53] T. Yanai, D. P. Tew, N. C. Handy, *Chem. Phys. Lett.* **2004**, *393*, 51–57.
- [54] Y. Zhao, D. G. Truhlar, *Theor. Chem. Acc.* **2008**, *120*, 215–241.
- [55] O. A. Vydrov, G. E. Scuseria, *J. Chem. Phys.* **2006**, *125*, 234109.
- [56] C. Riplinger, B. Sandhoefer, A. Hansen, F. Neese, *J. Chem. Phys.* **2013**, *139*, 134101.
- [57] F. Neese, *WIREs, Comput. Mol. Sci.* **2018**, *8*, e1327.
- [58] P. v. R. Schleyer, C. Maerker, A. Dransfeld, H. Jiao, N. J. v. E. Hommes, *J. Am. Chem. Soc.* **1996**, *118*, 6317–6318.
- [59] D. Geuenich, K. Hess, F. Köhler, R. Herges, *Chem. Rev.* **2005**, *105*, 3758–3772.
- [60] M. K. Cyrancki, *Chem. Rev.* **2005**, *105*, 3773–3811.
- [61] E. Matito, M. Duran, M. Solà, *J. Chem. Phys.* **2005**, *122*, 014109.
- [62] E. Matito, M. Duran, M. Solà, *J. Chem. Phys.* **2006**, *125*, 059901.
- [63] P. Bultinck, R. Ponec, S. Van Damme, *J. Phys. Org. Chem.* **2005**, *18*, 706–718.
- [64] E. Matito, *Phys. Chem. Chem. Phys.* **2016**, *18*, 11839–11846.
- [65] T. A. Keith, „AIMAll (Version 14.11.23)“, **2014**, tK Gristmill Software, Overland Park KS, USA (aim.tkgristmill.com).
- [66] E. Matito, „ESI-3D: Electron Sharing Indices Program for 3D Molecular Space Partitioning“, **2015**, institute of Computational Chemistry and Catalysis, University of Girona, Catalonia, Spain.

Chapter 9

Computational modeling of UV-Vis spectra and redox potentials

Computational modeling of UV-Vis spectra and redox potentials

Irene Casademont-Reig,^{a,b} Arnau Call,^c Carla Casadevall,^c Sergio Fernández,^c
Julio Lloret-Fillol,^{*c,d} Eloy Ramos-Cordoba^{*a,b} and Eduard Matito^{*a,e}

^a Donostia International Physics Center (DIPC), 20018 Donostia, Euskadi, Spain.

^b Polimero eta Material Aurreratuak: Fisika, Kimika eta Teknologia, Kimika Fakultatea, Euskal Herriko Unibertsitatea UPV/EHU, P.K. 1072, 20080 Donostia, Euskadi, Spain.

^c Institute of Chemical Research of Catalonia (ICIQ), The Barcelona Institute of Science and Technology, Avinguda Paisos Catalans 16, 43007 Tarragona, Catalonia, Spain.

^d Catalan Institution for Research and Advanced Studies (ICREA), Passeig Lluís Companys, 23, 08010 Barcelona, Spain.

^e Ikerbasque, Basque Foundation for Science, Plaza Euskadi 5, 48009 Bilbao, Euskadi, Spain.

^e Correspondence: eloy.raco@gmail.com; ematito@gmail.com

Abstract

Nowadays, the most available renewable energy source on the planet is sunlight. Since fossil fuels have a known limit and may run out shortly, it is vital to know how to take advantage of renewable energies. The effectiveness of the light-harvesting process plays a fundamental role in the production of electricity from sunlight. For this reason, it is essential to correctly describe the molecules in charge of absorbing light in this process, the photosensitizers, to later design more effective systems. In this work, we define a complete protocol to characterize the electronic structure of a set of copper and iridium photosensitizers. These systems will be used to calibrate the computational method to obtain the structures, the UV-Vis spectra, and the redox potentials. Then, the same method will be applied to characterize a cobalt family of complexes. It has been corroborated that tuning a range-separated functional improves the UV-Vis absorption spectra of the photosensitizers, which present metal-to-ligand charge transfer excitations. In addition, in general, this procedure also slightly improves the calculations of the reduction potentials.

1 Introduction

The increase in world population and the economic growth imply a higher energy demand. According to the BP Statistical Review of world energy Consumption 2020,^{1,2} the primary energy consumption grew by 1.3% in 2019. Despite the increase of energy consumption by renewables, still, the 84% of world's primary energy consumption came from fossil fuels in 2019. Oil remained on the top of the primary resources of energy (33%) while the remainder came from coal (27%), natural gas (24%), hydropower (6%), renewables (wind, geothermal, biomass, biofuels, and solar, 5%), and nuclear power (4%). With these data, it can be concluded that the current fossil fuel consumption rate is unsustainable since it is based on an essentially non-renewable energy store.

In order to improve the present situation around the world, an alternative is the usage of solar energy fuels, as they represent one of the most promising renewable energy sources due to their high availability.^{3,4} For this reason, in the last few years, research on how to convert sunlight into a clean and carbon-free source of energy and its storage has increased. The absence of cost-effective storage prevents solar energy from being a primary energy source for society due to the diurnal variation. Hence, new approaches are needed to provide sustainable resources for the obtention of fuels and commodities.⁵

Nowadays, a common option to produce electricity from solar light is photovoltaic solar cells. The vast majority of cells are made of highly pure silicon. However, as this highly pure silicon production is a very complex process, expensive, and high consumption energy process, the price of this type of solar cell is higher than other solar cells.⁶⁻⁸ One promising alternative to the highly pure silicon cells is solar cells based on dyes, named Dye-Sensitized Solar Cells (DSSC, DSC, or DYSC)^{9,10} because they are easier to build, very cheap, more flexible, and thinner (Figure 1). In addition, there are more emerging photovoltaic technologies besides DSSC, such as perovskite photovoltaics, organic photovoltaics, and inorganic quantum dot solar cells.³

Unfortunately, DSSCs do not have high efficiencies compared to highly pure silicon cells.^{11,12} While the best commercial silicon cell efficiency is about 23%, DSSCs achieved 13% in 2014.¹³ The improvement of DSSC efficiency would promote one of the most abundant renewable energy sources, as it is sunlight.

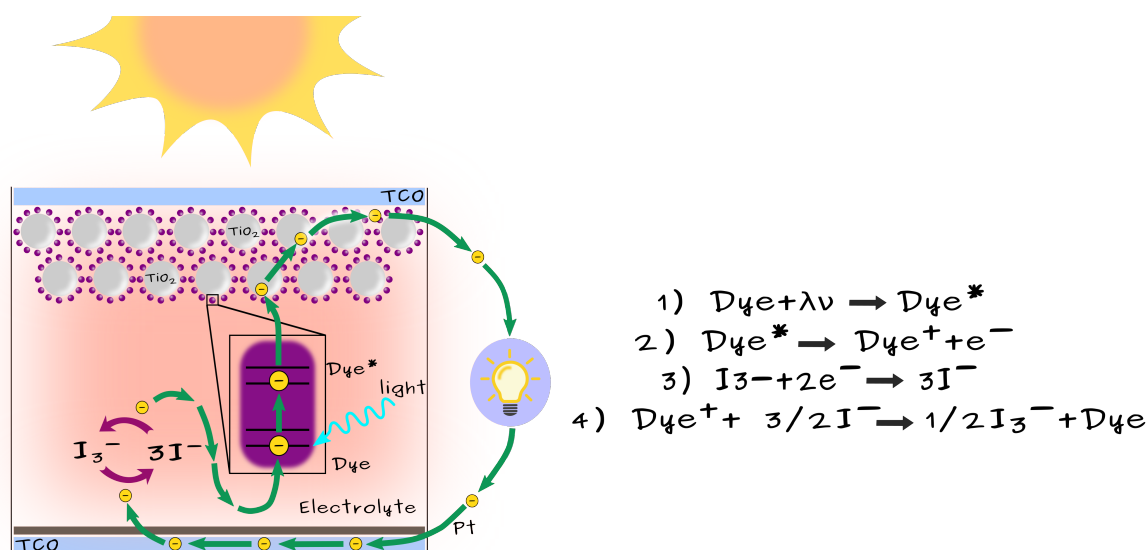


Figure 1: Schematic representation of DSSC operation process and the corresponding reactions.

Photosensitizers (PS) play a crucial role in ensuring effective light-harvesting in all photovoltaic devices and other photochemical processes. An ideal PS has to present the following features to guarantee maximum efficiency: (i) it should present a broad absorption spectrum in the visible region, and if possible, extended over the infrared zone, (ii) it must have a carboxylate or phosphonate group to anchor on the surface of a semiconductor oxide, (iii) the HOMO of the PS must be lower in energy to be able to accept an electron from the electrolyte, (iv) the LUMO of the PS must match with the edge of the conduction band of the oxide to minimize energy losses during the electron transfer, and (v) it should be chemically stable. Putting together (iii) and (iv) PS characteristics, an efficient PS would be the one that presents a large energy gap that will ensure long-lived excited states that suppress the non-radiative relaxation process.^{7,14,15} This is often attained with metal-to-ligand charge transfer (MLCT) states, where an electron is transferred from a metal orbital to a ligand-based orbital.¹⁵ For this reason, some of the most efficient photosensitizers are based on novel metals such as ruthenium (Ru^{II}),¹⁶ and iridium (Ir^{III})^{17,18} Although complexes based on the first-period transition metals are more abundant and cheaper, only Cu(I) complexes are commonly used.^{19–22} Indeed, these latter complexes are more difficult to control due to the presence of excited states centered in the metal with several multiplicities. To address this problem, a strong ligand field has been employed, leading to the discovery of new Cr, Mn, Fe, and Co metal complexes.^{22–24}

Dyes used in DSSCs are suitable for many other applications, such as in photocatalysis, luminescence, and in the water splitting (WS) process (see image 2).^{14,22,25,26} Hydrogen is a suitable energy carrier not found in the Earth in its molecular form, but it could be produced by WS driven by sunlight. The photocatalytic processes that produce H_2 from CO_2 reduction using sunlight directly or indirectly are described as artificial pho-

tosynthesis because they mimic the first step of natural photosynthesis.⁵ Under suitable conditions and design, the reverse operation of DSSC can produce light emission in the devices known as LEDs.^{27–29} A LED is an electronic device based on a semiconductor material that allows unidirectional electric circulation through its structure. LEDs have many advantages compared to conventional bulbs: reduced energy consumption, long life, small size, environmentally friendly, and they do not create strong magnetic fields. Most LEDs are constructed from inorganic compounds, but some devices use organic molecules (OLEDs). OLEDs are cheaper to produce, lighter, and more flexible than their inorganic counterparts. On the contrary, they are less efficient in transforming electricity into light.

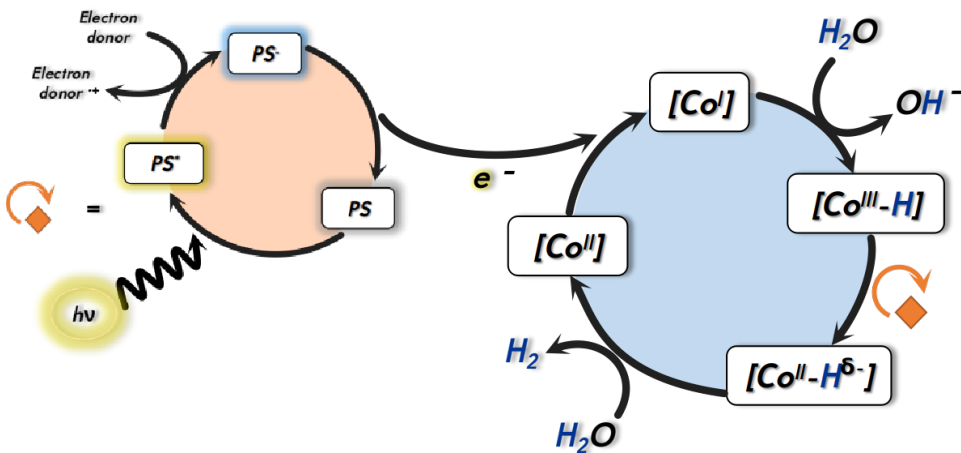


Figure 2: Schematic diagram of the light-driven water reduction mechanism for a cobalt catalyst.

Our aim is to find a computationally efficient procedure to correctly describe the electronic structure, simulate the UV-Vis absorption spectra, and compute the redox potentials of complexes involved in photocatalytic processes like photosensitizers and catalysts. As mentioned above, an ideal PS should have MLCT states. It is well known that CT excitations are not well-described by some density functionals approximations (DFAs) due to the wrong decay of the exchange-correlation (XC) potential.^{30–35} The XC potential of DFAs does not decay asymptotically as $-1/r$, as the exact XC potential does.^{36,37} Accordingly, we will use a range-separated functional, LC- ω PBE,^{38–40} optimizing the attenuating parameter (ω) to accurately simulate the UV-Vis spectrum of different PSs using the Δ SCF method.^{41–44} Optimally tuned (OT) versions of range-separated functionals have already been applied to large molecules to better describe (pseudo)one-electron properties such as fundamental gaps, photoelectron spectrum, and the CT excitation energy.^{41,45–47} There are different methods to tune the ω parameter,^{41–44,48} however, in this work, we will use the approach of Kronik, Baer, and co-workers⁴⁹. In this procedure, the range-separation parameter is optimized by forcing an exact condition, fulfilled by the exact Kohn-Sham (KS) functional ($\epsilon_{HOMO} = -IP$).⁵⁰ Later, this method was called as Δ SCF method.^{41–44} In addition, we will apply the same procedure to calculate the redox potentials of the pho-

tosensitizers. To the best of our knowledge, this latter analysis has never been done before. We expect that this procedure will help us to design in the future more efficient photosensitizers for photosensitizing, luminescence, light-harvesting and photocatalysis applications. In general, all these applications use a PS to harvest the light and present relatively similar processes in which an excitation takes place, and often a redox reaction is also involved. Therefore, the computational procedure can be applied to study any of them.

We have analyzed two families of photosensitizers based on copper and iridium (see Figure 3 and Tables 1 and 2) to study the effect of optimizing the attenuating parameter (ω) on the UV-Vis absorption spectra and redox potential calculations comparing them with the experimental data available. These dyes could be used in DSSC, OLEDs, and WS, among others procedures, if they present the optimal features.

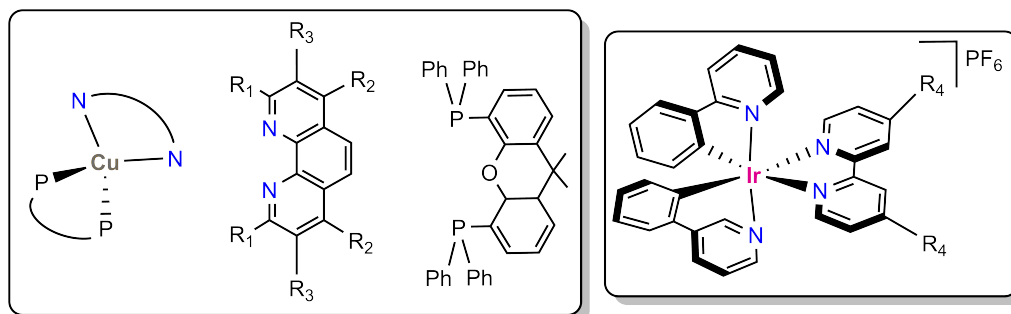


Figure 3: Structure of the studied copper and iridium photosensitizer families.

The family of copper(I) dyes is inspired by the photosensitizers that M. Beller developed,^{19,20} and they are known to be active in photocatalysis reactions as they have redox potentials close to the ones required by the catalyst. At the same time, iridium(III) complexes present outstanding photophysical and electrochemical properties. For this reason, we proposed to study the set of iridium complexes based on the ones synthesized by Zysman-Colman et al.¹⁸ We have labeled all the photosensitizers using the acronym PS and a number (See Tables 1 and 2).

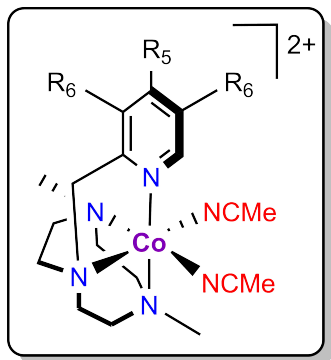
Table 1: Set of copper photosensitizers studied:

Photosensitizers:	R ₁	R ₂	R ₃
PS ₁	H	H	H
PS ₂	H	CF ₃	H
PS ₃	H	Ph	H
PS ₄	H	C ₆ F ₅	H
PS ₅	H	C ₉ N ₂ H ₁₀	H
PS ₆	CH ₃	H	H
PS ₇	CH ₃	CF ₃	H
PS ₈	CH ₃	Ph	H
PS ₉	CH ₃	C ₆ F ₅	H
PS ₁₀	CH ₃	I	H
PS ₁₁	CH ₃	Ph	SO ₃ ⁻
PS ₁₂	Ph	H	H
PS ₁₃	Ph	CF ₃	H
PS ₁₄	Ph	Ph	H
PS ₁₅	Ph	C ₆ F ₅	H
PS ₁₆	Ph	C ₉ N ₂ H ₁₀	H

Table 2: Set of iridium photosensitizers studied:

Photosensitizers:	R ₄
PS ₁₇	H
PS ₁₈	CO ₂ Et
PS ₁₉	NMe ₂

Finally, we have also applied the computational procedure to a family of cobalt complexes synthesized (see Figure 4 and Table 3) in the group of Prof. Lloret²⁵ which can be used in different photocatalytic processes like in the water reduction (see Figure 2)²⁵ and CO₂ reduction.²⁶ With this last family, we will verify if the suggested protocol could be applied to other complexes involved in photocatalytic processes.

**Figure 4:** Structure of cobalt complexes family.**Table 3:** Set of cobalt complexes family.

1^X	R₅	R₆
1 ^H	H	H
1 ^{CO2Et}	CO ₂ Et	H
1 ^{CN}	CN	H
1 ^{CF3}	CF ₃	H
1 ^{Cl}	Cl	H
1 ^{DMM}	OMe	Me

2 Computational Methods

All calculations have been performed using the Gaussian 09 and 16 software packages.^{51,52} The ground-state geometries of the photosensitizers have been optimized using the B3LYP^{53,54} (copper PS) and CAM-B3LYP⁵⁵ (iridium PS) functionals in combination with the LANL2DZ⁵⁶ basis set, including Grimme's D3 dispersion correction.⁵⁷ The starting structure of the copper family was obtained from the X-ray crystallographic data of a similar complex in ref. 58. Frequency calculations were made at the same level of theory

to verify that the structure corresponds to a minimum of the potential energy surface. All the calculations, except the optimization of the attenuating parameter, were made using the polarizable continuum model (PCM) to account for solvent effects.^{59,60} For copper PSs, we have simulated a 1:1 solution of water and acetonitrile, while for iridium PSs we have simulated an acetonitrile solution.

The optimal ω value in the liquid phase is too small compared to the default value.³⁸ Small values of the attenuating parameter indicate that there is practically no long-range correction in the functional. If LC- ω PBE functional is used, not having a long-range correction will mean that all the system will be treated with the PBE functional, which gives catastrophic results for CT states. For this reason, it is better to optimize the attenuating parameter in the gas phase.

Based on the optimized structures, TDDFT calculations were made using B3LYP, CAM-B3LYP, LC- ω PBE³⁸⁻⁴⁰ ($\omega = 0.4\text{au}^{-1}$), and LC- ω PBE with the optimal value of ω (LC- ω PBE-opt) functionals and LANL2DZ basis set. We have employed the same solvent as in the optimization calculations. UV-Vis absorption spectra plots were performed with Gnuplot.⁶¹ Equation 1 was used to plot the excitation energies as ε ($\text{M}^{-1} \cdot \text{cm}^{-1}$) vs λ (nm) and adjust to each peak a Gaussian function,⁶²

$$\varepsilon(\tilde{\nu}) = \sum_{i=1}^n \varepsilon_i(\tilde{\nu}) = \sum_{i=1}^n \left(1.3062974 \cdot 10^8 \cdot \frac{f_i}{\sigma} \exp \left[- \left(\frac{\tilde{\nu} - \tilde{\nu}_i}{\sigma} \right)^2 \right] \right) , \quad (1)$$

where i runs from the first to the n^{th} electronic excitation, $\tilde{\nu}$ is the excitation energy in wavenumbers, f_i is the oscillator strength of the i electronic excitation and σ is the standard deviation in wavenumbers related to the width of the simulated band.

The optimization of the attenuating parameter was carried out using the LC- ω PBE functional and LANL2DZ basis set in the gas phase. This procedure was performed using the Δ SCF method.^{34,41,44} This method is based on applying Koopmans'-type theorem in the framework of Kohn-Sham's theory,⁶³ where the energy of the ionization potential (IP) is equal to minus the HOMO orbital energy (ε_{HOMO}). This condition is fulfilled by the exact KS functional, but, in general, density functional approximations (DFAs) do not fulfill it.

Using the Δ SCF method, we have imposed $\varepsilon_{HOMO}(N) = -IP(N)$ and $\varepsilon_{HOMO}(N + 1) = -EA(N)$ by minimizing, through the golden section search numerical method,⁶⁴ the J^* function (Equation 2)⁴⁴ to find the optimal value of ω (ω_{opt}).

$$J^*(\omega) = \sqrt{J_0^2(\omega) + J_1^2(\omega)} , \quad (2)$$

where $J_0(\omega)$ is:

$$J_0(\omega) = |\varepsilon_{HOMO}^{\omega}(N) + IP(N)| , \quad (3)$$

and $J_1(\omega)$ correspond to:

$$J_1(\omega) = |\varepsilon_{HOMO}^{\omega}(N + 1) + EA(N)| . \quad (4)$$

To compute the redox potential, in addition to the B3LYP functional, we have also optimized and characterized the structures using CAM-B3LYP and LC- ω PBE-opt with the value of ω_{opt} of each complex. A solution of acetonitrile was simulated for all PSs and cobalt complexes. Employing these functionals, the energies were refined by single-point calculations with the cc-pVTZ^{65,66} basis set ($E_{cc-pVTZ}$) for all atoms except for the iodine atom, in which we used cc-pVTZ-PP.^{67,68} The methodology applied has been previously tested for B3LYP and different basis sets and it has shown notable agreement with experiments.⁶⁹⁻⁷¹

Specifically, the reduction potentials of all PSs and cobalt complexes have been calculated, *i.e.*, $E_{(Cu^I/Cu^0)}^\circ$, $E_{(Ir^{III}/Ir^{II})}^\circ$, and $E_{(Cu^{II}/Cu^I)}^\circ$, in volts (V). Standard reduction potentials, relative to the standard hydrogen electrode (SHE), were calculated by using the following equation:

$$E^\circ = \frac{\Delta G^\circ - \Delta G_{SHE}^\circ}{nF} \quad (5)$$

in which ΔG° is the free-energy change associated with reduction at standard conditions, ΔG_{SHE}° is the free-energy change of the reduction of a proton (4.47V).⁷² ΔG_{SHE}° is a reference that depends on the method and the solvent model. The n stands for the electrons involved in the reaction, and F is the Faraday constant.

The total Gibbs energy of each species was computed using the following equation:

$$G = E_{spin\ corr} + E_{disp} + G_{T\ corr} + E_{solv} + \Delta G^{o/*} \quad , \quad (6)$$

where E_{disp} corresponds to Grimme-D3 dispersion energy, and $G_{T\ corr}$ is the Gibbs energy thermal correction obtained from solvent frequency calculations. Solvent effects were taken into account, performing gas and solvent phase calculations and taking the difference of the resulting electronic energies (E_{solv}). Finally, $\Delta G^{o/*}$ corresponds to the free-energy change associated with the change of standard conditions from gas-phase pressure of 1 atm to a gas-phase concentration of 1 M. This value equals 1.9 kcal/mol for 1 M standard state solutes.⁷¹ All calculations utilized the spin-unrestricted formalism and spin-contaminated energies were addressed using Equations 7 and 8⁷¹ to obtain the spin-corrected electronic energy ($E_{spin\ corr}$):

$$E_{spin\ corr} = \frac{E_{cc-pVTZ} - a \cdot E_{cc-pVTZ/(S+1)}}{1 - a} \quad (7)$$

where a equals to:

$$a = \frac{\langle S^2 \rangle - S \cdot (S + 1)}{\langle S_{(S+1)}^2 \rangle - S \cdot (S + 1)} \quad (8)$$

and $\langle S^2 \rangle$ and $\langle S_{(S+1)}^2 \rangle$ are the square total spin angular momentum of S and $(S + 1)$ spin states, respectively. $E_{cc-pVTZ/(S+1)}$ is the energy corresponding to $(S + 1)$ spin state.

In summary, for the computation of redox potentials, four different calculations using the same computational method are needed if the energy is refined: (i) optimization and

frequency calculation with a small basis set including dispersion, (ii) gas-phase single-point calculation with a small basis set, (iii) gas-phase single-point calculation with a more extensive basis set, and (iv) gas-phase single-point calculation with the same bigger basis set for the $(S+1)$ spin state. From all of this data, we extract the energy components used to calculate the Gibbs free energy employing the Equation 6 in order to compute the reduction potential (E°).

3 Experimental data

The group of Prof. Lloret from the Institut Català d’Investigació Química (ICIQ) in Tarragona provided all the experimental data obtained from the characterization of three synthesized copper photosensitizers (PS₈, PS₁₀ and PS₁₁), the iridium ones, and the cobalt catalysts. They provided the data of UV-Vis absorption spectra and redox potentials of all these complexes, as well as the X-Ray of PS₈ and PS₁₀.

4 Results and Discussion

4.1 Validation of the computational method

The copper photosensitizer family has been used to validate the computational method used in: (i) the optimization of the PSs structures, (ii) the procedure to optimize the ω parameter, (iii) the simulation of UV-Vis spectra, and (iv) the redox potentials calculations.

In the optimization of the PSs structures, we have used the B3LYP^{53,54} functional and the LANL2DZ⁵⁶ basis set. The same functional has been employed in excited states calculations because the calculations of Biljana Bozic-Weber *et al.*⁷³ have shown good agreement with experimental data using this computational functional. However, density functional approximations (DFAs) with a low percentage of Hartree-Fock (HF) at long-range, like B3LYP, have been associated with large delocalization error (DE).⁷⁴⁻⁷⁸ For this reason, we have also optimized the structures with the CAM-B3LYP functional. Later, the comparison between the maximum wavelength of the UV-Vis absorption spectra showed that there was not much difference in the maximum wavelength (λ_{max}); the most significant difference was 20nm. For this reason, for the copper photosensitizer family, we decided to remain with B3LYP optimized structures. We had not tested the performance of other basis sets for the optimization because the basis set usually affects more the electronic properties than the geometric ones. Nevertheless, a comparison of the most critical distances (Cu-P and Cu-N) of the optimized geometry with the X-Ray data of two photosensitizers (see Table S1) ensured that the basis set provided a good agreement with the experimental data.

In the simulation of the UV-Vis absorption spectra, we have found that the basis

set used in the calculations importantly affects the obtained spectra. Consequently, we validated the basis set used in the excited state calculations by testing different basis sets. For PS₈ and PS₁₁, we tried the following basis sets: 6-31G*⁷⁹ and 6-311++G**.^{80,81} We used a different basis sets for PS₁₀ since the previous basis are not available for iodine: the first basis consists of a combination of 6-311G**⁸² for iodine and 6-311++G** for the rest of the atoms, and the second one, cc-pVDZ-PP⁶⁵ for copper and iodine and 6-31G* for the rest of the atoms.

The basis set of the excitation state calculations was tested using B3LYP as it is shown to work better than LC- ω PBE (see Section 4.3). The analysis of the basis set should be carried out before the optimization of the ω parameter. For this reason, we have performed all these calculations using B3LYP. We have collected the wavelength that has the maximum intensity and corresponds to a CT excitation for the three synthesized dyes obtained with the simulations of the spectra using the different basis sets mentioned before (Table 4).

Table 4: Maximum wavelength values (in nm) for the different basis sets used and the corresponding experimental value. For PS₈ and PS₁₁ we have employed LANL2DZ, 6-31G* (set 1), and 6-311++G** (set 2). For PS₁₀, we have used LANL2DZ, the combination of 6-311G** for iodine and 6-311++G** for the rest of the atoms (set 1), and cc-pVDZ-PP for copper and iodine atoms and 6-31G* for the rest of the atoms (set 2):

PS	λ_{max} (LANL2DZ)	λ_{max} (Set 1)	λ_{max} (Set 2)	Experimental λ_{max}
PS ₈	427.19	475.75	442.80	388.00
PS ₁₀	456.29	467.84	471.82	396.00
PS ₁₁	472.59	498.60	480.67	388.00

Although we only have experimental data for three photosensitizers, the fair comparison with the experimental UV-Vis absorption spectra suggested the use of LANL2DZ for all of our calculations. The choice was also motivated by the important reduction of the cost of our computational calculations as LANL2DZ is a smaller basis set.

4.2 Optimization of the attenuating parameter

The attenuating parameter of the LC- ω PBE functional has been optimized to achieve a more accurate description of the UV-Vis absorption spectrum. Moreover, we wanted to investigate if it also improves the calculation of redox potentials, particularly the reduction potential. In this work, to obtain the optimal value of ω , the J* function (Equation 2) was minimized. Analyzing all the parts of this process (see Supporting Information for further information), we estimate that the simulation of the UV-Vis absorption spectrum with ω_{opt} (including both: the ω optimization and the final UV-Vis spectrum calculation) is seven times more expensive than the simulation of the same spectrum with the default

value of the ω parameter (ω_{def}). The optimization of the ω parameter is more expensive than using the default value of ω , but it is worth doing it because, as we would see in the next section, the spectrum improves considerably compared to the one simulated with ω_{def} .

After applying the optimal tuning process to all the photosensitizers, we appreciate that the optimized ω value within the same family of dyes lies in a short interval of values. For the copper family, it takes values between 0.21 and 0.28 au⁻¹, and for the three iridium dyes, it takes values from 0.11 to 0.15 au⁻¹. For the cobalt set, the ω_{opt} within the family has values between 0.24 and 0.25 au⁻¹. Despite ω_{opt} lies in a short interval, each value is different, and this makes the LC- ω PBE-opt functional not universal for all of the molecules in the family. In other words, we need a different functional for each complex to simulate the UV-Vis absorption spectrum accurately. The need of a different functional for each molecule is not ideal because we want to find a functional that can be universal for a family of molecules and correctly describes the UV-Vis absorption spectrum. However, the fact that ω_{opt} belongs in a short interval greatly simplifies the ω optimization procedure within a family of complexes.

4.3 UV-Vis absorption spectra

Firstly, the UV-Vis absorption spectrum for all the PSs using B3LYP and LC- ω PBE functionals in the solvent phase were simulated. Then, after tuning the attenuating parameter, the spectrum using LC- ω PBE-opt and simulating the corresponding solvent was also computed. All UV-Vis absorption spectra can be found in the Supporting Information (Figures S1-S13). Here we will further discuss the spectra of the synthesized PSs.

Vertical excitations are calculated in the simulated UV-Vis absorption spectra. This type of excitations does not include vibronic couplings. Therefore, all the simulated spectra can not be compared directly with the experimental ones, but they can be used as a first approximation. The experimental solution of the three synthesized copper PSs was saturated. For this reason, the first band of the experimental spectra presents an oscillation around the maximum intensity. This problem could be solved by the use of a more diluted solution of the photosensitizer. However, for this study, it is not a relevant problem because we are interested in the band that is located at higher values of the wavelength, as it corresponds to the CT excitation. Nevertheless, it is crucial to have a functional that correctly describes the whole UV-Vis absorption spectra, not only the band in which we are interested.

In Figure 5, we can notice that the CT excitation band simulated with LC- ω PBE-opt is usually blue shifted with respect to the experimental band for all cases except PS₁₀ (see also Table 5 for iridium PS experimental data). In the absorption LC- ω PBE-opt spectrum of PS₁₀ (see Figure 5 b)), the CT excitation band overlaps with the experimental band. We should not overemphasize this result because after analyzing all the PSs we find that it is not the usual situation. Regarding the CT excitation band of the spectrum simulated

with B3LYP, with respect to the experimental band, it is red shifted for the copper PS and blue shifted for the iridium PS. Iridium PSs seem to be more complex and the computed results for both functionals are less accurate than copper PSs. On the other hand, the spectrum simulated with LC- ω PBE (with the default value of ω) is the worst one. This functional can not even reproduce the CT excitation band, and in addition, the first band is significantly blue-shifted compared to the other spectra.

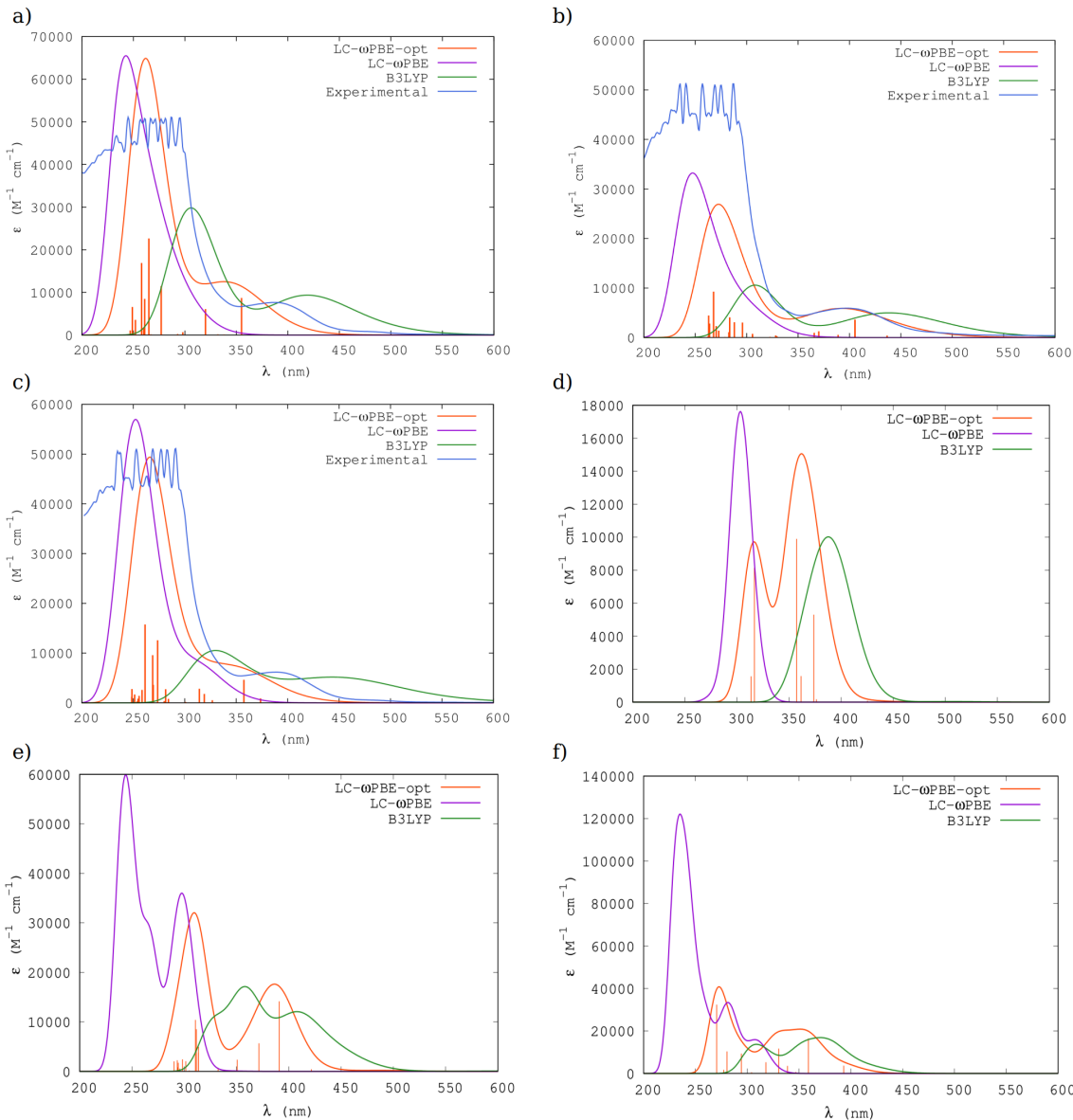


Figure 5: Simulated UV-Vis absorption spectra of synthesized photosensitizers corresponding to a) PS₈, b) PS₁₀, c) PS₁₁, d) PS₁₇, e) PS₁₈, and f) PS₁₉. The functionals used are LC- ω PBE-opt (optimal value of ω), LC- ω PBE (default value of ω), and B3LYP in combination with LANL2DZ basis set. The spectra are plotted using a standard deviation of 0.4 eV for Cu PSs and 0.2 eV for Ir PSs. Experimental available data is included when possible.

In general, for all PSs that we have experimental data, we can appreciate that B3LYP and LC- ω PBE-opt present the CT excitation band close to the experimental band (see Table 5). Nevertheless, with the copper PS, we can see that the first band of the B3LYP simulation (at lower values of wavelength) does not have a higher intensity than the second band. In these UV-Vis spectra, the first band needs to be more intensive respect the other because the absorption is more important in the ultraviolet region of the electromagnetic spectrum. For this reason, B3LYP is not accurate in simulating the UV-Vis absorption spectra. Furthermore, we can observe that the CT excitation band is not present in the LC- ω PBE spectrum. Therefore, LC- ω PBE-opt is the functional that better simulates the spectrum compared with the experimental data.

Table 5: Maximum wavelength (λ , in nm) corresponding to the CT excitation for B3LYP and LC- ω PBE-opt with LANL2DZ basis set of synthesized copper and iridium PSs. Redox potentials (E_{red}^o , in V) calculated using B3LYP, LC- ω PBE-opt, and CAM-B3LYP. The experimental available data is also included. Maximum error (MAX), root mean square error (RMSE), and mean absolute error (MAE) of each method are also given:

PS	λ_{max} (nm)		λ_{expi} (nm)	E_{red}^o (V)			$E_{red\ expi}^o$ (V)
	B3LYP	LC- ω PBE-opt		B3LYP	LC- ω PBE-opt	CAM-B3LYP	
PS ₈	427.19	354.95	388.00	-1.63	-1.60	-1.69	-1.60
PS ₁₀	456.29	405.40	396.00	-1.51	-1.46	-1.50	-1.47
PS ₁₁	472.59	357.54	388.00	-1.74	-1.74	-1.79	-1.66
PS ₁₇	385.19	357.30	483.00	-1.36	-1.32	-1.38	-1.40
PS ₁₈	414.05	390.92	470.00	-0.91	-0.94	-0.98	-1.01
PS ₁₉	379.77	359.02	468.00	-1.78	-2.50	-2.14	-1.80
MAX	97.81	125.70	0.00	0.10	0.70	0.34	0.00
MAE	71.01	64.45	0.00	0.05	0.16	0.11	0.00
RMSE	73.95	77.50	0.00	0.06	0.29	0.15	0.00

The rest of copper photosensitizers (see Table S5 and Figures S1-S13), for which we do not have experimental data available, also present a CT excitation band. The CT band of the LC- ω PBE-opt spectrum is located between 337 nm and 450 nm, while the B3LYP one between 405 nm and 529 nm. Moreover, for these PSs, the CT excitation band is also not observed in the spectra simulated with the LC- ω PBE functional.

Then we have applied the same protocol to simulate the UV-Vis absorption spectra of a cobalt complexes set (see Figures S14-S19). These complexes are not photosensitizers, they are used as catalysts in different photocatalytic processes.^{25,26} They do not present a CT excitation, but the are going to be analyzed to see if the protocol is applicable beyond photosensitizers (see Table 6).

Table 6: Maximum wavelength (λ , in nm) for the B3LYP, LC- ω PBE, and LC- ω PBE-opt simulated spectra with LANL2DZ basis set for cobalt catalysts. The available experimental data is included. Maximum error (MAX), root mean square error (RMSE), and mean absolute error (MAE) of each method are also given:

1^X	$\lambda_{max}(\text{nm})$			$\lambda_{expi}(\text{nm})$
	B3LYP	LC- ω PBE	LC- ω PBE-opt	
1^H	250.83	225.25	235.85	256.00
1^{CO2Et}	303.86	243.07	291.66	281.00
1^{CN}	306.23	240.30	295.27	281.00
1^{CF3}	296.25	235.10	289.81	-
1^{Cl}	261.17	225.60	272.94	217.00
1^{DMM}	249.08	230.38	245.54	260.00
MAX	44.17	40.70	55.94	0.00
MAE	21.67	29.52	23.10	0.00
RMSE	25.52	31.60	28.50	0.00

For this set of cobalt complexes, the optimization of ω is not as relevant as in the PSs for the computation of the UV-Vis spectra because they do not present CT excitations. Despite the maximum error, MAE, and RMSE are very similar for the three functionals, optimizing the ω parameter brings the results of B3LYP and LC- ω PBE closer. All the Co complexes, except 1^{Cl} , present closer values to the experimental ones using LC- ω PBE-opt rather than LC- ω PBE.

4.4 Redox potentials

In this section, we have applied the LC- ω PBE-opt to calculate the reduction potential of the photosensitizers as we have seen that this functional enhances the simulated UV-Vis absorption spectra. In addition, we have also calculated the redox potential using the B3LYP and CAM-B3LYP functionals. The redox potentials of the copper photosensitizers that were not synthesized can be found in the Supporting Information (see Table S5).

Comparing the results obtained for the synthesized PSs (see Table 5), we can see that, in general, the three functionals give values close to the experimental results. It seems that the calculation of the reduction potential of these systems is not significantly affected by the delocalization error present in some DFAs. In most of the cases, the LC- ω PBE-opt functional gives accurate results, except for PS₁₉. In addition, we can see that for copper PSs LC- ω PBE-opt is the best functional to calculate the reduction potentials. In contrast, it is not so evident for the iridium complexes. As there are no significant differences between the three functionals, if we only want to calculate redox potentials, it is not worthwhile to use the RSF with the optimal value of the attenuating parameter to calculate them. Nevertheless, if we have already optimized the attenuating parameter for some other chemical property (like UV-Vis spectra) and we want to be consistent with the

functional employed, LC- ω PBE-opt would be the most appropriate.

Finally, we have applied the same computational procedure to calculate the cobalt complexes' reduction potential ($E_{(Co^{II}/Co^I)}^o$). Values of Table 7 confirm similar trends as in the reduction potentials calculated for the photosensitizers. In general, the LC- ω PBE-opt functional give more accurate results compared to B3LYP, and the CAM-B3LYP functional looks pretty competitive for this calculation. However, compared to the experimental data, the three functionals present significant errors. Therefore, none of the functionals gave very accurate results for the reduction potentials of the cobalt family of catalyst.

Table 7: Reduction potentials (in V) calculated with the B3LYP, LC- ω PBE-opt, and CAM-B3LYP functionals. The available experimental data is included. Maximum error (MAX), root mean square error (RMSE), and mean absolute error (MAE) of each method are also given:

1^X	$E_{red}(V)$			$E_{red\ expi}^o(V)$
	B3LYP	LC- ω PBE-opt	CAM-B3LYP	
1^H	-0.84	-1.00	-1.16	-1.74
1^{CO2Et}	-0.69	-1.14	-1.91	-1.53
1^{CN}	-0.54	-0.85	-0.87	-1.44
1^{CF3}	-1.17	-0.91	-1.26	-
1^{Cl}	-1.10	-0.85	-1.25	-1.71
1^{DMM}	-0.92	-0.98	-1.32	-1.76
MAX	0.90	0.86	0.58	0.00
MAE	0.82	0.67	0.49	0.00
RMSE	0.83	0.69	0.49	0.00

5 Conclusions

In this paper, we have investigated the UV-Vis absorption spectra and the reduction potential of two families of photosensitizers based on Cu^I and Ir^{III} . We have seen that the simulation of a UV-Vis absorption spectrum including the optimization of the ω parameter is about seven times more expensive than the simulation of the same spectrum with the default value of ω (with an ω accuracy of 10^{-4}). Less accurate ω optimizations (10^{-2}) provide a significant cost reduction (only three times more expensive than the simulation with the default of ω) and barely affect the spectrum. The optimization process of the ω parameter is worth doing it because it considerably improves the simulation of the spectrum. This optimization process could be easily applied to any other RSF. Within the studied families, the optimal ω lies in a short interval but is different for each complex. Consequently, LC- ω PBE with the optimized ω parameter is not universal for all the molecules in the family. The simulated spectrum with LC- ω PBE-opt clearly improves the results obtained LC- ω PBE with the default value of ω , as the latter could not even reproduce the CT excitation bands. CT excitations bands of the LC- ω PBE-opt simulated

spectrum present a blue shift compared to the experimental data. In addition, we could appreciate that B3LYP is useful if we are only interested in the CT excitation, taking into account the respective shifting of the band (*e.g.*, red shifted for Cu PSs and blue shifted for Ir PSs). Contrary, if we want to simulate the whole UV-Vis absorption spectrum, it is not the appropriate functional as it tends to underestimate the excitation bands at lower wavelengths. Comparing the simulated spectra and the experimental ones, we can conclude that the LC- ω PBE-opt is the best functional to simulate the whole absorption spectrum of photosensitizers. We have seen that the ω optimization is not relevant for the cobalt complexes family as they do not present CT excitations.

Finally, we have observed that it is not essential to optimize the attenuating parameter of LC- ω PBE to compute the reduction potential of photosensitizers, but, in general, the most accurate results are also using LC- ω PBE-opt. However, we have seen that cobalt complexes' reduction potentials presented more error than PSs results, and none of the functionals gave very accurate results for this family of cobalt complexes. Therefore, to calculate reduction potentials, if we have already done the ω optimization process, we will employ this functional as it gives more accurate results; otherwise, it is not worth doing it since B3LYP and CAM-B3LYP seem really competitive for this calculation.

We expect that this project will be useful to researchers working in the fields of computational and experimental chemistry of photosensitizers to design new potential dyes with enhanced efficiency. However, the present article has not already been sent for publication because we want to complete the set of experimental data to further discuss the computational results.

Acknowledgments

I.C.R is very grateful to Dr. Mauricio Rodriguez for his help in the UV-Vis visualizations spectra script. This work has been supported by grants from the Spanish government MICINN (PGC2018-098212-B-C21, CTQ2016-80375-P, and EUR2019-103825), Diputación Foral de Gipuzkoa (2019-CIEN-000092-01), and Gobierno Vasco (IT1346-19, IT1254-19, PRE_2016_1_0159, and PIBA19-0004). E.R.C. acknowledges funding from the Juan de la Cierva program IJCI-2017-34658.

Supporting Information Available

The Supporting Information contains the UV-Vis absorption spectra for the rest of the complexes as well as other relevant results.

References

- [1] B. I. Limited, *Statistical Review of World Energy*, <https://www.bp.com/en/global/corporate/energy-economics/statistical-review-of-world-energy.html>, Accessed: 2021-04-12.
- [2] R. Rapier, *Fossil Fuels Still Supply 84 Percent Of World Energy - And Other Eye Openers From BP's Annual Review*, <https://www.forbes.com/sites/rrapier/2020/06/20/bp-review-new-highs-in-global-energy-consumption-and-carbon-emissions-in-2019/?sh=eb5fdfe66a16>, Accessed: 2021-04-12.
- [3] M. Jacoby, *Chem. Eng. News*, 2016, **94**, 30–35.
- [4] A. H. Proppe, Y. C. Li, A. Aspuru-Guzik, C. P. Berlinguette, C. J. Chang, R. Cogdell, A. G. Doyle, J. Flick, N. M. Gabor, R. van Grondelle *et al.*, *Nat. Rev. Mat.*, 2020, **5**, 828–846.
- [5] K. E. Dalle, J. Warnan, J. J. Leung, B. Reuillard, I. S. Karmel and E. Reisner, *Chem. Rev.*, 2019, **119**, 2752–2875.
- [6] N. A. Ludin, A. A.-A. Mahmoud, A. B. Mohamad, A. A. H. Kadhum, K. Sopian and N. S. A. Karim, *Renew. Sustain. Energy Rev.*, 2014, **31**, 386–396.
- [7] J. Gong, K. Sumathy, Q. Qiao and Z. Zhou, *Renewable and Sustainable Energy Reviews*, 2017, **68**, 234–246.
- [8] V. Rondán-Gómez, I. M. De Los Santos, D. Seuret-Jiménez, F. Ayala-Mató, A. Zamudio-Lara, T. Robles-Bonilla and M. Courel, *Appl. Phys. A*, 2019, **125**, 1–24.
- [9] B. O'regan and M. Grätzel, *Nature*, 1991, **353**, 737–740.
- [10] M. Kimura, H. Nomoto, H. Suzuki, T. Ikeuchi, H. Matsuzaki, T. N. Murakami, A. Furube, N. Masaki, M. J. Griffith and S. Mori, *Chem. Eur. J.*, 2013, **19**, 7496–502.
- [11] L. Han, A. Islam, H. Chen, C. Malapaka, B. Chiranjeevi, S. Zhang, X. Yang and M. Yanagida, *Energy Environ. Sci.*, 2012, **5**, 6057–6060.
- [12] A. Blakers, N. Zin, K. R. McIntosh and K. Fong, *Energy Procedia*, 2013, **33**, 1–10.
- [13] P. Ushasree and B. Bora, in *Solar Energy Capture Materials*, ed. E. A. Gibson, Royal Society of Chemistry, UK, 2019, pp. 1–55.
- [14] O. S. Wenger, *J. Am. Chem. Soc.*, 2018, **140**, 13522–13533.
- [15] O. S. Wenger, *Nat. Chem.*, 2020, **12**, 323–324.

- [16] A. Abbotto and N. Manfredi, *Dalton Trans.*, 2011, **40**, 12421–12438.
- [17] M. S. Lowry and S. Bernhard, *Chem. Eur. J.*, 2006, **12**, 7970–7977.
- [18] S. Ladouceur, D. Fortin and E. Zysman-Colman, *Inorg. Chem.*, 2010, **49**, 5625–5641.
- [19] E. Mejía, S.-P. Luo, M. Karnahl, A. Friedrich, S. Tschierlei, A.-E. Surkus, H. Junge, S. Gladiali, S. Lochbrunner and M. Beller, *Chem. Eur. J.*, 2013, **19**, 15972–15978.
- [20] S.-P. Luo, E. Mejía, A. Friedrich, A. Pazidis, H. Junge, A.-E. Surkus, R. Jackstell, S. Denurra, S. Gladiali, S. Lochbrunner *et al.*, *Angewandte Chemie*, 2013, **125**, 437–441.
- [21] A. Hossain, A. Bhattacharyya and O. Reiser, *Science*, 2019, **364**, 1–11.
- [22] N. Kandoth, J. P. Hernández, E. Palomares and J. Lloret-Fillol, *Sustainable Energy & Fuels*, 2021, **5**, 638–665.
- [23] F. Glaser and O. S. Wenger, *Coord. Chem. Rev.*, 2020, **405**, 213129.
- [24] E. Jakubikova and D. N. Bowman, *Acc. Chem. Res.*, 2015, **48**, 1441–1449.
- [25] A. Call, F. Franco, N. Kandoth, S. Fernández, M. González-Béjar, J. Pérez-Prieto, J. M. Luis and J. Lloret-Fillol, *Chem. Sci.*, 2018, **9**, 2609–2619.
- [26] S. Fernández, F. Franco, C. Casadevall, V. Martin-Diaconescu, J. M. Luis and J. Lloret-Fillol, *J. Am. Chem. Soc.*, 2020, **142**, 120–133.
- [27] P. Xiao, F. Dumur, J. Zhang, J. P. Fouassier, D. Gigmes and J. Lalevée, *Macromolecules*, 2014, **47**, 3837–3844.
- [28] C. Bizzarri, C. Strabler, J. Prock, B. Trettenbrein, M. Ruggenthaler, C.-H. Yang, F. Polo, A. Iordache, P. Brüggele and L. D. Cola, *Inorg. Chem.*, 2014, **53**, 10944–10951.
- [29] G. C. Dos Santos, E. F. Oliveira, F. C. Lavarda and L. C. da Silva-Filho, *J. Mol. Model.*, 2019, **25**, 1–13.
- [30] J. P. Perdew and A. Zunger, *Phys. Rev. B*, 1981, **23**, 5048.
- [31] A. Dreuw and M. Head-Gordon, *J. Am. Chem. Soc.*, 2004, **126**, 4007–4016.
- [32] O. A. Vydrov and G. E. Scuseria, *J. Chem. Phys.*, 2005, **122**, 184107.
- [33] J. L. Bao, L. Gagliardi and D. G. Truhlar, *J. Phys. Chem. Lett.*, 2018, **9**, 2353–2358.
- [34] R. Baer, E. Livshits and U. Salzner, *Ann. Rev. Phys. Chem.*, 2010, **61**, 85–109.

- [35] K. Hirao, H.-S. Bae, J.-W. Song and B. Chan, *J. Phys. Chem. A*, 2021, **125**, 3489–3502.
- [36] C.-O. Almbladh and U. von Barth, *Phys. Rev. B*, 1985, **31**, 3231–3244.
- [37] F. Della Sala and A. Görling, *Phys. Rev. Lett.*, 2002, **89**, 033003.
- [38] O. A. Vydrov and G. E. Scuseria, *J. Chem. Phys.*, 2006, **125**, 234109.
- [39] T. Vreven, M. Frisch, K. Kudin, H. Schlegel and K. Morokuma, *Mol. Phys.*, 2006, **104**, 701–714.
- [40] O. A. Vydrov, G. E. Scuseria and J. P. Perdew, *J. Chem. Phys.*, 2007, **126**, 154109.
- [41] E. Livshits and R. Baer, *Phys. Chem. Chem. Phys.*, 2007, **9**, 2932–2941.
- [42] T. Stein, L. Kronik and R. Baer, *J. Am. Chem. Soc.*, 2009, **131**, 2818–2820.
- [43] T. Stein, L. Kronik and R. Baer, *J. Chem. Phys.*, 2009, **131**, 244119.
- [44] O. S. Bokareva, G. Grell, S. I. Bokarev and O. Kühn, *J. Chem. Theory Comput.*, 2015, **11**, 1700–1709.
- [45] U. Salzner and A. Aydin, *J. Chem. Theory Comput.*, 2011, **7**, 2568–2583.
- [46] T. Körzdörfer, R. M. Parrish, N. Marom, J. S. Sears, C. D. Sherrill and J.-L. Brédas, *Phys. Rev. B*, 2012, **86**, 205110.
- [47] Z. Lin and T. Van Voorhis, *J. Chem. Theory Comput.*, 2019, **15**, 1226–1241.
- [48] K. Garrett, X. Sosa Vazquez, S. B. Egri, J. Wilmer, L. E. Johnson, B. H. Robinson and C. M. Isborn, *J. Chem. Theory Comput.*, 2014, **10**, 3821–3831.
- [49] H. Iikura, T. Tsuneda, T. Yanai and K. Hirao, *J. Chem. Phys.*, 2001, **115**, 3540–3544.
- [50] T. Koopmans, *Physica*, 1934, **1**, 104–113.
- [51] M. J. Frisch, G. W. Trucks, H. B. Schlegel, G. E. Scuseria, M. A. Robb, J. R. Cheeseman, G. Scalmani, V. Barone, B. Mennucci, G. A. Petersson, H. Nakatsuji, M. Caricato, X. Li, H. P. Hratchian, A. F. Izmaylov, J. Bloino, G. Zheng, J. L. Sonnenberg, M. Hada, M. Ehara, K. Toyota, R. Fukuda, J. Hasegawa, M. Ishida, T. Nakajima, Y. Honda, O. Kitao, H. Nakai, T. Vreven, J. A. Montgomery, Jr., J. E. Peralta, F. Ogliaro, M. Bearpark, J. J. Heyd, E. Brothers, K. N. Kudin, V. N. Staroverov, R. Kobayashi, J. Normand, K. Raghavachari, A. Rendell, J. C. Burant, S. S. Iyengar, J. Tomasi, M. Cossi, N. Rega, J. M. Millam, M. Klene, J. E. Knox, J. B. Cross, V. Bakken, C. Adamo, J. Jaramillo, R. Gomperts, R. E. Stratmann, O. Yazyev, A. J. Austin, R. Cammi, C. Pomelli, J. W. Ochterski, R. L. Martin, K. Morokuma, V. G. Zakrzewski, G. A. Voth, P. Salvador, J. J. Dannenberg, S. Dapprich, A. D. Daniels,

- Ö. Farkas, J. B. Foresman, J. V. Ortiz, J. Cioslowski and D. J. Fox, *Gaussian 09 Revision D.01*, Gaussian Inc. Wallingford CT 2009.
- [52] M. J. Frisch, G. W. Trucks, H. B. Schlegel, G. E. Scuseria, M. A. Robb, J. R. Cheeseman, G. Scalmani, V. Barone, G. A. Petersson, H. Nakatsuji, X. Li, M. Caricato, A. V. Marenich, J. Bloino, B. G. Janesko, R. Gomperts, B. Mennucci, H. P. Hratchian, J. V. Ortiz, A. F. Izmaylov, J. L. Sonnenberg, D. Williams-Young, F. Ding, F. Lipparini, F. Egidi, J. Goings, B. Peng, A. Petrone, T. Henderson, D. Ranasinghe, V. G. Zakrzewski, J. Gao, N. Rega, G. Zheng, W. Liang, M. Hada, M. Ehara, K. Toyota, R. Fukuda, J. Hasegawa, M. Ishida, T. Nakajima, Y. Honda, O. Kitao, H. Nakai, T. Vreven, K. Throssell, J. A. Montgomery, Jr., J. E. Peralta, F. Ogliaro, M. J. Bearpark, J. J. Heyd, E. N. Brothers, K. N. Kudin, V. N. Staroverov, T. A. Keith, R. Kobayashi, J. Normand, K. Raghavachari, A. P. Rendell, J. C. Burant, S. S. Iyengar, J. Tomasi, M. Cossi, J. M. Millam, M. Klene, C. Adamo, R. Cammi, J. W. Ochterski, R. L. Martin, K. Morokuma, O. Farkas, J. B. Foresman and D. J. Fox, *Gaussian 16 Revision C.01*, 2016, Gaussian Inc. Wallingford CT.
- [53] A. D. Becke, *J. Chem. Phys.*, 1993, **98**, 5648–5652.
- [54] P. J. Stephens, F. J. Devlin, C. F. Chabalowski and M. J. Frisch, *J. Phys. Chem.*, 1994, **98**, 11623–11627.
- [55] T. Yanai, D. P. Tew and N. C. Handy, *Chem. Phys. Lett.*, 2004, **393**, 51–57.
- [56] T. H. D. Jr. and P. J. Hay, *Methods of Electronic Structure Theory*, Ed. H. F. Schaefer III, Plenum, New York, 1977.
- [57] S. Grimme, J. Antony, S. Ehrlich and H. Krieg, *J. Chem. Phys.*, 2010, **132**, 154104.
- [58] D. G. Cuttell, S.-M. Kuang, P. E. Fanwick, D. R. McMillin and R. A. Walton, *J. Am. Chem. Soc.*, 2002, **124**, 6–7.
- [59] S. Miertuš, E. Scrocco and J. Tomasi, *Chemical Physics*, 1981, **55**, 117–129.
- [60] J. Tomasi, B. Mennucci and R. Cammi, *Chem. Rev.*, 2005, **105**, 2999–3094.
- [61] T. Williams, C. Kelley and many others, *Gnuplot 5.2: an interactive plotting program*, <http://gnuplot.sourceforge.net/>, 2016.
- [62] I. Gaussian, *Creating UV/Visible Plots from the Results of Excited States Calculations*, <https://gaussian.com/uvvisplot/>, Accessed: 2021-04-15.
- [63] V. U. Nazarov, *arXiv preprint arXiv:2104.07882*, 2021.
- [64] J. Kiefer, *Proc. Amer. Math. Soc.*, 1953, **4**, 502–506.
- [65] T. H. Dunning Jr., *J. Chem. Phys.*, 1989, **90**, 1007–1023.

- [66] R. A. Kendall, T. H. Dunning Jr. and R. J. Harrison, *J. Chem. Phys.*, 1992, **96**, 6796–6806.
- [67] K. A. Peterson, D. Figgen, E. Goll, H. Stoll and M. Dolg, *J. Chem. Phys.*, 2003, **119**, 11113–11123.
- [68] K. A. Peterson, B. C. Shepler, D. Figgen and H. Stoll, *J. Phys. Chem. A*, 2006, **110**, 13877–13883.
- [69] A. K. Vardhaman, C. V. Sastri, D. Kumar and S. P. de Visser, *Chem. Commun.*, 2011, **47**, 11044–11046.
- [70] S. P. de Visser, M. G. Quesne, B. Martin, P. Comba and U. Ryde, *Chem. Commun.*, 2014, **50**, 262–282.
- [71] F. Acuña-Parés, Z. Codolà, M. Costas, J. M. Luis and J. Lloret-Fillol, *Chem. Eur. J.*, 2014, **20**, 5696–5707.
- [72] C. P. Kelly, C. J. Cramer and D. G. Truhlar, *J. Phys. Chem. B*, 2007, **111**, 408–422.
- [73] B. Bozic-Weber, V. Chaurin, E. C. Constable, C. E. Housecroft, M. Meuwly, M. Neuburger, J. A. Rudd, E. Schönhofer and L. Siegfried, *Dalton Trans.*, 2012, **41**, 14157–14169.
- [74] P. Mori-Sánchez, A. J. Cohen and W. Yang, *Phys. Rev. Lett.*, 2008, **100**, 146401.
- [75] M. Torrent-Sucarrat, S. Navarro, F. P. Cossío, J. M. Anglada and J. M. Luis, *J. Comput. Chem.*, 2017, **38**, 2819–2828.
- [76] I. Casademont-Reig, T. Woller, J. Contreras-García, M. Alonso, M. Torrent-Sucarrat and E. Matito, *Phys. Chem. Chem. Phys.*, 2018, **20**, 2787–2796.
- [77] I. Casademont-Reig, E. Ramos-Cordoba, M. Torrent-Sucarrat and E. Matito, *Molecules*, 2020, **25**, 711.
- [78] I. Casademont-Reig, R. Guerrero-Avilés, M. Torrent-Sucarrat, E. Ramos-Cordoba and E. Matito, *ChemRxiv*, 2021.
- [79] W. J. Hehre, R. Ditchfield and J. A. Pople, *J. Chem. Phys.*, 1972, **56**, 2257–2261.
- [80] R. Krishnan, J. S. Binkley, R. Seeger and J. A. Pople, *J. Chem. Phys.*, 1980, **72**, 650–654.
- [81] T. Clark, J. Chandrasekhar, G. W. Spitznagel and P. v. R. Schleyer, *J. Comput. Chem.*, 1983, **4**, 294–301.
- [82] M. N. Glukhovtsev, A. Pross, M. P. McGrath and L. Radom, *J. Chem. Phys.*, 1995, **103**, 1878–1885.

Chapter 10

Results and discussion

In this chapter, the main achievements of the works presented in Chapters 5, 6, 8, and 9 are summarized and discussed. For a detailed analysis, the reading of the previous chapters is recommended.

First, we will present the results obtained from the study of the annulene series using the HMO method. Second, we will display a few examples of the aromatic character analysis using density functional approximations, including the investigation of the aromaticity indices' ability to identify the most aromatic pathway. Third, we will show some of the failures found due to the delocalization error present in some DFAs concerning the geometry assessment, the aromaticity indices, the UV-Vis absorption spectra, and finally, how the redox potentials are affected by DE.

10.1 Aromaticity from the HMO method

In the study of the annulene series, we first examined how Hückel's and Baird's rules fade away with the ring size calculating I_{ring} within the HMO method, I_{ring}^{HMO} (see Chapter 6). We have divided the results into different sets of annulenes according to the number of electrons ($4n+2$ and $4n$) and the spin multiplicity (singlet and triplet). Representing all the values of I_{ring}^{HMO} normalized index, we have realized that all the curves conform to the same expression, $a + b/N^2$, N being the number of carbon atoms (see Figure 10.1). In addition, we can appreciate that the initial (anti)aromatic character decreases smoothly with the annulene size. It is also noticeable that both Hückel and Baird rules break down and all the species become equally aromatic when the system is large.

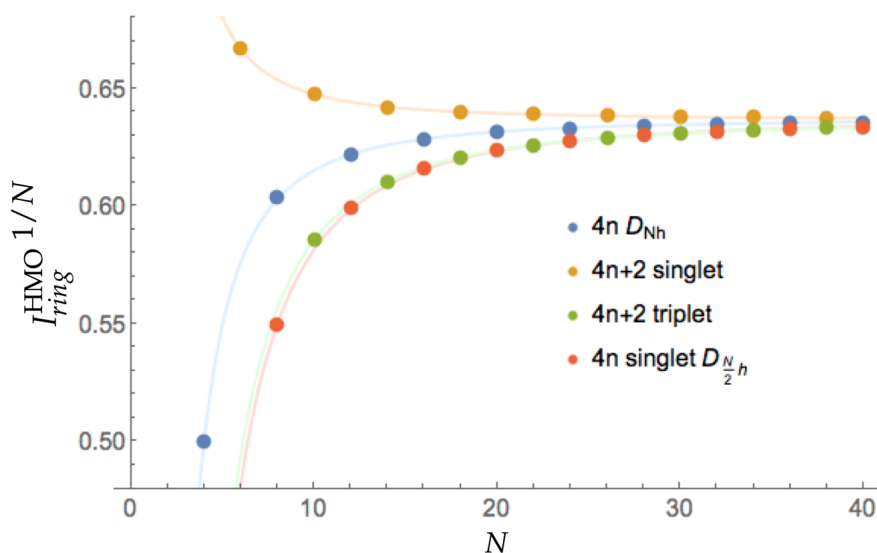


Figure 10.1: Values of the I_{ring}^{HMO} normalized index for the annulenes series against the number of carbon atoms (N) for different singlets and triplets.

The study of triplet states within the HMO method is complicated because this method does not distinguish between alpha and beta electrons. However, $4n+2$ triplets could be treated as systems where one electron is promoted from a l orbital to a $l+1$ orbital. Doing so, triplets can be addressed within the HMO theory, apart from the $4n$ annulenes. This is the reason why we observe that $4n D_{Nh}$ annulenes curve behave as if these molecules were antiaromatic and not aromatic as expected for $4n$ triplets. Contrarily, $4n+2$ singlets, which are aromatic, display values above the $2/\pi$ limit, whereas $4n + 2$ triplets and $4n$ singlets, which are expected to be antiaromatic, present values below this limit. Those three latter series of annulenes are well described from the delocalization measures of the HMO method.

10.2 Aromaticity from DFAs

Our aromaticity studies include a theoretical investigation of different (large) conjugated compounds using mainly three DFAs (B3LYP, CAM-B3LYP, and M06-2X) and several aromaticity descriptors that evaluate the different manifestations of this property (see Section 3.3). All these works include FLU, BOA, HOMA, BLA, AV1245, and AV_{min} values. In addition, some of them include I_{ring} , MCI, ACID, and NICS calculations. We have compared our results with the aromaticity rules' prediction or experimental data available in the literature.

10.2.1 Examples of presumably aromatic molecules

Here we will present the results obtained for some studied molecules expected to be aromatic according to Hückel's and Heilbronner's rules. With these examples, we will give a general idea of the values of the different calculated indices. It is essential to highlight that most of the obtained results are linked to the delocalization error present in some DFAs.

In Table 10.1, only the results computed with the CAM-B3LYP method are presented. We will further discuss the results primarily related to the delocalization error in Section 10.3.

Table 10.1: Aromaticity indices for different systems calculated at the CAM-B3LYP/6-311G(d,p) level of theory.

Molecule	FLU	BOA	HOMA	BLA	AV1245	AV_{min}
Benzene	0.000	0.000	1.000	0.000	10.71	10.71
$C_{14}H_{14}$	0.026	0.449	0.437	0.091	2.11	1.80
$C_{18}H_{18}$	0.026	0.446	0.448	0.090	2.00	1.80
18H	0.010	0.137	0.872	0.035	2.16	1.28
32M	0.020	0.287	0.666	0.064	1.41	0.55
c-P6 · T6 ⁶⁺ ^a	0.075	0.379	-0.164	0.077	1.48	0.64

^a 6-31G⁺ basis set

Benzene is the aromatic molecule per excellence, and its aromatic indices values are used as a reference for the FLU and HOMA descriptors (C–C bonds). As expected, benzene's AV1245 and AV_{min} values are the highest that we have found. BOA and BLA benzene's values equal zero, and as we have seen previously, these indices give the same results for cyclohexane because they measure the degree of homogeneity of bond orders and bond lengths, respectively. Therefore, small values of these two indices should be

taken with caution as they are not necessarily related to aromaticity.

Analyzing all the data obtained with the annulenes series, we were able to see that Hückel's and Baird's rules break down more rapidly with the ring size within DFAs calculations than using descriptors based on the HMO method. This is due to the geometry relaxation with respect to the original planar geometry taken into account in the HMO method. Annulenes with more than eight carbons usually show several conformations close in energy that exhibit different aromatic characters. In addition, using some aromaticity indices, no smooth trend is observed when increasing the ring size. The two annulenes exposed in Table 10.1 are a clear example that the aromaticity rules start to fail when the systems are larger and they lose symmetry and/or planarity. *[14]annulene* ($C_{14}H_{14}$) and *[18]annulene* ($C_{18}H_{18}$) described with the CAM-B3LYP functional are antiaromatic systems as they exhibit bond-order and bond-length alternation.

The last three examples of Table 10.1 (18H, 32M, and $c\text{-P6} \cdot T6^{6+}$) correspond to porphyrinoid systems. In these systems, different pathways can be drawn within the molecular structure. Here, the most aromatic path values are presented. *18H* or porphin is the simplest aromatic porphyrin (*vide supra*). Indeed, all the aromaticity indices identified it as an aromatic system. However, as expected, 18H is less aromatic than the aromatic annulenes because it is a larger system. *32M* corresponds to the [32]heptaphyrin in the Möbius conformation, and according to all the indices, it is aromatic.

Finally, the +6 oxidation state of the six-porphyrin structure, $c\text{-P6} \cdot T6^{6+}$ (see Image 10.8), was predicted initially to be an aromatic species.¹ However, with our studies, we have seen that this species is nonaromatic. The values of the indices presented in Table 10.1 could suggest that the $c\text{-P6} \cdot T6^{6+}$ is weakly aromatic, especially if we look at AV_{min} value and compare it with 32M (0.64 vs 0.55). Nevertheless, as discussed above, if we obtain small AV_{min} values for large conjugated systems, it is also better to analyze the individual MCI(1,2,4,5) values along the most aromatic pathway. With only the AV_{min} values it is sometimes difficult to define the molecule's aromatic character because they are in the middle of two situations (*e.g.*, weakly aromatic and nonaromatic). We have plotted these values (see Figure 10.10) and found that the $c\text{-P6} \cdot T6^{6+}$ species presents multiple low-delocalization fragments along the most conjugated path. Compared to the expanded porphyrins, which achieve the minimal value only twice or three times, $c\text{-P6} \cdot T6^{6+}$ presents a significant amount of low-delocalization fragments. For this reason, we conclude that this species is not aromatic.

10.2.2 The most aromatic path in porphyrinoid systems

We have tested for the first time the performance of the AV_{min} descriptor in large systems studying the aromaticity of nine porphyrinoid compounds (see Chapter 5). We have compared the results obtained using this descriptor with other aromaticity indices

like BLA, BOA, FLU, HOMA, and AV1245. In addition, one of the most exciting results regarding AV_{min} is that it is the only one able to predict the annulene path as the most aromatic one and sort the rest according to the aromaticity character.

First, we studied all the possible pathways of 18H (porphin) that arise from the possibility of passing through the nitrogen atom (inner path, labeled as 'i') or C–C bond (outer path, labeled as 'o') in the four five-membered rings (5-MRs) in 18H (see Figure 10.2). There are sixteen paths, some of which are equivalent by symmetry. Therefore, in the end, we are left with only nine different paths.

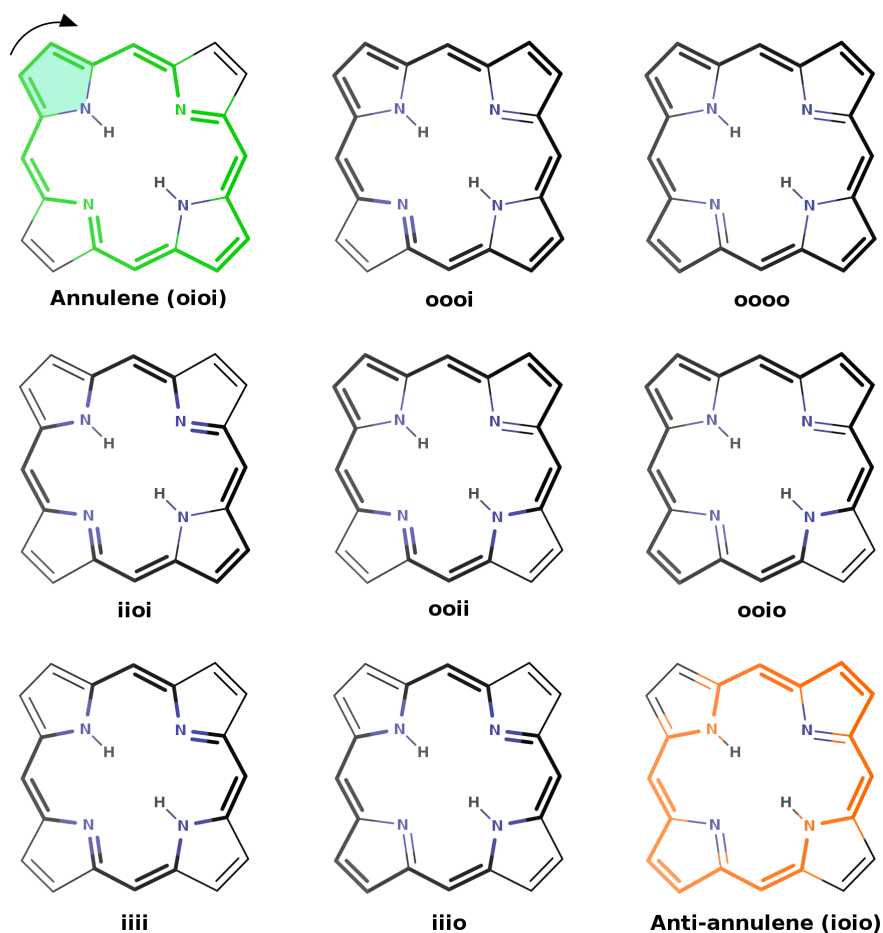


Figure 10.2: Porphin pathways. To label each path, the top left 5-MR is taken and follow the clockwise direction. The green and the orange circuits highlight the annulene and the anti-annulene paths, respectively.

The first entry of Table 10.2 corresponds to the annulene path (*oioi*). All the indices recognized this path as highly aromatic, but only BOA, BLA, AV1245, and AV_{min} identified it as the most aromatic one. FLU and HOMA indicate that *iiii* path is the most aromatic. FLU is smaller for the inner circuit than the annulene path because the DIs of C–NH bonds are closer to the reference values than the DIs of the

C–C bonds of the pyrrole are to the corresponding reference values (see Figure 10.3 for the DI values). But since the C–C bond of the pyrrole rings present larger values, the annulene path is expected to be more aromatic. On the other hand, BOA, and BLA also recognized the anti-annulene path (*ioio*, orange path in Figure 10.2) as much aromatic as the annulene path. These indices are measuring the degree of homogeneity along the path of the DIs and the bond lengths, respectively, which does not necessarily reflect the most aromatic pathway.

Table 10.2: Aromaticity indices for different pathways in 18H, calculated at the CAM-B3LYP/6-311G(d,p) level of theory. The number in parentheses indicates the equivalent pathways.

Path	FLU	BOA	HOMA	BLA	AV1245	AV _{min}
oioi	0.010	0.000	0.872	0.000	2.16	1.28
ooooi(2)	0.016	0.309	0.734	0.288	1.91	0.49
oooo	0.022	0.041	0.610	0.011	1.70	0.49
iiioi(2)	0.008	0.367	0.917	0.313	1.57	0.13
ooii(4)	0.015	0.023	0.769	0.006	1.36	0.13
ooio(2)	0.021	0.372	0.637	0.270	1.17	0.13
iiii	0.006	0.000	0.968	0.000	0.91	0.13
oiii(2)	0.013	0.388	0.808	0.307	0.73	0.13
ioio	0.019	0.000	0.666	0.000	0.57	0.13

To choose the second most aromatic pathway following the annulene model, we should select a different route in one 5-MR. Using an in-house program (ESI-3D)³⁰⁵ we have found and analyzed all the possible path permutations in the porphyrin structure. Ordering paths by aromaticity in porphyrinoid structures is complex, and after analyzing Table 10.2, we have seen that only AV1245 and AV_{min} can do it correctly. However, AV1245 does not recognize the annulene pathway as the most aromatic one in the rest of the studied porphyrins. In addition, it is important to remark here that AV1245 is an average-based index (like FLU, BOA, HOMA, and BLA), and it could hinder the values that deviate the most from the average. In aromaticity, it is crucial to detect the minimal values because they correspond to the fragments of the molecular ring that are less delocalized. For this reason, especially in larger molecules, we prefer to use the AV_{min} index.

Taking into account the results of the other porphyrinoid systems (16H, 26H, 26M, 28H, 28M, 32H, 32M, and 32F), we have seen, in general, that all the indices adequately describe the aromatic character of each molecule, but they disagree on which is the most aromatic path of the porphyrins. All the indices concur that the annulene path in Hückel aromatic conformers is more aromatic than the annulene path in analogous Möbius an-

tiaromatic systems. The annulene model serves well for simple porphyrins, but it gets more complicated if the porphyrins are protonated and deprotonated.^{370,371} In Ref. 370, we have studied different conjugation pathways of an expanded porphyrin set including neutral, anionic, and cationic states. We have employed different structural, magnetic, and electronic descriptors to characterize them. We have seen that the annulene pathway is the most aromatic pathway only in neutral macrocycles. The protonated and deprotonated macrocycles present other pathways with similar or even more aromatic character than the annulene pathways. Knowing the most aromatic pathways gets more complicated as the system becomes larger. However, this project is not included in the present dissertation.

10.2.3 AV1245 colored representations

In certain circumstances, it is useful to have a simple visual representation of the AV1245 values to easily detect which fragments of the ring structure present the most or the least electronic delocalization. To obtain them we have colored each bond according to the sum of the contributions to AV1245 that pass through the bond. We have selected three different colors: green, to represent bonds whose contribution is at least 75% the value of the highest bond; red, for bonds whose contribution is below 25% of this value, and the other bonds are colored in orange.

We have used the AV1245 colored representations to further discuss the most aromatic path in some porphyrinoid systems like porphin (18H) and [32]heptaphyrin in the figure-eight conformation (32E).

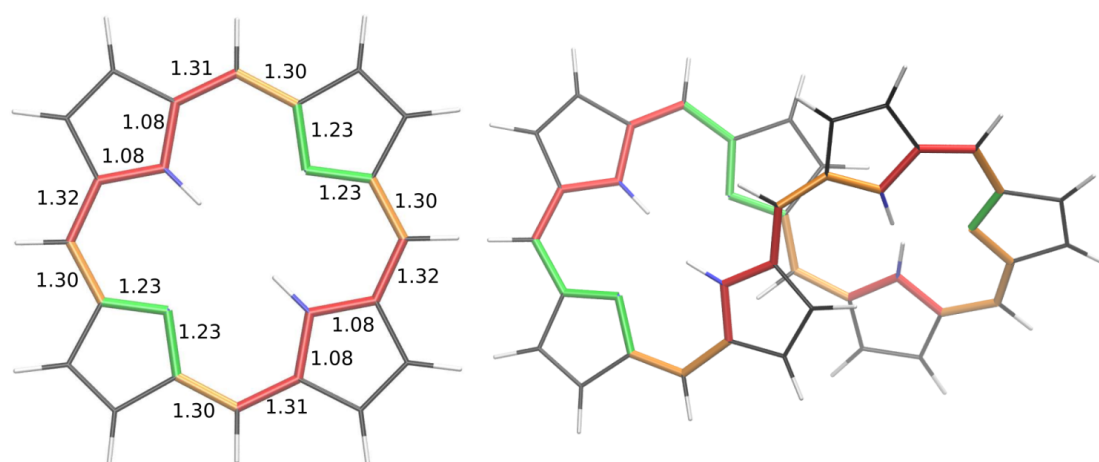


Figure 10.3: AV1245 colored representations for the inner pathway of 18H (left) and 32E (right). The numerical values correspond to the DIs.

According to Hückel's and Heilbronner's rules, the ground-state configuration of 18H and 32E are expected to be aromatic and antiaromatic, respectively. We have seen in

the previous section that FLU, BOA, HOMA, and BLA identify the inner path of 18H as more aromatic than the annulene path. However, AV_{min} shows very small value for the inner path (0.13) as a result of the small delocalization of the C–C–NH–C–C fragment of the pyrrole rings (colored in red in the left structure of Figure 10.3). This fact is also confirmed by the DIs values of C–NH bonds which are the smallest ones in the path. Contrary, we can observe that the most delocalized fragment of the inner path are the C–N bonds of the imine rings.

The figure-eight conformation of expanded porphyrins is a highly torsioned structure. The example illustrated in Figure 10.3 clearly shows that the regions of the maximal torsion correspond to the lowest value of the AV1245 index. The inner path of 32E is really affected by these torsions and that is the reason why the AV_{min} is really low (0.03).

10.3 Delocalization error in DFAs

Some density functionals approximations suffer from delocalization error, and as a consequence, they tend to give over-delocalized electronic densities. On the contrary, HF is prone to exaggerate the localization of the electrons. Therefore, DFAs with a low percentage of HF exchange usually suffer more from DE. Some authors suggest that the exact result lies between the two extreme solutions, the highly localized one (HF) and the highly delocalized one (LDA).¹⁶

In our studies, we have evaluated how the electron delocalization error affects our calculations mostly comparing HF; two hybrid functionals, B3LYP (19% of HF exchange), and M06-2X (54% of HF exchange); and the range-separated CAM-B3LYP functional (from 19% of HF exchange at short range to 65% at large interelectronic distances). In some cases, we have also made single-point DLPNO-CCSD(T) calculations. Moreover, we have compared the computational results against benchmark data already available in the literature (see Chapter 6) and experimental data (see Chapter 8), when possible.

In the following sections, we will see how the DE affects specific properties of the studied molecules: starting from the evaluation of the optimal geometry, the aromaticity measures, and the description of CT excitations.

10.3.1 Geometry evaluation

It has been seen that the percentage of exact exchange included in the functional has a significant effect on the correct description of the stationary points of the molecules. DFAs with a low percentage of HF exchange at long-range distances have been associated with significant delocalization errors that could even lead to spurious stationary points on the potential energy surface (PES).^{17–19,353}

In the study of the annulene series (see Chapter 6), we have observed that the largest $4n+2$ annulenes ([14]annulene and [18]annulene) optimized with the B3LYP functional present a minimal delocalized structure that corresponds to a transition state when it is computed with CAM-B3LYP or M06-2X functionals. This transition state connects two identical structures with complementary bond-length alternation. Consequently, the B3LYP optimized geometry is aromatic, while the CAM-B3LYP or M06-2X ones are antiaromatic. This inconsistency has been ascribed to DE of DFAs with a low percentage of HF exchange and confirmed by comparing experimental chemical shifts.²⁴⁵

The discrepancies found in the nature of the optimized stationary points of the PES affect the aromaticity measures calculated using different computational functionals.

In the annulene series, we have carefully examined the results of $\overline{I}_{ring}^{1/N}$. This index is an approximate version of I_{ring} including only two-center bond orders of bonded atoms to estimate the N-center delocalization. Our results confirm that, in most cases, B3LYP and HF give the most and the less aromatic species, respectively.

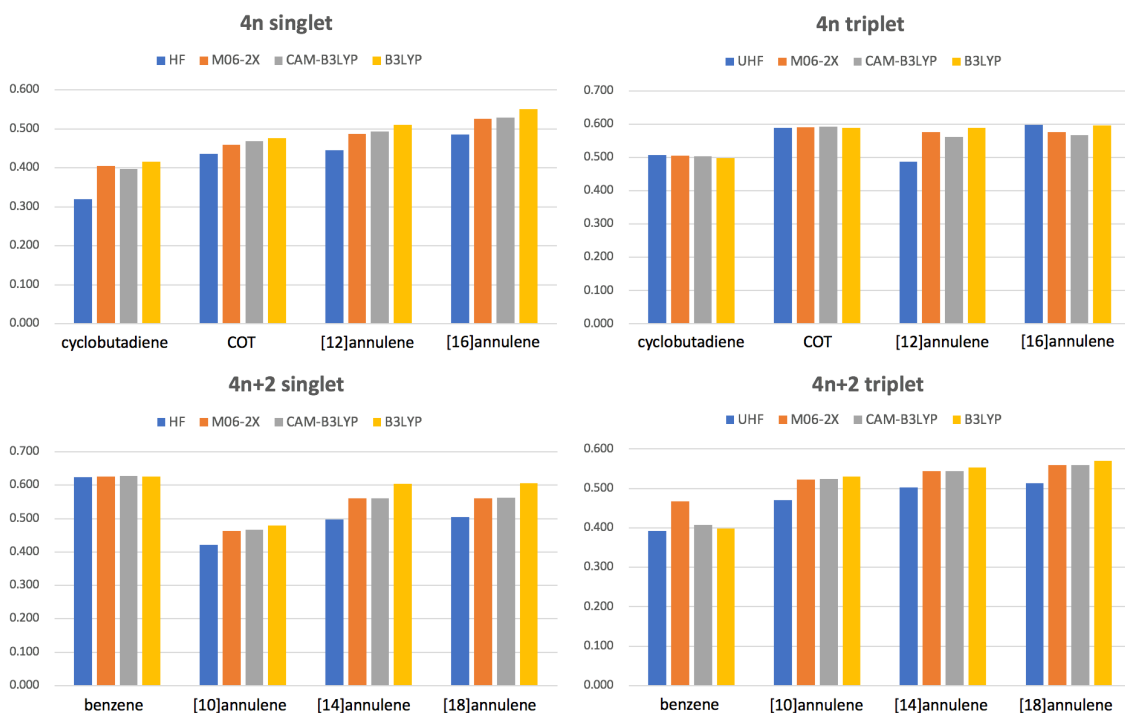


Figure 10.4: Values of $\overline{I}_{ring}^{1/N}$ for the singlet and triplet lowest-lying states of the studied annulenes obtained with HF, M06-2X, CAM-B3LYP, and B3LYP.

In Figure 10.4, we can appreciate that singlet benzene, triplet cyclobutadiene, and triplet COT present similar values with all the computational methods used because these molecules do not suffer from DE. In many cases, B3LYP tends to overestimate the delocalization of the electronic structures and sometimes even gives different geometrical structures. This is the opposite behavior of HF, which tends to overestimate the elec-

tron localization. The CAM-B3LYP and M06-2X methods present similar results lying between HF and B3LYP values. This fact corroborates the long-range part of HF exact exchange is crucial to decrease the DE (see Section 10.3.2). There are two annulenes that do not follow the general conclusions extracted from Figure 10.4: triplet benzene and [16]annulene. Triplet benzene described with M06-2X presents the highest DE. M06-2X is the only studied DFA that describes this molecule as a non-planar structure (Q-like conformation), and it does not identify the AQ conformation as a energy minimum in the PES. The Q-like structure is more antiaromatic than expected for the triplet state of the benzene molecule. In the case of [16]annulene, the $\overline{I}_{\text{ring}}^{-1/N}$ value calculated with HF is larger than the one obtained with CAM-B3LYP and M06-2X because the HF optimized structure is more planar than the ones obtained using these DFAs. The last conclusion extracted from all the data included in Figure 10.4 is that, in general, the singlet states tend to suffer more from the delocalization error than the triplet states.

Interestingly, in the study of the six-porphyrin nanoring structure, we found a similar situation to [14]annulene and [18]annulene, where the geometry assessment was not the same for all the methods used. In this work, we have studied four different oxidation states of the nanoring system (c-P6, c-P6⁴⁺, c-P6⁶⁺, and c-P6¹²⁺). All the methods used qualitatively agree on the same structure for c-P6 and c-P6¹²⁺ structures (nonaromatic molecules). However, there are more discrepancies for the c-P6⁴⁺ and c-P6⁶⁺ species. Here, we will further analyze and discuss the optimized geometry of the c-P6⁶⁺ species.

We have carefully examined the optimized geometry of the c-P6⁶⁺ species using the different DFAs mentioned above in addition to LC- ω HPBE, ω being 0.1 and 0.2, and single-point DLPNO-CCSD(T)/def-SVP-C calculations. Once again, we can appreciate discrepancies in the nature of the optimized structure using different computational methods (see Figure 10.5). The functionals with a large percentage of HF exchange at long range (CAM-B3LYP, M06-2X, and LC- ω HPBE ($\omega=0.2$)), describe a less symmetric structure than the functionals which include a lower percentage of HF (B3LYP and LC- ω HPBE ($\omega=0.1$)). This second group of functionals describes a fully delocalized structure, indicating that the molecule is aromatic. As the B3LYP and LC- ω HPBE ($\omega=0.1$) methods have a low percentage of HF exchange at long-range interelectronic distances, they may suffer more from delocalization errors. The single-point DLPNO calculations reinforce the conclusions drawn above, attributing lower energy to the less symmetric structure. In addition, the CAM-B3LYP and M06-2X functionals identify the symmetric structure as a transition state connecting two equivalent minimal structures with complementary bond-order and bond-length alternation (see Figure 10.5).

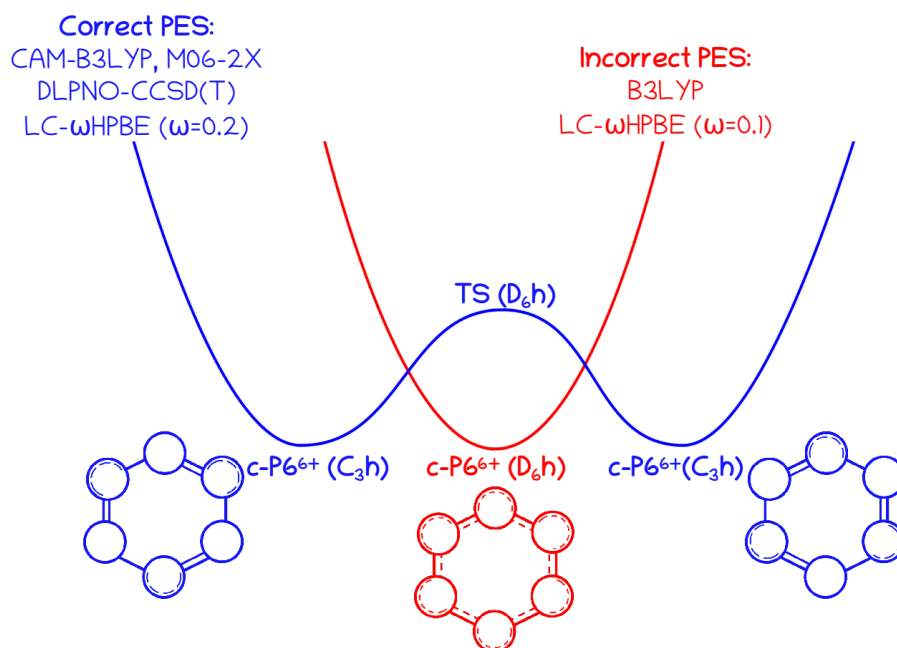


Figure 10.5: Schematic representation of the potential energy surface of c-P6⁶⁺ species described by different computational methods. Circles represent the porphyrins of the structure.

Our results further prove that using an inadequate methodology can even lead to spurious stationary points on the potential energy surface, especially in large systems as already mentioned by some authors.¹⁷

Consequently, the selection of the functional also has a critical role in the energetic, geometric, electronic, and magnetic results of the six-porphyrin nanoring. In other words, functionals with a low percentage of HF exchange at LR regime, like B3LYP, tend to overestimate the aromatic character in (large) systems.

The c-P6, c-P6⁴⁺, c-P6⁶⁺, and c-P6¹²⁺ species were initially described as nonaromatic, antiaromatic, aromatic, and nonaromatic species,¹ respectively. Peeks *et al.* studied them computationally using the B3LYP functional and experimental techniques (¹H-NMR). However, the calculations of several aromatic descriptors (FLU, BOA, HOMA, BLA, AV1245, AV_{min}, ACID, and NICS) with the CAM-B3LYP functional, and the simulated ¹H-NMR spectroscopy data showed us that none of the previous species were aromatic. The following figure is a schematic qualitative comparison of the aromaticity analysis performed on CAM-B3LYP (M06-2X) and B3LYP geometries.

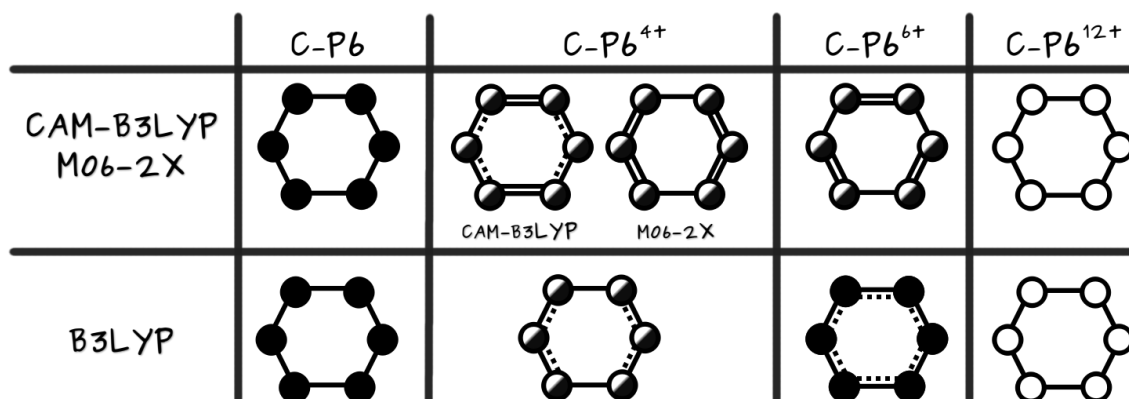


Figure 10.6: Scheme of the global aromatic character of the nanoring species according to the optimized geometries obtained with different DFAs. Full, half-full and empty circles represent aromatic, weakly aromatic and nonaromatic porphyrins, respectively. The electron delocalization in the linkers increases from single solid lines (no delocalization), to solid-dashed lines and double lines.

The latter scheme is a qualitative comparison of the global aromaticity analysis based on the local aromaticity from its constituent parts (porphyrins and linkers). As mentioned above, there are no significant differences for the c-P6 and c-P6¹²⁺ species, as expected from the geometries obtained from the different DFAs. Conversely, we appreciate considerable differences in the aromatic character of c-P6⁴⁺ and c-P6⁶⁺ for the different geometries. Mainly, there are more discrepancies in the case of c-P6⁴⁺, and there is not a good agreement between any DFAs and the experimental data (see Table 10.3). For this reason, c-P6⁴⁺ results should be taken with caution. The relative energies obtained with single-point calculations at the DLPNO-CCSD(T) level showed that the minima obtained with B3LYP and CAM-B3LYP were not so different (about 8 kcal/mol). However, there are more dissimilarities in the behavior of the electron delocalization that we can observe in ¹H-NMR chemical shifts, for example. As we can see in Table 10.3, B3LYP provides by far the worst agreement. Although CAM-B3LYP values are also far from the experimental results, this functional provides the closest agreement compared with B3LYP. Therefore, we speculate that the truth lies in between B3LYP and CAM-B3LYP values but closer to CAM-B3LYP.

In Figure 10.7, we present the plot corresponding to the c-P6⁶⁺ species as an example of the NICS(0)_{iso} grids in the x-y plane.

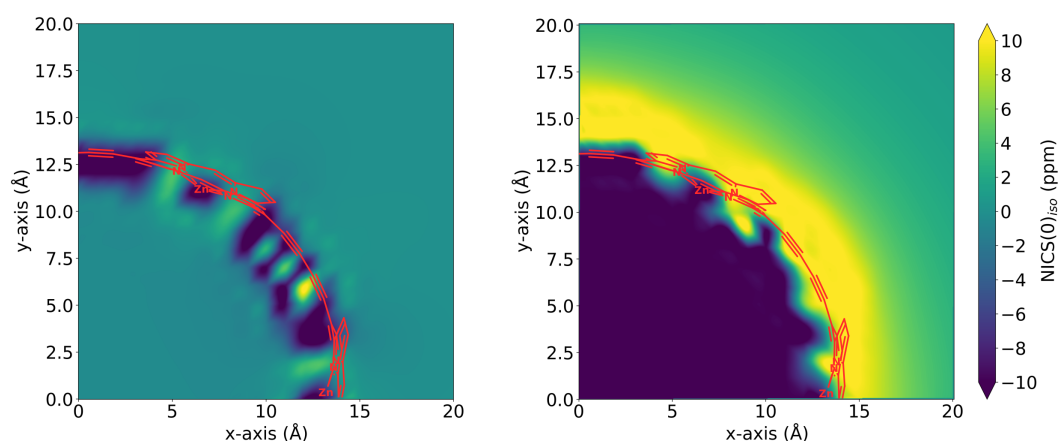


Figure 10.7: NICS(0)_{iso} grid plots for the c-P6⁶⁺ species. The *l.h.s.* plot corresponds to CAM-B3LYP optimized geometry and the *r.h.s.* to B3LYP one.

The NICS(0)_{iso} grid plots were calculated with 1 Å resolution on a 20 Å × 20 Å grid of one-fourth of the system. The NICS(0,0) value corresponds to the value at the center of the nanoring. In the NICS(0)_{iso} grid plot of the c-P6⁶⁺ species performed using CAM-B3LYP, we can observe values close to zero in the vicinity of the nanoring center while, in the B3LYP plot, large negative values are found. Therefore, these results indicate the B3LYP geometry is globally aromatic and, on the contrary, the CAM-B3LYP one is nonaromatic.

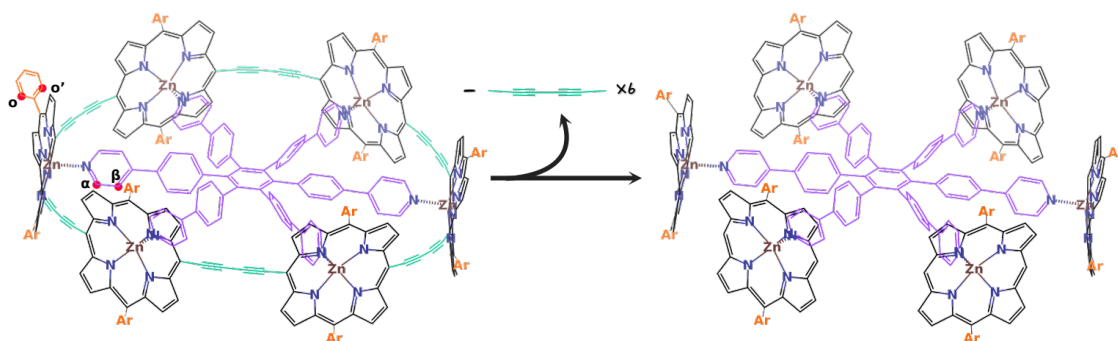
Finally, we have also computed the ¹H-NMR chemical shifts to compare with the ¹H-NMR experimental data.^{1,58} The most substantial experimental evidence of the aromatic nature of c-P6 · T6⁶⁺ comes from the shielding difference of the ortho protons (o'-o), the shielding difference between the α and β protons (see Figure 10.8) of the bound template and the free template, and the chemical shift of the THS groups' protons. However, we have not been able to compare the latter chemical shifts as in our structures the Ar group of each porphyrin were phenyls instead of THS (THS=(3,5-bis(hexylsilyl))phenyl).

As shown in Table 10.3, M06-2X and CAM-B3LYP results are in closer agreement with the experimental value than the B3LYP values.

Table 10.3: Selected $^1\text{H-NMR}$ chemical shifts differences of the different nanoring species (in ppm). Root-mean-square deviations (RMSD) are based on the experimental differences.^{1,58}

Method	data	c-P6 · T6	c-P6 · T6 ⁴⁺	c-P6 · T6 ⁶⁺	c-P6 · T6 ¹²⁺
CAM-B3LYP	o'-o	0.09	0.41	-0.19	-0.91
	α - α^{temp}	-6.34	-1.92	-0.97	1.88
	β - β^{temp}	-2.54	-0.44	-0.36	1.13
	RMSD	0.16	-	1.35	0.45
B3LYP	o'-o	0.31	36.36	-7.23	-2.67
	α - α^{temp}	-5.34	60.43	-12.26	5.63
	β - β^{temp}	-1.97	49.10	-9.85	2.68
	RMSD	0.30	-	5.36	1.41
Experimental	o'-o	0.26	-	-1.87	-0.74
	α - α^{temp}	-6.31	14.16	-2.83	2.77
	β - β^{temp}	-2.34	12.57	-2.06	1.50

According to Rikhaus *et al.*, $\Delta_{\delta_{\alpha}} < 0$ and $\Delta_{\delta_{\beta}} < 0$ will indicate a global ring current, while the opposite scenario will be an evidence of an antiaromatic ring current. Nevertheless, if such a statement is true, it will indicate that the c-P6 · T6 species is even more globally aromatic than the c-P6 · T6⁶⁺ species, which is not supported by any experimental or computational data. We have also calculated $\Delta_{\delta_{\alpha}}$ and $\Delta_{\delta_{\beta}}$ in a model in which we have eliminated the butadiyne linkers to further support our results (see Figure 10.8). If the linkers are removed, the alleged current is no longer present, and the model structure should be nonaromatic. The α and β chemical shift differences of the model show that although the porphyrins are not connected, a ring current is present. This is another evidence that c-P6 · T6⁶⁺ species is weakly aromatic or nonaromatic and that none of the studied species is aromatic.

**Figure 10.8:** Nanoring structure and the studied model without the bridging butadiyne linkers. Small red dots indicate the position of ortho protons of the aryl substituent and the α and β protons of the template, respectively.

10.3.2 Aromaticity indices

In all our aromaticity studies, we have evaluated how the electron delocalization affects the aromaticity measures using the different computational methods exposed before, focusing on the role of the exchange functional.

The study of nine porphyrinoid compounds, Chapter 5, compares several structural and electronic aromaticity indices values obtained using B3LYP, M06-2X, and CAM-B3LYP. This comparison allows us to find, in some systems, an excellent agreement between the results obtained with CAM-B3LYP and M06-2X, which suggests that the long-range part of the exact exchange is the one that plays an important role in the description of the aromaticity character of the molecules. As an example, in Figure 10.9 we have represented AV_{min} values calculated with B3LYP and M06-2X functionals *versus* CAM-B3LYP values.

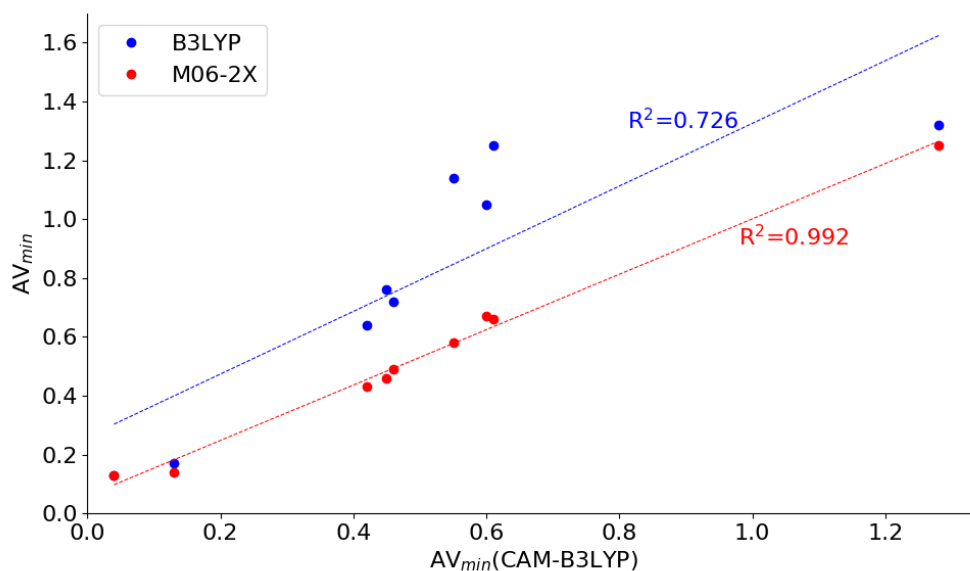


Figure 10.9: Relationship of AV_{min} among nine porphyrinoid systems calculated with M06-2x and B3LYP against CAM-B3LYP values for all the annulene pathways.

There is a perfect correlation between M06-2X and CAM-B3LYP values in the latter plot, whereas the values computed with B3LYP are not as good. Moreover, all the B3LYP values in Figure 10.9 are above the CAM-B3LYP values indicating a general overestimation of the AV_{min} values using the B3LYP functional. However, there are two exceptions in which the values are not overestimated, and they precisely correspond to the smaller porphyrins, 16H and 18H. Additionally, three values particularly overestimate the B3LYP results, and they correspond to 26H, 28M, and 32M expanded porphyrins. In some molecules, we have found a quantitative and qualitative agreement between M06-2X and CAM-B3LYP functionals, while in other sets of compounds, we only find

a qualitative agreement. However, for the most complicated porphyrinoid structures, this agreement is no longer observed. It is worth mentioning here that the optimized geometries with each DFAs present some differences, which can be responsible for the disagreements between B3LYP and CAM-B3LYP or M06-2X functionals.

Another proof that corroborates that the long-range part of HF exchange is relevant to decrease the delocalization error is the MCI(1,2,4,5) distribution plots. We have used these plots to describe the aromatic character when the AV_{min} values are too small to draw any solid conclusion. One example of a MCI(1,2,4,5) distribution plot is shown in Figure 10.10.

In MCI(1,2,4,5) distribution plots, the four-center delocalization index for each fragment is represented along the most aromatic pathway. The average value of these indices will be the AV1245 index.

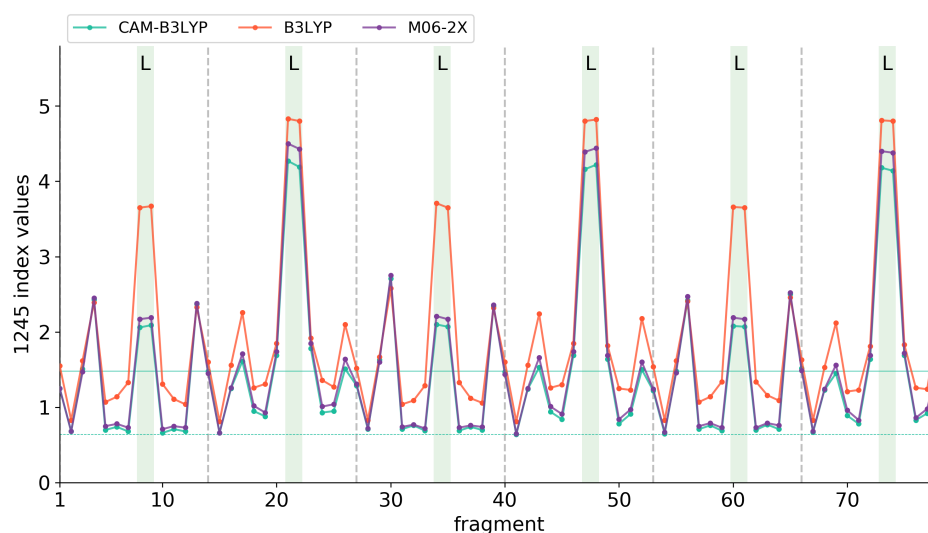


Figure 10.10: Comparison of the 1245-index distributions including the individual MCI(1,2,4,5) values along the most aromatic path of $c\text{-P6} \cdot \text{T6}^{6+}$ species calculated at different levels of theory. Horizontal solid line corresponds to the AV1245 value (1.48) and dashed horizontal line to the AV_{min} value (0.64), both from CAM-B3LYP calculation.

The plot represented above corresponds to the $c\text{-P6} \cdot \text{T6}^{6+}$ nanoring species. We can appreciate that all the values calculated with the different DFAs have the same qualitative trend. However, CAM-B3LYP values approximately match with M06-2X values, while the B3LYP ones are always higher. For this reason, we can conclude that B3LYP is overestimating the aromaticity of this species.

10.3.3 UV-Vis absorption spectra

In general, we have seen that to have an accurate description of the geometry, and the aromatic character of large conjugated systems a functional with a large percentage of HF exchange (at least above 50%) at the LR regime is needed. In RSF, the value of the attenuating parameter employed to split the SR and the LR regime is important. In the nanoring study, we have seen that using a RSF with an attenuating parameter equal to 0.1 au^{-1} is not enough to describe the nanoring structure correctly, suggesting that some delocalization error is still present. The exchange potential does not present the correct asymptotic decay, which affects various properties such as: ionization potentials, electron conjugation, charge-transfer excitations, among others. These errors are generally attributed to the delocalization error. The accuracy of the electronic excitation energies computed with a RSF also depends on the value of the attenuating parameter ω . This dependency is very pronounced when the excited state has a charge-transfer character. Different techniques have been proposed to optimally tune the value of ω for a given molecule.

In Chapter 9, we have applied a procedure to study a set of copper and iridium photosensitizers (PSs) and a family of cobalt catalysts. Particularly, we have analyzed a protocol to simulate the UV-Vis absorption spectra and redox potentials. As these PSs present CT excitations and these excitations are not correctly describe even by global hybrid DFAs²⁶ (see Section 1.1.1 and 2.2.1), a RSF has been used (LC- ω PBE). To analyze which value of ω is needed to obtain more accurate results, we have used an optimally tuned RSF. We have compared the results obtained with B3LYP, with the RSF without optimizing the ω parameter, and with the experimental data, when available.

In general, we have seen that the B3LYP hybrid functional correctly describes the CT excitation band with a red shift in the value of the wavelength for the synthesized copper PS and a blue shift for the iridium ones. Then, the LC- ω PBE functional ($\omega=0.4\text{au}^{-1}$), even if it is expected to describe CT excitation correctly, cannot even reproduce the CT excitation band (see Figure 10.11). We have obtained an accurate description of the CT excitation band with the LC- ω PBE method using the optimal value of ω (LC- ω PBE-opt). However, the excitation wavelength is blue shifted for all synthesized PSs with respect to the experimental data. We have seen that the optimal value of the attenuating parameter is not universal, but it lies in a short interval within a family of photosensitizers. This means that a different functional is needed to simulate the UV-Vis spectra for each molecule because small differences in the ω value will affect the UV-Vis absorption spectrum.

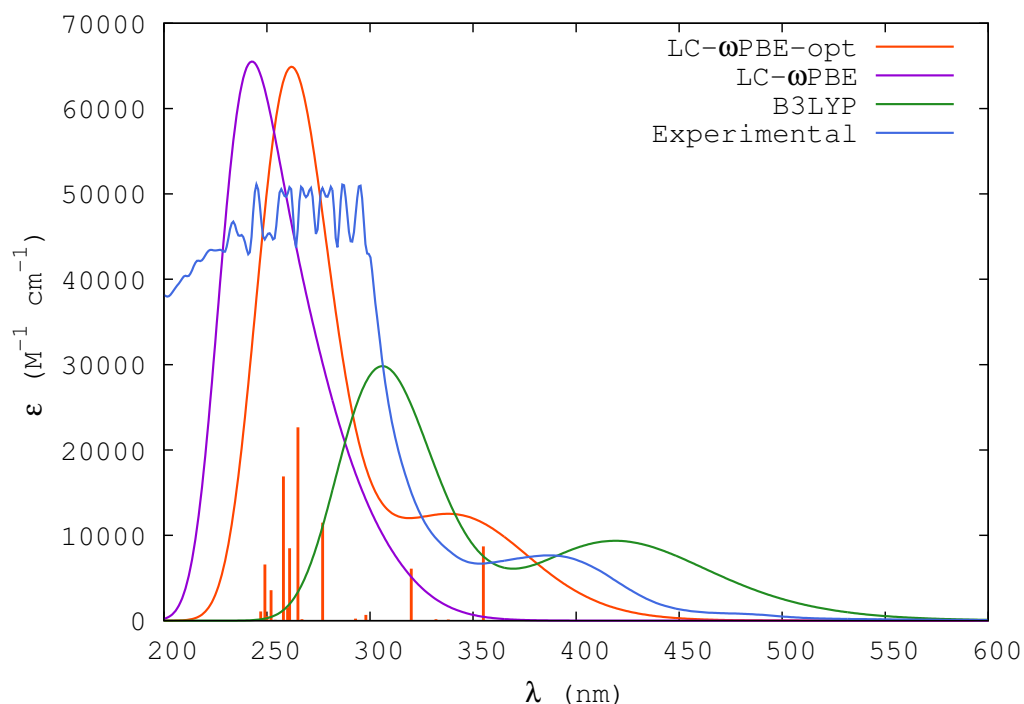


Figure 10.11: Simulated UV-Vis absorption spectrum with LC- ω PBE-opt, LC- ω PBE and B3LYP functionals, and the experimental spectrum of a copper photosensitizer (PS₈). The spectra are plotted using a standard deviation of 0.4eV. For LC- ω PBE-opt functional, we have also plotted the orange vertical lines corresponding to the different vertical excitations.

The UV-Vis absorption spectrum of PS₈ (Figure 10.11), is a clear example of the previous discussions, where we can observe the shifts of the B3LYP and LC- ω PBE-opt functionals. These shifts may be due to several factors: (i) we have not taken into account vibronic couplings, (ii) the shape of simulated spectra is the result of the summation of several Gaussian functions that represent different excitations, and (iii) in the simulated spectra we have not included any explicit solvent molecule (only implicit solvent was taken into account). Therefore, all the simulated spectra can not be compared directly with the experimental ones, but they can be used as a first approximation. Direct comparisons of theoretical data with experimental measurements remain challenging and computationally expensive.

Although we were interested in the CT excitation because it is the one that is important in the absorption process of Dye-sensitized solar cells and other photochemical processes, it is essential to describe the whole spectrum correctly. For this reason, B3LYP is not an excellent functional, and it is better to use LC- ω PBE-opt, which improves the simulation significantly due to the optimization process of the attenuating parameter.

The cobalt complexes do not present a CT excitation, and for this reason, they are not used as photosensitizers. Accordingly, they are used as catalysts in different photocatalytic processes.^{156,372} The fact that they do not have CT excitations makes

the optimization of the attenuating parameter not highly relevant for these Co complexes (see Chapter 9).

10.3.4 Redox potentials

Optimally tuned versions of range-separated functionals have already been applied to large molecules to better describe one-electron properties such as fundamental gaps, photoelectron spectrum, and the CT excitation energy.^{258,373–375} However, in Chapter 9, we have also applied the same ω optimization process to investigate if it also improves the reduction potentials of the photosensitizers and the set of cobalt catalysts.

Observing the calculated reduction potentials and comparing them with the experimental data (see Table 10.4), we can see that, in general, the three functionals give values close to the experimental ones, except the PS₁₉. For this reason, it seems that the delocalization error does not significantly affect the calculation of this chemical property.

Table 10.4: Redox potentials (E_{red}^o , in V) calculated using B3LYP, LC- ω PBE-opt, and CAM-B3LYP. The experimental available data is also included. Maximum error (MAX), root mean square error (RMSE), and mean absolute error (MAE) of each method are also given.

PS	B3LYP	LC- ω PBE-opt	CAM-B3LYP	$E_{red\ expt}^o$ (V)
PS ₈	-1.63	-1.60	-1.69	-1.60
PS ₁₀	-1.51	-1.46	-1.50	-1.47
PS ₁₁	-1.74	-1.74	-1.79	-1.66
PS ₁₇	-1.36	-1.32	-1.38	-1.40
PS ₁₈	-0.91	-0.94	-0.98	-1.01
PS ₁₉	-1.78	-2.50	-2.14	-1.80
MAX	0.10	0.70	0.34	0.00
MAE	0.05	0.16	0.11	0.00
RMSE	0.06	0.29	0.15	0.00

Despite the LC- ω PBE-opt functional gave accurate results for most of the PSs, it is not worthwhile using this functional if we only need to calculate the reduction potentials. It seems that B3LYP is sufficiently accurate to calculate reduction potentials of molecules with CT excitations. Additionally, we have seen similar trends in the reduction potentials of the cobalt complexes ($E_{(Co^{II}/Co^I)}^o$). However, the reduction potential of the Co complexes present larger errors compared to the PSs reduction potential.

Chapter 11

Conclusions

In this thesis, we have studied the aromaticity of (large) conjugated systems. We have determined the best DFAs to investigate this chemical property. In addition, we have also studied different protocols to characterize the UV-Vis absorption spectra and redox potentials of two families of photosensitizers, and a family of cobalt catalysts. These properties are, in principle, strongly affected by the choice of the functional approximation used to treat these systems.

The determination of the aromatic character of large conjugated systems is a challenging task. In this thesis, we focus on studying aromaticity using electronic indices. Two of the most popular and reliable electronic indices, I_{ring} and MCI, cannot be employed to treat large systems due to their high computational cost and numerical errors. For this reason, we decided to use the recently developed electronic aromaticity index, AV1245.

Firstly, we have tested AV1245 in a family of simple expanded porphyrins and a set of annulenes, comparing its performance with other electronic, structural, or even magnetic well-established indices. We have seen that AV1245 agrees with the other aromaticity descriptors on the general features of the studied compounds. However, we do not intend to obtain the same results with all the indices since we know that we do not measure the same manifestations of aromaticity using electronic, geometric, energetic, or magnetic indices. In some cases, we have seen that the AV1245 index does not provide all the information needed as it is an average descriptor and could hinder some crucial values. Accordingly, the minimal value of the AV1245 index, AV_{min} , was suggested as an alternative. In general, we have found that this index provides the expected aromatic character of the molecule according to the aromaticity rules, other aromaticity indices, or the experimental data. Moreover, it is essential to highlight that it is the only index capable of recognizing the annulene pathway as the most aromatic one in neutral por-

phyrinoid structures.¹⁸ Nevertheless, we have seen cases where it is difficult to assess the aromatic character with only the values of this index. Specifically to differentiate the antiaromatic molecules, as they present AV_{min} values between aromatic and nonaromatic systems.⁹⁰ In these cases, we have proposed to use the BOA values if the system is small or the individual MCI(1,2,4,5) distribution plots along the studied path for larger molecules.³⁵³

Secondly, studying the annulene series (C_nH_n , where n is an even number between 4 and 18), we have seen how the Hückel and Baird rules fade away with the ring size.¹⁹ As the ring size increases, molecules start to present more torsions. These torsions do not favor the optimal overlap of the p orbitals, thus breaking up the electron delocalization. Accordingly, for large conjugated systems, the main aromaticity rules may no longer apply.

Thirdly, we have verified that the percentage of HF exchange included in density functional approximations plays a crucial role in the description of the electronic structure as well as the description of the aromatic character as already stated by other authors.¹⁷ We have confirmed that functionals with a low percentage of exact exchange tend to overestimate the electron delocalization. Additionally, comparing different DFAs, we have seen that it is the long-range part of the exact exchange that has a dominant role in assessing aromaticity.¹⁸ Functionals with a low percentage of exact exchange are more prone to present failures when describing chemical properties like aromaticity^{18,19,90,353} or CT excitations³⁷⁶ due to the delocalization error, especially in large systems. The delocalization error exaggerates the delocalization of the electrons, overestimating the aromaticity and underestimating the charge-transfer excitation energies. Therefore, it is crucial to choose an adequate computational functional with a higher percentage (above 50%) of exact exchange at large interelectronic distances first to optimize the structure of (large) systems and then to compute the target chemical property.

Fourthly, we have examined the aromaticity character of four oxidation states of a six-porphyrin nanoring. Two of them are nonaromatic according to experimental data and B3LYP calculations,¹ and we have confirmed these results. However, we could not draw the same conclusion for the other two species that were considered aromatic (+6-oxidation state species) and antiaromatic (+4-oxidation state species) in the original article.¹ We found that none of the studied species was aromatic, and we have provided compelling evidence that the description of the +6 species suffers from severe delocalization errors that result in the overestimation of the aromaticity of this species.³⁵³ We have seen that functionals with a low percentage of HF exchange at long-range interelectronic distances provide a fully delocalized structure for the +6 species, point-

ing that the system is aromatic. Functionals with a large percentage of HF exchange at long-range regime, provide a less symmetric structure, indicating that the species is slightly aromatic or nonaromatic. Moreover, CAM-B3LYP and M06-2X recognize the symmetric structure as a transition state connecting two equivalent minimal structures with complementary bond-order and bond-length alternation.

Finally, we analyzed which value of the attenuating parameter is needed to describe the electronic structures and associated chemical properties accurately using a set of photosensitizers that present CT excitations and a family of cobalt catalysts.³⁷⁶ To describe this type of excitations accurately, a range-separated functional is needed. We have optimized the attenuating parameter of a RSF (LC- ω PBE) by minimizing the J^* descriptor of the Δ SCF method. We have seen that the optimal value of ω is not universal for all the studied molecules. However, it lies in a short interval within a family of complexes. The simulation of a UV-Vis absorption spectrum, including the optimization of the ω parameter, is seven times more expensive than the simulation of the same spectrum with the default value of ω (with an ω accuracy of 10^{-4}). Nevertheless, despite the computational cost, it is worth optimizing the ω parameter because it considerably improves the simulated spectrum. Then, we have verified that this optimally tuned RSF improves the UV-Vis spectra of the studied photosensitizers. However, for the cobalt complexes, the optimization of the ω parameter is not as relevant as in the photosensitizers for the simulation of UV-Vis spectra, as they do not present CT excitations. Moreover, we have applied this optimally tuned RSF to calculate the reduction potentials of the photosensitizers and the cobalt complexes. We have concluded that, in general, the redox potentials of the photosensitizers are slightly improved using LC- ω PBE with the optimal value of ω , and none of the functionals used give accurate reduction potentials of the cobalt complexes family.

Bibliography

- [1] M. D. Peeks, T. D. Claridge and H. L. Anderson, *Nature*, 2017, **541**, 200–205.
- [2] A. M. Turing, *Mind*, 1950, **59**, 433–460.
- [3] A. P. Saygin, I. Cicekli and V. Akman, *Minds and machines*, 2000, **10**, 463–518.
- [4] U. Becker and N. Allinger, *Molecular Mechanics*, 1982.
- [5] T. E. o. E. Britannica, *Electron*, <https://www.britannica.com/science/electron>, Accessed: 2021-05-20.
- [6] A. R. Leach and A. R. Leach, *Molecular modelling: principles and applications*, Pearson education, 2001.
- [7] M. Born and R. Oppenheimer, *Annalen der physik*, 1927, **389**, 457–484.
- [8] M. Jaeger, L. Freitag and L. Gonzalez, *Coord. Chem. Rev.*, 2015, **304**, 146–165.
- [9] W. Thiel, in *Theory and applications of computational chemistry*, Elsevier, 2005, pp. 559–580.
- [10] A. J. Cohen, P. Mori-Sánchez and W. Yang, *Science*, 2008, **321**, 792–794.
- [11] S. Grimme, S. Ehrlich and L. Goerigk, *J. Comput. Chem.*, 2011, **32**, 1456–1465.
- [12] P. Jurečka, J. Černý, P. Hobza and D. R. Salahub, *J. Comput. Chem.*, 2007, **28**, 555–569.
- [13] S. Grimme, J. Antony, S. Ehrlich and H. Krieg, *J. Chem. Phys.*, 2010, **132**, 154104.
- [14] P. Mori-Sánchez, A. J. Cohen and W. Yang, *Many-electron self-interaction error in approximate density functionals*, 2006.
- [15] J. Autschbach and M. Srebro, *Acc. Chem. Res.*, 2014, **47**, 2592–2602.

- [16] F. Peccati, R. Laplaza and J. Contreras-García, *J. Phys. Chem. C*, 2019, **123**, 4767–4772.
- [17] M. Torrent-Sucarrat, S. Navarro, F. P. Cossío, J. M. Anglada and J. M. Luis, *J. Comput. Chem.*, 2017, **38**, 2819–2828.
- [18] I. Casademont-Reig, T. Woller, J. Contreras-García, M. Alonso, M. Torrent-Sucarrat and E. Matito, *Phys. Chem. Chem. Phys.*, 2018, **20**, 2787–2796.
- [19] I. Casademont-Reig, E. Ramos-Cordoba, M. Torrent-Sucarrat and E. Matito, *Molecules*, 2020, **25**, 711.
- [20] A. Dreuw and M. Head-Gordon, *J. Am. Chem. Soc.*, 2004, **126**, 4007–4016.
- [21] W. Hieringer and E. J. Baerends, *J. Phys. Chem. A*, 2006, **110**, 1014–1021.
- [22] J. Autschbach, *ChemPhysChem*, 2009, **10**, 1757–1760.
- [23] C. A. Ullrich and Z.-h. Yang, *Braz. J. Phys.*, 2014, **44**, 154–188.
- [24] R. Zaleśny, M. Medved', S. P. Sitkiewicz, E. Matito and J. M. Luis, *J. Chem. Theory Comput.*, 2019, **15**, 3570–3579.
- [25] P. Besalú-Sala, S. P. Sitkiewicz, P. Salvador, E. Matito and J. M. Luis, *Phys. Chem. Chem. Phys.*, 2020, **22**, 11871–11880.
- [26] Y. Tawada, T. Tsuneda, S. Yanagisawa, T. Yanai and K. Hirao, *J. Chem. Phys.*, 2004, **120**, 8425–8433.
- [27] D. Harper, *Online Etymology Dictionary*, <https://www.etymonline.com/word/aroma>, Accessed: 2020-09-10.
- [28] C. B.-S. license, *Etymolgeek*, <https://etymologeek.com>, Accessed: 2020-11-23.
- [29] P. v. R. Schleyer, *Chem. Rev.*, 2001, **101**, 1115–1118.
- [30] M. Faraday, *Philosophical Transactions of the Royal Society of London*, 1825, 440–466.
- [31] M. Ruiza, T. Fernández and E. Tamaro, *Biografía de Michael Faraday. En Biografías y Vidas. La enciclopedia biográfica en líneas*, <https://www.biografiasyvidas.com/biografia/f/faraday.htm>, Accessed: 2020-11-24.
- [32] A. Kekulé, *Bull. Soc. Chim.*, 1865, **3**, 98–110.

-
- [33] Z. Chen, C. S. Wannere, C. Corminboeuf, R. Puchta and P. v. R. Schleyer, *Chem. Rev.*, 2005, **105**, 3842–3888.
- [34] F. Feixas Geronès, *Ph.D. thesis*, Univ. Girona, Girona, 2010.
- [35] M. Palusiak, S. Simon and M. Solà, *J. Org. Chem.*, 2006, **71**, 5241–5248.
- [36] M. Palusiak, S. Simon and M. Solà, *J. Org. Chem.*, 2009, **74**, 2059–2066.
- [37] E. C. Crocker, *J. Am. Chem. Soc.*, 1922, **44**, 1618–1630.
- [38] E. Matito, J. Poater, M. Duran and M. Solà, *J. Mol. Struct. (Theochem)*, 2005, **727**, 165–171.
- [39] P. v. R. Schleyer, J. I. Wu, F. P. Cossío and I. Fernández, *Chem. Soc. Rev.*, 2014, **43**, 4909–4921.
- [40] B. C. Streifel, J. L. Zafra, G. L. Espejo, C. J. Gómez-García, J. Casado and J. D. Tovar, *Angew. Chem. Int. Ed.*, 2015, **54**, 5888–5893.
- [41] K. Jorner, F. Feixas, R. Ayub, R. Lindh, M. Solà and H. Ottosson, *Chem. Eur. J.*, 2016, **22**, 2793–2800.
- [42] M. Ueda, K. Jorner, Y. M. Sung, T. Mori, Q. Xiao, D. Kim, H. Ottosson, T. Aida and Y. Itoh, *Nat. Chem.*, 2017, **8**, 346–354.
- [43] F. Feixas, J. Vandebussche, P. Bultinck, E. Matito and M. Solà, *Phys. Chem. Chem. Phys.*, 2011, **13**, 20690–20703.
- [44] A. Osuka and S. Saito, *Chem. Commun.*, 2011, **47**, 4330–4339.
- [45] F. Feixas, M. Solà and M. Swart, *Can. J. Chem.*, 2009, **87**, 1063–1073.
- [46] E. Marcos, J. M. Anglada and M. Torrent-Sucarrat, *J. Org. Chem.*, 2014, **79**, 5036–5046.
- [47] M. Alonso, B. Pinter, P. Geerlings and F. De Proft, *Chem. Eur. J.*, 2015, **21**, 17631–17638.
- [48] C. Liu, M. E. Sandoval-Salinas, Y. Hong, T. Y. Gopalakrishna, H. Phan, N. Aratani, T. S. Herng, J. Ding, H. Yamada, D. Kim *et al.*, *Chem*, 2018, **4**, 1586–1595.
- [49] X. Li, A. E. Kuznetsov, H.-F. Zhang, A. I. Boldyrev and L.-S. Wang, *Science*, 2001, **291**, 859–861.

- [50] A. I. Boldyrev and L.-S. Wang, *Chem. Rev.*, 2005, **105**, 3716–3757.
- [51] I. A. Popov, F.-X. Pan, X.-R. You, L.-J. Li, E. Matito, C. Liu, H.-J. Zhai, Z.-M. Sun and A. I. Boldyrev, *Angew. Chem. Int. Ed.*, 2016, **128**, 15570–15572.
- [52] F. Feixas, E. Matito, J. Poater and M. Solà, *WIREs, Comput. Mol. Sci.*, 2013, **3**, 105–122.
- [53] X. Min, I. A. Popov, F.-X. Pan, L.-J. Li, E. Matito, Z.-M. Sun, L.-S. Wang and A. I. Boldyrev, *Angew. Chem. Int. Ed.*, 2016, **55**, 5531–5535.
- [54] M. Garcia-Borràs, S. Osuna, M. Swart, J. M. Luis and M. Solà, *Angew. Chem. Int. Ed.*, 2013, **52**, 9275–9278.
- [55] Z. Chen, J. I. Wu, J. Corminboeuf, Clémence Bohmann, X. Lu, A. Hirsch and P. v. R. Schleyer, *Phys. Chem. Chem. Phys.*, 2012, **14**, 14886–14891.
- [56] M. D. Peeks, J. Q. Gong, K. McLoughlin, T. Kobatake, R. Haver, L. M. Herz and H. L. Anderson, *J. Phys. Chem. Lett.*, 2019, **10**, 2017–2022.
- [57] S. M. Kopp, H. Gotfredsen, J.-R. Deng, T. D. Claridge and H. L. Anderson, *J. Am. Chem. Soc.*, 2020, **142**, 19393–19401.
- [58] M. Rickhaus, M. Jirasek, L. Tejerina, H. Gotfredsen, M. D. Peeks, R. Haver, H.-W. Jiang, T. D. Claridge and H. L. Anderson, *Nat. Chem.*, 2020, **12**, 236–241.
- [59] M. Nencki and N. Sieber, *Arch. exp. Path. u. Pharmacol.*, 1884, **18**, 401–422.
- [60] H. Fischer and J. Klarer, *Justus Liebigs Annalen der Chemie*, 1926, **450**, 181–201.
- [61] M. Evans and E. Warhurst, *Trans. Faraday Soc.*, 1938, **34**, 614–624.
- [62] J. Grunenberg, *Int. J. Quantum Chem.*, 2017, **117**, e25359.
- [63] M. Goldstein and R. Hoffmann, *J. Am. Chem. Soc.*, 1971, **93**, 6193–6204.
- [64] M. J. Goldstein, *J. Am. Chem. Soc.*, 1967, **89**, 6357–6359.
- [65] W.-Y. Cha, T. Kim, A. Ghosh, Z. Zhang, X.-S. Ke, R. Ali, V. M. Lynch, J. Jung, W. Kim, S. Lee *et al.*, *Nat. Chem.*, 2017, **9**, 1243–1248.
- [66] J. K. Sprafke, D. V. Kondratuk, M. Wykes, A. L. Thompson, M. Hoffmann, R. Drevinskas, W.-H. Chen, C. K. Yong, J. Karnbratt, J. E. Bullock *et al.*, *J. Am. Chem. Soc.*, 2011, **133**, 17262–17273.

-
- [67] P. Cui, H.-S. Hu, B. Zhao, J. T. Miller, P. Cheng and J. Li, *Nat. Commun.*, 2015, **6**, 1–5.
- [68] M. Solà, *Front. Chem.*, 2017, **5**, 22.
- [69] G. Frenking and A. Krapp, *J. Comput. Chem.*, 2007, **28**, 15–24.
- [70] F. Sondheimer, *Pure Appl. Chem.*, 1963, **7**, 363–388.
- [71] A. R. Katritzky, P. Barczynski, G. Musumarra, D. Pisano and M. Szafran, *J. Am. Chem. Soc.*, 1989, **111**, 7–15.
- [72] A. R. Katritzky, K. Jug and D. C. Oniciu, *Chem. Rev.*, 2001, **101**, 1421–1450.
- [73] A. R. Katritzky, M. Karelson, T. M. Sild, S. and and K. Jug, *J. Org. Chem.*, 1998, **63**, 5228–5231.
- [74] T. M. Krygowski and M. K. Cyranski, *Chem. Rev.*, 2001, **101**, 1385–1420.
- [75] M. K. Cyrański, T. M. Krygowski, A. R. Katritzky and P. v. R. Schleyer, *J. Org. Chem.*, 2002, **67**, 1333–1338.
- [76] R. Hoffmann, *Am. Sci.*, 2015, **103**, 18–22.
- [77] R. Islas, T. Heine and G. Merino, *Acc. Chem. Res.*, 2011, **45**, 215–228.
- [78] J. I. Wu, in *Applied Theoretical Organic Chemistry*, ed. D. J. Tantillo, World Scientific, London, 2018, pp. 273–288.
- [79] R. H. Mitchell, *Chem. Rev.*, 2001, **101**, 1301–1316.
- [80] J.-Y. Shin, K. S. Kim, M.-C. Yoon, J. M. Lim, Z. S. Yoon, A. Osuka and D. Kim, *Chem. Soc. Rev.*, 2010, **39**, 2751–2767.
- [81] M. K. Cyranski, *Chem. Rev.*, 2005, **105**, 3773–3811.
- [82] R. Gershoni-Poranne and A. Stanger, *Chem. Soc. Rev.*, 2015, **44**, 6597–6615.
- [83] T. M. Krygowski, H. Szatyłowicz, O. A. Stasyuk, J. Dominikowska and M. Palusiak, *Chem. Rev.*, 2014, **114**, 6383–6422.
- [84] J. Poater, M. Duran, M. Solà and B. Silvi, *Chem. Rev.*, 2005, **105**, 3911–3947.
- [85] F. Feixas, E. Matito, J. Poater and M. Solà, *Chem. Soc. Rev.*, 2015, **44**, 6389–6646.
- [86] E. Matito, *Phys. Chem. Chem. Phys.*, 2016, **18**, 11839–11846.

- [87] C. García-Fernández, E. Sierda, M. Abadia, B. E. C. Bugenhagen, M. H. Proscenc, R. Wiesendanger, M. Bazarnik, J. E. Ortega, J. Brede, E. Matito and A. Arnau, *J. Phys. Chem. C*, 2017, **121**, 27118–27125.
- [88] F. Feixas, E. Matito, J. Poater and M. Sola, *J. Phys. Chem. A*, 2007, **111**, 4513–4521.
- [89] M. Solà i Puig, F. Feixas Geronès, J. Ó. C. Jiménez Halla, E. Matito i Gras and J. Poater i Teixidor, *Symmetry*, 2010, **2**, 1156–1179.
- [90] I. Casademont-Reig, E. Ramos-Cordoba, M. Torrent-Sucarrat and E. Matito, in *Aromaticity. Modern computational methods and applications*, ed. I. Fernandez, Elsevier, Amsterdam, 2021, pp. 235–258.
- [91] F. Feixas, J. Jiménez-Halla, E. Matito, J. Poater and M. Solà, *J. Chem. Theory Comput.*, 2010, **6**, 1118–1130.
- [92] F. Feixas, E. Matito, J. Poater and M. Solà, *J. Comput. Chem.*, 2008, **29**, 1543–1554.
- [93] L. J. Karas and J. I. Wu, in *Aromaticity. Modern computational methods and applications*, ed. I. Fernandez, Elsevier, Amsterdam, 2021, pp. 319–337.
- [94] K. Wade, *J. Chem. Soc. Chem. Commun.*, 1971, 792–793.
- [95] D. M. Mingos, *Acc. Chem. Res.*, 1984, **17**, 311–319.
- [96] A. Hirsch, Z. Chen and H. Jiao, *Angew. Chem. Int. Ed.*, 2000, **39**, 3915–3917.
- [97] J. Poater and M. Solà, *Chem. Commun.*, 2011, **47**, 11647–11649.
- [98] M. Solà, *WIREs, Comput. Mol. Sci.*, 2019, **9**, e1404.
- [99] F. Feixas, E. Matito, J. Poater and M. Solà, in *Applications of topological methods in molecular chemistry*, Springer, 2016, pp. 321–335.
- [100] E. Hückel, *Z. Physik*, 1931, **70**, 104–186.
- [101] E. Hückel, *Z. Physik*, 1931, **72**, 310–337.
- [102] R. Breslow, *Acc. Chem. Res.*, 1973, **6**, 393–398.
- [103] F. Feixas, E. Matito, M. Solà and J. Poater, *J. Phys. Chem. A*, 2008, **112**, 13231–13238.
- [104] E. Heilbronner, *Tetrahedron Lett.*, 1964, **5**, 1923–1928.

-
- [105] W. C. McKee, I. Wu, Judy, H. S. Rzepa and P. v. R. Schleyer, *Org. Lett.*, 2013, **15**, 3432–3435.
- [106] N. C. Baird and R. M. West, *J. Am. Chem. Soc.*, 1971, **93**, 4427–4432.
- [107] N. C. Baird, *J. Am. Chem. Soc.*, 1972, **94**, 4941–4948.
- [108] H. Ottosson, *Nat. Chem.*, 2012, **4**, 969–971.
- [109] P. B. Karadakov, *J. Phys. Chem. A*, 2008, **112**, 7303–7309.
- [110] P. B. Karadakov, *J. Phys. Chem. A*, 2008, **112**, 12707–12713.
- [111] E. Clar, *The aromatic sextet*, Wiley-Interscience, 1972.
- [112] M. Solà, *Front. Chem.*, 2013, **1**, 1–8.
- [113] A. Hirsch, Z. Chen and H. Jiao, *Angew. Chem. Int. Ed.*, 2001, **113**, 2916–2920.
- [114] J. Poater and M. Solà, *Chem. Commun.*, 2019, **55**, 5559–5562.
- [115] E. Hückel, *Z. Physik*, 1932, **76**, 628–648.
- [116] E. Hückel, *Z. Elektrochemie*, 1937, **43**, 752–788, 827–849.
- [117] E. Matito, F. Feixas and M. Solà, *J. Mol. Struct. (Theochem)*, 2007, **811**, 3–11.
- [118] S. Saito and A. Osuka, *Angew. Chem. Int. Ed.*, 2011, **50**, 4342–4373.
- [119] K. Kadish, K. M. Smith and R. Guilard, *The Porphyrin Handbook, Volume 3*, Elsevier, 2000, vol. 3.
- [120] M. Stępień, N. Sprutta and L. Latos-Grażyński, *Angew. Chem. Int. Ed.*, 2011, **50**, 4288–4340.
- [121] C. Liu, D.-M. Shen and Q.-Y. Chen, *J. Am. Chem. Soc.*, 2007, **129**, 5814–5815.
- [122] H. Flieg, R. Valiev, F. Pichierri and D. Sundholm, *Theoretical studies as a tool for understanding the aromatic character of porphyrinoid compounds*, Royal Society of Chemistry, London, 2018.
- [123] T. Tanaka and A. Osuka, *Chem. Rev.*, 2017, **117**, 2584–2640.
- [124] J. L. Sessler and D. Seidel, *Angew. Chem. Int. Ed.*, 2003, **115**, 5292–5333.
- [125] J. L. Sessler and D. Seidel, *Angew. Chem. Int. Ed.*, 2003, **42**, 5134–5175.
-

- [126] V. J. Bauer, D. L. Clive, D. Dolphin, J. B. Paine III, F. L. Harris, M. M. King, J. Loder, S. W. C. Wang and R. B. Woodward, *J. Am. Chem. Soc.*, 1983, **105**, 6429–6436.
- [127] P. C. Ford, *Acc. Chem. Res.*, 2008, **41**, 190–200.
- [128] J. L. Sessler, S. Camiolo and P. A. Gale, *Coord. Chem. Rev.*, 2003, **240**, 17–55.
- [129] R. Misra, R. Kumar, T. K. Chandrashekar, C. Suresh, A. Nag and D. Goswami, *J. Am. Chem. Soc.*, 2006, **128**, 16083–16091.
- [130] L. Schmidt-Mende, W. M. Campbell, Q. Wang, K. W. Jolley, D. L. Officer, M. K. Nazeeruddin and M. Grätzel, *ChemPhysChem*, 2005, **6**, 1253–1258.
- [131] J. Seenisamy, S. Bashyam, V. Gokhale, H. Vankayalapati, D. Sun, A. Siddiqui-Jain, N. Streiner, K. Shin-Ya, E. White, W. D. Wilson *et al.*, *J. Am. Chem. Soc.*, 2005, **127**, 2944–2959.
- [132] B. Franck and A. Nonn, *Angew. Chem. Int. Ed.*, 1995, **34**, 1795–1811.
- [133] R. Charriere, T. Jenny, H. Rexhausen and A. Gossauer, *Heterocycles (Sendai)*, 1993, **36**, 1561–1575.
- [134] J. L. Sessler, S. J. Weghorn, Y. Hiseada and V. Lynch, *Chem. Eur. J.*, 1995, **1**, 56–67.
- [135] Y. M. Sung, J. Oh, W.-Y. Cha, W. Kim, J. M. Lim, M.-C. Yoon and D. Kim, *Chem. Rev.*, 2017, **117**, 2257–2312.
- [136] R. Herges, *Chem. Rev.*, 2006, **106**, 4820–4842.
- [137] A. A. Frost and B. Musulin, *J. Chem. Phys.*, 1953, **21**, 572–573.
- [138] H. E. Zimmerman, *J. Am. Chem. Soc.*, 1966, **88**, 1564–1565.
- [139] M. Stępień and L. Latos-Grażyński, *Aromaticity in Heterocyclic Compounds*, 2009, 83–153.
- [140] E. Vogel, *Pure Appl. Chem.*, 1993, **65**, 143–152.
- [141] E. Vogel, *Angew. Chem. Int. Ed.*, 2011, **50**, 4278–4287.
- [142] J.-i. Aihara, Y. Nakagami, R. Sekine and M. Makino, *J. Phys. Chem. A*, 2012, **116**, 11718–11730.

-
- [143] M. K. Cyrański, T. M. Krygowski, M. Wisiorowski, N. J. van Eikema Hommes and P. v. R. Schleyer, *Angew. Chem. Int. Ed.*, 1998, **37**, 177–180.
- [144] J.-i. Aihara, E. Kimura and T. M. Krygowski, *Bull. Chem. Soc. Jpn.*, 2008, **81**, 826–835.
- [145] H. Fliegl, D. Sundholm, S. Taubert and F. Pichierri, *J. Phys. Chem. A*, 2010, **114**, 7153–7161.
- [146] J. I. Wu, I. Fernandez and P. v. R. Schleyer, *J. Am. Chem. Soc.*, 2013, **135**, 315–321.
- [147] P. Parkinson, D. V. Kondratuk, C. Menelaou, J. Q. Gong, H. L. Anderson and L. M. Herz, *J. Phys. Chem. Lett.*, 2014, **5**, 4356–4361.
- [148] C. Maeda, S. Toyama, N. Okada, K. Takaishi, S. Kang, D. Kim and T. Ema, *J. Am. Chem. Soc.*, 2020, **142**, 15661–15666.
- [149] M. D. Peeks, M. Jirasek, T. D. Claridge and H. L. Anderson, *Angew. Chem. Int. Ed.*, 2019, **58**, 15717–15720.
- [150] M. Rickhaus, A. Vargas Jentzsch, L. Tejerina, I. Grübner, M. Jirasek, T. D. Claridge and H. L. Anderson, *J. Am. Chem. Soc.*, 2017, **139**, 16502–16505.
- [151] M. Jirásek, M. Rickhaus, L. Tejerina and H. L. Anderson, *J. Am. Chem. Soc.*, 2021, **143**, 2403–2412.
- [152] J. Gong, K. Sumathy, Q. Qiao and Z. Zhou, *Renewable and Sustainable Energy Reviews*, 2017, **68**, 234–246.
- [153] O. S. Wenger, *J. Am. Chem. Soc.*, 2018, **140**, 13522–13533.
- [154] O. S. Wenger, *Nat. Chem.*, 2020, **12**, 323–324.
- [155] N. Kandoth, J. P. Hernández, E. Palomares and J. Lloret-Fillol, *Sustainable Energy & Fuels*, 2021, **5**, 638–665.
- [156] A. Call, F. Franco, N. Kandoth, S. Fernández, M. González-Béjar, J. Pérez-Prieto, J. M. Luis and J. Lloret-Fillol, *Chem. Sci.*, 2018, **9**, 2609–2619.
- [157] K. Maeda and K. Domen, *J. Phys. Chem. Lett.*, 2010, **1**, 2655–2661.
- [158] W. Rüttinger and G. C. Dismukes, *Chem. Rev.*, 1997, **97**, 1–24.
- [159] K. E. Dalle, J. Warnan, J. J. Leung, B. Reuillard, I. S. Karmel and E. Reisner, *Chem. Rev.*, 2019, **119**, 2752–2875.

- [160] H. Uoyama, K. Goushi, K. Shizu, H. Nomura and C. Adachi, *Nature*, 2012, **492**, 234–238.
- [161] P. Xiao, F. Dumur, J. Zhang, J. P. Fouassier, D. Gigmes and J. Lalevée, *Macromolecules*, 2014, **47**, 3837–3844.
- [162] C. Bizzarri, C. Strabler, J. Prock, B. Trettenbrein, M. Ruggenthaler, C.-H. Yang, F. Polo, A. Iordache, P. Brüggegger and L. D. Cola, *Inorg. Chem.*, 2014, **53**, 10944–10951.
- [163] G. C. Dos Santos, E. F. Oliveira, F. C. Lavarda and L. C. da Silva-Filho, *J. Mol Model*, 2019, **25**, 1–13.
- [164] N. A. Ludin, A. A.-A. Mahmoud, A. B. Mohamad, A. A. H. Kadhum, K. Sopian and N. S. A. Karim, *Renew. Sustain. Energy Rev.*, 2014, **31**, 386–396.
- [165] M. Jacoby, *Chem. Eng. News*, 2016, **94**, 30–35.
- [166] B. O'regan and M. Grätzel, *Nature*, 1991, **353**, 737–740.
- [167] M. Kimura, H. Nomoto, H. Suzuki, T. Ikeuchi, H. Matsuzaki, T. N. Murakami, A. Furube, N. Masaki, M. J. Griffith and S. Mori, *Chem. Eur. J.*, 2013, **19**, 7496–502.
- [168] H. Tributsch, *Photochem. Photobiol.*, 1972, **16**, 261–269.
- [169] L. Han, A. Islam, H. Chen, C. Malapaka, B. Chiranjeevi, S. Zhang, X. Yang and M. Yanagida, *Energy Environ. Sci.*, 2012, **5**, 6057–6060.
- [170] A. Blakers, N. Zin, K. R. McIntosh and K. Fong, *Energy Procedia*, 2013, **33**, 1–10.
- [171] P. Ushasree and B. Bora, in *Solar Energy Capture Materials*, ed. E. A. Gibson, Royal Society of Chemistry, UK, 2019, pp. 1–55.
- [172] H. J. Snaith, *Adv. Funct. Mat*, 2010, **20**, 13–19.
- [173] Y. H. Hu and W. Wei, *Comprehensive Energy Systems*, 2018, **2**, 150–181.
- [174] A. Abbotto and N. Manfredi, *Dalton Trans.*, 2011, **40**, 12421–12438.
- [175] M. S. Lowry and S. Bernhard, *Chem. Eur. J.*, 2006, **12**, 7970–7977.
- [176] S. Ladouceur, D. Fortin and E. Zysman-Colman, *Inorg. Chem.*, 2010, **49**, 5625–5641.

-
- [177] E. Mejía, S.-P. Luo, M. Karnahl, A. Friedrich, S. Tschierlei, A.-E. Surkus, H. Junge, S. Gladiali, S. Lochbrunner and M. Beller, *Chem. Eur. J.*, 2013, **19**, 15972–15978.
- [178] F. Glaser and O. S. Wenger, *Coord. Chem. Rev.*, 2020, **405**, 213129.
- [179] S.-P. Luo, E. Mejía, A. Friedrich, A. Pazidis, H. Junge, A.-E. Surkus, R. Jackstell, S. Denurra, S. Gladiali, S. Lochbrunner *et al.*, *Angewandte Chemie*, 2013, **125**, 437–441.
- [180] A. Hossain, A. Bhattacharyya and O. Reiser, *Science*, 2019, **364**, 1–11.
- [181] R. Baer, E. Livshits and U. Salzner, *Ann. Rev. Phys. Chem.*, 2010, **61**, 85–109.
- [182] K. Garrett, X. Sosa Vazquez, S. B. Egri, J. Wilmer, L. E. Johnson, B. H. Robinson and C. M. Isborn, *J. Chem. Theory Comput.*, 2014, **10**, 3821–3831.
- [183] R. A. Friesner, *Proc. Natl. Acad. Sci. U.S.A.*, 2005, **102**, 6648–6653.
- [184] J. E. Huheey, E. A. Keiter, R. L. Keiter and O. K. Medhi, *Inorganic chemistry: principles of structure and reactivity*, Pearson Education India, 2006.
- [185] J. C. Slater, *Phys. Rev.*, 1930, **36**, 57–64.
- [186] E. R. Davidson and D. Feller, *Chem. Rev.*, 1986, **86**, 681–696.
- [187] F. Jensen, *Wiley Interdisciplinary Reviews: Computational Molecular Science*, 2013, **3**, 273–295.
- [188] R. Krishnan, J. S. Binkley, R. Seeger and J. A. Pople, *J. Chem. Phys.*, 1980, **72**, 650–654.
- [189] T. Clark, J. Chandrasekhar, G. W. Spitznagel and P. v. R. Schleyer, *J. Comput. Chem.*, 1983, **4**, 294–301.
- [190] J. A. Pople, *Quantum Chemical Models*, Nobel Lecture, 1998.
- [191] T. H. Dunning Jr., *J. Chem. Phys.*, 1989, **90**, 1007–1023.
- [192] A. Szabo and N. S. Ostlund, *Modern quantum chemistry: introduction to advanced electronic structure theory*, Courier Corporation, 2012.
- [193] H. Cox and A. L. Baskerville, in *Advances in Quantum Chemistry*, ed. J. R. Sabin and E. J. Brändas, Academic Press, 2018, vol. 77 of *Advances in Quantum Chemistry*, pp. 201–240.
- [194] E. Wigner and F. Seitz, *Phys. Rev.*, 1933, **43**, 804–810.

- [195] E. Wigner and F. Seitz, *Phys. Rev.*, 1934, **46**, 509–524.
- [196] J. Slater, *Rev. Mod. Phys.*, 1953, **25**, 199–210.
- [197] P.-O. Löwdin, *Adv. Chem. Phys.*, 1959, **2**, 207–322.
- [198] C. J. Cramer, *Essentials of computational chemistry: theories and models*, John Wiley & Sons, 2013.
- [199] D. Pines, in *Solid State Phy.*, Elsevier, 1955, vol. 1, pp. 367–450.
- [200] S. Wilson, *Electron correlation in molecules*, Dover, New York, 2007.
- [201] W. Kutzelnigg, G. Del Re and G. Berthier, *Phys. Rev.*, 1968, **172**, 49–59.
- [202] J. E. Lennard-Jones, *J. Chem. Phys.*, 1952, **20**, 1024–1029.
- [203] M. Buijse and E. Baerends, *Density Functional Theory of Molecules, Clusters, and Solids*, Springer Science & Business Media, 1995, vol. 12.
- [204] M. Via-Nadal, *Ph.D. thesis*, Universidad del País Vasco / Euskal Herriko Unibertsitatea, Donostia, 2020.
- [205] O. Sinanoğlu, *Adv. Chem. Phys.*, 1964, **6**, 315–412.
- [206] E. Ramos-Cordoba, P. Salvador and E. Matito, *Phys. Chem. Chem. Phys.*, 2016, **18**, 24015–24023.
- [207] E. Ramos-Cordoba and E. Matito, *J. Chem. Theory Comput.*, 2017, **13**, 2705–2711.
- [208] M. Via-Nadal, M. Rodríguez-Mayorga, E. Ramos-Cordoba and E. Matito, *J. Phys. Chem. Lett.*, 2019, **10**, 4032–4037.
- [209] G. C. Lie and E. Clementi, *J. Chem. Phys.*, 1974, **60**, 1275–1287.
- [210] T. Helgaker, P. Jorgensen and J. Olsen, *Molecular Electronic Structure Theory*, Wiley, Chichester, 2000.
- [211] C. Møller and M. S. Plesset, *Phys. Rev.*, 1934, **46**, 618–622.
- [212] R. J. Bartlett and G. D. Purvis, *Int. J. Quantum Chem.*, 1978, **14**, 561–581.
- [213] B. O. Roos, *Adv. Chem. Phys.*, 1987, **69**, 399–445.
- [214] H. G. Kümmel, *Int. J. Mod. Phys. B*, 2003, **17**, 5311–5325.

- [215] J. Čížek, *J. Chem. Phys.*, 1966, **45**, 4256–4266.
- [216] J. A. Pople, M. Head-Gordon, D. J. Fox, K. Raghavachari and L. A. Curtiss, *J. Chem. Phys.*, 1989, **90**, 5622–5629.
- [217] G. D. Purvis III and R. J. Bartlett, *J. Chem. Phys.*, 1982, **76**, 1910–1918.
- [218] F. Jensen, *Introduction to computational chemistry*, John Wiley & Sons, 2017.
- [219] T. J. Lee and P. R. Taylor, *Int. J. Quantum Chem.*, 1989, **23**, 199–207.
- [220] M. L. Leininger, I. M. Nielsen, T. D. Crawford and C. L. Janssen, *Chem. Phys. Lett.*, 2000, **328**, 431–436.
- [221] I. M. B. Nielsen and C. L. Janssen, *Chem. Phys. Lett.*, 1999, **310**, 568–576.
- [222] F. Neese, F. Wennmohs and A. Hansen, *J. Chem. Phys.*, 2009, **130**, 114108.
- [223] C. Riplinger and F. Neese, *J. Chem. Phys.*, 2013, **138**, 034106.
- [224] C. Riplinger, B. Sandhoefer, A. Hansen and F. Neese, *J. Chem. Phys.*, 2013, **139**, 134101.
- [225] C. Riplinger, P. Pinski, U. Becker, E. F. Valeev and F. Neese, *J. Chem. Phys.*, 2016, **144**, 024109.
- [226] F. Neese, A. Hansen and D. G. Liakos, *J. Chem. Phys.*, 2009, **131**, 064103.
- [227] D. J. Thouless, *Nuclear Physics*, 1960, **21**, 225–232.
- [228] M. Saitow, U. Becker, C. Riplinger, E. F. Valeev and F. Neese, *J. Chem. Phys.*, 2017, **146**, 164105.
- [229] R. G. Parr and W. Yang, *Density-Functional Theory of Atoms and Molecules*, Oxford University Press, 1989.
- [230] M. E. Casida and M. Huix-Rotllant, *Ann. Rev. Phys. Chem.*, 2012, **63**, 287–323.
- [231] M.-C. Kim, E. Sim and K. Burke, *Phys. Rev. Lett.*, 2013, **111**, 073003.
- [232] L. H. Thomas, *Mathematical Proceedings of the Cambridge Philosophical Society*, 1927, pp. 542–548.
- [233] E. Fermi, *Rend. Accad. Naz. Lincei*, 1927, **6**, 5.
- [234] A. Dreuw and M. Head-Gordon, *Chem. Rev.*, 2005, **105**, 4009–4037.

- [235] W. Kohn and L. J. Sham, *Phys. Rev.*, 1965, **140**, A1133–A1138.
- [236] J. P. Perdew and K. Schmidt, AIP Conference Proceedings, 2001, pp. 1–20.
- [237] J. P. Perdew, A. Ruzsinszky, J. Tao, V. N. Staroverov, G. E. Scuseria and G. I. Csonka, *J. Chem. Phys.*, 2005, **123**, 062201.
- [238] X. Zheng, M. Liu, E. R. Johnson, J. Contreras-García and W. Yang, *J. Chem. Phys.*, 2012, **137**, 214106.
- [239] B. Champagne, E. A. Perpète, S. J. Van Gisbergen, E.-J. Baerends, J. G. Snijders, C. Soubra-Ghaoui, K. A. Robins and B. Kirtman, *J. Chem. Phys.*, 1998, **109**, 10489–10498.
- [240] C.-O. Almbladh and U. von Barth, *Phys. Rev. B*, 1985, **31**, 3231–3244.
- [241] F. Della Sala and A. Görling, *Phys. Rev. Lett.*, 2002, **89**, 033003.
- [242] T. Woller, J. Contreras-Garcia, P. Geerlings, F. De Proft and M. Alonso, *Phys. Chem. Chem. Phys.*, 2016, **18**, 11885–11900.
- [243] E. Marcos, J. M. Anglada and M. Torrent-Sucarrat, *J. Phys. Chem. C*, 2012, **116**, 24358–24366.
- [244] M. Alonso, P. Geerlings and F. De Proft, *Chem. Eur. J.*, 2013, **19**, 1617–1628.
- [245] C. S. Wannere, K. W. Sattelmeyer, H. F. Schaefer III and P. v. R. Schleyer, *Angew. Chem. Int. Ed.*, 2004, **43**, 4200–4206.
- [246] D. W. Szczepanik, M. Solà, M. Andrzejak, B. Pawełek, J. Dominikowska, M. Kukułka, K. Dyduch, T. M. Krygowski and H. Szatyłowicz, *J. Comput. Chem.*, 2017, **38**, 1640–1654.
- [247] T. Leininger, H. Stoll, H.-J. Werner and A. Savin, *Chem. Phys. Lett.*, 1997, **275**, 151–160.
- [248] H. Iikura, T. Tsuneda, T. Yanai and K. Hirao, *J. Chem. Phys.*, 2001, **115**, 3540–3544.
- [249] O. A. Vydrov and G. E. Scuseria, *J. Chem. Phys.*, 2006, **125**, 234109.
- [250] T. Yanai, D. P. Tew and N. C. Handy, *Chem. Phys. Lett.*, 2004, **393**, 51–57.
- [251] J.-D. Chai and M. Head-Gordon, *J. Chem. Phys.*, 2008, **128**, 084106.

-
- [252] J.-W. Song, T. Hirose, T. Tsuneda and K. Hirao, *J. Chem. Phys.*, 2007, **126**, 154105.
- [253] O. S. Bokareva, G. Grell, S. I. Bokarev and O. Kühn, *J. Chem. Theory Comput.*, 2015, **11**, 1700–1709.
- [254] K. Hirao, B. Chan, J.-W. Song and H.-S. Bae, *J. Phys. Chem. A*, 2020, **124**, 8079–8087.
- [255] K. Hirao, T. Nakajima, B. Chan, J.-W. Song and H.-S. Bae, *J. Phys. Chem. A*, 2020, **124**, 10482–10494.
- [256] Y. Mei, C. Li, N. Q. Su and W. Yang, *J. Phys. Chem. A*, 2018, **123**, 666–673.
- [257] R. L. A. Haiduke and R. J. Bartlett, *J. Chem. Phys.*, 2018, **149**, 131101.
- [258] E. Livshits and R. Baer, *Phys. Chem. Chem. Phys.*, 2007, **9**, 2932–2941.
- [259] T. Stein, L. Kronik and R. Baer, *J. Am. Chem. Soc.*, 2009, **131**, 2818–2820.
- [260] T. Stein, L. Kronik and R. Baer, *J. Chem. Phys.*, 2009, **131**, 244119.
- [261] K. Hirao, H.-S. Bae, J.-W. Song and B. Chan, *J. Phys. Chem. A*, 2021, **125**, 3489–3502.
- [262] V. U. Nazarov, *arXiv preprint arXiv:2104.07882*, 2021.
- [263] A. Karolewski, L. Kronik and S. Kümmel, *J. Chem. Phys.*, 2013, **138**, 204115.
- [264] L. Kronik, T. Stein, S. Refaely-Abramson and R. Baer, *J. Chem. Theory Comput.*, 2012, **8**, 1515–1531.
- [265] J. Kiefer, *Proc. Amer. Math. Soc.*, 1953, **4**, 502–506.
- [266] N. T. Maitra, *J. Chem. Phys.*, 2016, **144**, 220901.
- [267] C. Adamo and D. Jacquemin, *Chem. Soc. Rev.*, 2013, **42**, 845–856.
- [268] M. Ruggenthaler and R. van Leeuwen, *EPL*, 2011, **95**, 13001.
- [269] E. Runge and E. K. Gross, *Phys. Rev. Lett.*, 1984, **52**, 997–1000.
- [270] R. van Leeuwen, *Phys. Rev. Lett.*, 1999, **82**, 3863–3866.
- [271] M. E. Casida, in *Recent Advances In Density Functional Methods: (Part I)*, World Scientific, 1995, pp. 155–192.

- [272] C. A. Ullrich, *Time-dependent density-functional theory: concepts and applications*, OUP Oxford, 2011.
- [273] N. T. Maitra, F. Zhang, R. J. Cave and K. Burke, *J. Chem. Phys.*, 2004, **120**, 5932–5937.
- [274] M. E. Casida, F. Gutierrez, J. Guan, F.-X. Gadea, D. Salahub and J.-P. Daudey, *J. Chem. Phys.*, 2000, **113**, 7062–7071.
- [275] M. J. Peach, M. J. Williamson and D. J. Tozer, *J. Chem. Theory Comput.*, 2011, **7**, 3578–3585.
- [276] K. Yabana and G. Bertsch, *Int. J. Quantum Chem.*, 1999, **75**, 55–66.
- [277] B. G. Levine, C. Ko, J. Quenneville and T. J. Martínez, *Mol. Phys.*, 2006, **104**, 1039–1051.
- [278] S. Hirata and M. Head-Gordon, *Chem. Phys. Lett.*, 1999, **314**, 291–299.
- [279] M. Born, *Eur. Phys. J. A*, 1926, **38**, 803–827.
- [280] J. Von Neumann, *Nachrichten von der Gesellschaft der Wissenschaften zu Göttingen, Mathematisch-Physikalische Klasse*, 1927, **1927**, 245–272.
- [281] P. A. Dirac, *Mathematical proceedings of the Cambridge philosophical society*, 1930, pp. 376–385.
- [282] P.-O. Löwdin, *Phys. Rev.*, 1955, **97**, 1474–1489.
- [283] E. Davidson, *Reduced density matrices in quantum chemistry*, Elsevier, 2012, vol. 6.
- [284] R. S. Mulliken, *J. Chem. Phys.*, 1955, **23**, 1833–1840.
- [285] C. Gatti, *Zeit. Kristallogr.*, 2005, **220**, 399–457.
- [286] C. Fonseca Guerra, J.-W. Handgraaf, E. J. Baerends and F. M. Bickelhaupt, *J. Comput. Chem.*, 2004, **25**, 189–210.
- [287] F. L. Hirshfeld, *Theor. Chim. Acta (Berlin)*, 1977, **44**, 129–138.
- [288] I. Mayer and P. Salvador, *Chem. Phys. Lett.*, 2004, **383**, 368–375.
- [289] L. Guillaumes, P. Salvador and S. Simon, *J. Phys. Chem. A*, 2014, **118**, 1142–1149.

-
- [290] A. D. Becke, *J. Chem. Phys.*, 1988, **88**, 2547–2553.
- [291] E. Matito, M. Solà, P. Salvador and M. Duran, *Faraday Discuss.*, 2007, **135**, 325–345.
- [292] E. Francisco, A. Martín Pendás and M. A. Blanco, *J. Chem. Theory Comput.*, 2006, **2**, 90–102.
- [293] P. Salvador and E. Ramos-Cordoba, *J. Chem. Phys.*, 2013, **139**, 071103.
- [294] W. Heyndrickx, P. Salvador, P. Bultinck, M. Solà and E. Matito, *J. Comput. Chem.*, 2011, **32**, 386–395.
- [295] E. Ramos-Cordoba, V. Postils and P. Salvador, *J. Chem. Theory Comput.*, 2015, **11**, 1501–1508.
- [296] V. Postils, C. Delgado-Alonso, J. M. Luis and P. Salvador, *Angew. Chem. Int. Ed.*, 2018, **130**, 10685–10689.
- [297] I. Mayer, *J. Phys. Chem.*, 1996, **100**, 6249–6257.
- [298] I. Bakó, A. Stirling, A. Seitsonen and I. Mayer, *Chem. Phys. Lett.*, 2013, **563**, 97–101.
- [299] R. F. W. Bader, *Atoms in Molecules: A Quantum Theory*, Oxford University Press, Oxford, 1990.
- [300] M. Leboeuf, A. M. Köster, K. Jug and D. R. Salahub, *J. Chem. Phys.*, 1999, **111**, 4893–4905.
- [301] T. A. Keith, *AIMAll (Version 14.11.23)*, 2014, TK Gristmill Software, Overland Park KS, USA (aim.tkgristmill.com).
- [302] F. Biegler-König, J. Schönbohm and D. Bayles, *Software news and updates- AIM2000-A program to analyze and visualize atoms in molecules*, 2001.
- [303] F. Biegler-König and J. Schönbohm, *J. Comput. Chem.*, 2002, **23**, 1489–1494.
- [304] P. Salvador and E. Ramos-Cordoba, *APOST-3D program*, 2012, Universitat de Girona (Spain).
- [305] E. Matito, *ESI-3D: Electron Sharing Indices Program for 3D Molecular Space Partitioning*, 2015, Institute of Computational Chemistry and Catalysis, University of Girona, Catalonia, Spain.

- [306] C. A. Coulson, *Proc. R. Soc. London Ser. A*, 1938, **164**, 383–396.
- [307] C. A. Coulson, *Proc. R. Soc. London Ser. A*, 1939, **169**, 413–428.
- [308] R. L. Fulton and S. T. Mixon, *J. Phys. Chem.*, 1993, **97**, 7530–7534.
- [309] K. Ruedenberg, *Rev. Mod. Phys.*, 1962, **34**, 326–376.
- [310] I. Mayer, *Int. J. Quantum Chem.*, 1983, **23**, 341–363.
- [311] X. Fradera, M. A. Austen and R. F. W. Bader, *J. Phys. Chem. A*, 1999, **103**, 304–314.
- [312] X. Fradera, J. Poater, S. Simon, M. Duran and M. Solà, *Theor. Chem. Acc.*, 2002, **108**, 214–224.
- [313] J. Poater, X. Fradera, M. Solà, M. Duran and S. Simon, *Chem. Phys. Lett.*, 2003, **369**, 248–255.
- [314] J. Poater, X. Fradera, M. Duran and M. Solà, *Chem. Eur. J.*, 2003, **9**, 400–406.
- [315] E. Matito, M. Duran and M. Solà, *J. Chem. Phys.*, 2005, **122**, 014109.
- [316] E. Matito, M. Duran and M. Solà, *J. Chem. Phys.*, 2006, **125**, 059901.
- [317] I. Mayer, *Chem. Phys. Lett.*, 1983, **97**, 270–274.
- [318] J. G. Ángyán, M. Loos and I. Mayer, *J. Phys. Chem.*, 1994, **98**, 5244–5248.
- [319] A. M. K. Müller, *Phys. Lett.*, 1984, **105A**, 446–452.
- [320] I. Ruiz, E. Matito, F. J. Holguín-Gallego, E. Francisco, Á. M. Pendás and T. Rocha-Rinza, *Theor. Chem. Acc.*, 2016, **135**, 209.
- [321] G. N. Lewis, *J. Am. Chem. Soc.*, 1916, **38**, 762–786.
- [322] M. Giambiagi, M. S. de Giambiagi and K. C. Mundim, *Struct. Chem.*, 1990, **1**, 423–427.
- [323] A. B. Sannigrahi and T. Kar, *Chem. Phys. Lett.*, 1990, **173**, 569–572.
- [324] T. Kar and E. Sánchez Marcos, *Chem. Phys. Lett.*, 1992, **192**, 14–20.
- [325] R. Ponec and I. Mayer, *J. Phys. Chem. A*, 1997, **101**, 1738–1741.
- [326] K. C. Mundim, M. Giambiagi and M. S. de Giambiagi, *J. Phys. Chem.*, 1994, **98**, 6118–6119.

-
- [327] A. B. Sannigrahi and T. Kar, *Chem. Phys. Lett.*, 1999, **299**, 518–526.
- [328] M. S. de Giambiagi, M. Giambiagi and M. S. Fortes, *J. Mol. Struct. (Theochem)*, 1997, **391**, 141–150.
- [329] M. Giambiagi, M. S. de Giambiagi, C. D. dos Santos Silva and A. P. de Figueiredo, *Phys. Chem. Chem. Phys.*, 2000, **2**, 3381–3392.
- [330] P. Bultinck, R. Ponec and S. Van Damme, *J. Phys. Org. Chem.*, 2005, **18**, 706–718.
- [331] J. Cioslowski, E. Matito and M. Solà, *J. Phys. Chem. A*, 2007, **111**, 6521–6525.
- [332] F. Feixas, E. Matito, J. Poater and M. Solà, *J. Phys. Chem. A*, 2011, **115**, 13104–13113.
- [333] E. Matito, *New tools for chemical bonding analysis*, 2020, Notes of MACMoM master, Universitat de Girona.
- [334] F. Feixas, E. Matito, J. Poater, F. Maseras and M. Solà, *unpublished*.
- [335] E. Francisco, A. Martín Pendás and M. A. Blanco, *J. Chem. Phys.*, 2007, **126**, 094102.
- [336] M. Torrent-Sucarrat, J. M. Luis and M. Solà, *Chem. Eur. J.*, 2005, **11**, 6024–6031.
- [337] M. Alonso and B. Herradon, *J. Comput. Chem.*, 2010, **31**, 917–928.
- [338] L. Zhao, R. Grande-Aztatzi, C. Foroutan-Nejad, J. M. Ugalde and G. Frenking, *ChemistrySelect*, 2017, **2**, 863–870.
- [339] S. W. Slayden and J. F. Liebman, *Chem. Rev.*, 2001, **101**, 1541–1566.
- [340] J. Kruszewski and T. M. Krygowski, *Tetrahedron Lett.*, 1972, **13**, 3839–3842.
- [341] T. M. Krygowski, *J. Chem. Inf. Comput. Sci.*, 1993, **33**, 70–78.
- [342] J.-L. Bredas, *J. Chem. Phys.*, 1985, **82**, 3808–3811.
- [343] C. B. Gorman and S. R. Marder, *Proc. Natl. Acad. Sci. U.S.A.*, 1993, **90**, 11297–11301.
- [344] C. F. Matta and J. Hernández-Trujillo, *J. Phys. Chem. A*, 2003, **107**, 7496–7504.
- [345] S. Noorizadeh and E. Shakerzadeh, *Phys. Chem. Chem. Phys.*, 2010, **12**, 4742–4749.

- [346] D. W. Szczepanik, E. Žak, K. Dyduch and J. Mrozek, *Chem. Phys. Lett.*, 2014, **593**, 154–159.
- [347] E. Matito, J. Poater, M. Solà, M. Duran and P. Salvador, *J. Phys. Chem. A*, 2005, **109**, 9904–9910.
- [348] E. Matito, M. Solà, M. Duran and P. Salvador, *J. Phys. Chem. A*, 2006, **110**, 5108–5113.
- [349] C. G. Bollini, M. Giambiagi, M. S. d. Giambiagi and A. P. de Figueredo, *Struct. Chem.*, 2001, **12**, 113–120.
- [350] R. Ponec, P. Bultinck and A. Gallegos Saliner, *J. Phys. Chem. A*, 2005, **109**, 6606–6609.
- [351] J. M. Mercero, E. Matito, F. Ruipérez, I. Infante, X. Lopez and J. M. Ugalde, *Chem. Eur. J.*, 2015, **21**, 9610–9614.
- [352] F. Feixas, E. Matito, M. Solà and J. Poater, *Phys. Chem. Chem. Phys.*, 2010, **12**, 7126–7137.
- [353] I. Casademont-Reig, R. Guerrero-Avilés, M. Torrent-Sucarrat, E. Ramos-Cordoba and E. Matito, *ChemRxiv*, 2021.
- [354] J. Jusélius, D. Sundholm and J. Gauss, *J. Chem. Phys.*, 2004, **121**, 3952–3963.
- [355] H. Fliegl, S. Taubert, O. Lehtonen and D. Sundholm, *Phys. Chem. Chem. Phys.*, 2011, **13**, 20500–20518.
- [356] M. Bühl and C. van Wüllen, *Chem. Phys. Lett.*, 1995, **247**, 63–68.
- [357] R. Herges and D. Geuenich, *J. Phys. Chem. A*, 2001, **105**, 3214–3220.
- [358] D. Geuenich, K. Hess, F. Köhler and R. Herges, *Chem. Rev.*, 2005, **105**, 3758–3772.
- [359] C. Foroutan-Nejad, *J. Phys. Chem. A*, 2011, **115**, 12555–12560.
- [360] P. v. R. Schleyer, C. Maerker, A. Dransfeld, H. Jiao and N. J. v. E. Hommes, *J. Am. Chem. Soc.*, 1996, **118**, 6317–6318.
- [361] J. O. C. Jiménez-Halla, E. Matito, L. Blancafort, J. Robles and M. Solà, *J. Comput. Chem.*, 2009, **30**, 2764–2776.
- [362] J. O. C. Jiménez-Halla, E. Matito, J. Robles and M. Solà, *J. Organomet. Chem.*, 2006, **691**, 4359–4366.

- [363] A. Stanger, *J. Org. Chem.*, 2006, **71**, 883–893.
- [364] R. Gershoni-Poranne and A. Stanger, *Chem. Eur. J.*, 2014, **20**, 5673–5688.
- [365] I. Morao, B. Lecea and F. P. Cossío, *J. Org. Chem.*, 1997, **62**, 7033–7036.
- [366] C. Foroutan-Nejad, S. Shahbazian and P. Rashidi-Ranjbar, *Phys. Chem. Chem. Phys.*, 2010, **12**, 12630–12637.
- [367] A. C. Castro, E. Osorio, J. O. C. Jiménez-Halla, E. Matito, W. Tiznado and G. Merino, *J. Chem. Theory Comput.*, 2010, **6**, 2701–2705.
- [368] F. Feixas, J. Jiménez-Halla, E. Matito, J. Poater, M. Sola and J. Pol, *Polish J. Chem*, 2007, 783–797.
- [369] Z. Badri, C. Foroutan-Nejad and P. Rashidi-Ranjbar, *Phys. Chem. Chem. Phys.*, 2012, **14**, 3471–3481.
- [370] T. Woller, I. Casademont-Reig, V. García, J. Contreras-García, W. Tiznado, M. Torrent-Sucarrat, E. Matito and M. Alonso, *in preparation*.
- [371] T. Woller, *Ph.D. thesis*, Vrije Universiteit Brussel (VUB) and Sorbonne Université, Brussels and Paris, 2021.
- [372] S. Fernández, F. Franco, C. Casadevall, V. Martin-Diaconescu, J. M. Luis and J. Lloret-Fillol, *J. Am. Chem. Soc.*, 2020, **142**, 120–133.
- [373] U. Salzner and A. Aydin, *J. Chem. Theory Comput.*, 2011, **7**, 2568–2583.
- [374] T. Körzdörfer, R. M. Parrish, N. Marom, J. S. Sears, C. D. Sherrill and J.-L. Brédas, *Phys. Rev. B*, 2012, **86**, 205110.
- [375] Z. Lin and T. Van Voorhis, *J. Chem. Theory Comput.*, 2019, **15**, 1226–1241.
- [376] I. Casademont-Reig, A. Call, C. Casadevall, S. Fernández, J. Lloret-Fillol, E. Ramos-Cordoba and E. Matito, *in preparation*.

Appendices

Appendix A

Supporting Information Chapter 5

Electronic Supplementary Information

New Electron Delocalization Tools to Describe the Aromaticity in Porphyrinoids

Irene Casademont-Reig,^{1,a} Tatiana Woller,^{2,a} Julia Contreras-García,³

Mercedes Alonso,^{2,} Miquel Torrent-Sucarrat,^{1,4,*} Eduard Matito,^{1,4,*}*

¹ Kimika Fakultatea, Euskal Herriko Unibertsitatea (UPV/EHU), and Donostia
International Physics Center (DIPC), P.K. 1072, 20080 Donostia, Euskadi, Spain

² Eenheid Algemene Chemie (ALGC). Vrije Universiteit Brussel (VUB), Pleinlaan 2, 1050
Brussels (Belgium)

³ Sorbonne Universités, UPMC Univ. Paris, UMR 7616 Laboratoire de Chimie
Théorique, CNRS, UMR 7616, LCT 75005, Paris (France).

⁴ Ikerbasque, Basque Foundation for Science, María Díaz de Haro 3, 6º, 48013 Bilbao,
Euskadi, Spain.

^a These authors contributed equally to this work.

This PDF files includes:

Figures S1: Schematic representation of the different pathways in **18H** and their respective AV1245 values.

Figures S2 – S10: Delocalization index (DI) values for the studied porphyrinoids calculated at the CAM-B3LYP/6-311G(d,p) level of theory.

Tables S1 - S2: Aromaticity indices (FLU, BOA, HOMA, BLA, AV1245 and AV_{min}) for the different pathways in **18H** calculated at the B3LYP and M06-2X/6-311G(d,p) levels of theory.

Table S3: MCI values for the imine and pyrrole rings within **18H** at the B3LYP, CAM-B3LYP and M06-2X /6-311G(d,p) levels of theory.

Tables S4 – S5: Aromaticity indices for the annulene pathway of the nine porphyrinoid structures, calculated at the B3LYP and M06-2X/6-311G(d,p) levels of theory.

Table S6: Aromaticity indices for several pathways of the nine porphyrinoid structures, calculated at the B3LYP, CAM-B3LYP and M06-2X/6-311G(d,p) levels of theory.

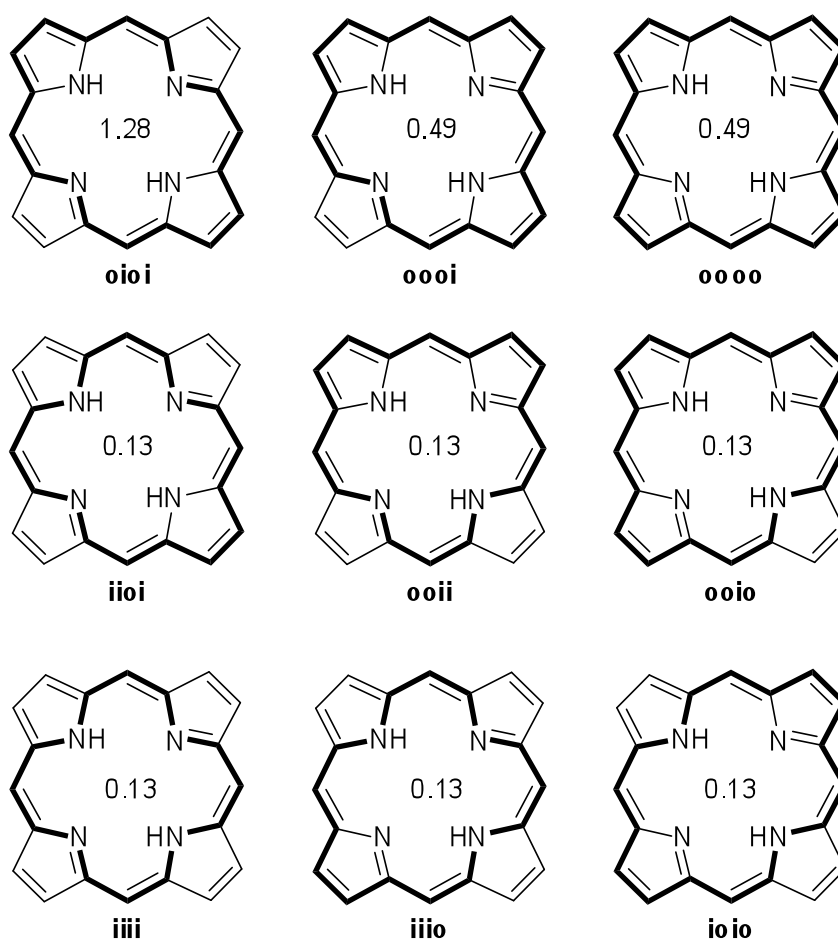


Figure S1. Schematic representation of the different pathways in **18H** and their respective AV1245 values.

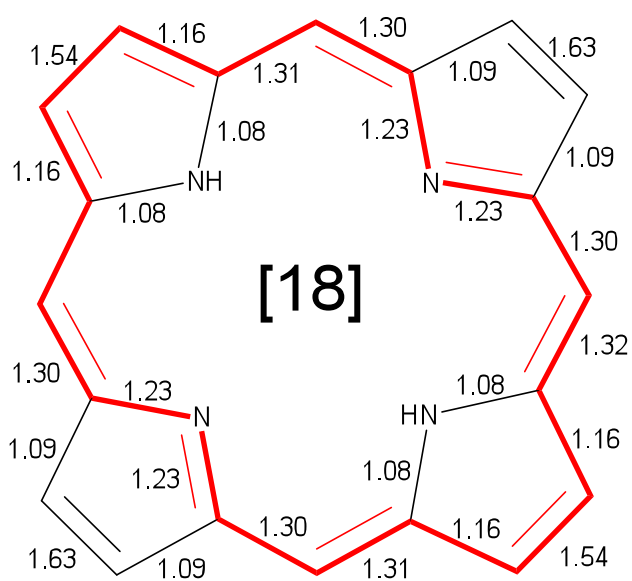


Figure S2. DI values for **18H** calculated at the CAM-B3LYP/6-311G(d,p) level of theory. The annulene-type conjugation pathway is depicted with bold red bonds.

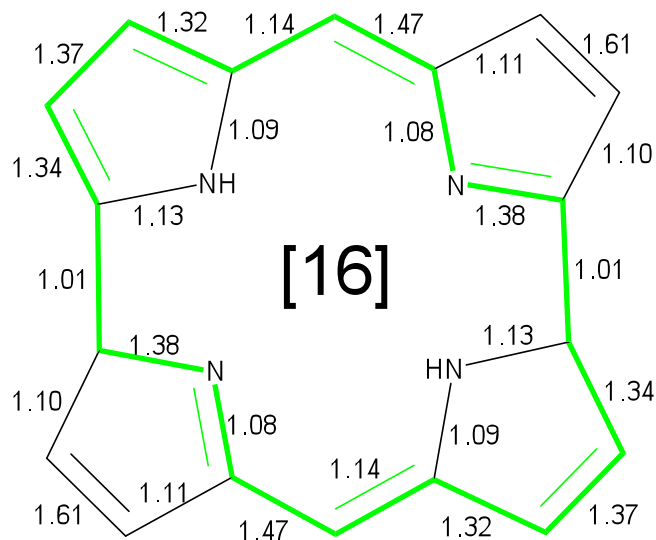


Figure S3. DI values for **16H** calculated at the CAM-B3LYP/6-311G(d,p) level of theory. The annulene-type conjugation pathway is depicted with bold green bonds.

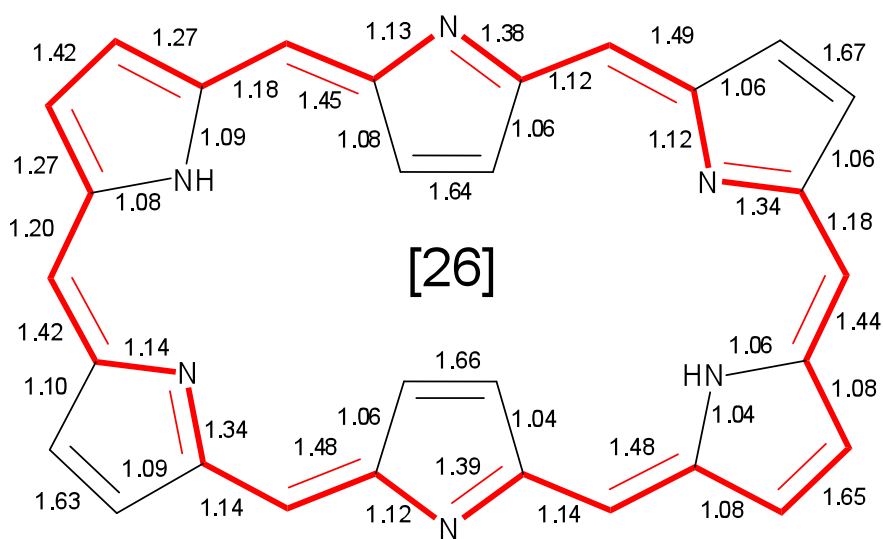


Figure S4. DI values for **26H** calculated at the CAM-B3LYP/6-311G(d,p) level of theory. The annulene-type conjugation pathway is depicted with bold red bonds.

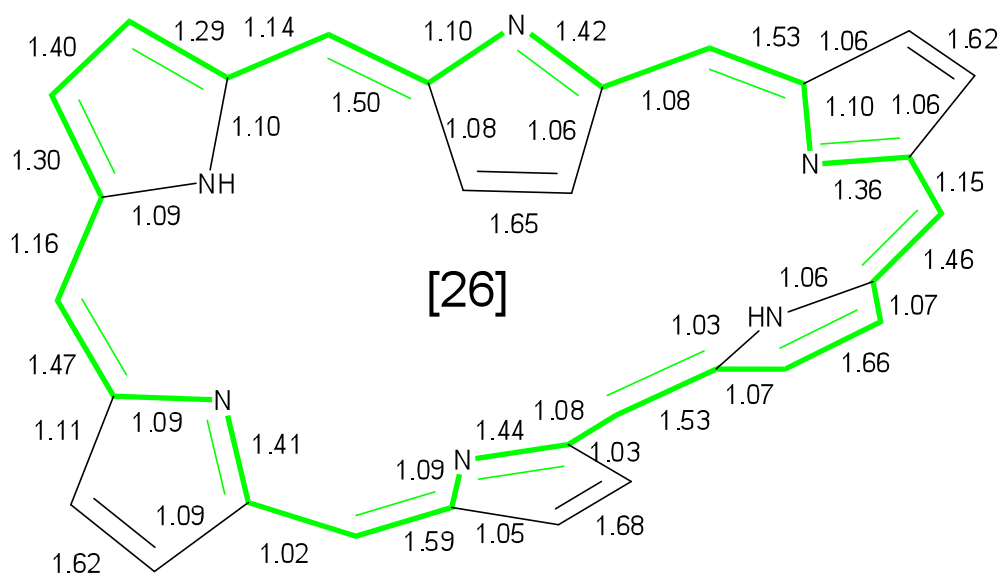


Figure S5. DI values for **26M** calculated at the CAM-B3LYP/6-311G(d,p) level of theory. The annulene-type conjugation pathway is depicted with bold green bonds.

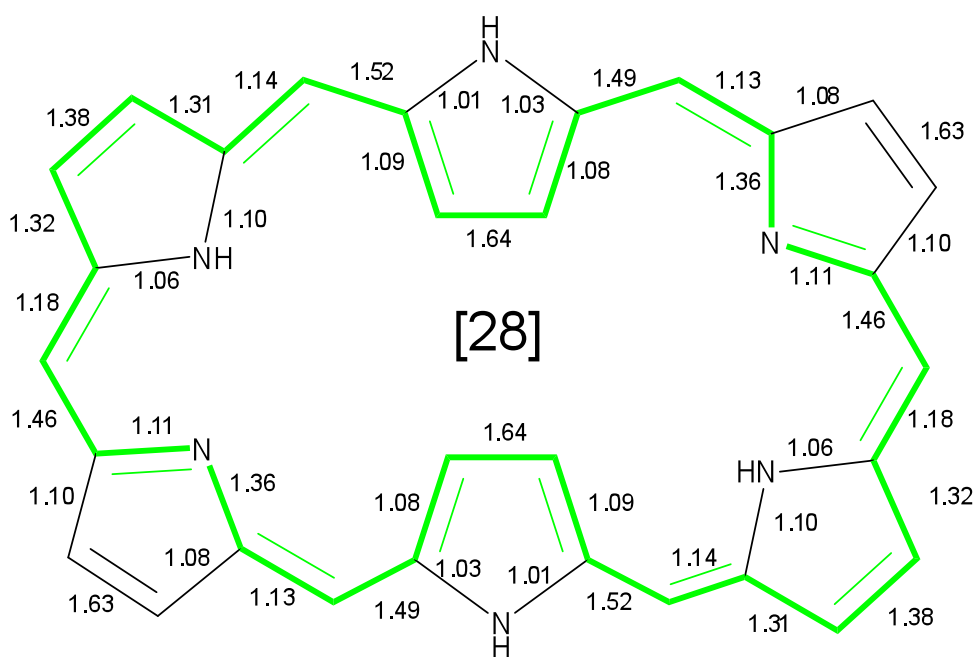


Figure S6. DI values for **28H** calculated at the CAM-B3LYP/6-311G(d,p) level of theory. The annulene-type conjugation pathway is depicted with bold green bonds.

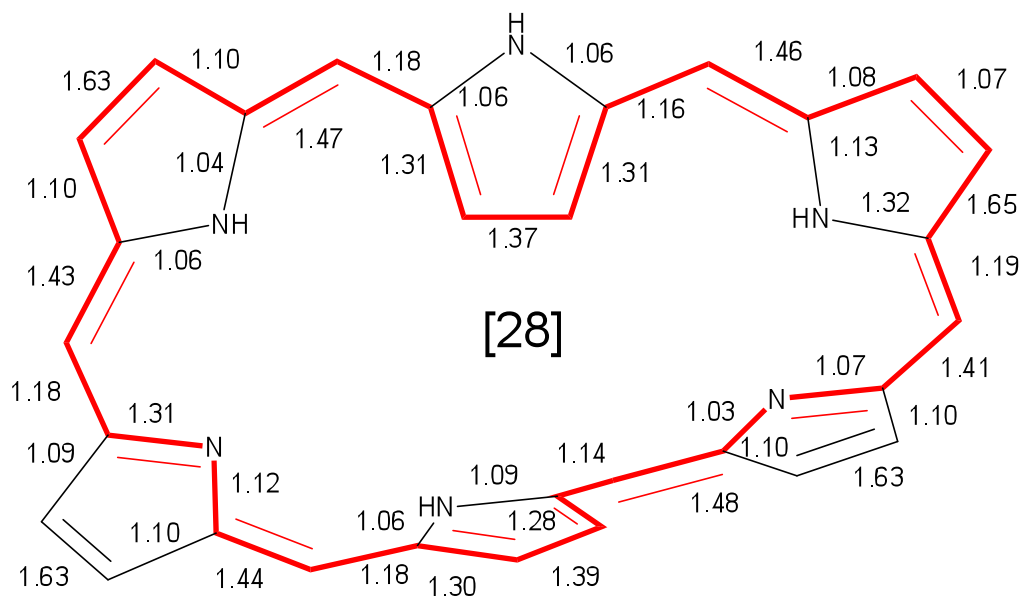


Figure S7. DI values for **28M** calculated at the CAM-B3LYP/6-311G(d,p) level of theory. The annulene-type conjugation pathway is depicted with bold red bonds.

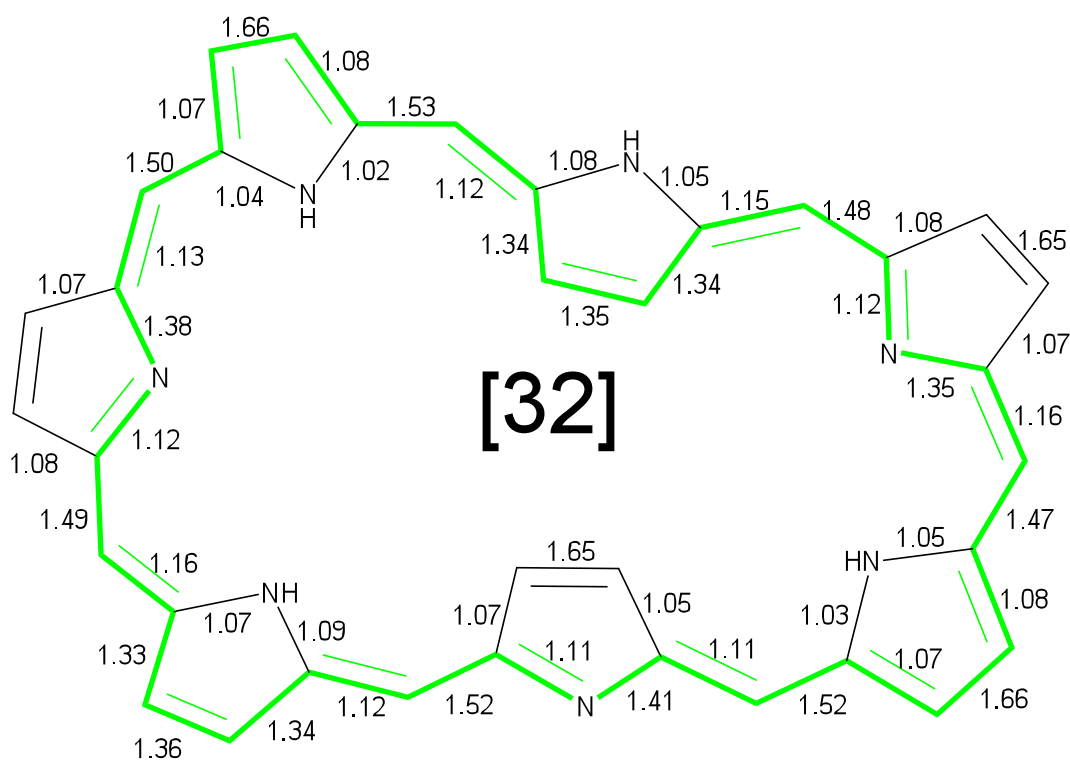


Figure S8. DI values for **32H** calculated at the CAM-B3LYP/6-311G(d,p) level of theory. The annulene-type conjugation pathway is depicted with bold green bonds.

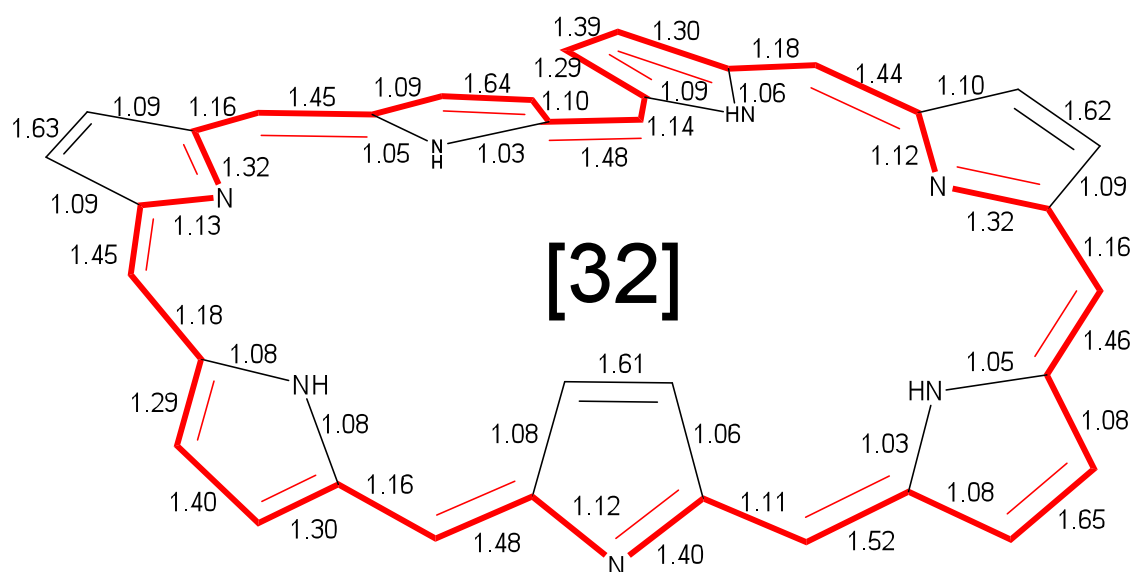


Figure S9. DI values for **32M** calculated at the CAM-B3LYP/6-311G(d,p) level of theory. The annulene-type conjugation pathway is depicted with bold red bonds.

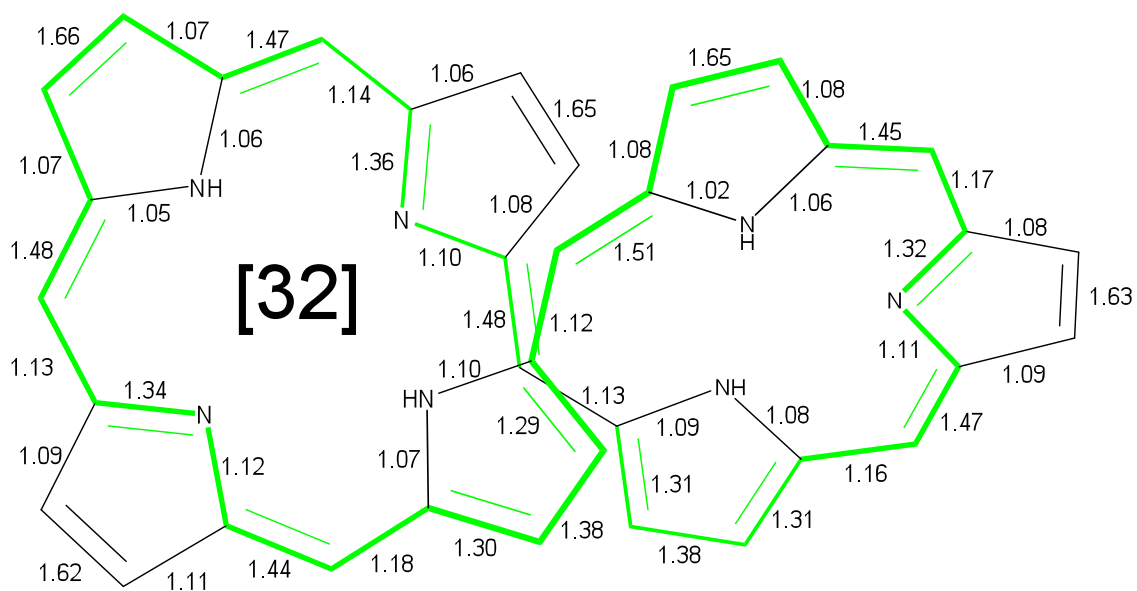


Figure S10. DI values for **32F** calculated at the CAM-B3LYP/6-311G(d,p) level of theory. The annulene-type conjugation pathway is depicted with bold green bonds.

Table S1. Aromaticity indices for the different pathways in **18H** calculated at the B3LYP/6-311G(d,p) level of theory.

Pathway ^{a)}	FLU	BOA	HOMA	BLA	AV1245	AV _{min}
oioi	0.010	0.000	0.850	0.000	2.19	1.31
oooi (2)	0.016	0.305	0.711	0.289	1.95	0.52
oooo	0.021	0.040	0.585	0.011	1.73	0.52
iiio (2)	0.008	0.362	0.894	0.316	1.59	0.18
ooii (4)	0.014	0.022	0.745	0.006	1.39	0.18
ooio (2)	0.020	0.367	0.611	0.272	1.20	0.18
iiii	0.006	0.000	0.944	0.000	0.93	0.18
iiio (2)	0.013	0.383	0.783	0.309	0.76	0.18
ioio	0.019	0.000	0.640	0.000	0.61	0.18

a) The number in brackets indicates the number of equivalent pathways.

Table S2. Aromaticity indices for the different pathway in **18H** calculated at the M06-2X /6-311G(d,p) level of theory.

Pathway ^{a)}	FLU	BOA	HOMA	BLA	AV1245	AV _{min}
oioi	0.011	0.000	0.859	0.000	2.13	1.25
oooi (2)	0.017	0.309	0.715	0.288	1.89	0.47
oooo	0.023	0.040	0.584	0.011	1.68	0.47
iiio (2)	0.009	0.366	0.909	0.314	1.55	0.12
ooii (4)	0.016	0.023	0.753	0.006	1.34	0.12
ooio (2)	0.022	0.371	0.614	0.271	1.15	0.12
iiii	0.007	0.000	0.964	0.000	0.90	0.12
iiio (2)	0.014	0.387	0.796	0.308	0.72	0.12
ioio	0.021	0.000	0.647	0.000	0.56	0.12

a) The number in brackets indicates the number of equivalent pathways.

Table S3. MCI values for the imine and pyrrole rings within **18H** at the B3LYP, CAM-B3LYP and M06-2X /6-311G(d,p) levels of theory.

Ring	B3LYP	CAM-B3LYP	M06-2X
Pyrrole	0.023	0.022	0.021
Imine	0.025	0.024	0.023

Table S4. Aromaticity indices for the annulene pathway of the nine porphyrinoid structures, calculated at the B3LYP/6-311G(d,p) level of theory. The numbers in parenthesis are the minimum value for BLA, BOA and FLU, and the maximum value for AV1245, AV_{min} and HOMA among all possible pathways.

Porphyrin	pathway	FLU	BOA	HOMA	BLA	AV1245	AV_{min}
16H	oioi	0.018	0.165 (0.000)	0.549	0.047 (0.000)	1.40 (1.84)	0.17
18H	oioi	0.010 (0.006)	0.000	0.850 (0.944)	0.000	2.19	1.31
26H	oioii	0.008 (0.006)	0.000	0.887 (0.943)	0.000	2.30	1.25
26M	oioii	0.020 (0.018)	0.259 (0.016)	0.655 (0.723)	0.063 (0.001)	1.33 (1.39)	0.13
28H	ooiooi	0.016 (0.013)	0.203 (0.000)	0.713 (0.811)	0.047 (0.000)	1.60 (1.70)	0.64
28M	oooioi	0.010 (0.009)	0.039 (0.002)	0.833 (0.886)	0.009 (0.000)	2.07	1.05
32H	ooioioi	0.016 (0.013)	0.219 (0.006)	0.723 (0.821)	0.051 (0.000)	1.56	0.76
32M	iooioio	0.010 (0.008)	0.038 (0.000)	0.849 (0.913)	0.009 (0.000)	2.08	1.14
32F	oioiooi	0.015 (0.011)	0.195 (0.001)	0.721 (0.830)	0.046 (0.001)	1.55 (1.62)	0.72

Table S5. Aromaticity indices for the annulene pathway of the nine porphyrinoid structures, calculated at the M06-2X/6-311G(d,p) level of theory. The numbers in parenthesis are the minimum value for BLA, BOA and FLU, and the maximum value for AV1245, AV_{min} and HOMA among all possible pathways.

Porphyrin	pathway	FLU	BOA	HOMA	BLA	AV1245	AV_{min}
16H	oioi	0.021	0.223 (0.000)	0.517	0.062 (0.000)	1.18 (1.56)	0.14
18H	oioi	0.011 (0.007)	0.000	0.859 (0.964)	0.000	2.13	1.25
26H	oioi	0.017 (0.014)	0.228 (0.000)	0.743 (0.823)	0.055 (0.001)	1.70	0.66
26M	oioi	0.027 (0.024)	0.328 (0.009)	0.546 (0.643)	0.080 (0.002)	1.06 (1.13)	0.13
28H	oioi	0.021 (0.017)	0.274 (0.000)	0.618 (0.772)	0.064 (0.000)	1.35 (1.48)	0.43
28M	oioi	0.017 (0.012)	0.219 (0.001)	0.730 (0.841)	0.051 (0.001)	1.58 (1.60)	0.67
32H	oioi	0.023 (0.018)	0.308 (0.006)	0.588 (0.732)	0.072 (0.001)	1.19 (1.24)	0.46
32M	oioi	0.019 (0.014)	0.241 (0.002)	0.678 (0.805)	0.057 (0.000)	1.48 (1.52)	0.58
32F	oioi	0.020 (0.015)	0.259 (0.004)	0.631 (0.784)	0.062 (0.000)	1.29 (1.40)	0.49

Table S6. Aromaticity indices for several pathways of the nine porphyrinoid structures, calculated at the B3LYP, CAM-B3LYP and M06-2X/6-311G(d,p) levels of theory.

Porphyrin	Pathway	B3LYP						CAM-B3LYP						M06-2X					
		FLU	BOA	HOMA	BLA	AV1245	AV _{min}	FLU	BOA	HOMA	BLA	AV1245	AV _{min}	FLU	BOA	HOMA	BLA	AV1245	AV _{min}
16H	oioi	0.018	0.165	0.549	0.047	1.40	0.17	0.021	0.227	0.547	0.063	1.19	0.13	0.021	0.223	0.517	0.062	1.18	0.14
	ioio	0.026	0.127	0.342	0.022	1.33	0.04	0.031	0.177	0.293	0.034	1.13	0.05	0.032	0.178	0.241	0.034	1.11	0.04
	iiii	0.021	0.000	0.532	0.000	0.78	0.13	0.025	0.000	0.505	0.000	0.62	0.07	0.026	0.000	0.478	0.000	0.61	0.08
	oooo	0.023	0.000	0.378	0.000	1.84	0.10	0.027	0.000	0.354	0.000	1.58	0.07	0.028	0.000	0.302	0.000	1.56	0.06
26H	oioii	0.008	0.000	0.887	0.000	2.30	1.25	0.019	0.256	0.716	0.062	1.58	0.61	0.017	0.228	0.743	0.055	1.70	0.66
	iooioo	0.023	0.003	0.494	0.002	0.54	0.06	0.031	0.000	0.374	0.001	0.51	0.02	0.031	0.000	0.363	0.002	0.50	0.02
	iiiiii	0.006	0.001	0.943	0.000	1.59	0.22	0.017	0.002	0.787	0.001	1.06	0.12	0.015	0.001	0.819	0.001	1.15	0.10
	oooooo	0.024	0.000	0.475	0.000	1.21	0.06	0.032	0.055	0.340	0.012	1.02	0.01	0.032	0.049	0.328	0.010	1.04	0.02
	oioooo	0.020	0.225	0.575	0.175	1.49	0.06	0.029	0.215	0.420	0.183	1.14	0.14	0.029	0.216	0.420	0.182	1.19	0.02
	oiiii	0.007	0.242	0.914	0.207	1.96	0.22	0.016	0.199	0.797	0.225	1.41	0.43	0.014	0.159	0.823	0.226	1.51	0.41
26M	oioii	0.020	0.259	0.655	0.063	1.33	0.13	0.028	0.340	0.542	0.083	1.02	0.04	0.027	0.328	0.546	0.080	1.06	0.13
	iooioo	0.030	0.016	0.311	0.005	0.60	0.06	0.036	0.011	0.231	0.004	0.56	0.03	0.037	0.009	0.200	0.003	0.55	0.04
	iiiiii	0.019	0.033	0.716	0.008	0.81	0.13	0.026	0.027	0.616	0.007	0.61	0.04	0.025	0.017	0.628	0.005	0.63	0.13
	oooooo	0.031	0.036	0.285	0.008	1.10	0.02	0.037	0.061	0.193	0.013	0.97	0.03	0.038	0.060	0.158	0.013	0.97	0.04
	oioooo	0.028	0.305	0.374	0.166	1.17	0.08	0.034	0.350	0.281	0.155	1.01	0.03	0.034	0.348	0.254	0.155	1.01	0.05
	iiioii	0.021	0.384	0.646	0.182	1.04	0.13	0.029	0.424	0.522	0.172	0.74	0.04	0.028	0.412	0.529	0.175	0.78	0.13
28H	ooiooi	0.016	0.203	0.713	0.047	1.60	0.64	0.021	0.286	0.617	0.066	1.32	0.42	0.021	0.274	0.618	0.064	1.35	0.43
	iooioo	0.021	0.000	0.626	0.000	0.29	0.05	0.026	0.000	0.599	0.000	0.28	0.03	0.026	0.000	0.560	0.000	0.25	0.00
	iiiiii	0.015	0.055	0.785	0.014	0.09	0.05	0.020	0.075	0.722	0.018	0.07	0.03	0.020	0.072	0.739	0.018	0.06	0.00
	oooooo	0.021	0.000	0.580	0.000	1.70	0.18	0.026	0.000	0.482	0.000	1.46	0.08	0.026	0.000	0.471	0.000	1.48	0.08
	ooooio	0.018	0.391	0.644	0.146	1.66	0.18	0.024	0.191	0.547	0.192	1.39	0.08	0.024	0.193	0.542	0.192	1.42	0.08
	ioiiii	0.016	0.227	0.732	0.221	0.50	0.05	0.022	0.223	0.643	0.221	0.38	0.03	0.022	0.292	0.654	0.204	0.39	0.00

Porphyrin	Pathway	B3LYP						CAM-B3LYP						M06-2X					
		FLU	BOA	HOMA	BLA	AV1245	AV _{min}	FLU	BOA	HOMA	BLA	AV1245	AV _{min}	FLU	BOA	HOMA	BLA	AV1245	AV _{min}
28M	ooioi	0.010	0.039	0.833	0.009	2.07	1.05	0.018	0.250	0.682	0.058	1.48	0.60	0.017	0.219	0.730	0.051	1.58	0.67
	iiioi	0.016	0.004	0.730	0.001	0.18	0.06	0.023	0.005	0.594	0.002	0.21	0.02	0.023	0.005	0.609	0.002	0.18	0.01
	iiiiii	0.009	0.002	0.900	0.001	0.07	0.06	0.016	0.000	0.790	0.000	0.12	0.02	0.015	0.001	0.817	0.001	0.10	0.01
	oooooo	0.017	0.004	0.690	0.002	2.01	0.53	0.024	0.042	0.519	0.008	1.50	0.04	0.024	0.037	0.530	0.006	1.58	0.06
	oooooi	0.014	0.222	0.763	0.184	2.06	0.61	0.021	0.265	0.602	0.173	1.50	0.08	0.020	0.258	0.618	0.175	1.60	0.11
	oiiii	0.010	0.241	0.874	0.216	0.64	0.07	0.018	0.281	0.721	0.207	0.53	0.02	0.017	0.276	0.749	0.208	0.54	0.01
32H	ooioi	0.016	0.219	0.723	0.051	1.56	0.76	0.023	0.314	0.594	0.073	1.18	0.45	0.023	0.308	0.588	0.072	1.19	0.46
	ioioio	0.024	0.209	0.525	0.171	0.38	0.04	0.029	0.223	0.439	0.167	0.36	0.06	0.031	0.226	0.416	0.166	0.33	0.06
	iiiiii	0.015	0.013	0.793	0.003	0.41	0.04	0.022	0.018	0.698	0.004	0.32	0.06	0.022	0.015	0.699	0.003	0.31	0.06
	ooooooo	0.024	0.186	0.491	0.152	1.47	0.10	0.030	0.190	0.373	0.151	1.20	0.02	0.031	0.189	0.347	0.151	1.19	0.01
	ooooioo	0.022	0.024	0.567	0.006	1.53	0.10	0.028	0.033	0.451	0.009	1.24	0.02	0.028	0.031	0.436	0.008	1.24	0.01
32M	ioioio	0.010	0.038	0.849	0.009	2.08	1.14	0.020	0.263	0.666	0.062	1.41	0.55	0.019	0.241	0.678	0.057	1.48	0.58
	oioioi	0.018	0.207	0.672	0.170	0.38	0.01	0.025	0.211	0.541	0.170	0.42	0.02	0.026	0.209	0.538	0.170	0.40	0.00
	iiiiii	0.008	0.000	0.913	0.000	0.49	0.01	0.018	0.006	0.767	0.001	0.33	0.02	0.017	0.002	0.787	0.000	0.34	0.00
	ooooooo	0.019	0.191	0.641	0.150	1.81	0.36	0.027	0.198	0.474	0.149	1.42	0.07	0.027	0.198	0.467	0.149	1.46	0.07
	oooooio	0.016	0.010	0.719	0.003	1.98	0.49	0.025	0.043	0.543	0.011	1.48	0.07	0.024	0.043	0.544	0.011	1.52	0.07
	iiiiioi	0.012	0.213	0.812	0.183	0.35	0.01	0.020	0.177	0.675	0.192	0.30	0.02	0.020	0.182	0.686	0.191	0.30	0.00
32F	oioioi	0.015	0.195	0.721	0.046	1.55	0.72	0.021	0.277	0.632	0.065	1.26	0.46	0.020	0.259	0.631	0.062	1.29	0.49
	ioioio	0.021	0.233	0.589	0.164	0.55	0.01	0.026	0.242	0.526	0.162	0.52	0.03	0.026	0.241	0.518	0.162	0.52	0.01
	iiiiii	0.013	0.010	0.820	0.002	0.44	0.01	0.017	0.016	0.756	0.004	0.38	0.03	0.017	0.015	0.768	0.003	0.39	0.01
	ooooooo	0.023	0.106	0.526	0.171	1.57	0.06	0.028	0.081	0.439	0.177	1.36	0.00	0.028	0.087	0.421	0.176	1.39	0.01
	ioiiii	0.016	0.273	0.720	0.169	0.410	0.01	0.021	0.295	0.659	0.163	0.38	0.03	0.021	0.289	0.660	0.164	0.38	0.01
	oiooooo	0.020	0.034	0.602	0.009	1.62	0.12	0.025	0.045	0.512	0.011	1.38	0.03	0.025	0.043	0.502	0.011	1.40	0.02

Appendix B

Supporting Information Chapter 6

4n+2 annulenes

Benzene												
Singlet												
	FLU	Ir(H)	BOA	HOMA	BLA	Iring	Iring ^{1/n}	MCI	AV	AV _{min}	AV _{min}	E (au)
HF	0.000	0.624	0.000	1.002	0.000	0.045	0.597	0.069	10.25	10.25	10.25	-230.754098
B3LYP	0.000	0.625	0.000	0.991	0.000	0.048	0.603	0.073	10.72	10.72	10.72	-232.308550
CAM-B3LYP	0.000	0.628	0.000	1.000	0.000	0.048	0.603	0.072	10.71	10.71	10.71	-232.164821
M06-2X	0.000	0.626	0.000	0.998	0.000	0.048	0.603	0.073	10.73	10.73	10.73	-232.196133
Triplet												
	FLU	Ir(H)	BOA	HOMA	BLA	Iring	Iring ^{1/n}	MCI	AV	AV _{min}	AV _{min}	E (au)
HF	0.024	0.393	0.246	-0.525	0.089	0.001	0.341	0.002	-0.59	-1.07	0.39	-230.653970
B3LYP	0.025	0.399	0.275	-0.513	0.090	0.002	0.353	0.000	-1.48	-2.98	1.51	-232.166392
CAM-B3LYP	0.025	0.408	0.276	-0.433	0.091	0.002	0.363	0.001	-1.26	-2.48	1.20	-232.023298
M06-2X	0.041	0.467	0.281	-0.107	0.056	0.004	0.380	0.002	1.25	0.28	0.28	-232.049781
[10]annulene												
Singlet												
	FLU	Ir(H)	BOA	HOMA	BLA	Iring	Iring ^{1/n}	MCI	AV	AV _{min}	AV _{min}	E (au)
HF twist	0.068	0.421	0.728	-0.668	0.157	0.000	0.339	0.000	0.02	-0.07	0.00	-384.468544
HF heart	0.065	0.436	0.712	-0.605	0.153	0.000	0.380	0.000	0.16	0.01	0.01	-384.461289
B3LYP twist	0.052	0.480	0.639	-0.171	0.128	0.000	0.322	0.000	0.22	-0.03	0.03	-387.063586
B3LYP heart	0.000	0.610	0.007	0.888	0.009	0.004	0.579	0.013	5.42	5.19	5.19	-387.074064
CAM-B3LYP twist	0.059	0.466	0.677	-0.285	0.137	0.000	0.341	0.000	0.12	-0.07	0.03	-386.825917
CAM-B3LYP heart	0.000	0.614	0.009	0.923	0.010	0.004	0.579	0.013	5.41	5.13	5.13	-386.825003
M06-2X twist	0.058	0.463	0.670	-0.291	0.136	0.000	0.325	0.000	0.17	-0.06	0.05	-386.886424
M06-2X heart	0.000	0.611	0.010	0.913	0.010	0.004	0.579	0.013	5.38	5.11	5.11	-386.882758
Triplet												
	FLU	Ir(H)	BOA	HOMA	BLA	Iring	Iring ^{1/n}	MCI	AV	AV _{min}	AV _{min}	E (au)
HF naphthalene	0.030	0.470	0.364	0.075	0.085	0.000	0.353	0.000	0.11	-0.40	0.14	-384.459329
HF twist	0.020	0.478	0.266	0.314	0.068	0.000	0.295	0.000	0.33	-0.05	0.05	-384.472319
B3LYP naphthalene	0.023	0.531	0.328	0.463	0.064	0.000	0.460	0.000	0.44	-0.96	0.91	-387.026485
B3LYP twist	0.020	0.517	0.305	0.421	0.066	0.000	0.352	0.000	0.61	-0.08	0.08	-387.023180
CAM-B3LYP naphthalene	0.027	0.524	0.364	0.411	0.072	0.000	0.446	0.000	0.36	-0.74	0.68	-386.784524
CAM-B3LYP twist	0.022	0.513	0.324	0.407	0.071	0.000	0.347	0.000	0.56	-0.07	0.07	-386.784056
M06-2X naphthalene	0.028	0.522	0.367	0.381	0.073	0.000	0.444	0.000	0.38	-0.63	0.63	-386.838379
M06-2X twist	0.022	0.511	0.328	0.384	0.072	0.000	0.337	0.000	0.49	-0.11	0.10	-386.835164
[14]annulene												
Singlet												
	FLU	Ir(H)	BOA	HOMA	BLA	Iring	Iring ^{1/n}	MCI	AV	AV _{min}	AV _{min}	E (au)
HF	0.050	0.497	0.626	-0.240	0.136	-	-	-	0.72	0.49	0.49	-538.293750
B3LYP	0.001	0.605	0.010	0.952	0.008	-	-	-	4.44	4.24	4.24	-541.949455
TS CAM-B3LYP	0.000	0.609	0.007	0.983	0.007	-	-	-	4.43	4.29	4.29	-541.598070
TS M06-2X	0.001	0.606	0.007	0.974	0.007	-	-	-	4.40	4.27	4.27	-541.681702
CAM-B3LYP	0.026	0.561	0.449	0.437	0.091	-	-	-	2.11	1.80	1.80	-541.602139
M06-2X	0.025	0.561	0.438	0.453	0.088	-	-	-	2.20	1.89	1.89	-541.685367
Triplet												
	FLU	Ir(H)	BOA(1)	HOMA	BLA	Iring	Iring ^{1/n}	MCI	AV	AV _{min}	AV _{min}	E (au)
UHF	0.021	0.502	0.282	0.327	0.069	-	-	-	0.37	-0.55	0.01	-538.297898
UB3LYP	0.017	0.554	0.302	0.564	0.060	-	-	-	0.87	-0.26	0.13	-541.900820
UCAM-B3LYP	0.023	0.544	0.348	0.486	0.071	-	-	-	0.81	-0.23	0.08	-541.562690
UM06-2X	0.022	0.544	0.349	0.482	0.071	-	-	-	0.84	-0.17	0.04	-541.636681
[18]annulene												
Singlet												
	FLU	Ir(H)	BOA	HOMA	BLA	Iring	Iring ^{1/n}	MCI	AV	AV _{min}	AV _{min}	E (au)
HF	0.049	0.504	0.616	-0.175	0.133	0.000	0.472	-	0.66	0.57	0.57	-692.115648
B3LYP	0.001	0.606	0.026	0.959	0.011	0.000	0.573	-	4.37	4.27	4.27	-696.816908
TS CAM-B3LYP	0.001	0.609	0.022	0.982	0.010	0.000	0.572	-	4.37	4.29	4.29	-696.359867
TS M06-2X	0.001	0.607	0.022	0.974	0.010	0.000	0.572	-	4.37	4.28	4.28	-696.462233
CAM-B3LYP	0.026	0.563	0.446	0.448	0.090	0.000	0.530	-	2.00	1.80	1.80	-696.365410
M06-2X	0.025	0.561	0.444	0.445	0.089	0.000	0.529	-	2.00	1.81	1.81	-696.467370
Triplet												
	FLU	Ir(H)	BOA	HOMA	BLA	Iring	Iring ^{1/n}	MCI	AV	AV _{min}	AV _{min}	E (au)
UHF	0.018	0.514	0.257	0.463	0.060	0.000	0.411	-	0.62	-0.39	0.12	-692.146760
UB3LYP	0.013	0.570	0.265	0.672	0.053	0.000	0.533	-	1.46	0.58	0.58	-696.772610
UCAM-B3LYP	0.019	0.559	0.324	0.574	0.066	0.000	0.513	-	1.27	0.30	0.30	-696.333162
UM06-2X	0.019	0.559	0.324	0.573	0.065	0.000	0.517	-	1.33	0.46	0.46	-696.425412

4n annulenes

Cyclobutadiene

Singlet												
	FLU	Ir(H)	BOA	HOMA	BLA	Iring	Iring ^{1/n}	MCI	AV	AV _{min}	AV _{min}	E (au)
HF	0.101	0.391	0.888	-3.732	0.249	0.005	0.262	0.009	-	-	-	-153.678713
B3LYP	0.104	0.416	0.900	-4.094	0.247	0.005	0.266	0.009	-	-	-	-154.718514
CAM-B3LYP	0.103	0.398	0.898	-3.786	0.245	0.005	0.264	0.009	-	-	-	-154.621763
M06-2X	0.103	0.405	0.898	-3.754	0.242	0.005	0.268	0.010	-	-	-	-154.643340
Triplet												
	FLU	Ir(H)	BOA	HOMA	BLA	Iring	Iring ^{1/n}	MCI	AV	AV _{min}	AV _{min}	E (au)
HF	0.010	0.507	0.000	0.604	0.000	0.035	0.433	0.122	-	-	-	-153.686831
B3LYP	0.012	0.499	0.000	0.314	0.000	0.038	0.440	0.126	-	-	-	-154.708900
CAM-B3LYP	0.011	0.504	0.000	0.478	0.000	0.037	0.439	0.126	-	-	-	-154.611405
M06-2X	0.011	0.505	0.000	0.468	0.000	0.037	0.438	0.125	-	-	-	-154.625105

COT

Singlet												
	FLU	Ir(H)	BOA	HOMA	BLA	Iring	Iring ^{1/n}	MCI	AV	AV _{min}	AV _{min}	E (au)
HF	0.067	0.436	0.726	-0.599	0.156	0.001	0.406	0.001	-0.30	-0.30	0.30	-307.593865
B3LYP	0.056	0.477	0.664	-0.228	0.134	0.001	0.441	0.001	-0.72	-0.72	0.72	-309.665257
CAM-B3LYP	0.061	0.468	0.693	-0.309	0.140	0.001	0.428	0.001	-0.52	-0.52	0.52	-309.474490
M06-2X	0.062	0.460	0.694	-0.336	0.141	0.001	0.427	0.001	-0.51	-0.51	0.51	-309.518754
Triplet												
	FLU	Ir(H)	BOA	HOMA	BLA	Iring	Iring ^{1/n}	MCI	AV	AV _{min}	AV _{min}	E (au)
HF	0.001	0.590	0.000	0.990	0.000	0.007	0.534	0.026	-4.07	-4.07	4.07	-307.553620
B3LYP	0.001	0.589	0.000	0.943	0.000	0.007	0.540	0.028	-4.31	-4.31	4.31	-309.601832
CAM-B3LYP	0.001	0.593	0.000	0.981	0.000	0.007	0.539	0.027	-4.29	-4.29	4.29	-309.441037
M06-2X	0.001	0.591	0.000	0.965	0.000	0.007	0.539	0.027	-4.29	-4.29	4.29	-309.477016

[12]annulene

Singlet												
	FLU	Ir(H)	BOA	HOMA	BLA	Iring	Iring ^{1/n}	MCI	AV	AV _{min}	AV _{min}	E (au)
HF	0.063	0.445	0.698	-0.583	0.153	-	-	-	0.20	-0.11	0.04	-461.380728
B3LYP	0.042	0.511	0.565	0.022	0.115	-	-	-	0.58	-0.21	0.01	-464.498264
CAM-B3LYP	0.050	0.494	0.624	-0.135	0.128	-	-	-	0.41	-0.14	0.02	-464.210977
M06-2X	0.050	0.488	0.624	-0.160	0.128	-	-	-	0.42	-0.15	0.06	-464.283242
Triplet												
	FLU	Ir(H)	BOA	HOMA	BLA	Iring	Iring ^{1/n}	MCI	AV	AV _{min}	AV _{min}	E (au)
HF	0.021	0.487	0.280	0.265	0.067	-	-	-	0.37	-0.30	0.07	-461.380989
B3LYP	0.002	0.590	0.033	0.901	0.012	-	-	-	0.04	-0.50	0.07	-464.470613
CAM-B3LYP	0.015	0.562	0.288	0.648	0.056	-	-	-	0.39	-0.26	0.21	-464.173466
M06-2X	0.008	0.577	0.208	0.784	0.039	-	-	-	0.27	-0.54	0.13	-464.238704

[16]annulene

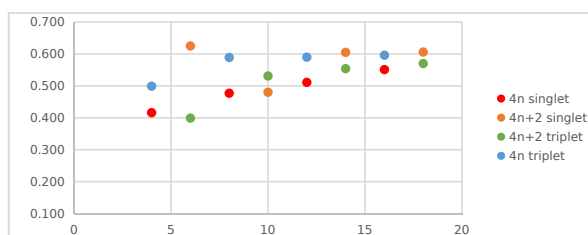
Singlet												
	FLU	Ir(H)	BOA	HOMA	BLA	Iring	Iring ^{1/n}	MCI	AV	AV _{min}	AV _{min}	E (au)
HF (S ₄)	0.054	0.486	0.651	-0.288	0.139	0.000	0.440	-	0.37	0.33	0.33	-615.212342
HF (C ₁)	0.053	0.488	0.643	-0.296	0.139	0.000	0.452	-	0.45	0.25	0.25	-615.205778
B3LYP (S ₄)	0.029	0.551	0.476	0.367	0.095	0.000	0.513	-	1.16	0.96	0.96	-619.371721
B3LYP (C ₁)	0.029	0.548	0.474	0.339	0.096	0.000	0.512	-	1.17	0.78	0.78	-619.368275
CAM-B3LYP (S ₄)	0.041	0.529	0.564	0.143	0.113	0.000	0.484	-	0.74	0.64	0.64	-618.983469
CAM-B3LYP (C ₁)	0.040	0.530	0.555	0.138	0.113	0.000	0.487	-	0.82	0.55	0.55	-618.980237
M06-2X (S ₄)	0.040	0.526	0.562	0.138	0.113	0.000	0.484	-	0.74	0.63	0.63	-619.076857
M06-2X (C ₁)	0.039	0.526	0.553	0.133	0.112	0.000	0.487	-	0.83	0.58	0.58	-619.074775
Triplet												
	FLU	Ir(H)	BOA	HOMA	BLA	Iring	Iring ^{1/n}	MCI	AV	AV _{min}	AV _{min}	E (au)
HF	0.001	0.598	0.013	0.983	0.005	-	-	-	1.45	1.08	1.08	-615.138406
B3LYP	0.002	0.596	0.057	0.938	0.013	-	-	-	1.51	1.16	1.16	-619.349773
CAM-B3LYP	0.015	0.568	0.294	0.676	0.059	-	-	-	1.23	0.35	0.35	-618.953069
M06-2X	0.011	0.576	0.252	0.753	0.050	-	-	-	1.36	0.74	0.74	-619.040163

Hückel I_{ring} Study

B3LYP		SINGLET	
$4n$	I_{ring} (Hückel)	$4n+2$	I_{ring} (Hückel)
4	0.416	6	0.625
8	0.477	10	0.480
12	0.511	14	0.605
16	0.551	18	0.606

TRIPLET	
$4n$	I_{ring} (Hückel)
4	0.499
8	0.589
12	0.590
16	0.596

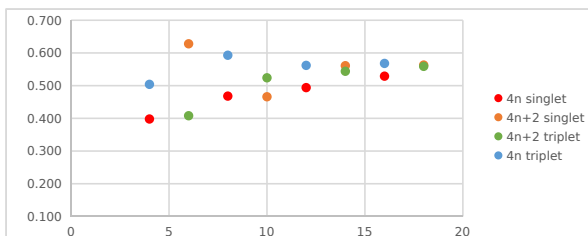
$4n+2$		I_{ring} (Hückel)	
$4n$	I_{ring} (Hückel)	$4n+2$	I_{ring} (Hückel)
6	0.399	10	0.531
10	0.531	14	0.554
14	0.554	18	0.570



CAM-B3LYP		SINGLET	
$4n$	I_{ring} (Hückel)	$4n+2$	I_{ring} (Hückel)
4	0.398	6	0.628
8	0.468	10	0.466
12	0.494	14	0.561
16	0.529	18	0.563

TRIPLET	
$4n$	I_{ring} (Hückel)
4	0.504
8	0.593
12	0.562
16	0.568

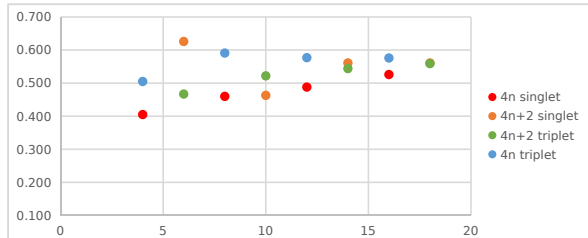
$4n+2$		I_{ring} (Hückel)	
$4n$	I_{ring} (Hückel)	$4n+2$	I_{ring} (Hückel)
6	0.408	10	0.524
10	0.524	14	0.544
14	0.544	18	0.559



M06-2X		SINGLET	
$4n$	I_{ring} (Hückel)	$4n+2$	I_{ring} (Hückel)
4	0.405	6	0.626
8	0.460	10	0.463
12	0.488	14	0.561
16	0.526	18	0.561

TRIPLET	
$4n$	I_{ring} (Hückel)
4	0.505
8	0.591
12	0.577
16	0.576

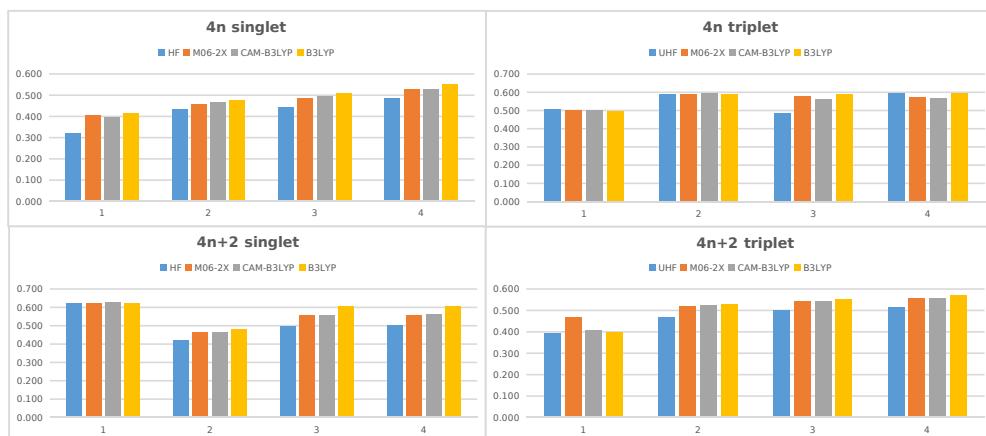
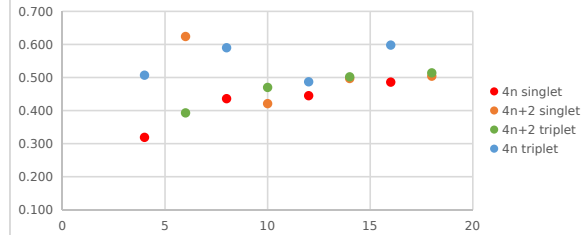
$4n+2$		I_{ring} (Hückel)	
$4n$	I_{ring} (Hückel)	$4n+2$	I_{ring} (Hückel)
6	0.467	10	0.522
10	0.522	14	0.544
14	0.544	18	0.559



HF		SINGLET	
$4n$	I_{ring} (Hückel)	$4n+2$	I_{ring} (Hückel)
4	0.319	6	0.624
8	0.436	10	0.421
12	0.445	14	0.497
16	0.486	18	0.504

TRIPLET	
$4n$	I_{ring} (Hückel)
4	0.507
8	0.590
12	0.487
16	0.598

$4n+2$		I_{ring} (Hückel)	
$4n$	I_{ring} (Hückel)	$4n+2$	I_{ring} (Hückel)
6	0.393	10	0.470
10	0.470	14	0.502
14	0.502	18	0.514

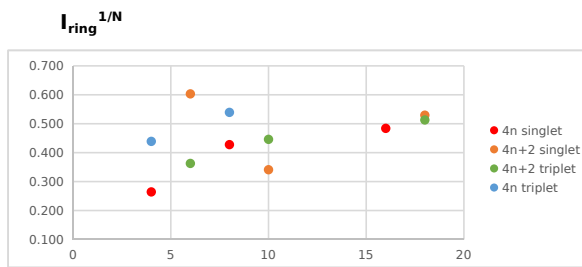


CAM-B3LYP		SINGLET	
4n	$I_{ring}^{1/N}$		
4	0.264		
8	0.428		
12			
16	0.484		

4n+2		$I_{ring}^{1/N}$	
6		0.603	
10		0.341	
14			
18		0.530	

TRIPLET			
4n	$I_{ring}^{1/N}$		
4	0.44		
8	0.54		
12			
16			

4n+2		$I_{ring}^{1/N}$	
6		0.363	
10		0.446	
14			
18		0.513	

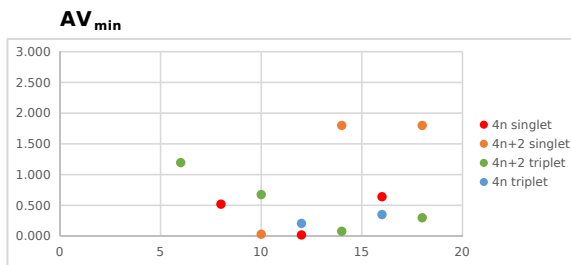


CAM-B3LYP		SINGLET	
4n	$ AV_{min} $		
4			
8	0.52		
12	0.02		
16	0.64		

4n+2		$ AV_{min} $	
6		10.71	
10		0.03	
14		1.80	
18		1.80	

TRIPLET			
4n	$ AV_{min} $		
4			
8	4.29		
12	0.21		
16	0.35		

4n+2		$ AV_{min} $	
6		1.20	
10		0.68	
14		0.08	
18		0.30	

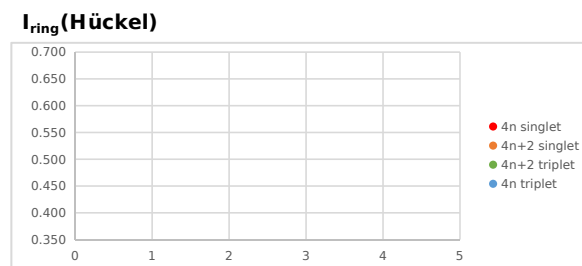


CAM-B3LYP		SINGLET	
4n	$I_{ring}(\text{Hückel})$		
4	#REF!		
8	#REF!		
12	#REF!		
16	#REF!		

4n+2		$I_{ring}(\text{Hückel})$	
6		#REF!	
10		#REF!	
14		#REF!	
18		#REF!	

TRIPLET			
4n	$I_{ring}(\text{Hückel})$		
4	#REF!		
8	#REF!		
12	#REF!		
16	#REF!		

4n+2		$I_{ring}(\text{Hückel})$	
6		#REF!	
10		#REF!	
14		#REF!	
18		#REF!	

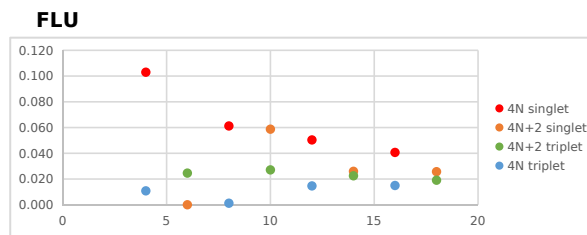


CAM-B3LYP		SINGLET	
4n	FLU		
4	0.103		
8	0.061		
12	0.050		
16	0.041		

4n+2		FLU	
6		0.000	
10		0.059	
14		0.026	
18		0.026	

TRIPLET			
4n	FLU		
4	0.011		
8	0.001		
12	0.015		
16	0.015		

4n+2		FLU	
6		0.025	
10		0.027	
14		0.023	
18		0.019	

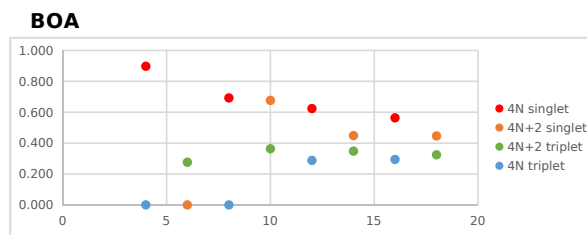


CAM-B3LYP		SINGLET	
4n	BOA		
4	0.898		
8	0.693		
12	0.624		
16	0.564		

4n+2		BOA	
6		0.000	
10		0.677	
14		0.449	
18		0.446	

TRIPLET			
4n	BOA		
4	0.000		
8	0.000		
12	0.288		
16	0.294		

4n+2		BOA	
6		0.276	
10		0.364	
14		0.348	
18		0.324	

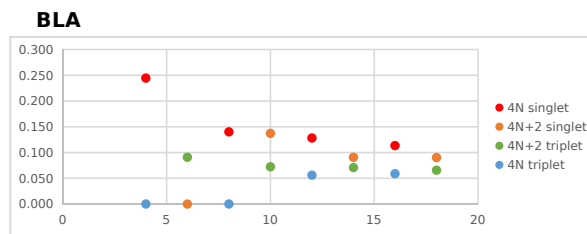


CAM-B3LYP		SINGLET	
4n	BLA		
4	0.245		
8	0.140		
12	0.128		
16	0.113		

4n+2		FLU	
6		0.000	
10		0.137	
14		0.091	
18		0.090	

TRIPLET			
4n	BLA		
4	0.000		
8	0.000		
12	0.056		
16	0.059		

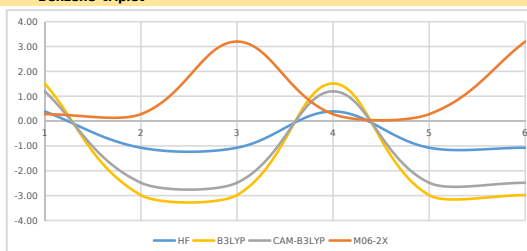
4n+2		BLA	
6		0.091	
10		0.072	
14		0.071	
18		0.066	



Four-atom MCI profiles

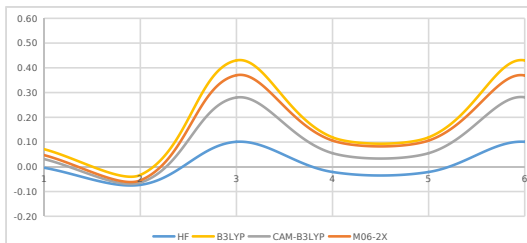
Benzene triplet

Fragment	HF	B3LYP	CAM-B3LYP	M06-2X
1	0.39	1.51	1.20	0.28
2	-1.07	-2.98	-2.48	0.28
3	-1.07	-2.98	-2.48	3.20
4	0.39	1.51	1.20	0.28
5	-1.07	-2.98	-2.48	0.28
6	-1.07	-2.98	-2.48	3.20



[10]annulene singlet (twist)

Fragment	HF	B3LYP	CAM-B3LYP	M06-2X
1	0.00	0.07	0.03	0.05
2	-0.07	-0.03	-0.06	-0.06
3	0.10	0.43	0.28	0.37
4	-0.02	0.12	0.06	0.11
5	-0.02	0.12	0.06	0.11
6	0.10	0.43	0.28	0.37
7	-0.07	-0.03	-0.07	-0.06
8	-0.01	0.07	0.03	0.05
9	0.08	0.50	0.29	0.36
10	0.08	0.50	0.29	0.36



Appendix C

Supporting Information Chapter 8

Supporting Information: How aromatic are molecular nanoring? The case of a six-porphyrin nanoring[†]

Irene Casademont-Reig,^{a,b} Raúl Guerrero-Avilés,^{a,c} Eloy Ramos-Cordoba,^{*a,b} Miquel Torrent-Sucarrat,^{*a,d,e} and Eduard Matito^{*a,d}

1 Computational details

Following the computational work of Ref. 1, we have studied four different oxidation states of the six-porphyrin nanoring: neutral, +4, +6, and +12. The molecules have been studied considering not only the isolated belt structure (c-P6, c-P6⁴⁺, c-P6⁶⁺, and c-P6¹²⁺) but also taking into account the encapsulated template and the two phenyl substituents in each porphyrin (c-P6·T6, c-P6·T6⁴⁺, c-P6·T6⁶⁺, and c-P6·T6¹²⁺).

Geometry optimizations and frequency calculations have been performed with the Gaussian16 software package² using B3LYP,^{3,4} CAM-B3LYP,⁵ LC- ω HPBE, and M06-2X⁶ density functional approximations (DFAs) including Grimme's D3 dispersion correction (for the first two DFAs)⁷ and in combination with the 6-31G* basis set.⁸ The initial structures have been obtained from previous works.¹ Single-point coupled-cluster calculations were performed with ORCA software package⁹ using DLPNO-CCSD(T)¹⁰ with resolution of identity¹¹ in combination with the Def-SVP/C basis set¹² and the corresponding auxiliary basis set in order to obtain accurate reference calculations to assess the accuracy of DFAs.

The calculation of the electronic aromaticity indices (AV1245,¹³ AV_{min},¹⁴ BOA,¹⁵ and FLU^{16,17}) and the delocalization indices (DIs)^{18,19} employs the quantum theory of atoms in molecules (QTAIM)²⁰ atomic partition performed by the AIMAll software.²¹ The atomic overlap matrices resulting from this partition and the wavefunction files are the input of the in-house ESI-3D code,^{16,22,23} which provides AV1245,¹³ AV_{min},¹⁴ BLA,¹⁵ BOA,¹⁵ DIs,^{19,23} FLU,^{16,17} HOMA,²⁴ and MCI²⁵ values. The numerical integrations of the atoms in the QTAIM²⁰ as well as the corresponding oxidation states have errors below 0.004 and 0.03 electrons for c-P6 (and all its oxidation states) and c-P6·T6 (and all its oxidation states), respectively. The ESI-3D code is available upon request (ematito@gmail.com).^{16,22,23} ACID²⁶ and NICS²⁷ calculations were conducted using the CSGT and GIAO methods, respectively, using Gaussian software packages (Gaussian09²⁸ and Gaussian16²). NICS grids were calculated with 1Å resolution (plots 20Å x 20Å grid) and the plots were generated with a Python script. The version 2.0.0 of the AICD program²⁶ was used to generate ACID results and they were visualized using POV-Ray.²⁹

The effective oxidation state (EOS) analysis^{30,31} was performed with APOST-3D. The software provided in Ref. 32 was used to assess the similarity of two molecular geometries through the calculation of the root mean square deviation (RMSD) of the atomic distances.

NMR calculations were also performed using GIAO method in Gaussian16 software package² with B3LYP,^{3,4} CAM-B3LYP,⁵ and M06-2X⁶ functionals including Grimme's D3 dispersion correction⁷ and in combination with the 6-31G* basis set.⁸ Solvent effects of dichloromethane were taken into account using the Polarizable Continuum Model (PCM).³³

2 Geometry assessment

In order to quantify the structural differences among the several optimized geometries, the root mean square deviation (RMSD) of two molecules has been calculated. The RMSD of two structures was calculated using the software provided in Ref. 32. This program calculates the RMSD between two Cartesian geometries in either .xyz or .pdb format and uses the Kabsch algorithm (1976)³⁴ or Quaternion algorithm³⁵ if rotation is needed before the calculation of RMSD. All the RMSD values included in this work compare two structures ignoring all the hydrogen atoms.

From the data in Table S1, we conclude that the structures found by Anderson *et al.* at the B3LYP/6-31G* level of theory were not absolute minima of the corresponding potential energies for c-P6, c-P6⁴⁺, c-P6⁶⁺, and c-P6¹²⁺. However, their geometries are very similar to the ones we have found in this work at the same level of theory.

^a Donostia International Physics Center (DIPC), 20018 Donostia, Euskadi, Spain. E-mail: eloy.raco@gmail.com, miqueltorrentsucarrat@gmail.com; ematito@gmail.com

^b Polimero eta Material Aurreratuak: Fisika, Kimika eta Teknologia, Kimika Fakultatea, Euskal Herriko Unibertsitatea UPV/EHU, P.K. 1072, 20080 Donostia, Euskadi, Spain.

^c Centro de Física de Materiales, CFM-MPC CSIC-UPV/EHU, 20018 Donostia, Euskadi, Spain.

^d Ikerbasque, Basque Foundation for Science, Plaza Euskadi 5, 48009 Bilbao, Euskadi, Spain.

^e Department of Organic Chemistry I, Universidad del País Vasco/Euskal Herriko Unibertsitatea (UPV/EHU), 20018 Donostia, Euskadi, Spain.

[†] Dedication: We dedicate this paper to the memory of our friend and colleague, Professor Istvan Mayer, whose works have been a continuous inspiration.

Table S1 Energy comparison and the RMSD of the minimum geometries calculated by Anderson *et al.*¹ and this work at the B3LYP/6-31G* level of theory. Energy units are atomic units (au) while RMSD are in Ångstroms (Å).

Species	Energy (Ref. 1) ^a	Energy (this work)	RMSD
c-P6	-17512.513898	-17512.514222	0.001
c-P6 ⁴⁺	-17511.456927	-17511.457194	0.040
c-P6 ⁶⁺	-17510.640233	-17510.640427	0.033
c-P6 ¹²⁺	-17507.033356	-17507.033566	0.015

^a Geometries from Ref. 1.

Table S2 Comparison between the geometries calculated at the B3LYP, CAM-B3LYP, and M06-2X methods. The columns 2-4 give the total energy of the molecules at the corresponding geometry. The third last columns correspond to the RMSD values obtained from these geometries. All the calculations employed the 6-31G* basis set. Energy units are atomic units (au) while RMSD are in Ångstroms (Å).

Species	G ₁ (B3LYP)	G ₂ (CAM-B3LYP)	G ₃ (M06-2X)	RMSD(G ₁ -G ₂)	RMSD(G ₂ -G ₃)	RMSD (G ₁ -G ₃)
c-P6	-17512.514222	-17509.042830	-17509.271928	0.049	0.021	0.041
c-P6 ⁴⁺	-17511.457194	-17507.935387	-17508.138955	0.661	0.666	0.201
c-P6 ⁶⁺	-17510.640427	-17507.119479	-17507.306773	0.224	0.031	0.206
c-P6 ¹²⁺	-17507.033566	-17503.560977	-17503.701580	0.040	0.031	0.036

The results of Table S2 demonstrate that the B3LYP energy minima found for c-P6 and c-P6¹²⁺ structures are well reproduced by the CAM-B3LYP and M06-2X methods. However, the geometries of the B3LYP energy minima of c-P6⁴⁺ and c-P6⁶⁺ are significantly different from those found at the M06-2X and CAM-B3LYP levels of theory. Since the latter functional approximations do not suffer from large electron delocalization errors, one is prompted to conclude that B3LYP overestimates the symmetry of c-P6⁶⁺ (and, hence, its aromaticity, see below), whereas it overestimates the asymmetry of c-P6⁴⁺ (RMSD=0.661) resulting in a spurious enhancement of the antiaromatic features of this molecule (see below). Similar results have been recently reported by our group^{15,36-39} and others.⁴⁰⁻⁴³

We have also characterized the structure of c-P6⁶⁺ using the LC- ω HPBE^{44,45} method with $\omega=0.1$ and $\omega=0.2$ in combination with the 6-31G* basis set. Using LC- ω HPBE with $\omega=0.1$, the optimized structure lies in between the B3LYP and CAM-B3LYP ones, as confirmed by the fact that the RMSD values between the LC- ω HPBE($\omega=0.1$) geometry and these two geometries are quite similar (0.160 and 0.142, for B3LYP and CAM-B3LYP, respectively). On the contrary, LC- ω HPBE with $\omega=0.2$ provides a geometry closer to the CAM-B3LYP one (RMSD=0.095). This further demonstrates the importance of including a large percentage (typically above 50%) of HF exchange in the functional in order to correctly characterize conjugated molecules (avoiding the delocalization error⁴⁶).

3 $^1\text{H-NMR}$ calculations

We have calculated the $^1\text{H-NMR}$ spectra for all species, including the template structure and the phenyl substituents. The most important protons for the study of aromaticity are highlighted in the following figure.

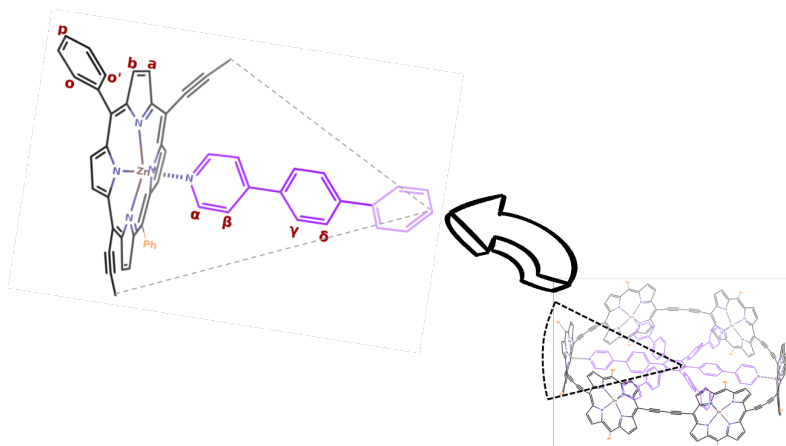


Figure S1 Nanoring's structure where the most important protons of the $^1\text{H-NMR}$ spectra are highlighted (see also Table S3).

In Table S3, we have summarized the shielding of the most relevant protons for the study of aromaticity and compared them with the experimental values from the literature.¹

Table S3 $^1\text{H-NMR}$ values (in ppm) calculated using CAM-B3LYP, M06-2X, and B3LYP methods in combination with 6-31G* basis set and using CH_2Cl_2 as a solvent (PCM model).³³ We have compared with the experimental data from the literature.¹ Maximum error (MAX), root mean square error (RMSE), and mean absolute error (MAE) of each method are also given.

Proton	c-P6·T6				c-P6·T6 ⁴⁺				c-P6·T6 ⁶⁺				c-P6·T6 ¹²⁺			
	CAM-B3LYP	M06-2X	B3LYP	Experimental	CAM-B3LYP	M06-2X	B3LYP	Experimental	CAM-B3LYP	M06-2X	B3LYP	Experimental	CAM-B3LYP	M06-2X	B3LYP	Experimental
α	2.28	2.72	3.18	2.41	6.69	9.02	68.95	22.7	7.65	8.08	-3.74	5.71	10.50	11.32	14.15	11.31
β	4.68	5.23	5.13	4.99	6.79	8.81	56.20	19.9	6.87	7.38	-2.75	5.27	8.35	9.10	9.78	8.83
γ	5.32	5.74	5.65	5.45	6.90	8.62	50.52	-	6.85	7.25	-1.65	5.17	7.96	8.55	8.93	7.94
δ	5.55	5.94	5.83	5.56	6.91	8.49	49.97	-	6.82	7.18	-1.03	5.17	7.84	8.35	8.58	7.73
a	9.74	10.39	9.38	9.56	8.29	9.08	14.10	-	7.44	8.02	6.02	6.52	6.50	6.97	4.31	6.05
b	8.95	9.58	8.66	8.75	7.82	8.60	17.05	-	7.06	7.57	4.94	5.99	6.04	6.51	4.28	5.77
o	8.13	8.84	7.92	8.06	7.71	8.10	-0.63	-	7.69	8.39	9.36	7.78	7.90	8.56	8.49	7.31
o'	8.21	8.85	8.23	8.32	8.12	9.50	35.74	-	7.51	8.03	2.13	5.91	6.99	7.55	5.82	6.57
p	7.97	8.51	7.85	8.02	7.98	8.74	14.66	-	7.85	8.41	6.51	7.92	7.98	8.61	7.78	7.58
MAX	0.31	0.83	0.77	0.00	-	-	-	-	1.94	2.37	9.45	0.00	0.81	1.25	2.84	0.00
MAE	0.13	0.52	0.23	0.00	-	-	-	-	1.18	1.65	4.31	0.00	0.39	0.71	1.22	0.00
RMSE	0.16	0.57	0.30	0.00	-	-	-	-	1.35	1.77	5.36	0.00	0.45	0.80	1.41	0.00

All the errors presented in Table S3 (MAX, MAE, and RMSE) clearly indicate that the functional that better reproduces the experimental data is CAM-B3LYP. While errors are of similar magnitude for c-P6·T6, they are much larger for c-P6·T6⁶⁺, indicating that B3LYP geometry is quite different from the experimental one.

To assess to which extent we can rely on the $^1\text{H-NMR}$ data to analyze the aromaticity of these systems, we have constructed a structure that has no current, therefore, is not aromatic. To construct it, we have taken the optimized structure of each species and replaced all the bridging butadiyne linkers by capping hydrogen atoms. Then, we made a single-point calculation to obtain the chemical shieldings of the disconnected structure (see Figure S2). In the following table, the chemical shielding of the protons that are used to analyze of the aromatic character are presented for both disconnected and connected structures of the nanoring's species. In addition, the $^1\text{H-NMR}$ chemical shift of α and β protons of the free template are presented in Table S5.

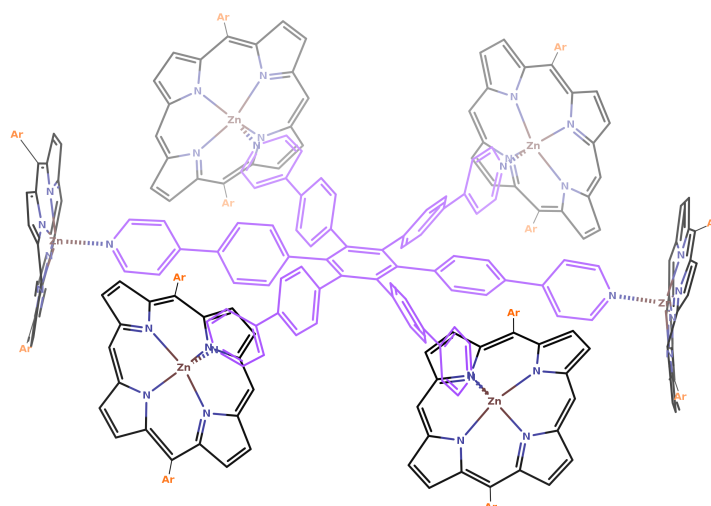


Figure S2 Nanoring's disconnected structure where the bridging butadiyne linkers have been removed.

Table S4 Selected $^1\text{H-NMR}$ chemical shift (in ppm) calculated using CAM-B3LYP and B3LYP methods in combination with 6-31G* basis set and using CH_2Cl_2 as a solvent (PCM model).³³ Experimental data is taken from Ref. 1 and Ref. 47. For each species we include the values of the nanoring's structure (connected) and an idealized model, where the bridging butadiyne linkers have been removed (disconnected) (See Figure S2)

Method	data	c-P6 · T6		c-P6 · T6 ⁴⁺		c-P6 · T6 ⁶⁺		c-P6 · T6 ¹²⁺	
		Connected	Disconnected	Connected	Disconnected	Connected	Disconnected	Connected	Disconnected
CAM-B3LYP	α	2.28	1.93	6.69	9.95	7.65	13.62	10.50	10.60
	β	4.68	4.47	6.79	7.77	6.87	9.32	8.35	8.35
	o	8.13	8.17	7.71	7.38	7.69	7.36	7.90	7.93
	o'	8.21	8.24	8.12	6.88	7.51	6.21	6.99	6.98
B3LYP	α	3.18	2.09	68.95	9.03	-3.74	15.34	14.15	14.42
	β	5.13	4.46	56.20	6.66	-2.75	9.89	9.78	9.84
	o	7.92	8.02	-0.63	7.48	9.36	7.07	8.49	8.52
	o'	8.23	8.12	35.74	6.05	2.13	5.68	5.82	5.82
Experimental	α	2.41	-	22.7	-	5.71	-	11.31	-
	β	4.99	-	19.9	-	5.27	-	8.83	-
	o	8.06	-	-	-	7.78	-	7.31	-
	o'	8.32	-	-	-	5.91	-	6.57	-

Table S5 $^1\text{H-NMR}$ chemical shift of α and β protons of the free template (in ppm) calculated using CAM-B3LYP and B3LYP methods in combination with 6-31G* basis set and using CH_2Cl_2 as a solvent (PCM model).³³ Experimental data is taken from Ref. 1.

data	CAM-B3LYP	B3LYP	Experimental
α	8.62	8.52	8.54
β	7.22	7.10	7.33

Comparing the $^1\text{H-NMR}$ data of all the species' connected and disconnected structures, we can appreciate that the values are pretty similar. Even in some cases, the disconnected structure presents a slightly higher value. Therefore, these results show that, although the porphyrins are not connected, a ring current is present. For this reason, we can say that this is another piece of evidence that proves that none of the species studied is aromatic.

4 Aromaticity

4.1 Porphyrinoid reference systems

In order to assess the aromaticity of the molecules presented in the manuscript, we have collected in Table S6 the aromaticity indices for the different pathways of a simple aromatic porphyrin molecule, porphin (**18H**). All the values presented in this section regarding **18H** were calculated at the CAM-B3LYP/6-311G(d,p) level of theory.³⁶ A molecular graph of porphin, with delocalization indices values included, can be found in Figure S3. If the pathway goes either through C-N bonds of the pyrrole or the imine groups, this fragment is labeled as "i" (inner), otherwise "o" (outer) is used. As a result, all the pathways are characterized by four letters, the first of which corresponds to pyrrole group at the top-left corner of Figure S3. The "oioi" pathway corresponds to the annulene pathway.

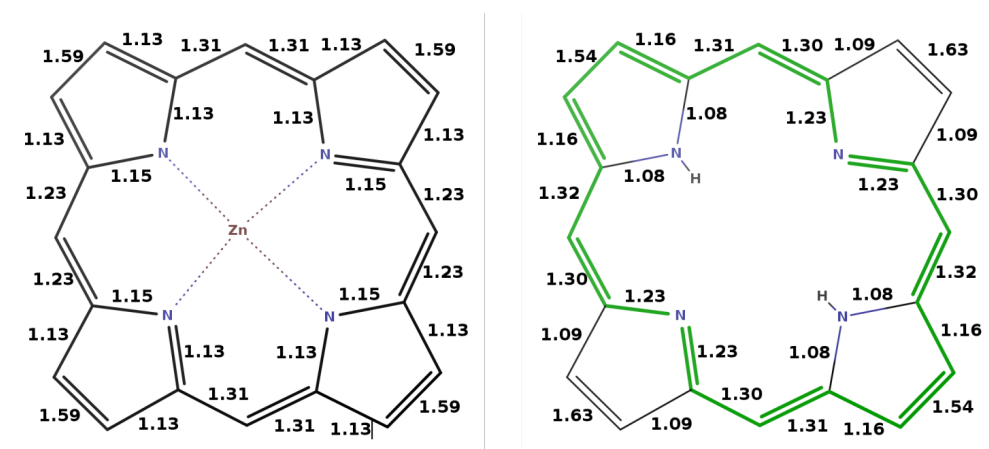


Figure S3 Delocalization indices of (left) c-P6 porphyrins and (right) porphin. In green, we have highlighted the annulene pathway (the most aromatic one) of **18H**.³⁶ Calculations employed the CAM-B3LYP functional in combination with 6-31G* and 6-311G** basis set, respectively.

Table S6 Aromaticity indices for the different pathways of porphin (**18H**). Geometries and some results extracted from Ref. 36. The number in parentheses indicates the number of pathways that are equivalent by symmetry.

pathway	FLU	BOA ^a	HOMA	BLA ^a	AV1245	AVmin
oioi	0.010	0.137	0.872	0.035	2.16	1.28
oooi (2)	0.016	0.202	0.734	0.047	1.91	0.49
oooo	0.022	0.260	0.610	0.058	1.70	0.49
ii oi (2)	0.008	0.111	0.917	0.026	1.57	0.13
ooii (4)	0.015	0.180	0.769	0.040	1.36	0.13
ooio (2)	0.021	0.243	0.637	0.052	1.17	0.13
iiii	0.006	0.081	0.968	0.016	0.91	0.13
iiio (2)	0.013	0.157	0.808	0.031	0.73	0.13
ioio	0.019	0.224	0.666	0.045	0.57	0.13

^a BOA and BLA were recalculated according to the formulation of Ref. 37.

In order to compare 1245-index distribution graphs of the nanoring structure with different oxidation states, we have included the 1245-index distribution plots of the 26 π -electron porphyrin in Hückel conformation (**26H**) and the 32 π -electron porphyrin in Möbius conformation (**32M**) as examples of aromatic expanded porphyrins (see Figure S4). For a detailed analysis of the aromaticity of **26H** and **32M** see Ref 36.

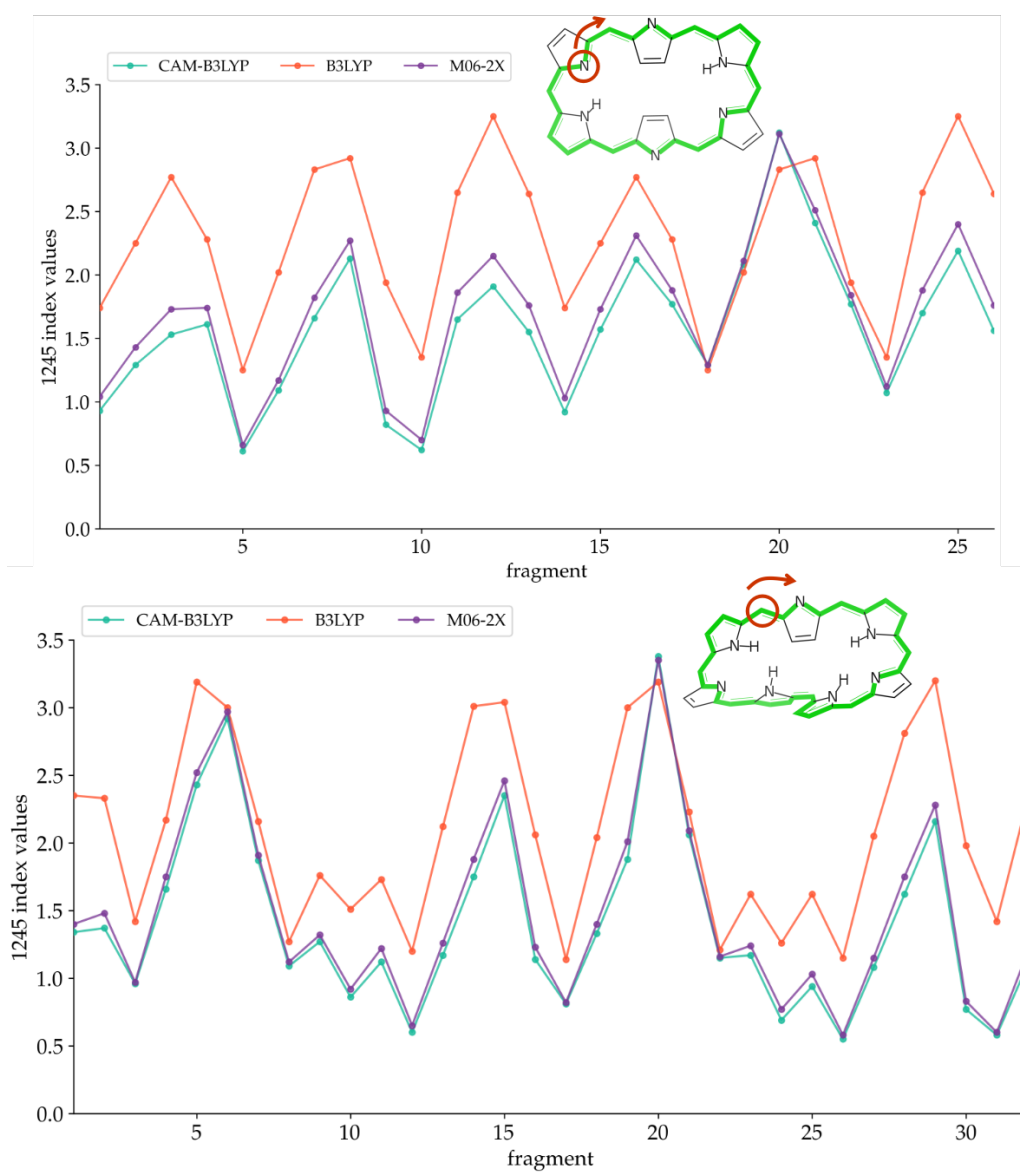


Figure S4 1245-index distribution along the most aromatic path, the annulene path, of (top) **26H** and (bottom) **32M** for the three DFAs exposed in combination with the 6-311G(d,p) basis set.⁴⁸ We have highlighted the first atom of the starting fragment of the 1245-index distribution with an orange circle and used an arrow to indicate the direction of the x-axis.

Table S13 Aromaticity indices for several pathways of c-P6·T6, c-P6·T6⁴⁺, c-P6·T6⁶⁺, and c-P6·T6¹²⁺ calculated at the B3LYP, CAM-B3LYP, and M06-2X/6-31G* levels of theory.

pathway	B3LYP						CAM-B3LYP						M06-2X						
	FLU	BOA	HOMA	BLA	AV1245	AV _{min}	FLU	BOA	HOMA	BLA	AV1245	AV _{min}	FLU	BOA	HOMA	BLA	AV1245	AV _{min}	
c-P6·T6	ii ii ii ii ii ii	0.081	0.354	-0.138	0.064	1.25	0.42	0.096	0.412	-0.196	0.070	1.01	0.35	0.096	0.407	-0.189	0.071	1.03	0.37
	oo oo oo oo oo oo	0.082	0.425	-0.235	0.073	1.44	0.16	0.096	0.484	-0.315	0.082	1.21	0.00	0.096	0.481	-0.324	0.081	1.22	0.01
	oo ii oo ii oo ii	0.082	0.392	-0.197	0.069	1.35	0.16	0.096	0.451	-0.266	0.076	1.12	0.00	0.096	0.447	-0.270	0.076	1.13	0.01
	oo oo ii oo oo ii	0.082	0.403	-0.212	0.070	1.38	0.16	0.096	0.462	-0.285	0.078	1.15	0.00	0.096	0.459	-0.291	0.078	1.16	0.01
	oo oo oo ii oo oo	0.082	0.414	-0.224	0.071	1.41	0.16	0.096	0.473	-0.301	0.080	1.18	0.00	0.096	0.470	-0.308	0.079	1.19	0.01
	oi oi oi oi oi oi	0.082	0.392	-0.196	0.069	1.36	0.16	0.096	0.450	-0.265	0.076	1.12	0.00	0.096	0.446	-0.269	0.076	1.14	0.01
	oi io oi io oi io	0.082	0.392	-0.196	0.069	1.35	0.17	0.096	0.451	-0.266	0.076	1.11	0.01	0.096	0.447	-0.271	0.076	1.12	0.02
oi ii ii io ii ii	0.081	0.368	-0.161	0.066	1.28	0.18	0.096	0.426	-0.223	0.072	1.04	0.01	0.096	0.421	-0.221	0.073	1.06	0.03	
c-P6·T6 ⁴⁺	ii ii ii ii ii ii	0.068	0.328	-0.078	0.065	1.85	0.87	0.073	0.352	-0.094	0.070	1.67	0.75	0.073	0.006	-0.087	0.072	1.73	0.75
	oo oo oo oo oo oo	0.069	0.383	-0.169	0.067	1.55	0.08	0.074	0.402	-0.184	0.070	1.49	0.06	0.074	0.409	-0.200	0.071	1.51	0.00
	oo ii oo ii oo ii	0.068	0.357	-0.134	0.066	1.69	0.08	0.074	0.379	-0.149	0.070	1.57	0.08	0.074	0.385	-0.156	0.071	1.62	0.01
	oo oo ii oo oo ii	0.069	0.369	-0.155	0.068	1.64	0.08	0.074	0.392	-0.172	0.072	1.53	0.06	0.074	0.397	-0.187	0.073	1.57	0.00
	oo oo oo ii oo oo	0.069	0.374	-0.158	0.067	1.60	0.08	0.074	0.397	-0.179	0.071	1.51	0.06	0.074	0.402	-0.187	0.071	1.54	0.00
	oi oi oi oi oi oi	0.068	0.357	-0.132	0.066	1.70	0.09	0.074	0.379	-0.146	0.070	1.58	0.06	0.074	0.385	-0.152	0.071	1.63	0.01
	oi io oi io oi io	0.068	0.357	-0.133	0.066	1.69	0.09	0.074	0.379	-0.148	0.070	1.57	0.08	0.074	0.385	-0.156	0.071	1.61	0.00
oi ii ii io ii ii	0.068	0.339	-0.102	0.066	1.79	0.09	0.073	0.359	-0.109	0.069	1.64	0.13	0.073	0.366	-0.113	0.071	1.69	0.08	
c-P6·T6 ⁶⁺	ii ii ii ii ii ii	0.066	0.322	-0.088	0.066	1.92	0.81	0.075	0.379	-0.164	0.077	1.48	0.64	0.075	0.375	-0.157	0.077	1.54	0.65
	oo oo oo oo oo oo	0.068	0.377	-0.173	0.066	1.43	0.04	0.074	0.409	-0.225	0.071	1.27	0.06	0.075	0.410	-0.240	0.071	1.28	0.05
	oo ii oo ii oo ii	0.067	0.352	-0.140	0.066	1.66	0.04	0.075	0.395	-0.202	0.074	1.37	0.07	0.075	0.394	-0.209	0.074	1.40	0.07
	oo oo ii oo oo ii	0.067	0.361	-0.153	0.066	1.58	0.05	0.074	0.399	-0.211	0.073	1.34	0.06	0.075	0.399	-0.221	0.073	1.36	0.05
	oo oo oo ii oo oo	0.068	0.369	-0.163	0.066	1.50	0.04	0.074	0.404	-0.218	0.072	1.30	0.06	0.075	0.405	-0.232	0.072	1.32	0.05
	oi oi oi oi oi oi	0.067	0.352	-0.138	0.066	1.66	0.05	0.074	0.395	-0.200	0.074	1.38	0.08	0.075	0.393	-0.207	0.074	1.41	0.05
	oi io oi io oi io	0.067	0.347	-0.141	0.066	1.67	0.14	0.075	0.391	-0.216	0.074	1.43	0.07	0.075	0.390	-0.222	0.075	1.46	0.08
oi ii ii io ii ii	0.067	0.331	-0.109	0.066	1.83	0.14	0.075	0.384	-0.185	0.076	1.46	0.07	0.075	0.380	-0.183	0.076	1.51	0.08	
c-P6·T6 ¹²⁺	ii ii ii ii ii ii	0.082	0.425	-0.300	0.080	1.45	0.24	0.105	0.552	-0.523	0.106	0.95	0.01	0.104	0.544	-0.514	0.105	0.99	0.02
	oo oo oo oo oo oo	0.082	0.449	-0.365	0.078	0.94	0.02	0.103	0.553	-0.609	0.098	0.70	0.01	0.103	0.550	-0.610	0.098	0.71	0.01
	oo ii oo ii oo ii	0.082	0.438	-0.341	0.079	1.18	0.02	0.104	0.552	-0.577	0.102	0.82	0.01	0.104	0.547	-0.574	0.101	0.84	0.01
	oo oo ii oo oo ii	0.082	0.443	-0.355	0.079	1.09	0.03	0.104	0.553	-0.594	0.101	0.77	0.02	0.104	0.549	-0.592	0.100	0.79	0.02
	oo oo oo ii oo oo	0.082	0.446	-0.359	0.078	1.02	0.02	0.103	0.553	-0.600	0.099	0.74	0.01	0.103	0.549	-0.599	0.099	0.75	0.01
	oi oi oi oi oi oi	0.082	0.439	-0.348	0.079	1.16	0.03	0.105	0.556	-0.601	0.102	0.78	0.01	0.105	0.550	-0.597	0.102	0.80	0.00
	oi io oi io oi io	0.083	0.440	-0.354	0.079	1.14	0.02	0.104	0.554	-0.587	0.102	0.79	0.01	0.104	0.549	-0.584	0.101	0.82	0.00
oi ii ii io ii ii	0.083	0.431	-0.325	0.080	1.33	0.06	0.105	0.552	-0.544	0.105	0.90	0.01	0.104	0.545	-0.537	0.104	0.94	0.00	

4.3.1 1245-index distribution plots

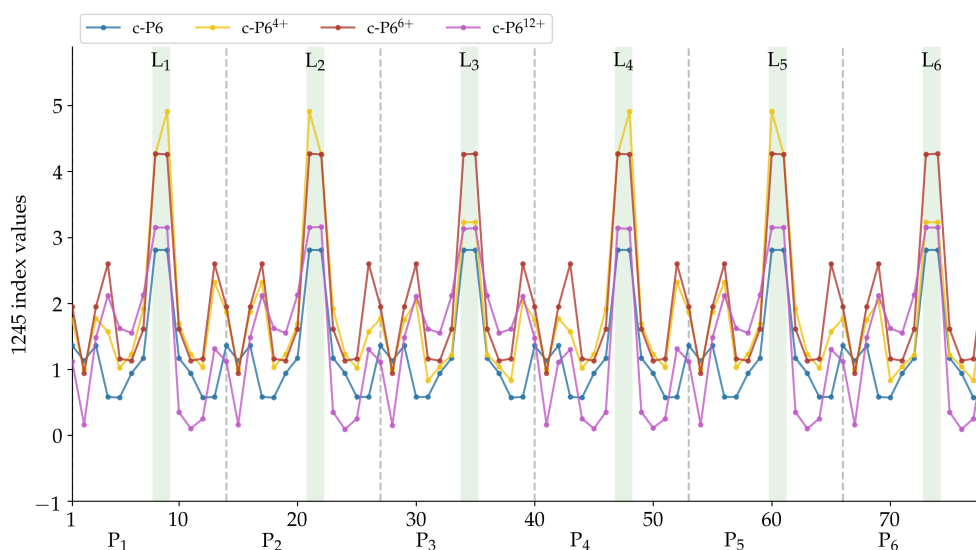


Figure S5 1245-index distribution including the individual MCI(1,2,4,5) values along the most aromatic path of c-P6, c-P6⁴⁺, c-P6⁶⁺, and c-P6¹²⁺ calculated at the B3LYP/6-31G* level of theory.

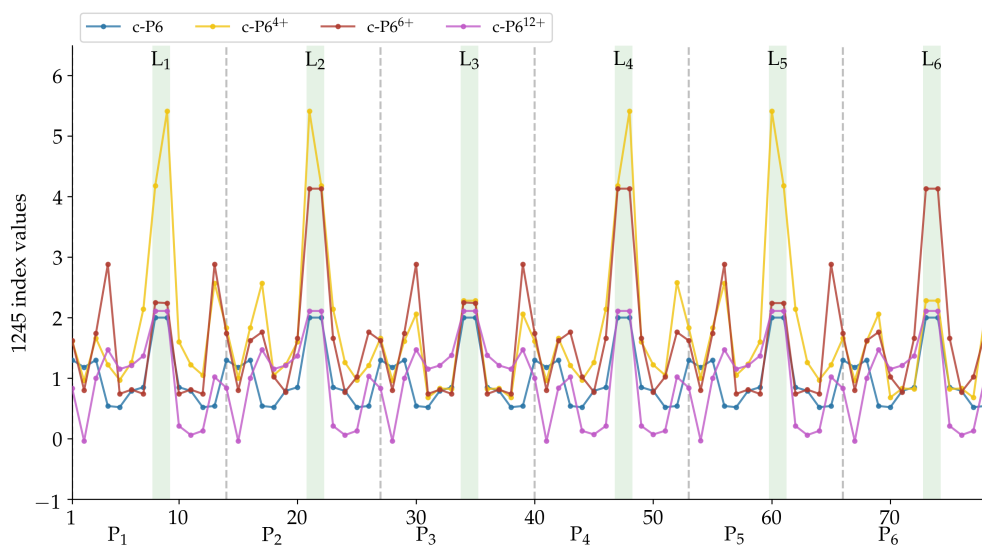


Figure S6 1245-index distribution including the individual MCI(1,2,4,5) values along the most aromatic path of c-P6, c-P6⁴⁺, c-P6⁶⁺, and c-P6¹²⁺ calculated at the M06-2X/6-31G* level of theory.

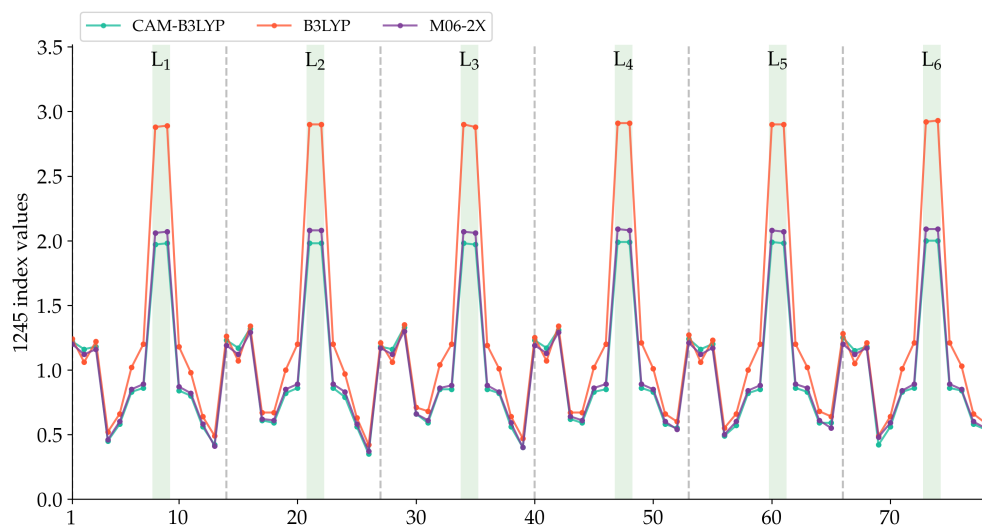


Figure S7 Comparison of the 1245-index distributions including the individual MCI(1,2,4,5) values along the most aromatic path of c-P6·T6 calculated at different levels of theory.

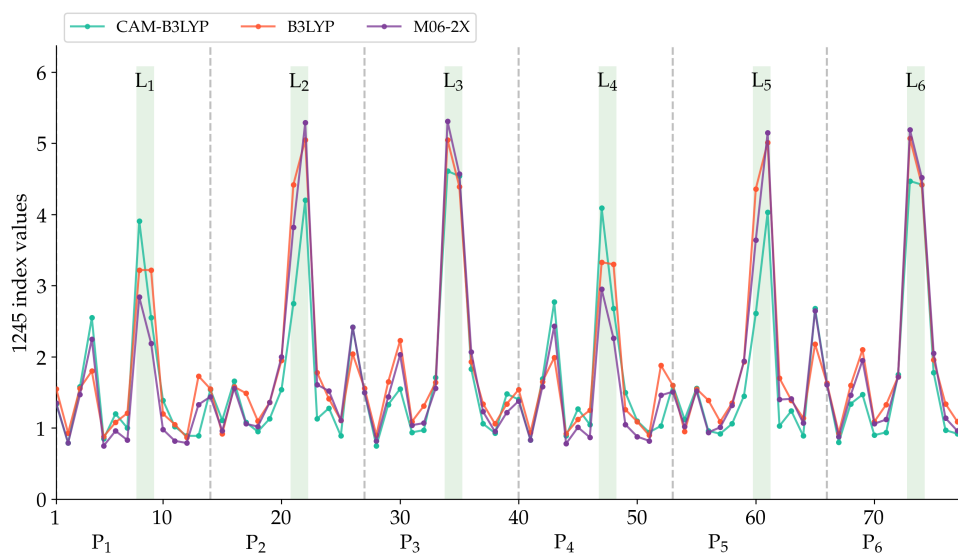


Figure S8 Comparison of the 1245-index distributions including the individual MCI(1,2,4,5) values along the most aromatic path of c-P6·T6⁴⁺ calculated at different levels of theory.

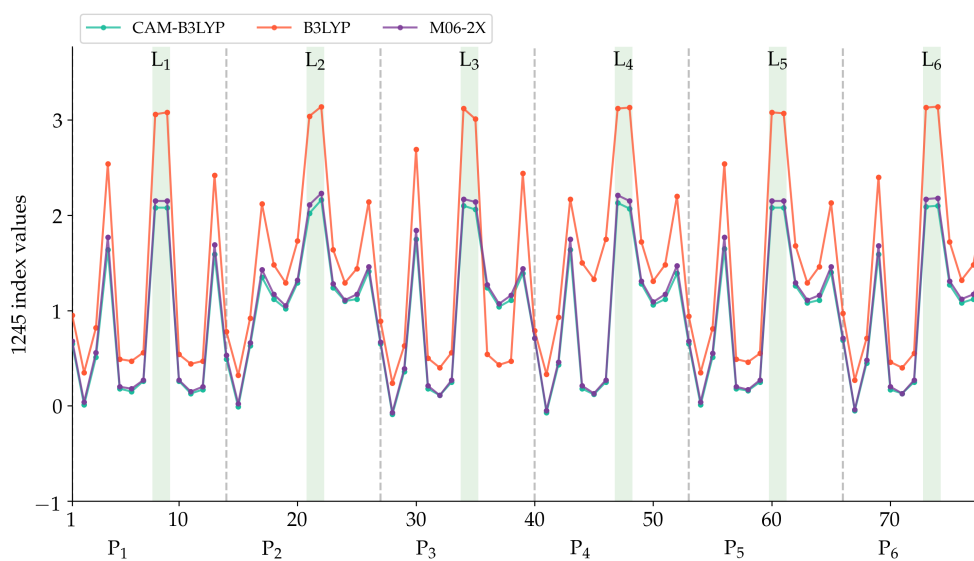


Figure S9 Comparison of the 1245-index distributions including the individual MCI(1,2,4,5) values along the most aromatic path of c-P6·T6¹²⁺ calculated at different levels of theory.

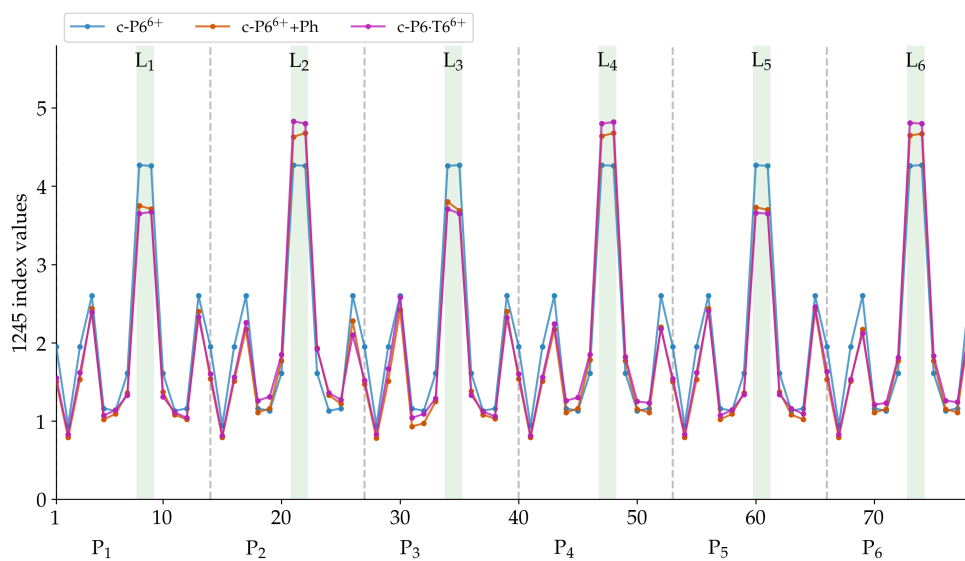


Figure S10 1245-index distribution including the individual MCI(1,2,4,5) values along the most aromatic path of c-P6⁶⁺, c-P6⁶⁺ with Ph substituents, and c-P6·T6⁶⁺ calculated at the B3LYP/6-31G* level of theory.

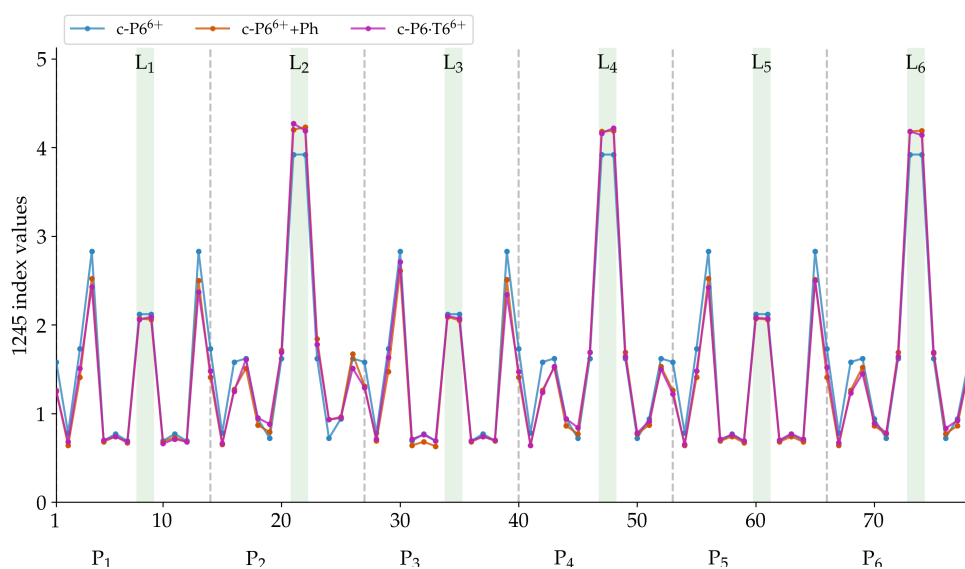


Figure S11 1245-index distribution including the individual MCI(1,2,4,5) values along the most aromatic path of c-P6⁶⁺, c-P6⁶⁺ with Ph substituents, and c-P6·T6⁶⁺ calculated at the CAM-B3LYP/6-31G* level of theory.

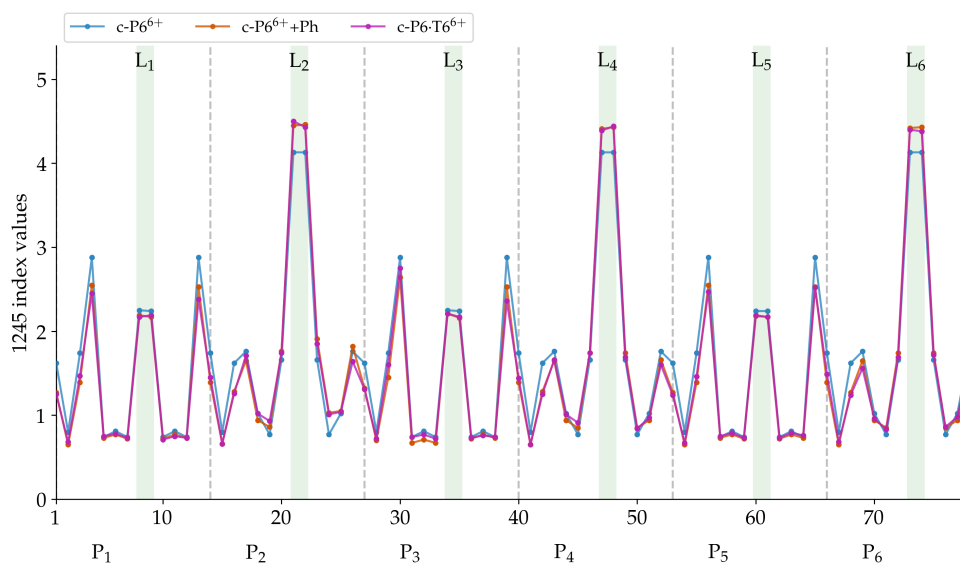


Figure S12 1245-index distribution along the most aromatic path of $c\text{-P6}^{6+}$, $c\text{-P6}^{6+}$ with Ph substituents, and $c\text{-P6}\cdot\text{T6}^{6+}$ calculated at the M06-2X/6-31G* level of theory.

4.3.2 ACID plots

ACID calculations were performed using the CSGT method with B3LYP and CAM-B3LYP density functional approximations in combination with the 6-31G* basis set, including Grimme's dispersion (no solvent model was employed). In Figures S13 and S14, we present two perspectives of the ACID plots for the four oxidation states of the nanoring at the B3LYP/6-31G* computational level. The former picture can be used to assess the local aromaticity of the porphyrin, whereas the latter is useful in analyzing the global aromaticity of nanoring. Similar pictures of the CAM-B3LYP geometries can be found in the manuscript.

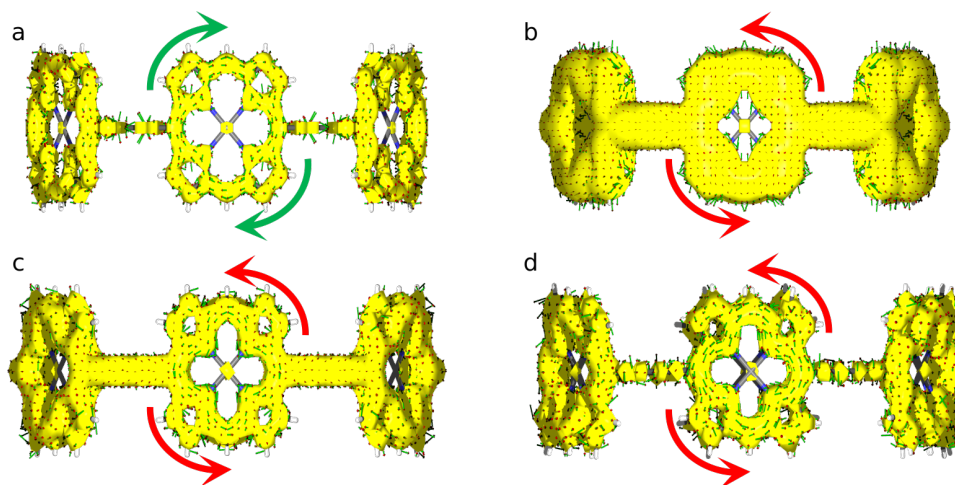


Figure S13 ACID isosurface plots (isocontour value 0.06) for a) $c\text{-P6}$, b) $c\text{-P6}^{4+}$, c) $c\text{-P6}^{6+}$, and d) $c\text{-P6}^{12+}$ at the B3LYP/6-31G* level of theory (employed for both geometry optimization and ACID calculation).

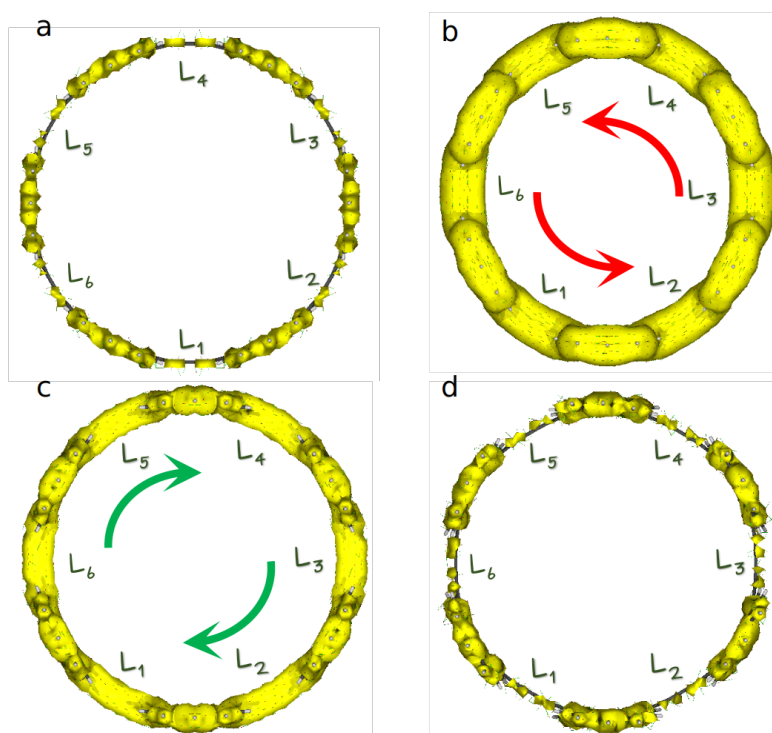
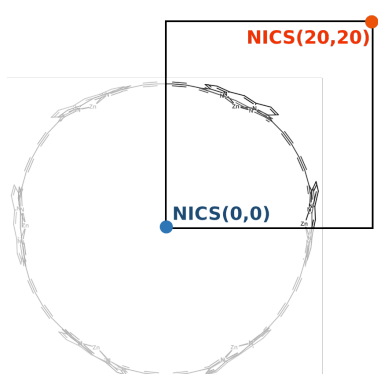


Figure S14 ACID isosurface plots (isocontour value 0.06) for a) c-P6, b) c-P6⁴⁺, c) c-P6⁶⁺, and d) c-P6¹²⁺ using B3LYP/6-31G* level of theory (employed for both geometry optimization and ACID calculation).

4.3.3 NICS

NICS values calculated with CAM-B3LYP and B3LYP density functional approximations in combination with the 6-31G* basis set. NICS(0,0) refers to the NICS value computed at the center of the nanoring (blue circle), whereas NICS(20,20) corresponds to the NICS value calculated at point (20,20) (orange circle) of a frame centered at the center of the nanoring with x- and y-axis pointing towards one linker and the center of a porphyrin, respectively (see Figure S15). Therefore, (20,20) corresponds to a point outside the nanoring at a fairly large distance. The distance unit is Ångstroms (Å).



Species	CAM-B3LYP		B3LYP	
	NICS(0,0)	NICS(20,20)	NICS(0,0)	NICS(20,20)
c-P6	-1.68	-0.08	-1.42	-0.09
c-P6 ⁴⁺	0.88	-0.12	102.24	-6.46
c-P6 ⁶⁺	-0.42	-0.01	-13.36	0.86
c-P6 ¹²⁺	0.47	0.02	1.37	0.08

Figure S15 & Table S14 NICS(0,0) and NICS(20,20) values.

5 Aromaticity indices

In the present section, the aromaticity indices used in the manuscript will be briefly reviewed. Henceforth, we will use the short-hand notation $\mathbf{1} \equiv (\vec{r}_1, \sigma_1)$ to denote the coordinates of an electron and $d\mathbf{1} \equiv d\vec{r}_1, d\sigma_1$ for the electron positions and their derivatives. To provide a general expression, we will consider a molecule including at least one ring structure consisting of n atoms, represented by the string $\mathcal{A} = \{A_1, A_2, \dots, A_n\}$ and whose elements are ordered according to the connectivity of the atoms in the ring.

First of all, we will define the delocalization index (DI)^{18,19,23} using the exchange-correlation density (XCD)⁴⁹ between points belonging to two different atoms A_1 and A_2 ,

$$\delta(A_1, A_2) = 2 \int_{A_1} \int_{A_2} d\mathbf{1} d\mathbf{2} \rho_{xc}(\mathbf{1}, \mathbf{2}) = -2cov(N_{A_1}, N_{A_2}), \quad (1)$$

where N_{A_1} and N_{A_2} are the atomic populations of atoms A_1 and A_2 . The delocalization index is related to the covariance of these populations and, for this reason, the DI is a measure of the number of electrons fluctuating between these atoms concurrently. On the other hand, the localization index (LI) is defined as

$$\lambda(\mathcal{A}) = \int_A \int_A d\mathbf{1} d\mathbf{2} \rho_{xc}(\mathbf{1}, \mathbf{2}), \quad (2)$$

where we integrate the two points of the XCD over the same atom A_1 .

Secondly, we define the geometric aromaticity indices: the so-called harmonic oscillator model of aromaticity (HOMA)⁵⁰ and the bond-length alternation (BLA). Kruszewski and Krygowski defined the former, and they used bond-length references, R_{opt} , to compare with the actual bond length of the ring structure:

$$HOMA(\mathcal{A}) = 1 - \frac{1}{n} \sum_i^n \alpha_i (r_{opt} - r_{A_i, A_{i+1}})^2, \quad (3)$$

where $r_{A,B}$ is the distance between atoms A and B , and α_i is an empirical constant fixed to give values close to one for aromatic species and small or negative values for non-aromatic and antiaromatic species. The geometrical data of reference (R_{opt}) is such that the compression energy of the double bond and the expansion energy of the single bond are minimal in accordance with the harmonic potential model. The bond-length alternation indicator compares the bond-length among the consecutive bonds along the perimeter of the ring,

$$BLA(\mathcal{A}) = \frac{1}{2n} \sum_{i=1}^n |r_{A_i, A_{i+1}} - r_{A_{i+1}, A_{i+2}}|, \quad (4)$$

where $n_1 = \lfloor (n+1)/2 \rfloor$ and $n_2 = \lfloor n/2 \rfloor$, $\lfloor n \rfloor$ being floor function of x , which returns the largest integer less than or equal to x .

We now consider the electronic aromaticity indices. The bond-order alternation (BOA) is one of the most popular aromatic indicators, and it corresponds to the electronic structure analogous to BLA. BOA uses bond orders or electron-sharing indices²³ rather than the bond length,

$$BOA(\mathcal{A}) = \frac{1}{2n} \sum_{i=1}^n |\delta(A_i, A_{i+1}) - \delta(A_{i+1}, A_{i+2})|. \quad (5)$$

Aromaticity indicators based on bond orders, such as BLA or FLU (see below), do not have a strong dependency on the computational method used.⁵¹

Just as we had the electronic counterpart of BLA, we have the counterpart of HOMA, the aromatic fluctuation index (FLU), which goes beyond the bond length information employed in HOMA.^{16,17} The FLU index also employs references to measure the electron delocalization:

$$FLU(\mathcal{A}) = \frac{1}{n} \sum_{i=1}^n \left[\left(\frac{\delta(A_i)}{\delta(A_{i-1})} \right)^\alpha \left(\frac{\delta(A_i, A_{i-1}) - \delta_{ref}(A_i, A_{i-1})}{\delta_{ref}(A_i, A_{i-1})} \right) \right]^2 \quad (6)$$

where α is a simple function to ensure the first term in Eq. 6 is always greater or equal to 1,

$$\alpha \begin{cases} 1 & \delta(A_{i-1}) \leq \delta(A_i) \\ -1 & \delta(A_i) < \delta(A_{i-1}) \end{cases} \quad (7)$$

and $\delta_{ref}(A,B)$ is the DI of an aromatic molecule of reference. For C-C bonds, benzene is used as a reference while the C-N value is taken from pyridine.¹⁶ When the molecule is aromatic, the FLU index will be close to zero, whereas for non-aromatic or antiaromatic species it will be greater than zero.

Giambiagi employed one of the most reliable electronic multicenter indices as an aromaticity index. This many-center electron delocalization index (I_{ring}) measures the delocalization along the ring:⁵²

$$I_{ring}(\mathcal{A}) = \sum_{i_1 i_2 \dots i_n}^{occ} S_{i_1 i_2}(A_1) S_{i_2 i_3}(A_2) \dots S_{i_n, i_1}(A_n) \quad (8)$$

and if one takes into account all the permutations of the atoms in the ring, thus including delocalization patterns across the ring, we obtain the expression of the multicenter index (MCI):²⁵

$$MCI(\mathcal{A}) = \frac{1}{2n} \sum_{\mathcal{P}(\mathcal{A})} I_{ring}(\mathcal{A}) = \frac{1}{2n} \sum_{\mathcal{P}(\mathcal{A})} \sum_{i_1 i_2 \dots i_n}^{occ} S_{i_1 i_2}(A_1) S_{i_2 i_3}(A_2) \dots S_{i_n, i_1}(A_n) \quad (9)$$

where $\mathcal{P}(\mathcal{A})$ stands for the $n!$ permutations of the elements in the string \mathcal{A} . Like I_{ring} , MCI gives large numbers for aromatic species and the authors claim negative values for antiaromatic molecules.⁵³ However, these two electronic indices are not suitable for large (anti)aromatic molecules because they scale exponentially with the number of atoms in the ring and present large numerical errors derived from the numerical integration of the atomic overlap matrices.

In order to solve the drawbacks of I_{ring} and MCI, one of us defined the AV1245 index¹³ as the average value of the four-atom MCI index between relative positions 1-2 and 4-5 constructed from every five consecutive atoms along the perimeter of the ring. Lately, it has been seen that the average value could hinder some important values and that the minimal value of the index, AV_{min} ,^{14,36} could be more useful. The AV_{min} value corresponds to the least delocalized fragment of the ring. Aromatic molecules present large values of AV_{min} while non-aromatic molecules exhibit low values. Antiaromatic molecules are more difficult to identify because they usually present intermediate values of AV_{min} . To identify the antiaromatic molecules, we could help ourselves using BOA values (if the species are smaller) or the 1245-index distributions plots (from which the average value, AV1245, is obtained) along the ring (see *e.g.*, Figure S12).

Finally, we have the magnetic aromaticity indices. When an (anti)aromatic species is exposed to an external field, this field induces a π -electron ring current that can be measured to characterize the molecule either as an aromatic or antiaromatic molecule. Aromatic molecules will show diatropic ring currents. On the contrary, the antiaromatic species will present paratropic ring currents. The most important and popular magnetic index of aromaticity is the nucleus independent chemical shift (NICS) due to Paul Schleyer and co-workers.²⁷ NICS is defined as the negative value of the absolute shielding computed at a certain point of the space. It is usually calculated at the center of the ring, NICS(0). However, it could also be calculated in other important points (see *e.g.*, Table S14), or one could calculate a NICS scan along some region of the space to obtain a NICS grid plot (see manuscript).⁵⁴ Negative values are a signature of aromaticity, whereas positive values indicate antiaromaticity. Another well-known magnetic index is the Anisotropy of the Induced Current Density (ACID)²⁶. Using the ACID software,²⁶ one can visualize ACID scalar field isosurfaces and the current density vectors (see *e.g.* Figure S14).

Notes and references

- [1] M. D. Peeks, T. D. Claridge, H. L. Anderson, *Nature* **2017**, *541*, 200–205.
- [2] M. J. Frisch, G. W. Trucks, H. B. Schlegel, G. E. Scuseria, M. A. Robb, J. R. Cheeseman, G. Scalmani, V. Barone, G. A. Petersson, H. Nakatsuji, X. Li, M. Caricato, A. V. Marenich, J. Bloino, B. G. Janesko, R. Gomperts, B. Mennucci, H. P. Hratchian, J. V. Ortiz, A. F. Izmaylov, J. L. Sonnenberg, D. Williams-Young, F. Ding, F. Lipparini, F. Egidi, J. Goings, B. Peng, A. Petrone, T. Henderson, D. Ranasinghe, V. G. Zakrzewski, J. Gao, N. Rega, G. Zheng, W. Liang, M. Hada, M. Ehara, K. Toyota, R. Fukuda, J. Hasegawa, M. Ishida, T. Nakajima, Y. Honda, O. Kitao, H. Nakai, T. Vreven, K. Throssell, J. A. Montgomery, Jr., J. E. Peralta, F. Ogliaro, M. J. Bearpark, J. J. Heyd, E. N. Brothers, K. N. Kudin, V. N. Staroverov, T. A. Keith, R. Kobayashi, J. Normand, K. Raghavachari, A. P. Rendell, J. C. Burant, S. S. Iyengar, J. Tomasi, M. Cossi, J. M. Millam, M. Klene, C. Adamo, R. Cammi, J. W. Ochterski, R. L. Martin, K. Morokuma, O. Farkas, J. B. Foresman, D. J. Fox, „Gaussian–16 Revision C.01“, **2016**, gaussian Inc. Wallingford CT.
- [3] A. D. Becke, *J. Chem. Phys.* **1993**, *98*, 5648–5652.
- [4] P. J. Stephens, F. J. Devlin, C. F. Chabalowski, M. J. Frisch, *J. Phys. Chem.* **1994**, *98*, 11623–11627.
- [5] T. Yanai, D. P. Tew, N. C. Handy, *Chem. Phys. Lett.* **2004**, *393*, 51–57.
- [6] Y. Zhao, D. G. Truhlar, *Theor. Chem. Acc.* **2008**, *120*, 215–241.
- [7] S. Grimme, *J. Chem. Phys.* **2006**, *124*, 034108.
- [8] W. J. Hehre, R. Ditchfield, J. A. Pople, *J. Chem. Phys.* **1972**, *56*, 2257–2261.
- [9] F. Neese, *WIREs, Comput. Mol. Sci.* **2018**, *8*, e1327.
- [10] C. Riplinger, B. Sandhoefer, A. Hansen, F. Neese, *J. Chem. Phys.* **2013**, *139*, 134101.
- [11] F. Weigend, A. Köhn, C. Hättig, *J. Chem. Phys.* **2002**, *116*, 3175–3183.
- [12] F. Weigend, R. Ahlrichs, *Phys. Chem. Chem. Phys.* **2005**, *7*, 3297–3305.
- [13] E. Matito, *Phys. Chem. Chem. Phys.* **2016**, *18*, 11839–11846.
- [14] C. García-Fernández, E. Sierda, M. Abadía, B. E. C. Bugenhagen, M. H. Prosenc, R. Wiesendanger, M. Bazarnik, J. E. Ortega, J. Brede, E. Matito, A. Arnau, *J. Phys. Chem. C* **2017**, *121*, 27118–27125.
- [15] I. Casademont-Reig, E. Ramos-Cordoba, M. Torrent-Sucarrat, E. Matito, *Molecules* **2020**, *25*, 711.
- [16] E. Matito, M. Duran, M. Solà, *J. Chem. Phys.* **2005**, *122*, 014109.
- [17] E. Matito, M. Duran, M. Solà, *J. Chem. Phys.* **2006**, *125*, 059901.
- [18] R. F. W. Bader, M. E. Stephens, *J. Am. Chem. Soc.* **1975**, *97*, 7391–7399.
- [19] X. Fradera, M. A. Austen, R. F. W. Bader, *J. Phys. Chem. A* **1999**, *103*, 304–314.
- [20] R. F. W. Bader, *Atoms in Molecules: A Quantum Theory*, Oxford University Press, Oxford, **1990**.
- [21] T. A. Keith, „AIMAll (Version 14.11.23)“, **2014**, tk Gristmill Software, Overland Park KS, USA (aim.tkgristmill.com).
- [22] E. Matito, „ESI-3D: Electron Sharing Indices Program for 3D Molecular Space Partitioning“, **2015**, institute of Computational Chemistry and Catalysis, University of Girona, Catalonia, Spain.
- [23] E. Matito, M. Solà, P. Salvador, M. Duran, *Faraday Discuss.* **2007**, *135*, 325–345.
- [24] M. K. Cyranski, *Chem. Rev.* **2005**, *105*, 3773–3811.
- [25] P. Bultinck, R. Ponsec, S. Van Damme, *J. Phys. Org. Chem.* **2005**, *18*, 706–718.
- [26] D. Geuenich, K. Hess, F. Köhler, R. Herges, *Chem. Rev.* **2005**, *105*, 3758–3772.
- [27] P. v. R. Schleyer, C. Maerker, A. Dransfeld, H. Jiao, N. J. v. E. Hommes, *J. Am. Chem. Soc.* **1996**, *118*, 6317–6318.
- [28] M. J. Frisch, G. W. Trucks, H. B. Schlegel, G. E. Scuseria, M. A. Robb, J. R. Cheeseman, G. Scalmani, V. Barone, B. Mennucci, G. A. Petersson, H. Nakatsuji, M. Caricato, X. Li, H. P. Hratchian, A. F. Izmaylov, J. Bloino, G. Zheng, J. L. Sonnenberg, M. Hada, M. Ehara, K. Toyota, R. Fukuda, J. Hasegawa, M. Ishida, T. Nakajima, Y. Honda, O. Kitao, H. Nakai, T. Vreven, J. A. Montgomery, Jr., J. E. Peralta, F. Ogliaro, M. Bearpark, J. J. Heyd, E. Brothers, K. N. Kudin, V. N. Staroverov, R. Kobayashi, J. Normand, K. Raghavachari, A. Rendell, J. C. Burant, S. S. Iyengar, J. Tomasi, M. Cossi, N. Rega, J. M. Millam, M. Klene, J. E. Knox, J. B. Cross, V. Bakken, C. Adamo, J. Jaramillo, R. Gomperts, R. E. Stratmann, O. Yazyev, A. J. Austin, R. Cammi, C. Pomelli, J. W. Ochterski, R. L. Martin, K. Morokuma, V. G. Zakrzewski, G. A. Voth, P. Salvador, J. J. Dannenberg, S. Dapprich, A. D. Daniels, Ö. Farkas, J. B. Foresman, J. V. Ortiz, J. Cioslowski, D. J. Fox, „Gaussian 09 Revision D.01“, gaussian Inc. Wallingford CT 2009.
- [29] T. Plachetka, in *Proc. of Spring Conf. on Computer Graphics, Budmerice, Slovakia*, Bd. 123Bd. 123, **1998**.
- [30] E. Ramos-Cordoba, V. Postils, P. Salvador, *J. Chem. Theory Comput.* **2015**, *11*, 1501–1508.
- [31] V. Postils, C. Delgado-Alonso, J. M. Luis, P. Salvador, *Angew. Chem. Int. Ed.* **2018**, *130*, 10685–10689.
- [32] J. Charnley, L. Bratholm, „Calculate Root-mean-square deviation (RMSD) of Two Molecules Using Rotation“, [gitHub](#), v1.3.2.
- [33] J. Tomasi, B. Mennucci, R. Cammi, *Chem. Rev.* **2005**, *105*, 2999–3094.
- [34] W. Kabsch, *Acta Crystallographica Section A: Crystal Physics, Diffraction, Theoretical and General Crystallography* **1976**, *32*, 922–923.
- [35] M. W. Walker, L. Shao, R. A. Volz, *CVGIP: image understanding* **1991**, *54*, 358–367.
- [36] I. Casademont-Reig, T. Woller, J. Contreras-García, M. Alonso, M. Torrent-Sucarrat, E. Matito, *Phys. Chem. Chem. Phys.* **2018**, *20*, 2787–2796.
- [37] I. Casademont-Reig, E. Ramos-Cordoba, M. Torrent-Sucarrat, E. Matito, *Aromaticity: Modern Computational Methods and Applications* Aromaticity descriptors based on electron delocalization, S. 235–258, Elsevier, The Netherlands, **2021**.
- [38] M. Torrent-Sucarrat, S. Navarro, F. P. Cossío, J. M. Anglada, J. M. Luis, *J. Comput. Chem.* **2017**, *38*, 2819–2828.
- [39] M. Torrent-Sucarrat, S. Navarro, E. Marcos, J. M. Anglada, J. M. Luis, *J. Phys. Chem. C* **2017**, *121*, 19348–19357.
- [40] C. S. Wannere, K. W. Sattelmeyer, H. F. Schaefer III, P. v. R. Schleyer, *Angew. Chem. Int. Ed.* **2004**, *43*, 4200–4206.
- [41] J. Sancho-García, A. Pérez-Jiménez, *Phys. Chem. Chem. Phys.* **2007**, *9*, 5874–5879.

- [42] D. W. Szczepanik, M. Solà, M. Andrzejak, B. Pawełek, J. Dominikowska, M. Kukułka, K. Dyduch, T. M. Krygowski, H. Szatyłowicz, *J. Comput. Chem.* **2017**, *38*, 1640–1654.
- [43] T. Woller, A. Banerjee, N. Sylvetsky, G. Santra, X. Deraet, F. De Proft, J. M. Martin, M. Alonso, *J. Phys. Chem. A* **2020**, *124*, 2380–2397.
- [44] O. A. Vydrov, G. E. Scuseria, *J. Chem. Phys.* **2006**, *125*, 234109.
- [45] T. M. Henderson, A. F. Izmaylov, G. Scalmani, G. E. Scuseria, *J. Chem. Phys.* **2009**, *131*, 044108.
- [46] A. J. Cohen, P. Mori-Sánchez, W. Yang, *Science* **2008**, *321*, 792–794.
- [47] M. Rickhaus, M. Jirasek, L. Tejerina, H. Gotfredsen, M. D. Peeks, R. Haver, H.-W. Jiang, T. D. Claridge, H. L. Anderson, *Nat. Chem.* **2020**, *12*, 236–241.
- [48] R. Krishnan, J. S. Binkley, R. Seeger, J. A. Pople, *J. Chem. Phys.* **1980**, *72*, 650–654.
- [49] K. Ruedenberg, *Rev. Mod. Phys.* **1962**, *34*, 326–376.
- [50] J. Kruszewski, T. M. Krygowski, *Tetrahedron Lett.* **1972**, *13*, 3839–3842.
- [51] E. Matito, M. Solà, M. Duran, P. Salvador, *J. Phys. Chem. A* **2006**, *110*, 5108–5113.
- [52] M. Giambiagi, M. S. de Giambiagi, C. D. dos Santos Silva, A. P. de Figueiredo, *Phys. Chem. Chem. Phys.* **2000**, *2*, 3381–3392.
- [53] R. Ponec, P. Bultinck, A. G. Saliner, *J. Phys. Chem. A* **2005**, *109*, 6606.
- [54] J. O. C. Jiménez-Halla, E. Matito, L. Blancafort, J. Robles, M. Solà, *J. Comput. Chem.* **2009**, *30*, 2764–2776.

Appendix D

Supporting Information Chapter 9

Supporting Information: Computational modeling of UV-Vis spectra and redox potentials

Irene Casademont-Reig,^{a,b} Arnau Call,^c Carla Casadevall,^c Sergio Fernández,^c Julio Lloret-Fillol,^{*c,d} Eloy Ramos-Cordoba^{*a,b} and Eduard Matito^{*a,e}

^a Donostia International Physics Center (DIPC), 20018 Donostia, Euskadi, Spain.

^b Polimero eta Material Aurreratuak: Fisika, Kimika eta Teknologia, Kimika Fakultatea, Euskal Herriko Unibertsitatea UPV/EHU, P.K. 1072, 20080 Donostia, Euskadi, Spain.

^c Institute of Chemical Research of Catalonia (ICIQ), The Barcelona Institute of Science and Technology, Avinguda Paisos Catalans 16, 43007 Tarragona, Catalonia, Spain.

^d Catalan Institution for Research and Advanced Studies (ICREA), Passeig Lluís Companys, 23, 08010 Barcelona, Spain.

^e Ikerbasque, Basque Foundation for Science, Plaza Euskadi 5, 48009 Bilbao, Euskadi, Spain.

Basis set validation

To validate the basis set chosen for the optimization calculations, we compared the most important distances (Cu-P and Cu-N) of the optimized geometry with the X-Ray data of two photosensitizers.

Table S1. Cu-N and Cu-P bond distances in Ångstroms (Å) of PS₈ and PS₁₀ from experimental data and computational data using B3LYP-GD3/LANL2DZ. We also include the difference between the experimental and the computational values (Δ_d):

PS	bond	X-Ray distance	optimized distance	Δ_d
PS ₈	Cu-N ₁	2.107	2.090	0.016
	Cu-N ₂	2.126	2.099	0.028
	Cu-P ₁	2.222	2.376	0.154
	Cu-P ₂	2.290	2.375	0.085
PS ₁₀	Cu-N ₁	2.075	2.096	0.021
	Cu-N ₂	2.086	2.106	0.020
	Cu-P ₁	2.294	2.394	0.100
	Cu-P ₂	2.256	2.338	0.083

As we can appreciate in Table S1, the optimized geometry presents Cu–P bond distances longer than the Cu–N bond in comparison with experimental data. Nevertheless, both sets of distances, the experimental and the computational, are in a reasonable agreement. Hence, the basis set used for the geometry optimization of the complexes is good enough for the present purposes. Even though the experimental data should be taken as a reference to the computational calculations, one should bear in mind that the experimental data results from several macroscopic measurements, which are the response of more than one molecule, and the interaction between the solvent and the molecule plays a role. In contrast, computational results are obtained from the treatment of only one molecule and to account for solvent effects we performed simulations with the PCM model. In addition, there is always an uncertainty associated to the measurement. Therefore, we do not expect, neither we pretend, to obtain an absolute agreement of our computational data with the available experiment. Instead, we will focus on obtaining a similar qualitative picture from both analyses.

Optimization of the attenuating parameter

As stated, the attenuating parameter has been optimized in order to obtain a more accurate description of the UV-Vis absorption spectrum and to try the performance of LC- ω PBE-opt in the redox potential calculations.

In the following table (Table S2), we have summarized the results obtained from the calculations of the optimization of the ω parameter. To obtain the ω_{opt} value, the J^* function should be minimal.

All the optimization processes of the ω parameter required 17 or 18 optimization steps. The number of steps that the script needs to optimize the attenuating parameter depends on the initial range of ω that we have chosen and on the accuracy of the ω parameter requested. Since most current calculations run in parallel, we have also performed calculations with four cores and we have evaluated the cpu time per core of the optimization process and the spectra calculations (see Table S2).

Table S2. Cpu time/proc (h) of the whole ω optimization calculation and the calculation that allows to simulate the UV-Vis spectrum. In addition, there is the number of basis functions used for each photosensitizer using LANL2DZ basis set and the total SCF cycles of the optimization process:

PS	ω_{opt} cpu time/proc (h)	Total SCF cycles	spectrum calculation cpu time/proc (h)	basis functions
PS ₁	34.3	1136	4.7	604
PS ₂	46.1	1410	6.9	672
PS ₃	46.0	1161	7.7	728
PS ₄	52.1	1244	10.0	798
PS ₅	128.3	2080	6.5	838
PS ₆	41.1	1045	5.5	630
PS ₇	35.0	904	4.5	698
PS ₈	41.0	955	9.7	754
PS ₉	56.5	1168	12.0	824
PS ₁₀	42.5	1067	9.5	642
PS ₁₁	65.0	1249	13.7	820
PS ₁₂	75.9	1448	8.4	728
PS ₁₃	67.8	1186	9.8	796
PS ₁₄	75.7	1149	12.3	852
PS ₁₅	80.7	1140	13.0	922
PS ₁₆	89.7	1125	10.2	962

Cpu time per core is the effective calculation time per core, which is the average time per core when we split the total cost of a parallelized calculation. The time will increase with the number of SFC cycles done, the number of basis functions, and the number of ω optimization steps. We will assume that the number of ω optimization steps is constant in all the studied complexes, as it barely changes from complex to complex. Overall, with the data of copper dyes, we estimate that the simulation of UV-Vis absorption spectrum with ω_{opt} is seven times more expensive than the simulation of the same spectrum with the default value of the ω parameter.

In the following table, we have all important data of the ω parameter optimization process for all the photosensitizers (copper and iridium families).

Table S3. From left to right, ionization potential (IP) of the system with N electrons, the electron affinity with N electrons (EA), the optimized attenuating parameter minimizing J*, the HOMO energy of the system with N electrons ($\varepsilon_{HOMO}(N)$) and with N+1 electrons ($\varepsilon_{HOMO}(N+1)$), and the value of J* function of PSs:

PS	IP(N)(au)	EA(N)(au)	$\omega_{opt}(\text{au}^{-1})$	$\varepsilon_{HOMO}(N)(\text{au})$	$\varepsilon_{HOMO}(N+1)(\text{au})$	J*(au)
PS ₁	0.3627	0.1155	0.2524	-0.3576	-0.1259	0.0116
PS ₂	0.3799	0.1528	0.2664	-0.3763	-0.1606	0.0086
PS ₃	0.3602	0.1148	0.2583	-0.3527	-0.1304	0.0173
PS ₄	0.3733	0.1426	0.2676	-0.3685	-0.1535	0.0120
PS ₅	0.4956	0.3151	0.2286	-0.4898	-0.3255	0.0120
PS ₆	0.3486	0.1145	0.2155	-0.3456	-0.1204	0.0066
PS ₇	0.3638	0.1467	0.2110	-0.3598	-0.1532	0.0076
PS ₈	0.3560	0.1174	0.2469	-0.3489	-0.1315	0.0158
PS ₉	0.3699	0.1309	0.2277	-0.3616	-0.1477	0.0188
PS ₁₀	0.3516	0.1296	0.2086	-0.3475	-0.1370	0.0084
PS ₁₁	0.2029	-0.0303	0.2811	-0.1961	0.0125	0.0190
PS ₁₂	0.3526	0.1193	0.2385	-0.3475	-0.1306	0.0124
PS ₁₃	0.3604	0.1503	0.2142	-0.3553	-0.1597	0.0106
PS ₁₄	0.3413	0.1203	0.2159	-0.3381	-0.1295	0.0097
PS ₁₅	0.3524	0.1442	0.2191	-0.3490	-0.1529	0.0094
PS ₁₆	0.4859	0.3065	0.2151	-0.4798	-0.3176	0.0127
PS ₁₇	0.3507	0.1462	0.2059	-0.3496	-0.1479	0.0020
PS ₁₈	0.3507	0.1570	0.2003	-0.3489	-0.1601	0.0036
PS ₁₉	0.3292	0.1176	0.1969	-0.3272	-0.1204	0.0034

Additionally, in Table S4, we have all important data of the ω parameter optimization process for the cobalt catalyst family.

Table S4. From left to right, ionization potential (IP) of the system with N electrons, the electron affinity with N electrons (EA), the optimized attenuating parameter minimizing J*, the HOMO energy of the system with N electrons ($\varepsilon_{HOMO}(N)$) and with N+1 electrons ($\varepsilon_{HOMO}(N+1)$), and the value of J* function of cobalt complexes family:

1^X	IP(N)(au)	EA(N)(au)	$\omega_{opt}(\text{au}^{-1})$	$\varepsilon_{HOMO}(N)(\text{au})$	$\varepsilon_{HOMO}(N+1)(\text{au})$	J*(au)
1^H	0.5327	0.2440	0.2447	-0.5037	-0.2902	0.0545
1^{CO2Et}	0.5315	0.2456	0.2401	-0.5009	-0.2964	0.0593
1^{CN}	0.5447	0.2546	0.2414	-0.5108	-0.3089	0.0640
1^{CF3}	0.5467	0.2557	0.2446	-0.5135	-0.3084	0.0622
1^{Cl}	0.5367	0.2495	0.2421	-0.5071	-0.2963	0.0554
1^{DMM}	0.5238	0.2436	0.2500	-0.4976	-0.2841	0.0483

As we can see, the J^* function attains a minimum, but in any case is exactly zero because we work with two systems, N and $N+1$ electron systems. To obtain a zero, the same parameter ω should force the condition fulfilled by the exact functional in both systems simultaneously.

UV-Vis absorption spectra and redox potentials

Here we present the data of the UV-Vis absorption spectra of the copper photosensitizers that have not been synthesized.

Table S5. For copper PSs, maximum wavelength (λ , in nm) corresponding to a CT excitation for B3LYP and LC- ω PBE-opt with LANL2DZ, and the reduction potentials ($E_{(Cu^I/Cu^0)}^o(V)$) with the same functionals:

PS	$\lambda_{max}(nm)$		$E_{(Cu^I/Cu^0)}^o(V)$	
	B3LYP	LC- ω PBE-opt	B3LYP	LC- ω PBE-opt
PS ₁	424.99	360.15	-1.78	-1.58
PS ₂	506.07	403.65	-1.23	-1.19
PS ₃	435.12	361.95	-1.62	-1.56
PS ₄	481.08	379.46	-1.53	-1.46
PS ₅	524.66	450.01	-0.82	-0.76
PS ₆	428.85	376.91	-1.71	-1.66
PS ₇	507.95	435.70	-1.35	-1.27
PS ₉	452.34	362.92	-1.50	-1.55
PS ₁₂	405.62	337.96	-1.92	-1.61
PS ₁₃	529.19	453.61	-1.10	-1.09
PS ₁₄	440.47	402.13	-1.51	-1.46
PS ₁₅	504.24	426.82	-1.35	-1.29
PS ₁₆	503.45	450.31	-0.74	-0.75

For all the studied PS and the cobalt catalyst family we have plotted the UV-Vis absorption spectrum with LC- ω PBE-opt (optimal value of ω), LC- ω PBE (default value of ω) and B3LYP in combination with LAN2DZ in solvent phase.

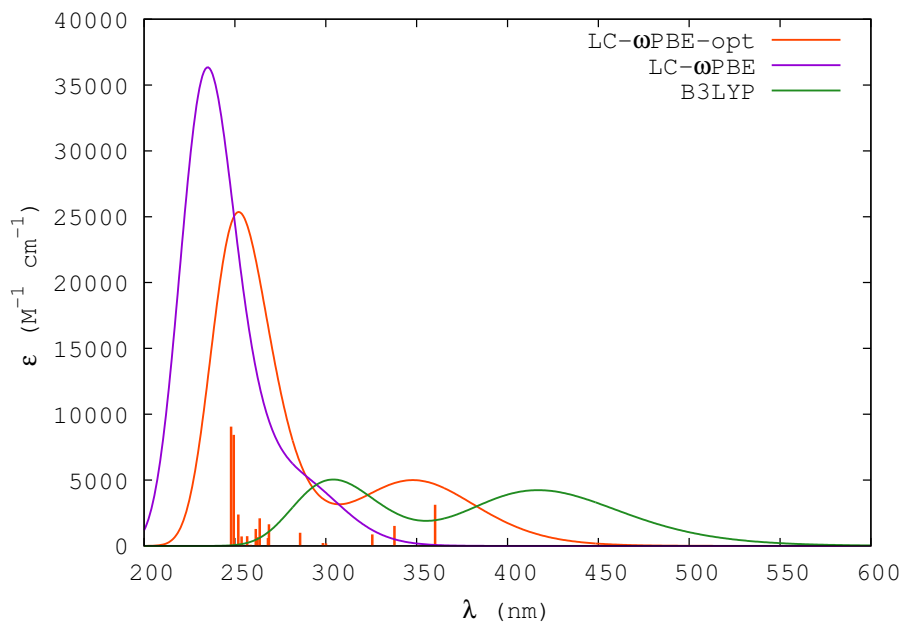


Figure S1. Simulated UV-Vis absorption spectra of PS₁ with LC- ω PBE-opt, LC- ω PBE, and B3LYP functionals. The spectra are plotted using a standard deviation of 0.4eV. For LC- ω PBE-opt functional, we have also plotted the orange vertical lines corresponding to the different vertical excitations.

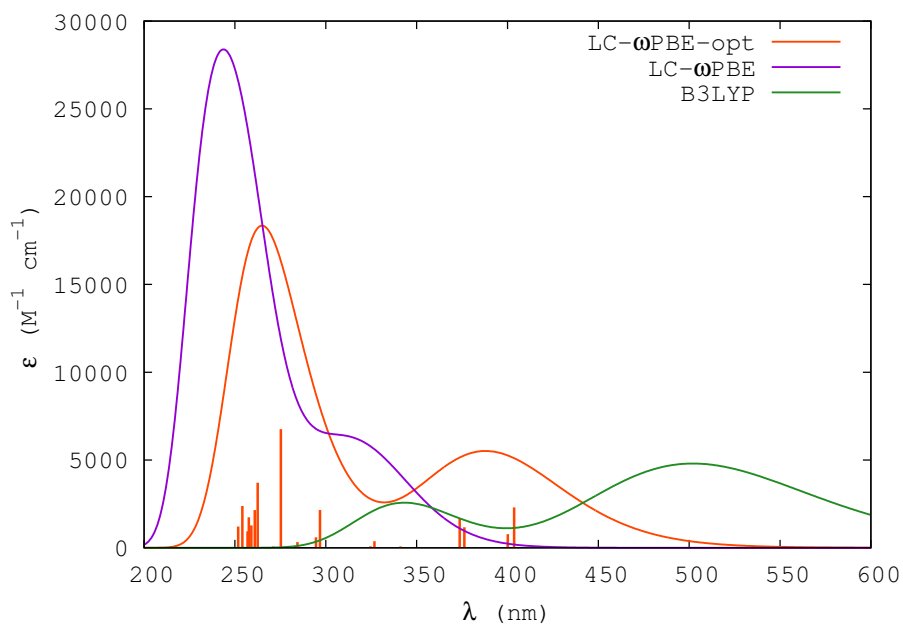


Figure S2. Simulated UV-Vis absorption spectra of PS₂ with LC- ω PBE-opt, LC- ω PBE, and B3LYP functionals. The spectra are plotted using a standard deviation of 0.4 eV. For LC- ω PBE-opt functional, we have also plotted the orange vertical lines corresponding to the different vertical excitations.

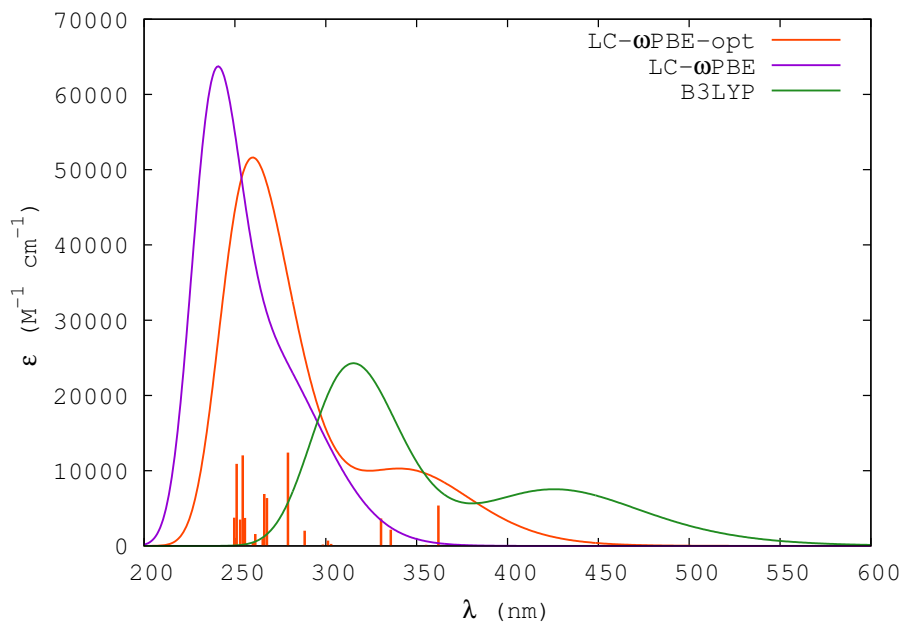


Figure S3. Simulated UV-Vis absorption spectra of PS₃ with LC- ω PBE-opt, LC- ω PBE, and B3LYP functionals. The spectra are plotted using a standard deviation of 0.4 eV. For LC- ω PBE-opt functional, we have also plotted the orange vertical lines corresponding to the different vertical excitations.

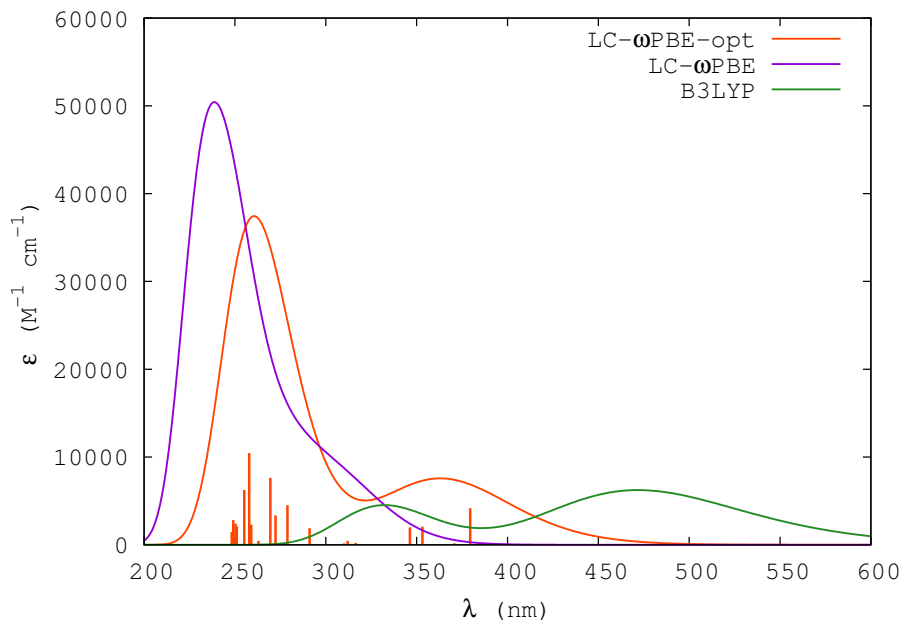


Figure S4. Simulated UV-Vis absorption spectra of PS₄ with LC- ω PBE-opt, LC- ω PBE, and B3LYP functionals. The spectra are plotted using a standard deviation of 0.4 eV. For LC- ω PBE-opt functional, we have also plotted the orange vertical lines corresponding to the different vertical excitations.

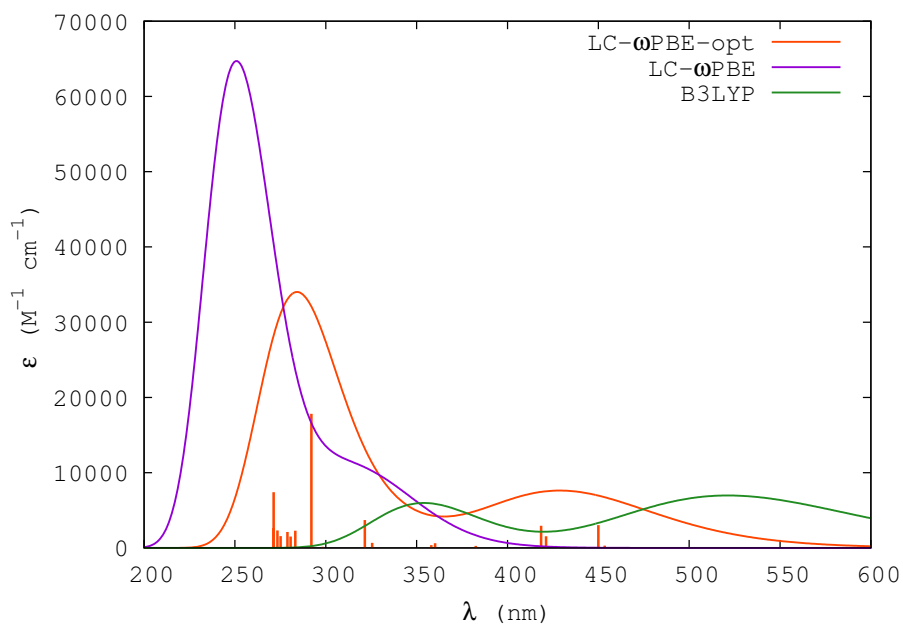


Figure S5. Simulated UV-Vis absorption spectra of PS₅ with LC- ω PBE-opt, LC- ω PBE, and B3LYP functionals. The spectra are plotted using a standard deviation of 0.4 eV. For LC- ω PBE-opt functional, we have also plotted the orange vertical lines corresponding to the different vertical excitations.

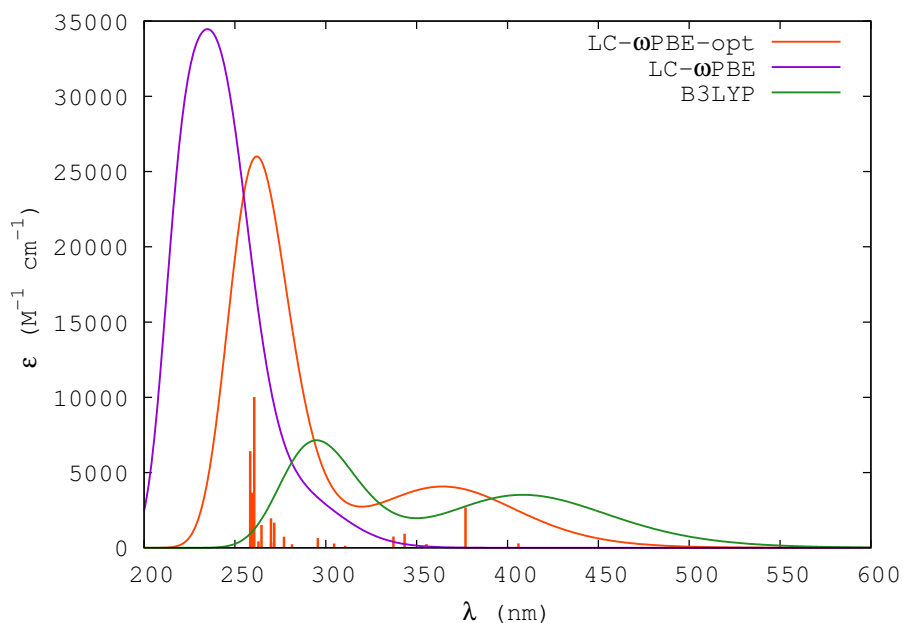


Figure S6. Simulated UV-Vis absorption spectra of PS₆ with LC- ω PBE-opt, LC- ω PBE, and B3LYP functionals. The spectra are plotted using a standard deviation of 0.4 eV. For LC- ω PBE-opt functional, we have also plotted the orange vertical lines corresponding to the different vertical excitations.

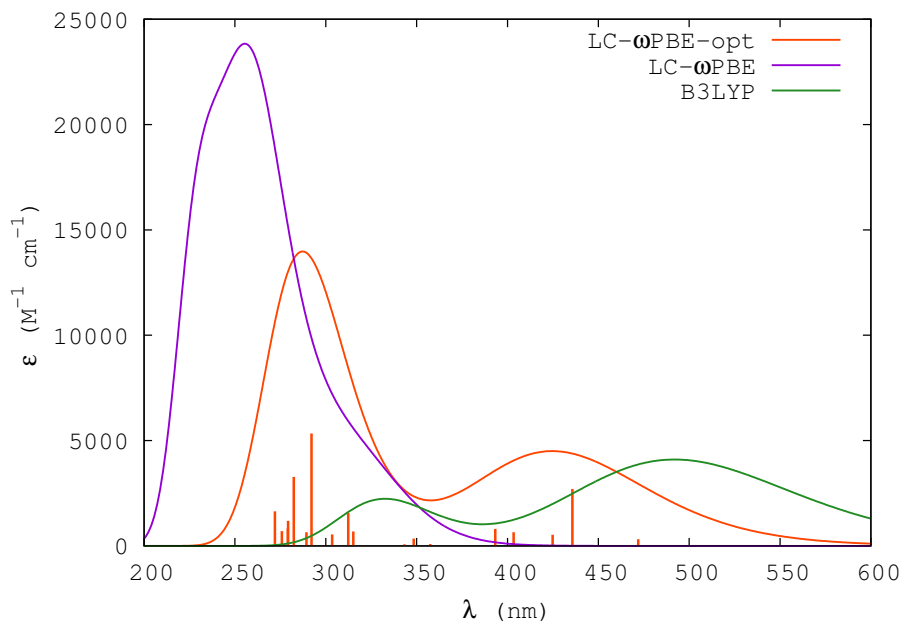


Figure S7. Simulated UV-Vis absorption spectra of PS₇ with LC- ω PBE-opt, LC- ω PBE, and B3LYP functionals. The spectra are plotted using a standard deviation of 0.4 eV. For LC- ω PBE-opt functional, we have also plotted the orange vertical lines corresponding to the different vertical excitations.

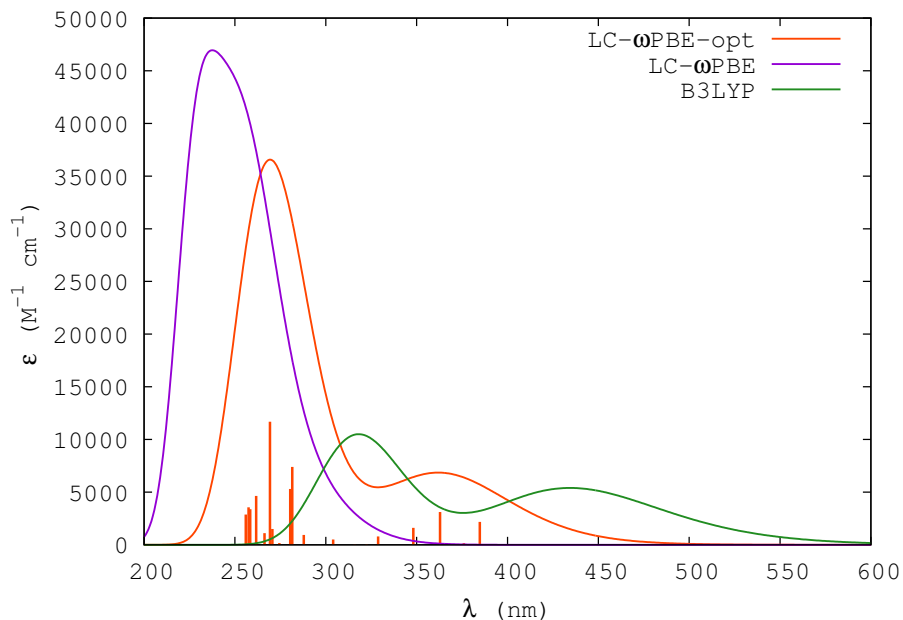


Figure S8. Simulated UV-Vis absorption spectra of PS₉ with LC- ω PBE-opt, LC- ω PBE, and B3LYP functionals. The spectra are plotted using a standard deviation of 0.4 eV. For LC- ω PBE-opt functional, we have also plotted the orange vertical lines corresponding to the different vertical excitations.

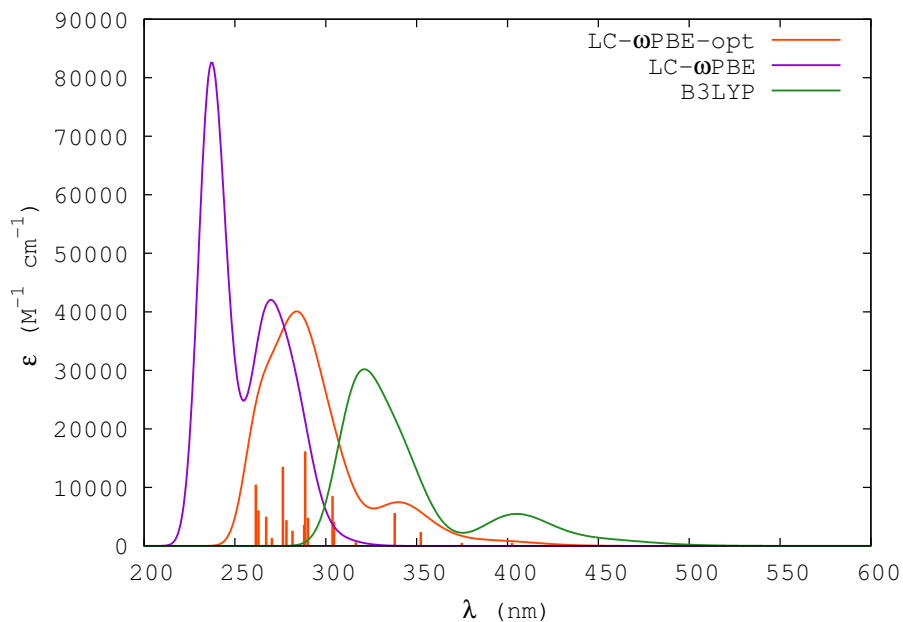


Figure S9. Simulated UV-Vis absorption spectra of PS₁₂ with LC- ω PBE-opt, LC- ω PBE, and B3LYP functionals. The spectra are plotted using a standard deviation of 0.2 eV. For LC- ω PBE-opt functional, we have also plotted the orange vertical lines corresponding to the different vertical excitations.

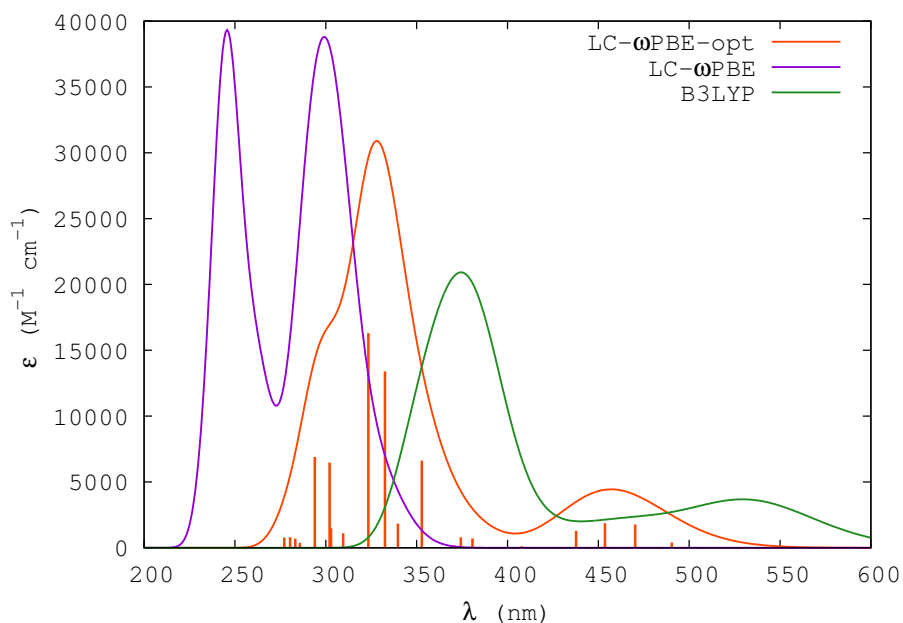


Figure S10. Simulated UV-Vis absorption spectra of PS₁₃ with LC- ω PBE-opt, LC- ω PBE, and B3LYP functionals. The spectra are plotted using a standard deviation of 0.2 eV. For LC- ω PBE-opt functional, we have also plotted the orange vertical lines corresponding to the different vertical excitations.

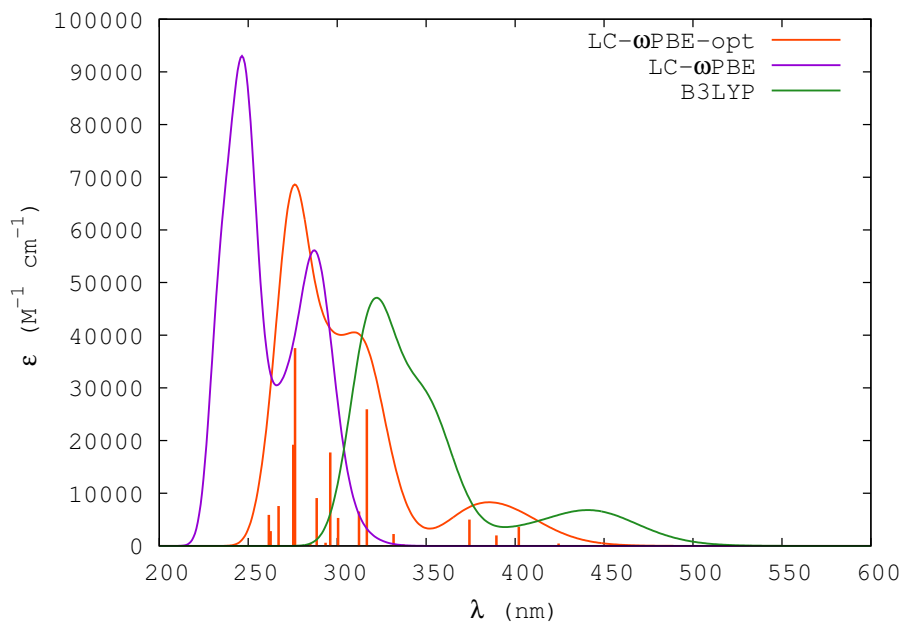


Figure S11. Simulated UV-Vis absorption spectra of PS₁₄ with LC- ω PBE-opt, LC- ω PBE, and B3LYP functionals. The spectra are plotted using a standard deviation of 0.2 eV. For LC- ω PBE-opt functional, we have also plotted the orange vertical lines corresponding to the different vertical excitations.

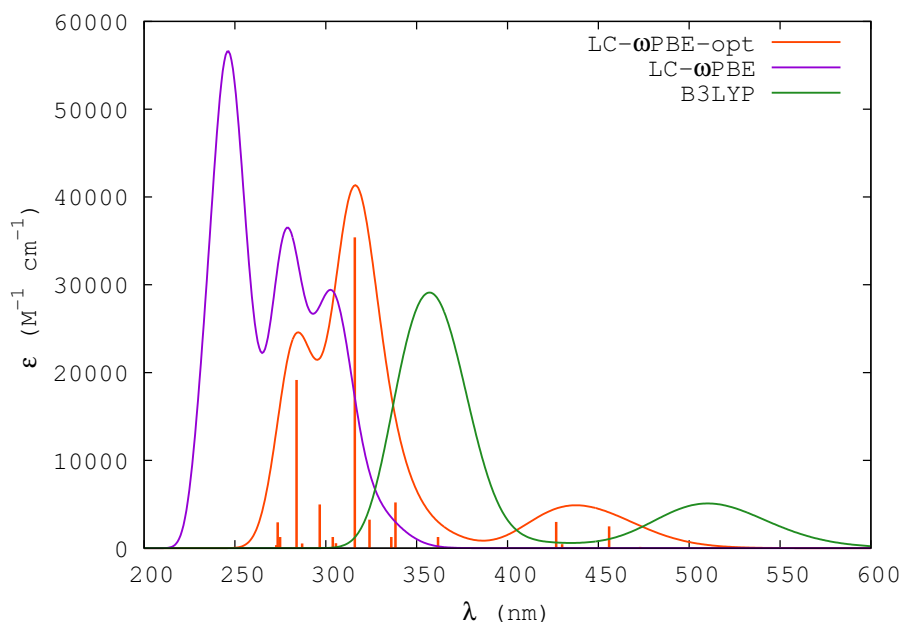


Figure S12. Simulated UV-Vis absorption spectra of PS₁₅ with LC- ω PBE-opt, LC- ω PBE, and B3LYP functionals. The spectra are plotted using a standard deviation of 0.2 eV. For LC- ω PBE-opt functional, we have also plotted the orange vertical lines corresponding to the different vertical excitations.

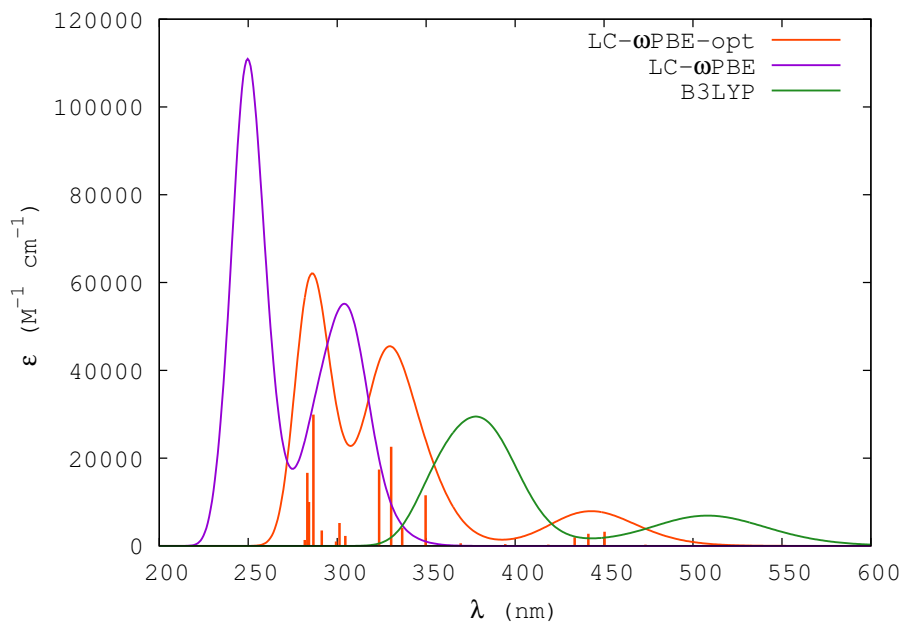


Figure S13. Simulated UV-Vis absorption spectra of PS_{16} with LC- ω PBE-opt, LC- ω PBE, and B3LYP functionals. The spectra are plotted using a standard deviation of 0.2 eV. For LC- ω PBE-opt functional, we have also plotted the orange vertical lines corresponding to the different vertical excitations.

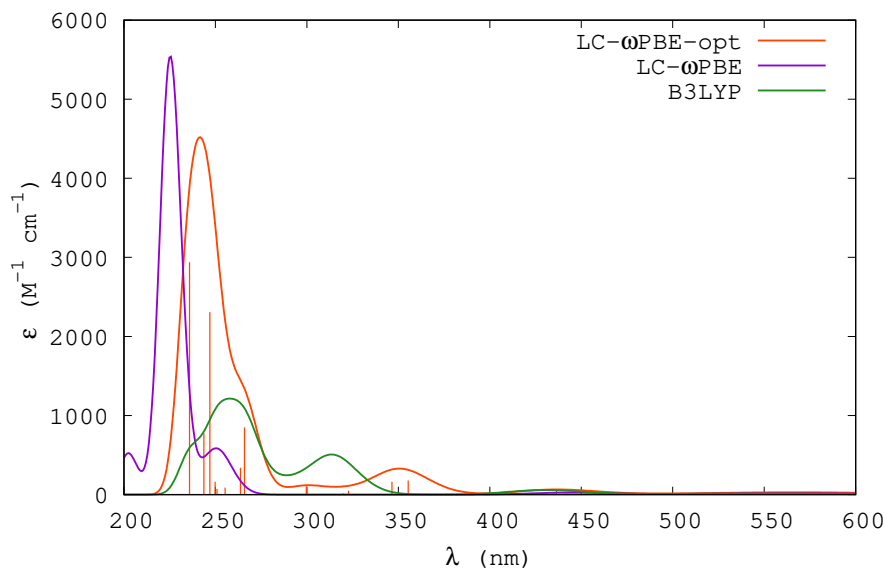


Figure S14. Simulated UV-Vis absorption spectra of 1^H with LC- ω PBE-opt, LC- ω PBE, and B3LYP functionals. The spectra are plotted using a standard deviation of 0.2 eV. For LC- ω PBE-opt functional, we have also plotted the orange vertical lines corresponding to the different vertical excitations.

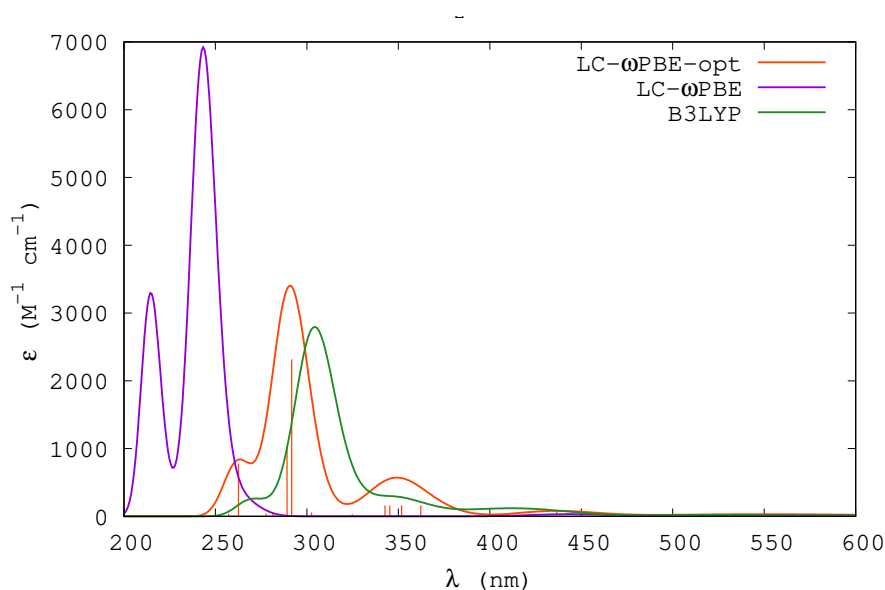


Figure S15. Simulated UV-Vis absorption spectra of 1^{CO_2Et} with LC- ω PBE-opt, LC- ω PBE, and B3LYP functionals. The spectra are plotted using a standard deviation of 0.2 eV. For LC- ω PBE-opt functional, we have also plotted the orange vertical lines corresponding to the different vertical excitations.

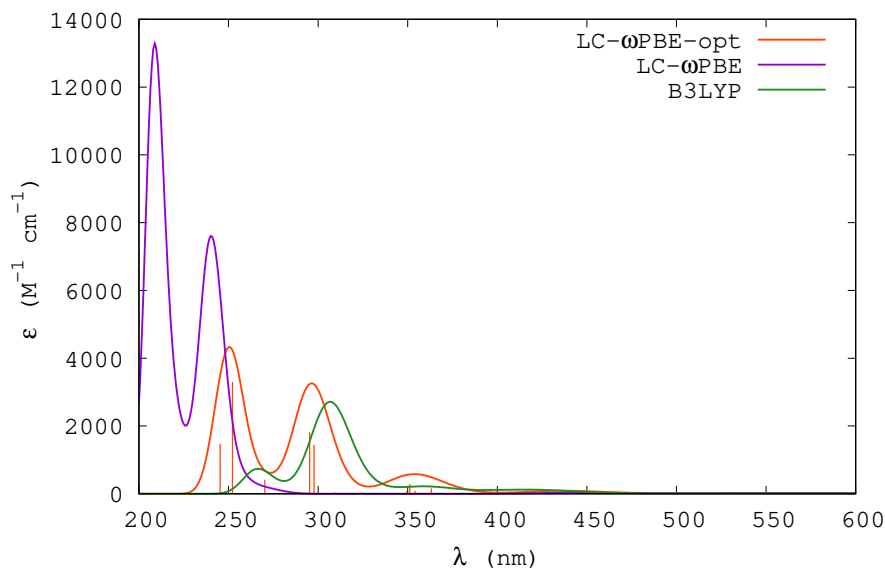


Figure S16. Simulated UV-Vis absorption spectra of 1^{CN} with LC- ω PBE-opt, LC- ω PBE, and B3LYP functionals. The spectra are plotted using a standard deviation of 0.2 eV. For LC- ω PBE-opt functional, we have also plotted the orange vertical lines corresponding to the different vertical excitations.

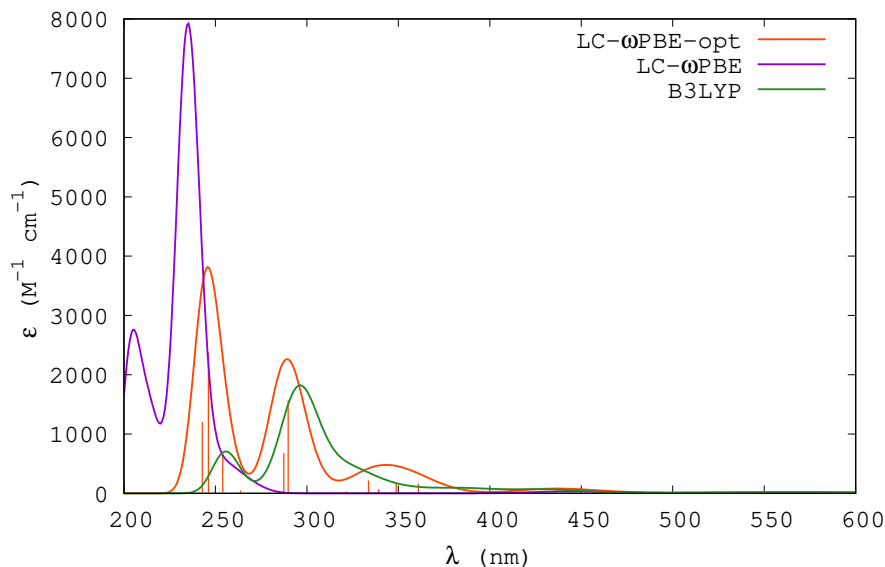


Figure S17. Simulated UV-Vis absorption spectra of 1^{CF3} with LC- ω PBE-opt, LC- ω PBE, and B3LYP functionals. The spectra are plotted using a standard deviation of 0.2 eV. For LC- ω PBE-opt functional, we have also plotted the orange vertical lines corresponding to the different vertical excitations.

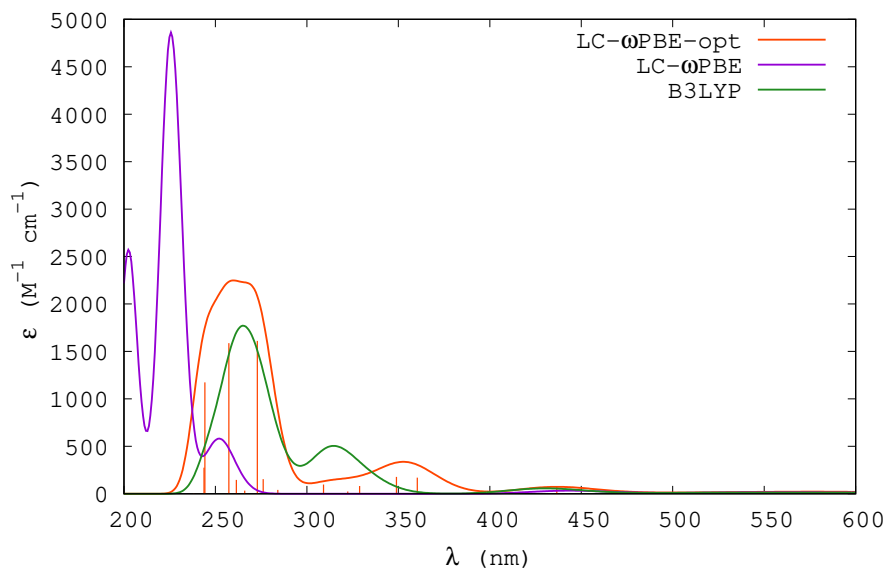


Figure S18. Simulated UV-Vis absorption spectra of 1^{Cl} with LC- ω PBE-opt, LC- ω PBE, and B3LYP functionals. The spectra are plotted using a standard deviation of 0.2 eV. For LC- ω PBE-opt functional, we have also plotted the orange vertical lines corresponding to the different vertical excitations.

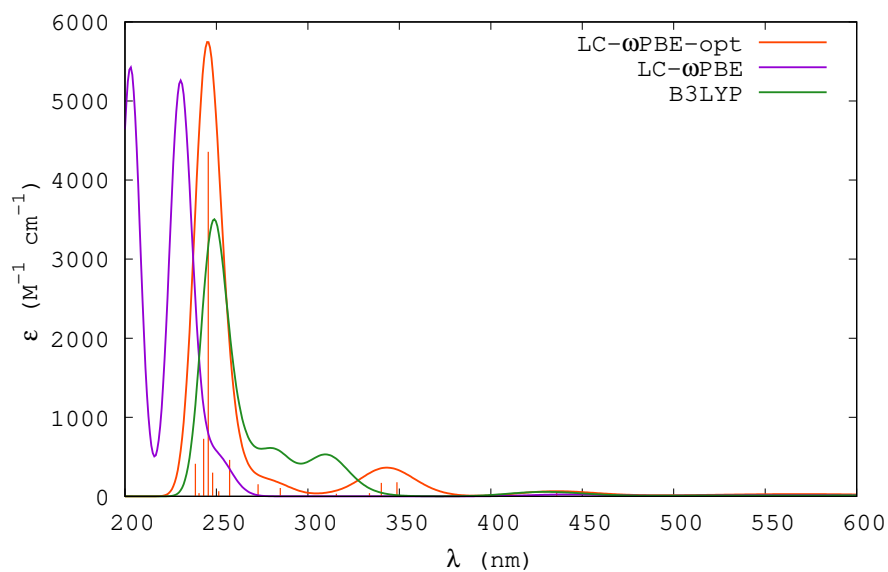


Figure S19. Simulated UV-Vis absorption spectra of 1^{DMM} with LC- ω PBE-opt, LC- ω PBE, and B3LYP functionals. The spectra are plotted using a standard deviation of 0.2 eV. For LC- ω PBE-opt functional, we have also plotted the orange vertical lines corresponding to the different vertical excitations.

